

Influence of Particle Shape and Texture on Broken Sandstone Strength Behavior

by

Saleh Balideh

A thesis submitted in partial fulfillment of the requirements for the degree of

Doctor of Philosophy

in

Mining Engineering

Department of Civil and Environmental Engineering
University of Alberta

© Saleh Balideh, 2015

ABSTRACT

A good understanding of the behavior of broken rock helps us to make more informed decisions regarding geo-structures. The geometry of particles and confining pressure play a significant role on the behavior of broken rock. Angularity, form and texture are three parameters that represent the geometry of a particle. Investigating the effect of particle geometry on the frictional sliding, rolling resistance and packing density not only is important to determine the behavior of broken rock but also is the key point to understand the post peak behavior of a rock mass at low confining pressure. Previous work showed that the particle shape formed after peak strength dominate the post peak behavior of a rock mass at low confining pressure; therefore, the investigation of the broken rock particle geometry can help explain the post peak behavior of a rock mass. The particle geometry characteristics have different impacts on the broken rock behavior. For example, an increase of the aspect ratio increases the rolling resistance while decreases the packing density.

The following question drives this dissertation: How does the particle geometry affect the broken rock behavior?

In order to answer the question, this study pursues three objectives:(i) determining the particle geometry through employing image processing techniques; (ii) determining peak strength of broken rock through triaxial compression tests; and (iii) investigating the broken rock behavior through using the particle geometry.

The main contribution of this thesis to the body of knowledge is a better understanding of broken rock behavior through investigating the impact of particle geometry characteristics on the broken rock behavior at low confining pressure.

This Thesis is lovingly dedicated:

To my wonderful parents, Fatemeh and Ayyoub

Who taught me that even the largest task can be accomplished if it is done one step at a time

To my lovely wife, Sona

Who gave me hope and encouragement to be successful

To my sister and brother and brother in law, Maryam, Bahram and
Morteza

Who always being there for me and because of them I will always have friends

And to Sons's family, Forough, Abazar and Roshan

Who always believed and supported me

ACKNOWLEDGMENT

I would like to express my special appreciation and thanks to my advisors Dr. Tim Joseph and Dr. Jozef Szymanski, who have been a tremendous mentor for me. They supported me throughout my thesis with their patience and knowledge and providing me with an excellent atmosphere for doing research. Their advice on both research as well as on my career have been priceless. Without their supervision and constant help this dissertation would not have been possible.

I would like to express the deepest appreciation to my committee members Dr. Derek Martin, Dr. Peter Cain and Dr. Ward Wilson for their appreciable inspiration and support. They were always willing to help and give their best suggestions.

Saleh Balideh, January 2015

Table of Contents

LIST OF TABLES.....	ix
LIST OF FIGURES.....	x
LIST OF SYMBOLS.....	xvi
CHAPTER 1 : INTRODUCTION	1
1.1 Introduction.....	2
1.2 Statement of the problem.....	3
1.3 Objectives of the study.....	3
1.4 Postulates and assumptions of the study.....	4
1.5 Scope and limitations of the study	4
1.6 Research methodology.....	5
1.7 Original scientific contributions and industrial significance of the study.....	6
CHAPTER 2 : LITERATURE REVIEW	7
2.1 Introduction.....	8
2.2 Behavior of broken rock	8
2.3 Post-peak behavior of intact rock.....	14
2.4 Post failure of a rock mass	18
2.5 Determining the geometry of a particle	23
2.5.1 Methods to determine the form of particles:.....	24
2.5.2 Methods to determine the angularity of particles:.....	28
2.5.3 Methods to determine the texture of particles:.....	32
2.6 Summary and Conclusions.....	34
CHAPTER 3 : TRIAXIAL TESTS ON BROKEN ROCK AND NECESSARY CORRECTION	36
3.1 Introduction.....	37
3.2 Triaxial Testing Procedures and Specimen Preparing	42
3.3 Failed Tests Prematurely.....	54
3.4 Triaxial Test Results	57
3.5 Membrane correction	60
3.6 Summary and Conclusions.....	71

CHAPTER 4 : DETERMINING THE PARTICLE SHAPE CHARACTERISTICS OF SPECIMENS.....	72
4.1 Introduction.....	73
4.2 Developed code using MATLAB.....	73
4.3 Representative sample of specimen.....	80
4.4 Statistical analysis on the image processing results.....	83
4.5 Comparing the specimens with actual Rockfill.....	90
4.5.1 Case study of some actual Rockfill.....	91
4.5.2 Size distribution of actual Rockfill based on production method.....	97
4.5.3 Shape characteristic of actual Rockfill.....	103
4.6 Summary and Conclusions.....	106
 CHAPTER 5 : BEHAVIOR OF BROKEN ROCK BASED ON PARTICLES GEOMETRY.....	 108
5.1 Introduction.....	109
5.2 Effect of confining pressure on the peak strength of broken rock.....	109
5.3 Effect of shape characteristics on the peak strength of broken rock.....	115
5.3.1 Effect of form index.....	119
5.3.2 Effect of angularity index.....	121
5.3.3 Effect of Void ratio.....	123
5.4 Shear strength of broken rock.....	126
5.5 Effect of water on the strength of broken rock.....	132
5.5.1 Effect of pore pressure on the strength of broken rock.....	132
5.5.2 Effect of water on the strength of particles.....	134
5.6 Summary and Conclusions.....	136
 CHAPTER 6 : CONCLUSION AND DISCUSSION.....	 138
6.1 Summary of Research.....	139
6.2 A review on the behavior of broken rock.....	141
6.2.1 Frictional behavior of broken rock.....	141
6.2.2 Void ratio and strength of broken rock.....	142
6.2.3 Dilation of broken rock.....	148
6.3 Conclusions.....	152
6.4 Contributions of PhD Research.....	153
6.5 Recommendations for Future Research.....	154
 BIBLIOGRAPHY.....	 156

APPENDIX (A) TRIAXIAL TESTS USING HOEK CELL.....	165
APPENDIX (B) PREMATURELY FAILED TESTS.....	171
APPENDIX (C) TRIAXIAL TESTS ON BROKEN SANDSTONE	182
APPENDIX (D) SECIMENS PARTICLES	197
APPENDIX (E) DEVELOPED CODE USING MATLAB	244
APPENDIX (F) PARTICLE SIZE DISTRIBUTION OF SPECIMENS	266

LIST OF TABLES

Table 2-1- Suggested criteria by rock type, after Hobbs (1970).....	9
Table 2-2- Suggested value for post failure of rock mass, after Hoek et al., (2001).	20
Table 3-1- Selected standards for triaxial test on intact rock.....	38
Table 3-2- Summary of acceptable results of compression tests on intact sandstone.....	49
Table 3-3- Summary of the physical and mechanical properties of sandstone.....	51
Table 3-4- The ultimate strength of the specimens determined by triaxial tests.....	58
Table 4-1- The particles geometry of the specimens determined by image processing technique	87
Table 4-2- Statistical parameters of particle geometry of the specimens	87
Table 4-3- Categorized specimens in group (A).....	88
Table 4-4- Categorized specimens in group (B)	88
Table 4-5- Categorized specimens in group (C)	88
Table 4-6- A summary of the specimens particles size.....	89
Table 4-7- Size distribution parameters for actual dams	93
Table 4-8- Size distribution parameters for actual overburden waste dumps	94
Table 4-9- Size distribution parameters for actual block caving	96
Table 4-10- Shape and angularity characteristics of Pradesh dam.....	106
Table 4-11- Shape and angularity characteristics of Salma dam	106
Table 5-1- Categorized specimens in group (A).....	115
Table 5-2- Categorized specimens in group (B)	116
Table 5-3- Categorized specimens in group (C)	116
Table 5-4- Form index and angularity index of typical particles.....	117
Table 5-5- Average of form-index and angularity-index of group (A), (B) and (C), and fitted power function parameters	119
Table 5-6- The calculated internal friction angle from result of triaxial tests.....	128
Table 6-1- 2D particle geometry at different aspect ratios and different shape parameters (m).....	145

LIST OF FIGURES

Figure 1-1: Concept of pre-peak and post- peak regions in the stress-strain curve.	2
Figure 2-1- Variation of internal friction angle with respect to confining pressure, after Hussaini (1983).....	10
Figure 2-2- Increase in ultimate strength of the broken rock due to particle size increase, after Hussaini (1983).....	11
Figure 2-3- Variation of peak strength of broken rock with respect to void ratio, after Fumagalli (1969).....	12
Figure 2-4- Stress-strain curves for intact and broken rock, after Joseph (2000).	13
Figure 2-5- Boundary condition of effective friction angle, after Joseph (2000).	14
Figure 2-6- Stress-strain curve of intact rock in four regions until peak strength, after Brace et al., (1963).....	15
Figure 2-7- The post peak region at stress-strain curve, after Bieniawski et al., (1968) and Rajendra et al., (2006).....	16
Figure 2-8- Stress-strain curve, after Price et al., (1979) and Farmer et al., (1968).	17
Figure 2-9- The influence of specimen size on the strength of rock, after Bieniawski et al., (1968).....	19
Figure 2-10- The concept of the particle geometry parameters: Form, Angularity and Texture	23
Figure 2-11- Two particles with the same form and different angularity.	24
Figure 2-12- Two particles with the same form and different texture.	24
Figure 2-13- Relationship between aspect ratio and form factor	25
Figure 2-14- The concept of radius of the particle at θ direction.....	26
Figure 2-15- Relationship between aspect ratio and form index	27
Figure 2-16- Relationship between aspect ratio and Roundness parameter.....	28
Figure 2-17- Relationship between internal angle and angularity index	29
Figure 2-18- Relationship between internal angle and angularity parameter	30
Figure 2-19- Relationship between internal angle and Convexity.....	31
Figure 2-20- Relationship between particle texture and standard deviation of Intensity..	32

Figure 2-21- Relationship between particle texture and texture parameter	34
Figure 3-1- Triaxial test on broken sandstone by Hoek-Franklin Cell, with confining pressure set at 345 kPa.....	39
Figure 3-2- Triaxial test on broken sandstone by Hoek-Franklin Cell, with confining pressure set at 275 kPa.....	40
Figure 3-3- Triaxial test on broken sandstone by Hoek-Franklin Cell, with confining pressure set at 138 kPa.....	40
Figure 3-4- The triaxial soil cell used in this research.....	41
Figure 3-5- Triaxial test equipment for broken rock.....	41
Figure 3-6- Uniaxial compression tests on the intact sandstone, D=20mm and L=46 mm	43
Figure 3-7- Uniaxial compression tests on the intact sandstone, D=20mm and L=45 mm	43
Figure 3-8- Uniaxial compression tests on the intact sandstone, D=20mm and L=40 mm	44
Figure 3-9- Failure mode of the intact sandstone after uniaxial compression tests, D=20mm and L=46 mm.....	44
Figure 3-10- Failure mode of the intact sandstone after uniaxial compression tests, D=20mm and L=45 mm.....	45
Figure 3-11- Failure mode of the intact sandstone after uniaxial compression tests, D=20mm and L=40 mm.....	45
Figure 3-12- Triaxial compression tests on the intact sandstone, D=20mm, L=40mm and $\sigma_3=1$ MPa.	46
Figure 3-13- Triaxial compression tests on the intact sandstone, D=20mm, L=40mm and $\sigma_3=3.45$ MPa.	46
Figure 3-14- Failure mode of the intact sandstone after triaxial compression tests, D=20mm, L=40mm and $\sigma_3=1$ MPa.	47
Figure 3-15- Failure mode of the intact sandstone after triaxial compression tests, D=20mm, L=40mm and $\sigma_3=3.45$ MPa.	47
Figure 3-16- Linear relationship between confining pressure (σ_3) and ultimate strength (σ_1) of intact sandstone.....	50
Figure 3-17- Mohr-Coulomb failure envelopes for intact sandstone.....	50
Figure 3-18- Used mould in conducted tests.....	53

Figure 3-19- A punctured membrane with a sharp particle, with a sudden decrease at confining pressure after puncturing	55
Figure 3-20- A punctured membrane with a sharp particle, without a sudden decrease at confining pressure after puncturing	55
Figure 3-21- An eccentric deformation of specimen in triaxial test on broken rock	56
Figure 3-22- Axial stress-strain graph obtained from triaxial compression test on specimen of broken rock at confining pressure equal to 276 kPa	57
Figure 3-23- An example of compression test on intact rock	59
Figure 3-24- The sketch for measuring the extension modulus of a rubber membrane, after Bishop (1962)	61
Figure 3-25- Stress- strain curve of rubber membranes	62
Figure 3-26- Newton per Meter curve for rubber membrane	62
Figure 3-27- Lateral confining pressure correction through compression shell theory	64
Figure 3-28- Lateral confining pressure correction through Hoop tension theory	65
Figure 3-29- A section of membrane in a axisymmetric model	67
Figure 3-30- Boundary conditions of model	68
Figure 3-31- Deformation of membrane by pushing a rigid part	68
Figure 3-32- Membrane buckling in numerical modeling	69
Figure 3-33- Average of lateral correction stress and maximum of lateral strain of membrane	70
Figure 3-34- Average of lateral correction stress and maximum lateral displacement of membrane	70
Figure 4-1- The photo box	74
Figure 4-2- A photo that has been taken over the photo box	75
Figure 4-3- An example of a binary image	75
Figure 4-4- Steps of unwanted small particles deleting	76
Figure 4-5- Filling the existing hole in a particle photo	77
Figure 4-6- An example of a particle that cannot pass sieve while it is smaller than sieve opening	78
Figure 4-7- Size distribution of particles with form index equal to 1.6, using image processing method and sieve method	79

Figure 4-8-Size distribution of particles with form index equal to 2.4, using image processing method and sieve method.....	79
Figure 4-9- Size distribution of particles with form index equal to 2.7, using image processing method and sieve method.....	80
Figure 4-10- Representative part preparing steps	81
Figure 4-11- Form characteristics of representative quarter sample vs. specimen	82
Figure 4-12- Angularity characteristics of representative quarter sample vs. specimen..	82
Figure 4-13- Texture characteristics of representative quarter sample vs. specimen	83
Figure 4-14- Equivalent diameter of representative quarter sample vs. specimen	83
Figure 4-15- Form factor histogram calculated by Freedman-Diaconis method	84
Figure 4-16- Form factor histogram calculated by Scott method	84
Figure 4-17- Form factor histogram calculated by Sturges method.....	85
Figure 4-18- Conceptual figure of two broken rock specimens with the same contact points and parallel particle size distribution.....	90
Figure 4-19- Size distribution of some actual Rockfill dams, this figure was adapted from Tao (2002), Goldin (2012) and Anderson (2012)	92
Figure 4-20- Size distribution of actual overburden waste dumps, this figure was adapted from Habte (2012), Kusuma (2012), Hungr (2002) and Fox (2011).	94
Figure 4-21- Particle size distribution of an actual mine stockpile, this figure was adapted from Pourghahramani (2010).....	95
Figure 4-22- Primary and secondary fragmentation of actual block caving, this figure was adapted from Butcher (2002) and Golder Associates (2012).....	96
Figure 4-23- Rosin-Rammler distribution of the Test 4 specimen.....	98
Figure 4-24- Rosin-Rammler distribution of the Test 6 specimen.....	99
Figure 4-25- Rosin-Rammler distribution of the Test 11 specimen.....	99
Figure 4-26- Rosin-Rammler distribution of the Test 13 specimen.....	100
Figure 4-27- Rosin-Rammler distribution of the Test 14 specimen.....	100
Figure 4-28- Rosin-Rammler distribution of the Test 17 specimen.....	101
Figure 4-29- Gaudin-Schuhmann distribution of some specimens as an example	102
Figure 4-30- Shape of particles in the Pradesh Rockfill dam, this figure was adapted from Honkanadavar (2014).....	104

Figure 4-31- Shape of particles in the Salma Rockfill dam, this figure was adapted from Honkanadavar (2014).....	104
Figure 4-32- Black-White photo of particles in the Pradesh Rockfill dam.....	105
Figure 4-33- Black-White photo of particles in the Salma Rockfill dam	105
Figure 5-1- Linear function fitted on the triaxial tests data results high unconfined compressive strength for broken rock	110
Figure 5-2- A linear function fitted on the triaxial tests data that cannot determine the strength of broken rock accurately at low confining pressure	111
Figure 5-3- The power function fitted on the triaxial tests results can estimate more accurately the strength of broken rock.....	112
Figure 5-4- Prepared specimen for unconfined compression test on broken rock.....	113
Figure 5-5- Result of unconfined compression test on broken rock	113
Figure 5-6- Specimen of broken rock before deformation.....	114
Figure 5-7- Buckling deformation of a broken rock specimen in unconfined compression test.....	114
Figure 5-8- Fitted power function on group (A), (B) and (C) data	118
Figure 5-9- Average of form index of group (A), (B) and (C) versus fitted function parameter (α).....	120
Figure 5-10- Average of form index of group (A), (B) and (C) versus fitted function parameter (β).....	120
Figure 5-11- Average of angularity index of group (A), (B) and (C) versus fitted function parameter (α).....	121
Figure 5-12- Average of angularity index of group (A), (B) and (C) versus fitted function parameter (β).....	122
Figure 5-13-Ratio of broken rock strength to confining pressure versus ratio of form index to angularity index.....	122
Figure 5-14- Relationship between void ratio and fitted function parameter (α).....	123
Figure 5-15 Relationship between void ratio and fitted function parameter (β).....	124
Figure 5-16- Relationship between void ratio and strength of broken rock at different confining pressure.....	125
Figure 5-17- Shear strength of broken rock calculated by triaxial test results.....	129
Figure 5-18- Relationship between peak internal friction angle and confining pressure	129

Figure 5-19- Relationship between peak internal friction angle and confining pressure for group (A), (B) and (C) separately	130
Figure 5-20- Relationship between peak internal friction angle and ratio of form index to angularity index	131
Figure 5-21- Relationship between peak internal friction angle and void ratio	132
Figure 5-22- Sketch of pore pressure in the broken rock.....	133
Figure 5-23- Effect of pore pressure based on Mohr-Coulomb criterion	134
Figure 5-24- Axial stress-strain curve for unsaturated broken sandstone, at a confining pressure of 138 kPa.....	135
Figure 5-25- Axial stress-strain curve for saturated broken sandstone, at a confining pressure of 138 kPa.....	135
Figure 6-1- Workflow of this research.....	140
Figure 6-2- Relationship between the aspect ratio of particles and packing density at different shape parameters (m), this figure was adapted from Delaney (2010).....	144
Figure 6-3- Relationship between form index and aspect ratio at different shape parameter (m).....	146
Figure 6-4- Relationship between angularity index and shape parameter (m) at different aspect ratio	147
Figure 6-5- Conceptual figure shows the relationship between dilation angle and confining pressure.....	149

LIST OF SYMBOLS

A	Area of the aggregate particle
AI	Angularity index of particles
AP	Angularity parameter of particles
A_{Convex}	Convex polygon area of particle
a	Hoek-Brown criterion parameter for intact rock
a_r	Hoek-Brown criterion parameter for rock mass
CO	Convexity of particles
D	Initial diameter of the specimen
d	Diameter of the bar
D_{60}	A size that 60% is smaller than this size
D_{50}	A size that 50% is smaller than this size
D_{10}	Effective diameter (A size that 10% is smaller than this size)
D_p	Packing density
E	Young's modulus
E_{pp}	Post peak modulus
$E_{pp(n)}$	Normalized post peak modulus
e	Void ratio
e	Axial engineering strain
e_b	Strain at base strength
e_{pp}	Strain at post peak region
F	Axial force

F_{corr}	Correction factor to convert the results of image processing method to sieve analyzing method
FF	Form factor of particles
FI	Form index of particles
F_{in}	Load per inch
GSI_r	Geological strength index for residual strength for rock
HRC	Rockwell hardness on the C scale
J'_c	Residual joint condition factor
K	Constant parameter in Mogami equation
K_1	Constant parameter in Mogami equation
L	Overall length of the membrane
L_m	Mean length of the membrane
M	Extension modulus of the membrane
M_c	Compression modulus of the membrane
m	Shape parameter
m_b	Hoek-Brown criterion parameter for rock mass
m_i	Hoek-Brown criterion parameter for intact rock
m_r	Hoek-Brown criterion parameter for residual strength
N	Newton
P	Perimeter of the particle
P_{convex}	The perimeter of the bounding polygon
P_{ellipse}	The perimeter of the equivalent ellipsoid
$R_{EE\theta}$	The radius of the equivalent ellipsoid at θ direction

R_{θ}	The radius of the particle at θ direction
s	Hoek-Brown criterion parameter for rock mass
s_r	Hoek-Brown criterion parameter for residual strength
TP	Texture parameter of particles
SD	Standard deviation of the particle's surface intensity
SD_N	The normalized standard deviation of the particle's surface intensity
SD_{Smooth}	The standard deviation of intensity of a polished and completely smooth surface
u	Pore pressure
V_b^r	Residual block volume
t	Membrane thickness
σ	Total stress
σ_1	Major principal stress
σ_2	Intermediate principal stress
σ_3	Minor principal stress
σ_c	Uniaxial compressive strength
σ_{ci}	Yield strength of intact rock
σ_{cd}	Damaged crack initiation threshold
σ_f	Ultimate strength
σ_{pp}	Post peak stress
σ_n	Normal stress on the failure plane
σ_r	Membrane correction
σ'	Effective stress due to pore pressure

σ'_1	Effective major principal stress
σ'_3	Effective minor principal stress
τ	Shear strength
τ_i	Shear strength of intact rock
ϕ	Internal friction angle
ε	The axial strain of the specimen
θ	Angle made with the normal of failure plane to major principal stress
o	Degrees

CHAPTER 1 : INTRODUCTION

Chapter 1 is an overview of the study. This chapter talks about the background of the research, the problem statement, the objectives of the study, the study's limitations, the proposed methodology and the scientific contributions of the research.

1.1 Introduction

Engineers need to know the strength of broken rock in structures such as tunnels, underground mining stopes, pillars, open pit mines and foundations. The geometry of particles and confining pressure play a significant role on the behavior of broken rock. The effect of confining pressure has been investigated previously; however, angularity, shape and roughness of particles are important parameters that affect the strength of broken rock. Good understanding of the behavior of broken rock is not only necessary for construction projects but also a key to defining the post peak behavior of a rock mass.

Accurate determination of rock strength and deformation modulus in pre and post peak regions are required for the effective design of underground cavern support and slope stability. In conservative design methods, engineers consider only the yield and ultimate strength of rock, and assume that the rock suddenly changes from peak strength to residual strength. This assumption causes an overly conservative design. Figure 1-1 shows the concept of pre-peak and post peak regions in the stress-strain curve.

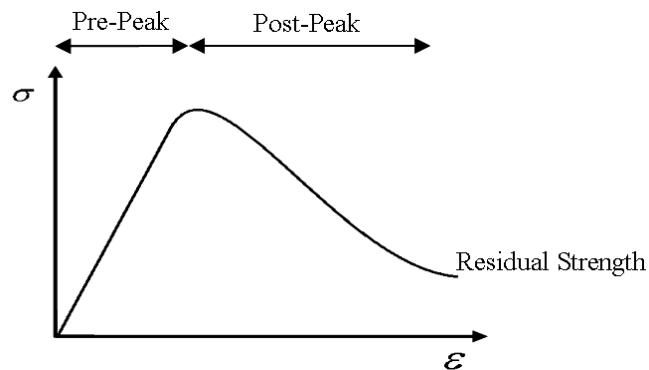


Figure 1-1: Concept of pre-peak and post- peak regions in the stress-strain curve.

Many researchers have worked to explain the failure of intact rock and determination of the yield and residual strength of rock. Also there are specified laboratory test methods to determine the yield strength of rock. However, for post peak behavior of rock, there is insufficient research, and there are few

comprehensive formulae or laboratory tests for assessing the strength parameters of rock in the post peak region; Joseph (2000). The strength of rock in the post peak region has been located between peak and residual strength, Joseph (2000). Previous work shows that the frictional properties of rock generated particles after failure have a major influence on the post peak behavior of rock; where, investigation results of the behavior of broken rock can be used to determine post peak behavior parameters at the same confining pressure and particles geometry. The behavior of broken rock has been studied by several researchers such as Hoek (1980), Hobbs (1970), Hussaini (1983) and Joseph (2000). This study extended the behavior of broken rock at different confining pressures, Joseph (2000). The results of broken rock behavior will be used here to refine the post peak behavior of rock.

1.2 Statement of the problem

There are many criteria to specify the behavior of broken rock; however, there is a need for a refined expression in terms of particle character. In addition, most of the previous studies show that the post peak behavior of rock depends on the behavior of particles generated after peak strength at low confining pressure. There is no complete research on the behavior of broken rock to determine the post peak behavior of rock by considering fragment size distribution, shape, angularity or texture. Beyond peak strength, in the post peak region, new particles are formed, and intact rock changes to broken rock.

In this study, behavior of broken rock at low confining pressure was investigated using the geometry of particles with the following objectives.

1.3 Objectives of the study

Phase1:

To determine the geometry of particles through employing image processing techniques.

Phase2:

To determine example peak strength of broken rock samples through using triaxial compressive tests.

Phase3:

To investigate the behavior of broken rock at low confining pressure accounting for particle geometry characteristics.

Investigation the behavior of broken rock at low confining pressure is important because in some actual rockfill piles and overburden waste dumps there is no large confining pressure.

1.4 Postulates and assumptions of the study

This study will be based on the following postulates and assumptions:

Postulate 1:

Particle geometry plays an important role in defining post peak behavior of broken rock.

Postulate 2:

Slip mechanisms dominate over generation of new surfaces via particle breakage.

1.5 Scope and limitations of the study

As this study deals with explaining the behavior of broken rock at low confining pressure based on the geometry of particles, the behavior of a broken rock mass is considered located between intact rock behavior and residual broken rock behavior and is dominated by frictional response, complying with the postulates.

It should be noted that this study has limitations due to the assumptions and methodologies:

- The kind of failure in this research has been assumed to be brittle slip, such that the confining pressure of all tests will be conducted at low

values. It is clear that complete brittle slip is not possible and strain will occur in the designed tests.

- The same broken rock specimen is assumed to be isotropic and there are no specific discontinuity planes in the prepared specimens.
- Extrapolation of the triaxial test results will be used to predict the behavior of large block size broken rock, where each extrapolation is likely to introduce errors which may not be measurable.
- For post peak behavior of a rock mass, it is assumed that the failure will be controlled by the discontinuity structure orientation instead of intact rock strength.

1.6 Research methodology

This study was based on experimental tests. The compression triaxial test method was chosen to determine the strength of broken rock. Specimens of broken rock were prepared of broken Berea sandstone. The selected sandstone in this research has very fine grains. The fine grains of sandstone allow assuming the rock homogeneity and neglecting the effect of particles grains on the behavior of broken rock. The major reason to choose this type of sandstone in this research work was the homogeneity of sandstone. In order to achieve the objectives of this research, the following research tasks will be completed:

- To quantify shape characteristics of broken rock
- To perform triaxial tests on specimens of broken rock
- To analyze and discuss the results of the triaxial tests to explain the behavior of broken rock
- To propose an empirical modeling approach to specify the behavior of broken rock.

1.7 Original scientific contributions and industrial significance of the study

The main contribution of this research to the body of knowledge is a better understanding of the effect of particle shape parameters on the behavior of broken rock. Another major aspect of this study is specifying existing problems in the triaxial test on broken rock for further research. In addition, the code developed by using MATLAB can be employed to determine the shape parameters of particles in future research. The results of this study can be useful for some actual design projects:

- Determining the stability of a mine waste dump
- Determining the stability of a mine bench of very weak rock mass
- Improving the production scheduling of caving extraction methods in underground mines
- Reducing the support cost in underground structures with a better understanding of rock post peak strength.

CHAPTER 2 : LITERATURE REVIEW

Chapter 2 provides an overview of previous research on broken rock, and a brief literature review about intact rock and rock mass are summarized in this chapter. In addition, chapter 2 presents summary of particle shape characteristics: Form, Angularity and Texture are three parameters to describe the geometry of a particle.

2.1 Introduction

The behavior of broken rock plays a significant role in construction and mining projects. Slope stability, backfill design, waste dump, and the importance of rockfill engineering in embankment dams indicate the significance of broken rock behavior. In addition, the behavior of broken rock is the key point in understanding the post peak behavior of a rock. The behavior of particles in the post peak region plays an important role in defining post peak behavior of a rock. This chapter covers a brief literature review on broken rock and a review on the previous research that points out the effect of broken rock on the post peak region.

2.2 Behavior of broken rock

Hobbs, (1966) and (1970), investigated the behavior of broken rock using triaxial compression tests. Hobbs (1966) did extensive experiments on broken rock to design tunnels and roadways in mines. His research showed that confining pressure has an important impact on the peak strength of broken rock. Hobbs (1970) introduced a criterion to predict the strength of broken rock with respect to confining pressure. He illustrated the relationship between shear and normal stress via an exponential function. Equations (2-1) and (2-2) show Hobbs' (1970) formulae.

$$\sigma_1 = B\sigma_3^b + \sigma_3 \quad (2-1)$$

$$\tau = K\sigma^a \quad (2-2)$$

Where B, b, K and a are empirical defined constants that are a function of rock type. B and b parameters for four rock types are illustrated in Table 2-1.

Table 2-1- Suggested criteria by rock type, after Hobbs (1970).

Rock Type	Equation
Ormonde siltstone	$\sigma_1 = 7.93\sigma_3^{0.566} + \sigma_3$
Bilsthorpe silty mudstone	$\sigma_1 = 7.37\sigma_3^{0.595} + \sigma_3$
Hucknall shale	$\sigma_1 = 7.32\sigma_3^{0.652} + \sigma_3$
Bilsthorpe mudstone	$\sigma_1 = 4.82\sigma_3^{0.709} + \sigma_3$

Hobbs demonstrated an effective Young's modulus for broken rock depends on the magnitude of the applied confining pressure. In addition, Hobbs believed that an increase in confining pressure reduces the difference between a Young's modulus for intact rock and an effective Young's modulus for broken rock; where for a confining pressure greater than 6.9 MPa the values would be effectively equivalent.

Hussaini (1970), (1971) and (1983) tested the behavior of crushed basalt and found that the relationships between major and minor principal stresses are non-linear. Hussaini (1970) explained the stress-strain diagram is linear at the onset of deformation but gradually flatness as it approaches peak strength. Hussaini (1970) introduced Equation (2-3) to calculate an initial tangent modulus based on confining pressure and Relative-Density of broken rock.

$$E_i = (KDr_i)^n \left(\frac{\sigma_3}{Pa} \right)^m \quad (2-3)$$

Where Dr_i is the Relative-Density of specimen, σ_3 is the confining pressure, Pa is the atmospheric pressure, assumed equal to 14.7 psi, and K , m and n are constants.

Hussaini (1983) believed that grain size and confining pressure generate the maximum impact on broken rock strength. In addition, compressibility showed a decrease with increase in grain size. Hussaini's research indicated that an increase in maximum grain size causes an enhancement in internal friction angle. Figure

2-1 shows the impact of the maximum grain size and confining pressure on internal friction angle.

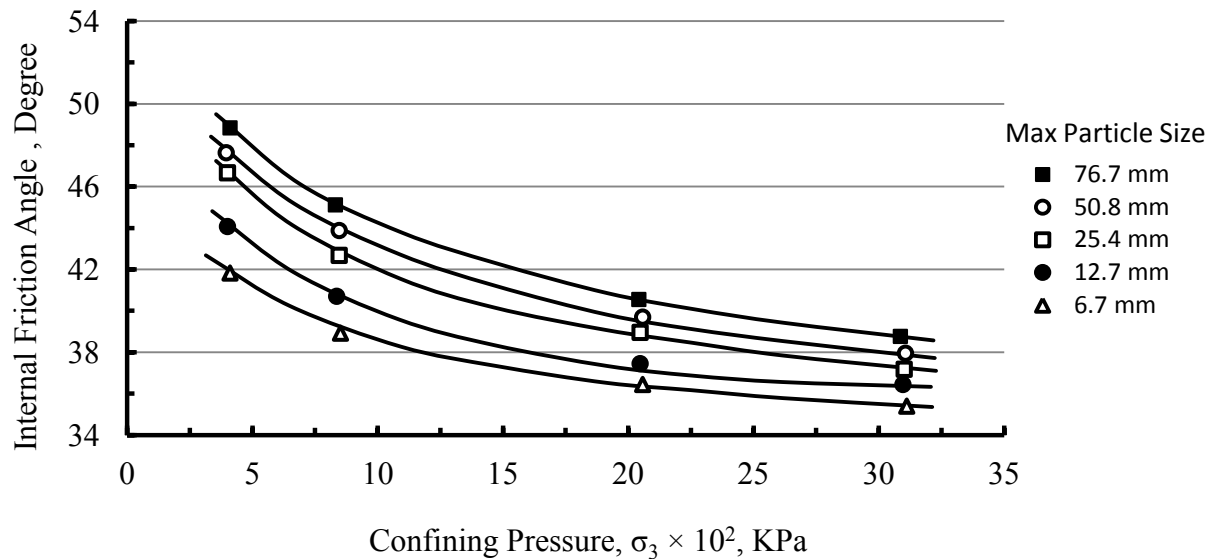


Figure 2-1- Variation of internal friction angle with respect to confining pressure, after Hussaini (1983).

Hussaini (1983) used effective diameter (D_{10}) to investigate particle size change on the behavior of broken rock. Effective diameter (D_{10}) represents a particle diameter in which 10% of specimen's particles are finer than it. The effective diameter can be determined by using particle size distribution graph. The sieve analysis is a method to plot the particle size distribution of a broken rock, ASTM 447 (1972).

Hussaini illustrated that an increase in particle size enhances the ultimate strength of broken rock. Figure 2-2 depicts the enhancement of the peak strength of broken rock due to a particle size increase. However, broken rock with 50.4 mm size shows greater strength than broken rock with 76.2 mm deposit of other results. The unexpected strength of the specimen with 50.4 mm particle size not only can imply an outlier result but also can explain the complex behavior of broken rock while the behavior of broken rock is affected by particle geometry characteristics.

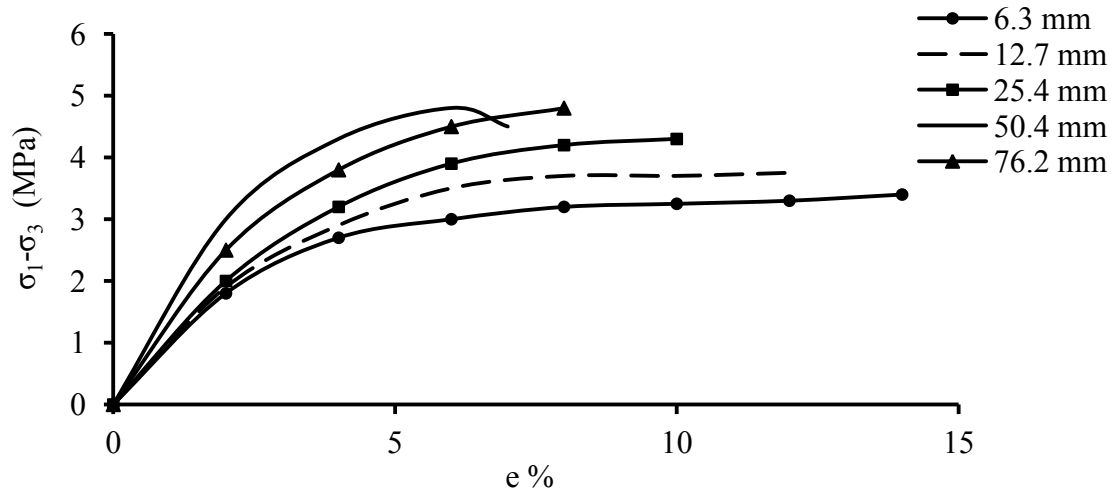


Figure 2-2- Increase in ultimate strength of the broken rock due to particle size increase, after Hussaini (1983).

Lee (1967) investigated the behavior of granular material to determine the compressibility and strength of a granular soil. He believed that angular material is more compressible than rounded material, such that research showed that coarse soil has more breakage and compressibility than fine soil.

Fumagalli (1969) carried out triaxial tests on broken rock to study cohesionless material for rockfill dams. He demonstrated that the initial void ratio of broken rock has a significant impact on modulus of broken rock. The modulus of broken rock decreases with a void ratio increase. Figure 2-3 shows the variation of broken rock modulus with respect to the void ratio of specimens. The effective parameters on the behavior of broken rock are dependent to each other. For example, void ratio and particle size affect the broken rock in addition particle size distribution impact the void ratio.

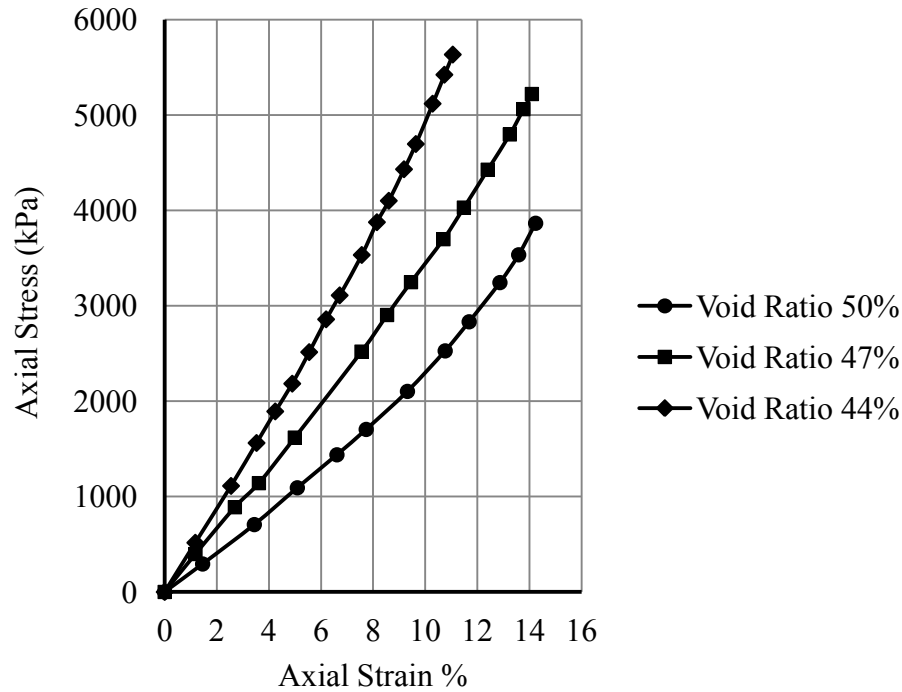


Figure 2-3- Variation of peak strength of broken rock with respect to void ratio, after Fumagalli (1969).

Joseph (2000) and (2003) explained that stress-strain curves are the same for both intact and broken rock in the post peak region at any given confining pressure. Figure 2-4 shows the stress-strain curves for intact and broken rock at several confining pressures. Also, he demonstrated that intact and broken rock have similar functions to define post peak modulus. Joseph used an effective friction angle to calculate the strength of broken rock by equations (2-4) and (2-5). He employed a 2nd order polynomial to predict the effective friction angle, and he demonstrated that the effective friction angle has the same equation for peak and residual regions through Equation (2-6). Using Equation (2-7), Joseph (2000) determined that the post peak modulus is the change in post peak stress for a given change in post peak strain.

$$\tau = f(\sigma) \quad (2-4)$$

$$\phi_e = \tan^{-1} \left[\frac{\tau}{\sigma} \right] \quad (2-5)$$

$$\phi_e = R + S(e_{pp}) + T(e_{pp})^2 \quad (2-6)$$

$$E_{pp} = \frac{\sin 2\theta}{\sin^2 \phi_e} \frac{(\sigma_{pp} - \sigma_3)^2}{\sigma_3} \frac{(\phi_e - \phi_b)}{(e_{pp} - e_b)} \quad (2-7)$$

Where R, S and T are constant parameters based on rock type, and e_{pp} is the post peak strain.

Figure 2-5 shows the effective friction angle curve and the boundary conditions.

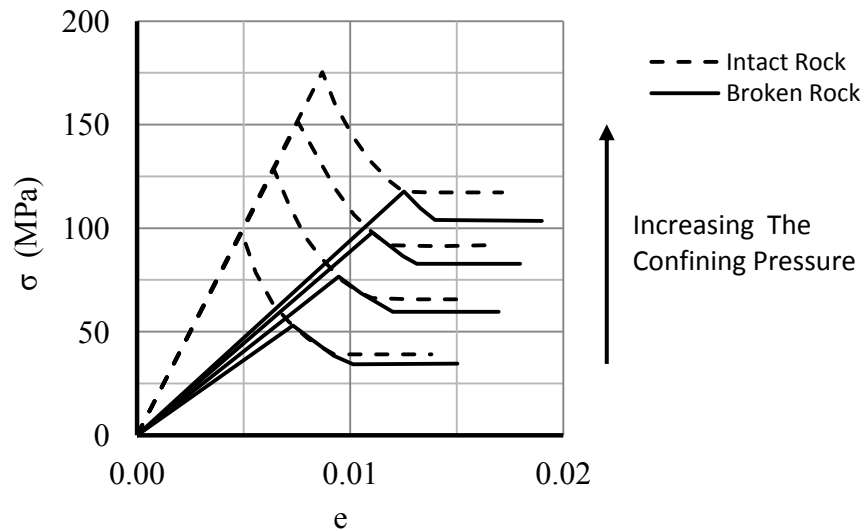


Figure 2-4- Stress-strain curves for intact and broken rock, after Joseph (2000).

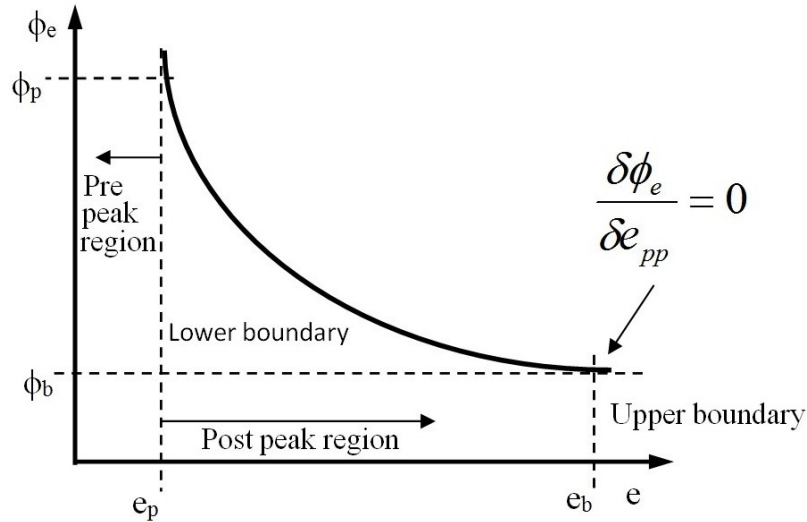


Figure 2-5- Boundary condition of effective friction angle, after Joseph (2000).

A number of researchers have investigated the strength of granular materials such as gravel, sand and crushed rock to design backfill and rockfill dams, e.g., Kolbuszewski and Frederick (1963), Holtz and Gibbs (1956), Marschi (1972) and Marsal (1973). They demonstrated that particle shape, size and roughness affect the strength of cohesion-less materials.

2.3 Post-peak behavior of intact rock

Investigating the behavior of intact rock is the first step to understand the strength of a rock mass; where researchers have studied the failure of intact rock through empirical work, Hoek (1965), Mogi (1971), Brace (1963), Bieniawski (1967), Price (1979) and Hudson (1997).

Brace (1963) investigated the brittle failure of rock with cylindrical specimens under compressive pressure. He divided the stress-strain curve of intact rock, up to peak strength into four regions and explained the behavior of rock in each region. Figure 2-6 shows the stress-strain curve and the four regions proposed by Brace (1963). Based on Brace research (1963), rock in regions 1 and 2 has elastic behavior and rock in regions 3 and 4 has plastic behavior. Also research by

Wawersik and Brace (1971) on post failure of granite showed that the behavior of granite after failure is dominated by shear fracturing and the frictional strength of broken rock.

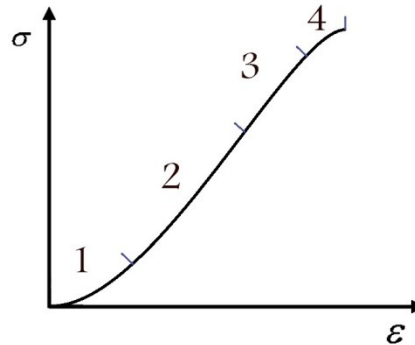


Figure 2-6- Stress-strain curve of intact rock in four regions until peak strength, after Brace et al., (1963).

Bieniawski (1967) discussed the mechanism of brittle failure through experimental tests. He investigated crack initiation and crack propagation using Griffith's theory, (Griffith(1921). He concluded that it is possible to specify stable and unstable cracks at intact rock failure through rate of growth. Bieniawski (1968) explained that post peak behavior is not a characteristic property of the rock material. Figure 2-7 shows the post peak region on the stress-strain curve. The post peak behavior depends on the structure of the rock after failure and the loading conditions. In other words, the post peak behavior of rock is a function of the boundary conditions and is not a pure material property.

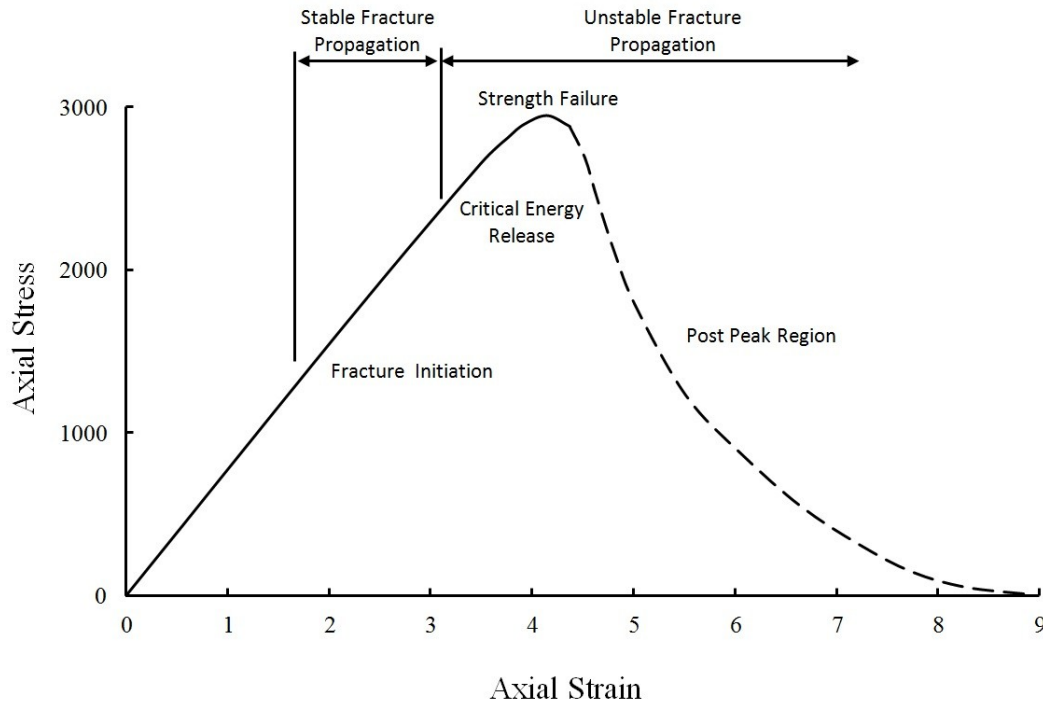


Figure 2-7- The post peak region at stress-strain curve, after Bieniawski et al., (1968) and Rajendra et al., (2006).

The complete stress-strain curve was discussed by Price (1979) and Farmer (1968). Figure 2-8 shows the complete stress-strain curve proposed by Price. They explained that rock is not intact in region F. At region F, the specimen will be broken, and the sliding on failure planes dominates the behavior of rock after failure. Therefore, the friction on a failure plane has a major influence on the post failure behavior of rock.

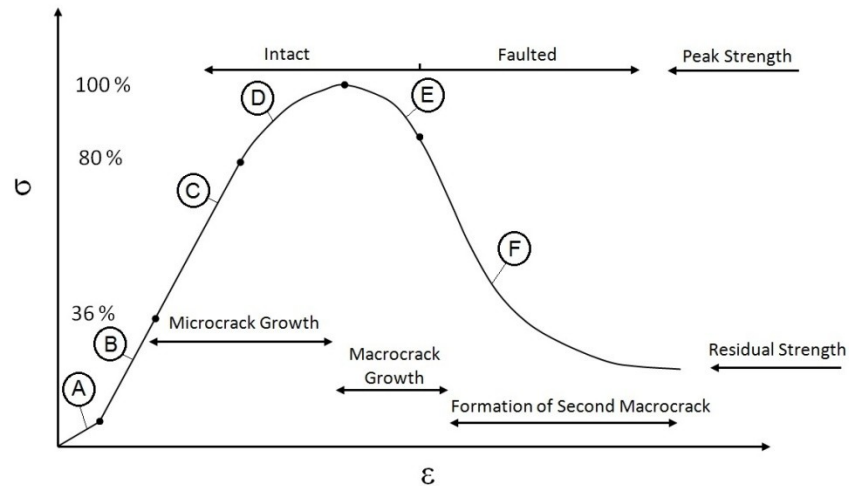


Figure 2-8- Stress-strain curve, after Price et al., (1979) and Farmer et al., (1968).

Martin and Chandler (1994) and Hajiabdolmajid (2001) showed that the impact of the cohesion component of strength will decrease and the impact of the friction component will increase during the complete failure of a rock. The mobilization of friction and cohesion is a function of axial strain in compressive tests. Therefore, the friction component of strength has a major influence on the post-failure behavior of rock. Martin (1993) introduced a crack initiation threshold (σ_{ci}) which is independent of damage level and specimen diameter.

As mentioned earlier Joseph (2000) and (2003) investigated the post peak stiffness of broken rock, introducing a 2nd order polynomial criterion to determine the post peak strength of rock. He also explained an approach to determine the parameters of the criterion through easily available information such as uniaxial compressive strength, derived from actual lab data sets and confining pressures. In Joseph's approach, two components have major influence on broken rock behavior:

- 1- Frictional resistance to sliding
- 2- Asperities of the rough surface

Joseph (2000) demonstrated that a post peak modulus and the stress-strain curve at post peak region may be determined, even if only the peak strength and base friction angle of a rock is known.

2.4 Post failure of a rock mass

The behavior of a rock mass is very important for rock engineering, and many researchers have worked to determine the pre and post-failure behavior of rock masses. Bieniawski (1968) and (1969) discussed the failure of fractured rock and the impact of specimen size on the peak strength. He showed that specimen size and rock strength have an inverse relationship because a larger specimen will have more discontinuities and weak planes than a small specimen. Figure 2-9 illustrates the influence of specimen size on the strength of rock.

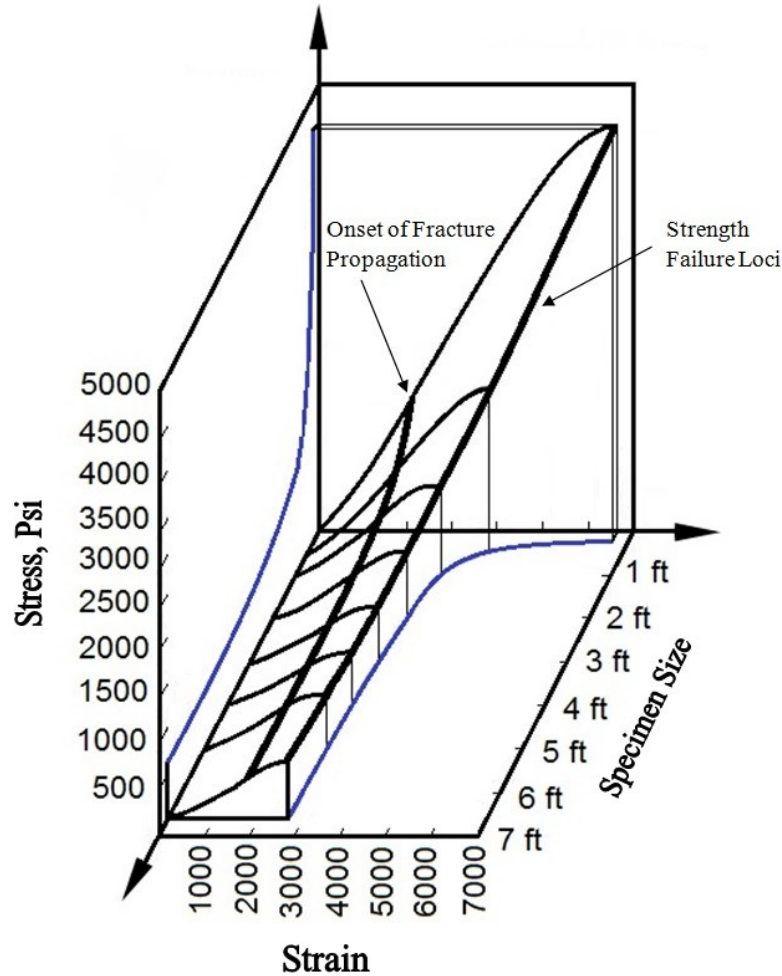


Figure 2-9- The influence of specimen size on the strength of rock, after Bieniawski et al., (1968).

Hoek (1964) proved that angles between open Griffith cracks and the major principal stress has significant influence on the strength of anisotropic rock because the strength of the rock mass depends on the strength of joints at a critical angle. Hoek (1966) investigated the effect of the spacing between discontinuities on the strength of a rock mass. Hoek (1980) showed that the spacing of discontinuities has a direct relationship with the strength of a rock mass and introduced the Hoek-Brown criterion to characterize the strength of a rock mass. The Hoek-Brown criterion has two important parameters (m and s) to predict the behavior of a rock mass. The magnitudes of m and s change from maximum to

minimum values from intact to residual strength, respectively. Hoek (1995) introduced a new rock mass classification system and called it the Geological Strength Index (GSI). Hoek used GSI to estimate the Hoek-Brown criterion parameters. Hoek (1997) and (2001) suggested some values for post failure of rock mass, Table 2-2 . He mentioned that the post-failure behavior of a rock mass might be defined by the behavior of broken rock in constant confining pressure. This agrees with the research work of Joseph (2000).

Table 2-2- Suggested value for post failure of rock mass, after Hoek et al., (2001).

	Very good quality hard rock mass	Average quality rock mass	Very poor quality rock mass	
Intact rock strength (MPa)	150	80	20	
Hoek-Brown constant (m_i)	25	12	8	
Geological Strength Index (GSI)	75	50	30	
Friction angle	46	33	24	
Cohesive strength (MPa)	13	3.5	0.55	
Rock mass compressive strength (MPa)	64.8	13	1.7	
Rock mass tensile strength (MPa)	-0.9	-0.15	-0.01	
Deformation modulus (MPa)	42000	9000	1400	
Poisson's ratio	0.2	0.25	0.3	
Post-peak characteristics	Dilation angle	11.5	4	0
	Friction angle	38	-	-
	Cohesive strength (MPa)	0	-	-
	Deformation modulus(MPa)	10000	5000	1400
	Broken rock mass strength (MPa)	-	8	1.7

Majority of the research works developed after the Hoek-Brown criterion are devoted to predict the residual and post failure strength of a rock mass by using a form of Hoek-Brown criterion. Ribacchi (2000) proposed the ratio between Hoek-Brown criterion parameters at peak and residual strength. Ribacchi (2000) and other researchers much earlier in (1960) mentioned that the Young's modulus of a rock mass will be increased by increasing the confining pressure. Crowder and Bawden (2010) explained that the initial GSI should not be changed to residual GSI directly. They recommended usage of residual m and s (m_r , s_r) to predict the residual strength of a rock mass. Bawden (2010), Crowder and Bawden (2006) and Crowder and Coulson (2006) explained the significance of post-failure behavior on mining cost and support design. They used residual parameters from the Hoek-Brown criterion to simulate the residual behavior of a rock mass.

Cai and Kaiser (2007) introduced a method to determine the residual parameters of the Hoek-Brown criterion via residual block volume (V_b^r) and residual joint condition factor (J_c^r). Cai suggested the following steps to determine the residual parameters of Hoek-Brown criterion:

- 1- Determine the V_b^r and J_c^r according to the suggested relationships and recommendations by Cai and Kaiser (2007).
- 2- Determine the residual Geological Strength Index (GSI_r) by Equation (2-8).
- 3- Determine the residual Hoek-Brown parameters (m_r , s_r and a_r) by equations (2-9), (2-10) and (2-11).
- 4- Determine the residual strength criterion for rock mass by Equation (2-12).

$$GSI_r = (V_b^r, J_b^r) = \frac{26.5 + 8.79 \ln J_b^r + 0.9 \ln V_b^r}{1 + 0.0151 \ln J_b^r - 0.0253 \ln V_b^r} \quad (2-8)$$

$$m_r = m_i \exp\left(\frac{GSI_r - 100}{28}\right) \quad (2-9)$$

$$s_r = \exp\left(\frac{GSI_r - 100}{9}\right) \quad (2-10)$$

$$a_r = 0.5 + \frac{1}{6} \left(e^{-GSI_r/15} - e^{-20/3} \right) \quad (2-11)$$

$$\sigma_1 = \sigma_3 + \sigma_{ci} \left(mr \frac{\sigma_3}{\sigma_{ci}} + s_r \right)^{a_r} \quad (2-12)$$

Cai and Kaiser verified the validity of the equations by experimental tests and concluded that the block volume (V_b^r) and joint condition (J_c^r) have significant influence on the post-failure and residual behavior of a rock mass.

Diederichs (2007), Carter (2007), Carvalho (2007) and Carter (2008) investigated the strength of a rock mass, where they developed formulae to determine the Hoek-Brown criterion parameters for very strong rock masses (with GSI > 65) and very weak rock masses (with intact uniaxial compressive strength < 10 MPa). They demonstrated that the behavior of a rock mass that has an intact uniaxial compressive strength (σ_c) > 10 MPa will be dominated by rock structures at low confining pressure. This is a key driver for this research.

Rajendra (2006) continued the Wagner (1968) research and tested cubic specimens to model post-failure behavior of a rock mass. The research by Rajendra showed that joint geometry has a major role in post-failure behavior of a rock mass at low confining stress. More recently researchers have used numerical methods to simulate the failure of rock mass such as Kovrizhnykh (2000), Park (2006), Sainsbury (2008), Stefanizzi, Barla and Kaiser (2008), Liang (2008), Van (2008), Villeneuve and Diederichs and Kaiser (2009), Wu(2009), Valley, Suorineni and Kaiser (2010) and Moraes (2011). However, good understanding of the behavior of a rock mass in the pre and post peak regions via experimental tests is very important for accurate numerical verification. Numerical simulation methods need improved data and criteria about post peak behavior for verification. This is the target of this research.

Previous research on post peak behavior of a rock shows the importance of the behavior of broken rock. There is little complete research to determine the behavior of broken rock through considering particle geometry. In this study, the behavior of broken rock at low confining pressure was investigated with a focus on particle shape and geometry.

2.5 Determining the geometry of a particle

The shape characteristics of particles should be specified as a first step to investigate the broken rock strength. The behavior of broken rock depends not only on the confining pressure but also on the particle geometry and size distribution. Barrett (1980), Masad (2001), (2003), (2007), Little (2003) and Al-Rousan (2004), (2007) determined that the geometry of particles can be completely explained through three independent characteristics:

1. Form
2. Angularity
3. Texture

Form, angularity and texture are three independent parameters in concept and description. However, in practice, preparing some specimens in which only one parameter is changed is difficult. For example, preparing two specimens of actual broken rock with different form and same angularity is difficult.

Figure 2-10 illustrates the concept of particle geometry parameters.

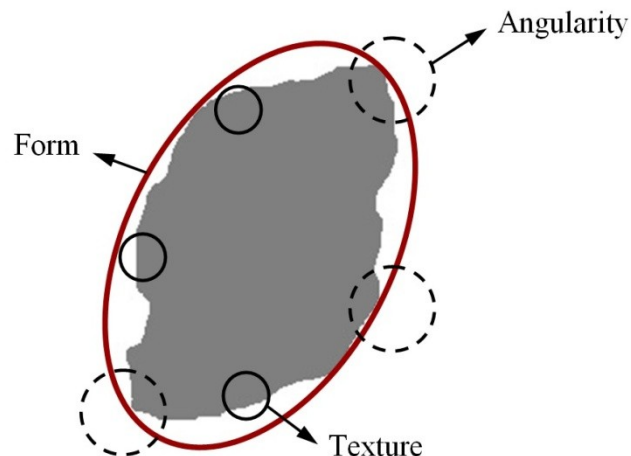


Figure 2-10- The concept of the particle geometry parameters: Form, Angularity and Texture

Form describes the overall shape of a particle. Particles may have different forms; for example, some particles are similar to triangles, circles, quadrangles or other shapes. Angularity expresses the variations at the apexes of each fragment. Figure 2-11 shows two particles with the same form and different angularity. Texture is the last parameter to characterize the geometry of particles, and it describes the surface roughness and inequality at such a scale that it cannot affect the shape of particles. Figure 2-12 shows two particles with the same form and different texture.



Figure 2-11- Two particles with the same form and different angularity.



Figure 2-12- Two particles with the same form and different texture.

Recently image processing technology has been used to quantify particle geometry. Powerful computers and software provide applicable tools to determine shape characteristics. Yeggoni (1994), Janoo (1998), Kuo (2000), Tutumluer (2000), Masad (2001), (2003), Fletcher (2003), Swift (2007), Wang (2009), Lindström (2010), Gates (2010) and Arasan (2010) have introduced some formulae to determine form, angularity and texture through image processing. Some of the methods that have been presented by researchers to determine form, angularity and texture are summarized below.

2.5.1 Methods to determine the form of particles:

These parametric equations describe the overall shape of particles.

2.5.1.1 Form factor

Form factor is expressed by the following equation and has been used frequently by researchers to describe the form of an aggregate. Form factor is a dimensionless parameter that is equal to one for circle particles. Kuo (2000), Masad (2001), Wang (2003), Al-Rousan (2004), (2007) and Arasan (2010) used Equation (2-13) to calculate the form factor of a particle.

$$FormFactor = \frac{4A\pi}{P^2} \quad (2-13)$$

Where A is area and P is perimeter of the aggregate particle.

Figure 2-13 shows relationship between particle shape and form factor. Circular particles have form factor equal to one while form factor for elliptical particles is less than one.

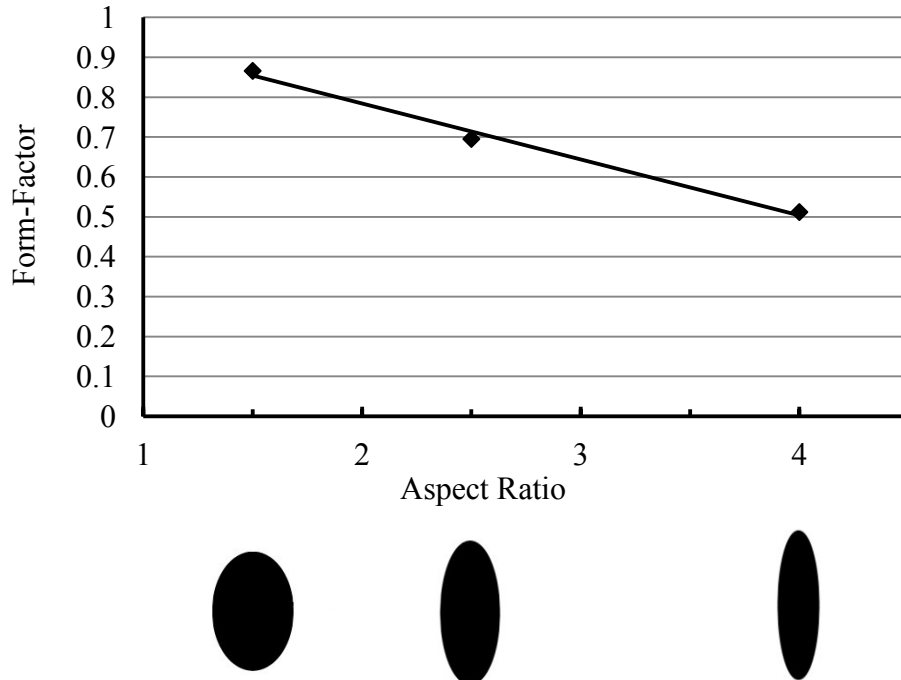


Figure 2-13- Relationship between aspect ratio and form factor

The particle shape characteristics in Figure 2-13 to Figure 2-21 were calculated by digital image processing method through using a developed code in this research (Chapter 4). The calculated geometry characteristics for simple geometry shapes by using analytical method is different from calculated geometry characteristics by using image processing method (like the difference between numerical modeling and analytical solution).

2.5.1.2 Form index

Form index is a dimensionless parameter that reflects the form of particles. Little (2003), Masad (2003) and Al-Rousan (2004),(2007) introduced this parameter. Form index is expressed by Equation (2-14) and is zero for circle particles.

$$FormIndex = \sum_{\theta=0}^{\theta=360-\Delta\theta} \frac{|R_{\theta+\Delta\theta} - R_{\theta}|}{R_{\theta}} \quad (2-14)$$

Where R_{θ} is the radius of the particle at θ direction. The radius of the particle is the length between the geometric center and boundary of the particle. Figure 2-14 shows the radius of the particle at θ direction.

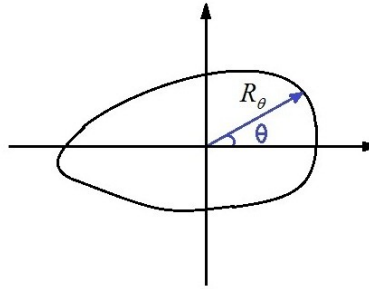


Figure 2-14- The concept of radius of the particle at θ direction

Figure 2-15 illustrates form index parameter of particles (calculated by image processing method). Form index of elliptical particles is greater than circular particles.

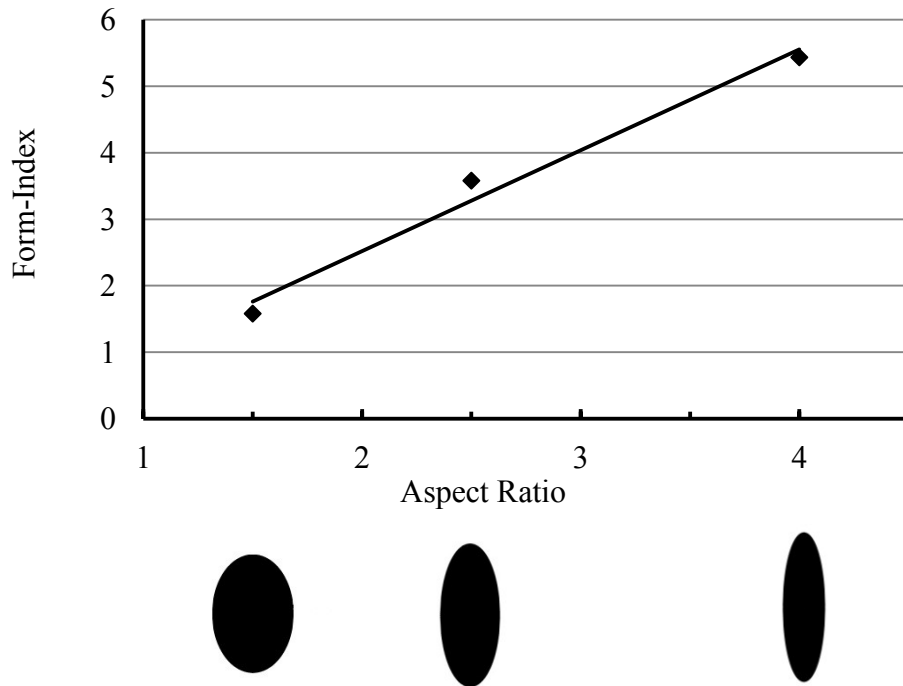


Figure 2-15- Relationship between aspect ratio and form index

2.5.1.3 Roundness

Roundness is another parameter that was introduced by researchers to describe the form of particles. Roundness is a dimensionless parameter that is the inverse of the form factor. It is equal to one for circular particles and is greater than one for elliptical particles. Figure 2-16 shows the relationship between particle shape and Roundness parameter (calculated by image processing method). Equation (2-15) expresses Roundness parameter.

$$\text{Roundness} = \frac{1}{\text{FormFactor}} \quad (2-15)$$

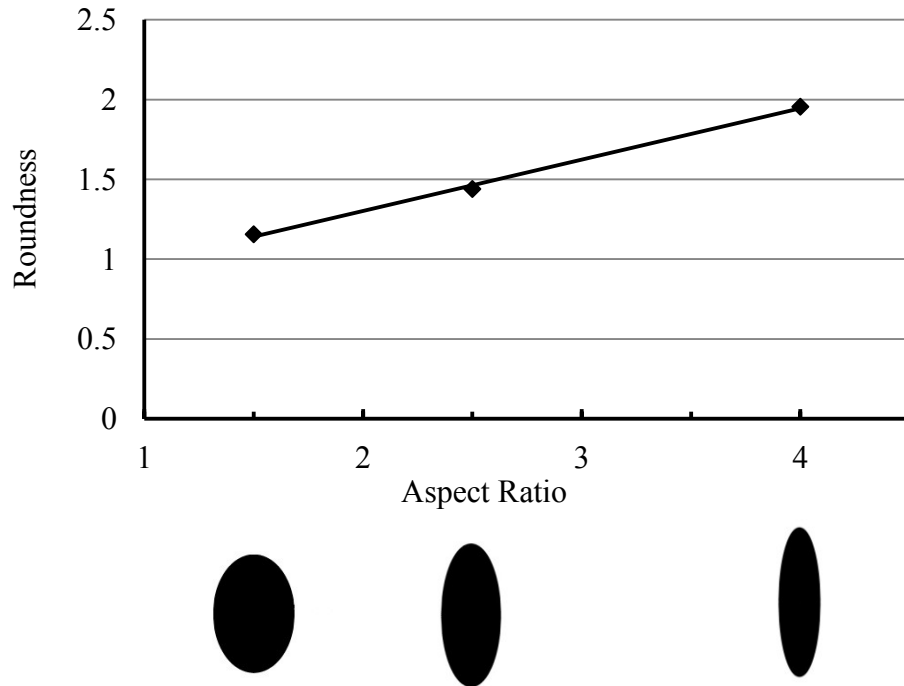


Figure 2-16- Relationship between aspect ratio and Roundness parameter

2.5.2 Methods to determine the angularity of particles:

To calculate the angularity of particles, the following parameters have been selected from previous literature. These parametric equations quantify the angularity of particles.

2.5.2.1 Angularity index

Little (2003), Masad (2001), (2003), (2007) and Al-Rousan (2004), (2007) introduced the angularity index to quantify the angularity of particles by the normalized difference between particle radius and equivalent ellipsoid radius at the same direction. Equation (2-16) expresses the angularity index.

$$\text{Angularity Index} = \sum_{\theta=0}^{\theta=360-\Delta\theta} \frac{|R_{\theta} - R_{EE\theta}|}{R_{EE\theta}} \quad (2-16)$$

Where R_{θ} is radius of the particle at θ direction and $R_{EE\theta}$ is the radius of the equivalent ellipsoid at θ direction. The equivalent ellipsoid has the same area, as well as the same first and second-degree moments of the particle.

Figure 2-17 depicts the particle angularity and angularity index (calculated by image processing method). This parameter is a dimensionless parameter that is equal to zero for completely rounded particle. Angular particles have greater angularity index than rounded particles. Angularity of a particle and angularity index has positive affinity.

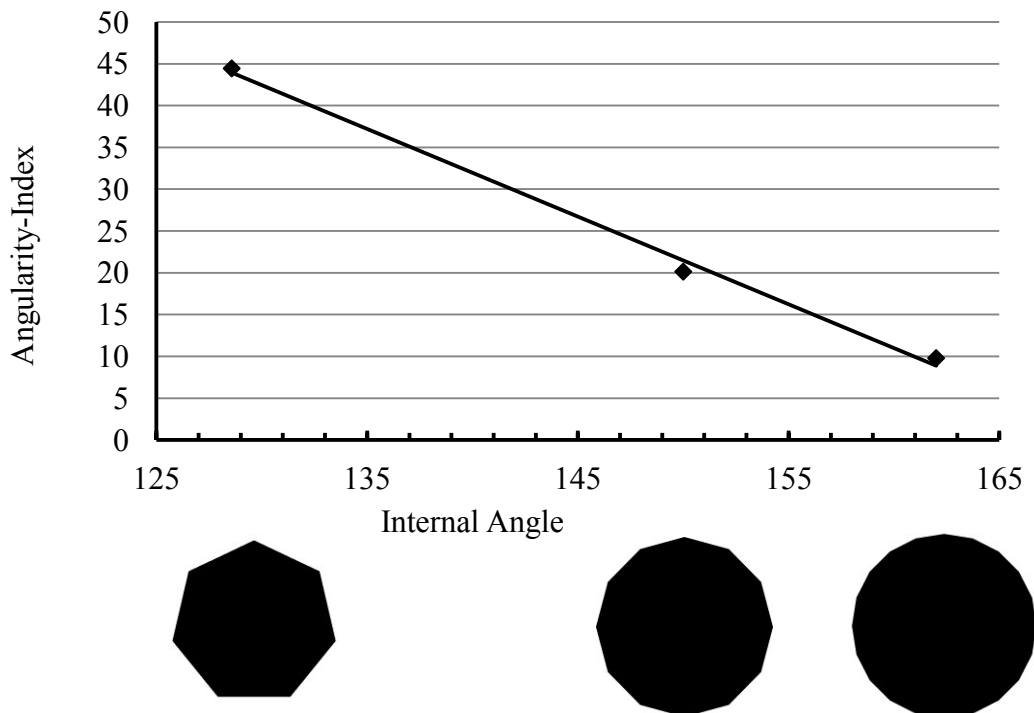


Figure 2-17- Relationship between internal angle and angularity index

2.5.2.2 Angularity parameter

Kuo (2000) and Masad (2001) and (2007) introduced Equation (2-17) to determine the angularity parameter. This parameter is a dimensionless parameter that is equal to one for completely rounded particles. Angular particles have greater angularity parameter than rounded particles. Figure 2-18 shows relationship between particle angularity and angularity parameter (calculated by image processing method). An increase on a particle angularity increases the angularity parameter.

$$\text{Angularity Parameter} = \left(\frac{P_{convex}}{P_{ellipse}} \right)^2 \quad (2-17)$$

Where P_{convex} is the perimeter of the bounding polygon and $P_{ellipse}$ is the perimeter of the equivalent ellipsoid.

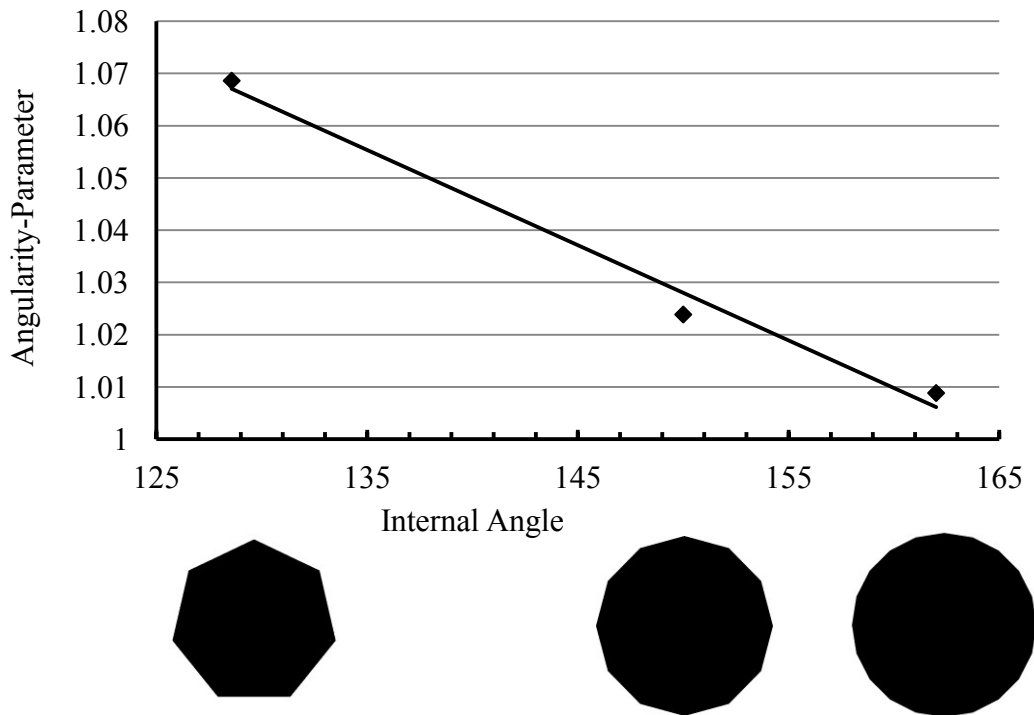


Figure 2-18- Relationship between internal angle and angularity parameter

2.5.2.3 Convexity

Convexity is a dimensionless parameter that describes the angularity based on the convex area of the particle. A rounded particle has greater convexity than an angular particle. Convexity of a completely rounded particle is equal to one. Equation (2-18) indicates the Convexity parameter. Figure 2-19 illustrates relationship between particle angularity and Convexity parameter (calculated by image processing method). Angularity of a particle and Convexity parameter has positive affinity.

$$\text{Convexity} = \sqrt{\frac{A}{A_{\text{Convex}}}} \quad (2-18)$$

Where A is the area of the particle and A_{Convex} is the area of the smallest convex polygon that can surround the particle.

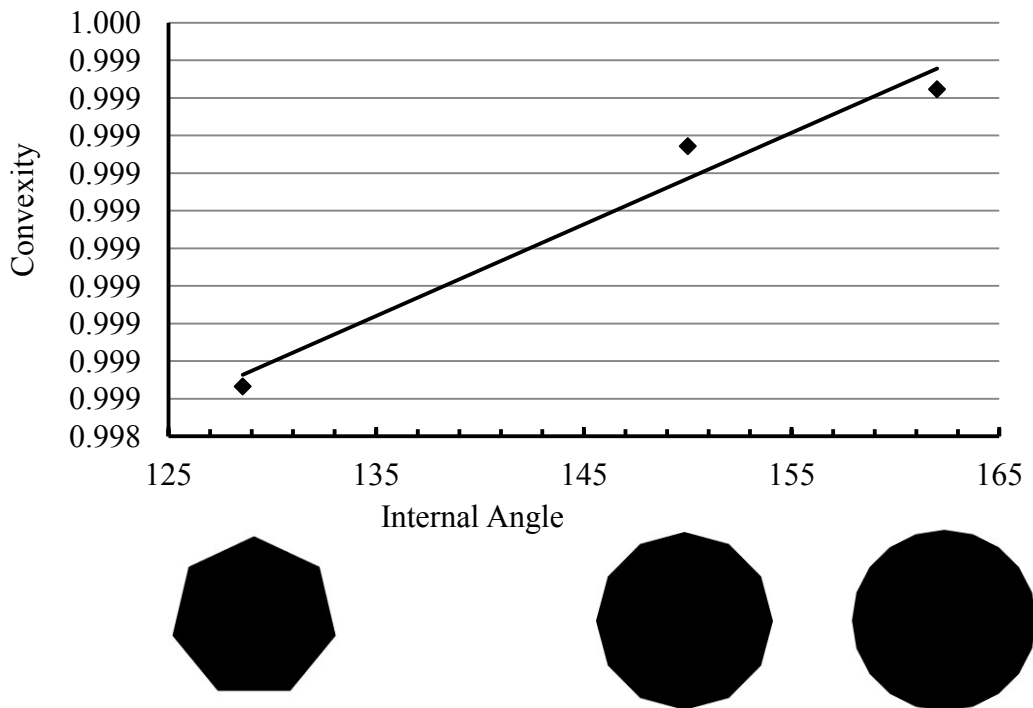


Figure 2-19- Relationship between internal angle and Convexity

2.5.3 Methods to determine the texture of particles:

To calculate the texture of particles there are some methods. The following methods are well-known methods to determine the texture of particles.

2.5.3.1 Intensity histogram method

The intensity histogram method has been used by Masad (2001), (2007) and Little (2003) to describe the surface texture. Researchers believe that the intensity of each image pixel of the particle surface depends on the roughness and inequality of the particle surface; therefore, mean and standard deviation of the particle surface intensity can represent the texture of the particle. Hence, the intensity histogram for each particle can specify the surface texture. Smooth particles have lower intensity standard deviation than rough particles. Figure 2-20 shows relationship between particle texture and standard deviation of Intensity for two particles (calculated by image processing method): the first particle is completely smoothed particle, but the second is natural particle with inequality on the particle surface.

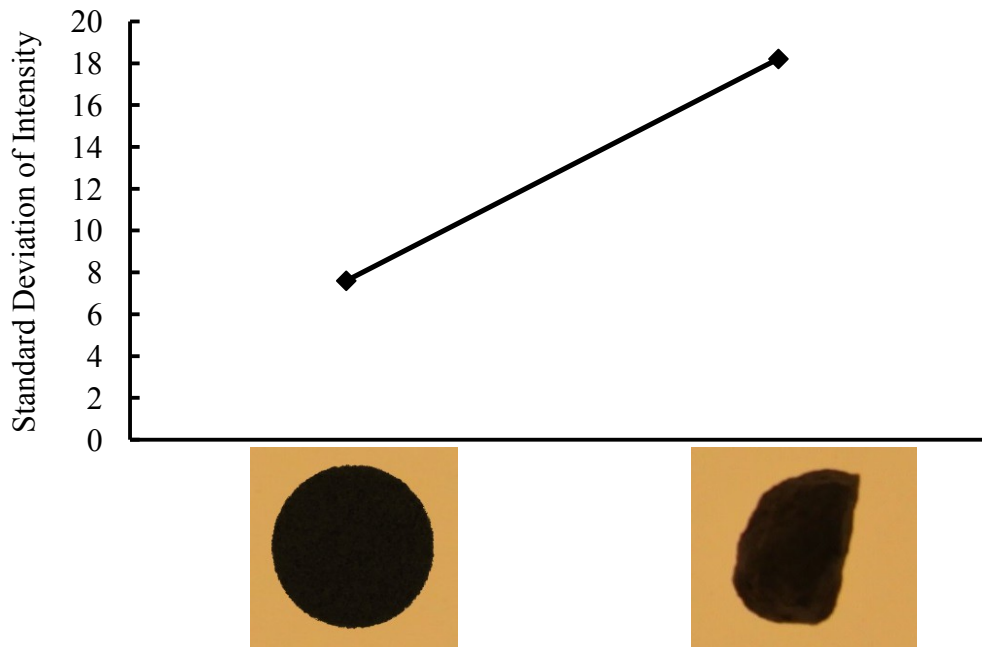


Figure 2-20- Relationship between particle texture and standard deviation of Intensity

The standard deviation of Intensity is affected by many parameters such as variable optical properties, minerals' color, lighting conditions, camera sensitivity, equipment setup condition and etc. Therefore, the calculated standard deviation of Intensity can be different for a same particle at different environmental conditions. Normalizing particle's standard deviation of Intensity by the standard deviation of Intensity of a completely smooth surface may remove the effects of environmental parameters and give a dimensionless parameter that the mentioned parameters do not affect it. Equation (2-19) can be used to normalize the particle's standard deviation of Intensity. However the validity of Equation (2-19) and specifying how much this equation remove the effect of mentioned parameters on the particle's standard deviation of Intensity, needs more investigation.

$$SD_N = \frac{SD}{SD_{Smooth}} \quad (2-19)$$

Where SD_N is the normalized standard deviation of the particle's surface intensity, SD is standard deviation of the particle's surface intensity and SD_{Smooth} is the standard deviation of intensity of a polished and completely smooth surface.

2.5.3.2 Texture parameter

Texture Parameter describes the surface texture of aggregate particles. Kuo (2000) and Masad (2007) developed Equation (2-20) to determine the Texture Parameter. This parameter is a dimensionless parameter that is equal to one for a completely smooth particle and greater than one for a rough particle. Figure 2-21 illustrates relationship between particle texture and texture parameter (calculated by image processing method). Particle roughness and Texture Parameter have positive affinity.

$$\text{TextureParameter} = \left(\frac{P}{P_{convex}} \right)^2 \quad (2-20)$$

Where P is the perimeter of the particle and P_{convex} is the perimeter of the bounding polygon.

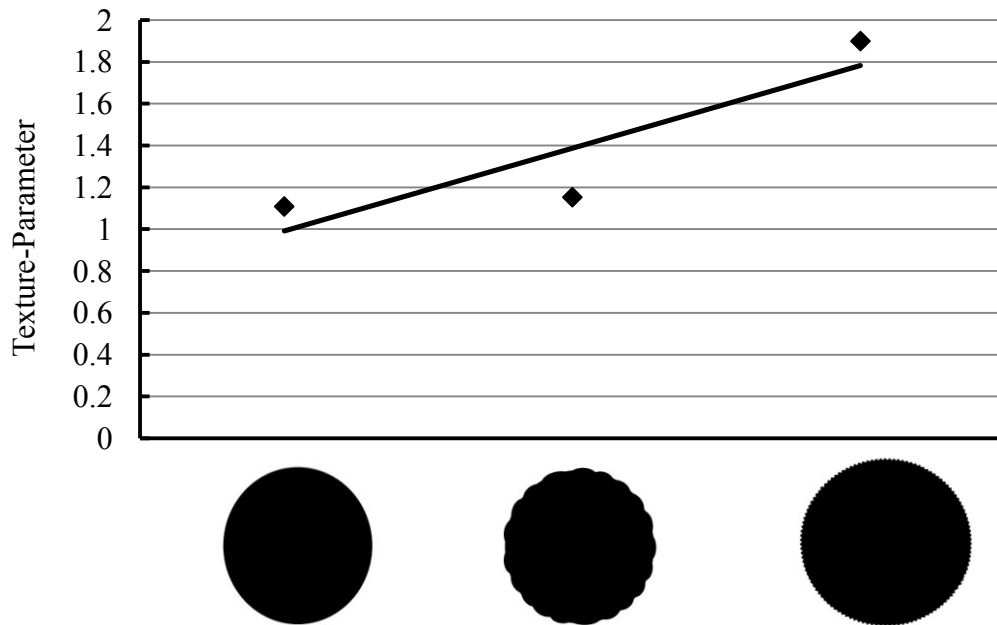


Figure 2-21- Relationship between particle texture and texture parameter

2.6 Summary and Conclusions

A review of the literature shows that confining pressure, void ratio and geometry of particles are important on the behavior of broken rock. The behavior of broken rock is complex because not only do many variables affect it but also the variables are dependent to each other. For example, confining pressure and particle shape parameters affect the broken rock void ratio. In addition, the literature shows that the behavior of generated particles after peak strength dominate the post peak behavior of a rock. Therefore, a good understanding of the broken rock behavior

can specify the post peak behavior of a rock. Determining the effective parameters on the strength of broken rock can define how much the post peak behavior can be modeled by broken rock.

The Form, Angularity and Texture are three independent parameters that quantify the particle geometry. The particles geometry was determined by image processing method using proposed formulas in the literature. Based on proposed equations in the literature and developed code in this research, we can conclude that the angularity index and angularity parameter have positive affinity with particle angularity, but convexity has negative affinity with the particle angularity. The form index of a circular particle is smaller than elliptical particles; however, a circular particle has greater form-factor than an elliptical particle. Texture parameter and standard deviation of intensity of a rough particle is greater than a smooth particle.

CHAPTER 3 : TRIAXIAL TESTS ON BROKEN ROCK AND NECESSARY CORRECTION

Chapter 3 contains the mechanical properties of intact sandstone that was crushed to prepare the broken rock specimens. In addition, this chapter presents an explanation of the conducted triaxial tests, equipment setup and membrane correction where membrane correction is an important part of triaxial tests. Two analytical methods, Compression Shell Theory and Hoop Tension Theory, have been investigated to calculate the rubber membrane error. Finally, a numerical modeling of membranes estimated the lateral stress of a membrane due to the specimen buckling deformation. Also, a summary of conducted triaxial test results is in this chapter.

3.1 Introduction

This research is based on experimental tests to investigate the influence of geometric characteristics of particles and confining pressure on the strength of broken rock. The triaxial test is a well-known method used to determine the mechanical properties of rock, soil and granular materials; defining Young's modulus, bulk modulus, internal friction angle and cohesion coefficients. The triaxial test was identified as the best choice to examine the behavior of broken rock because it provides acceptable conditions for deformation of a specimen without imposing any preset failure plane on a specimen.

The American Society for Testing and Materials (ASTM) provides a guideline to undertake triaxial compression tests. In common triaxial tests, the minimum (σ_3) and the intermediate (σ_2) principal stresses are equal ($\sigma_2 = \sigma_3$) and considered to be the confining pressure. During the triaxial test the confining pressure (σ_3) is constant and the axial pressure (σ_1) increases gradually. Finally, the axial stress-strain curve can be determined at a constant held confining pressure. The test may be repeated for several increasing confining pressures on the same specimen, and the peak strength and stress-strain curve determined for each confining pressure. With due care triaxial tests allow the post peak behavior to be recorded for a given single confinement.

ASTM D2938-95 (1995), ASTM D2850-03 (2003), ASTM D2664-04 (2004), ASTM D4543-08 (2008) and ASTM D4767-11 (2011) provide standards for performing triaxial compression tests. These codes have been prepared for intact rock specimens, but offer some general advice about the accuracy of measurement equipment, strain and stress ratios in performing triaxial tests. Some of the significant codes are summarized in Table 3-1.

Table 3-1- Selected standards for triaxial test on intact rock

Parameters	Selected of Standards
Strain Ratio	$10^{-2}/s - 10^{-5}/s$
Rockwell hardness	58 (HRC)
Testing Time	2-15 (Min)
Stiffness of Sleeve	60-70 (Shore)
Accuracy of Confining Pressure	2%
Accuracy Strain Measurements	2%

In this research, the following equipment was set up to conduct triaxial tests:

1. Confining pressure board

During the triaxial test, the confining pressure should be kept constant; therefore, a low level confining pressure control board was designed and built. This pressure control board can apply a constant confining pressure up to 100 psi.

2. Loading frame

The loading frame applies the axial force. Beyond peak strength, this frame can continue the test because it can apply the axial displacement at a constant rate.

3. Load cell and data acquisition

To record the applied force by the frame, a load cell and data acquisition system was set up in conjunction with the frame. The sampling frequency of the data acquisition unit was adjusted to sufficiently record data from the load cell.

4. Triaxial cell

The last part of the assembled equipment is the triaxial load cell to apply the lateral pressure to the specimen. Cell selection is an important step of the triaxial test.

The Hoek-Franklin Cell is the common triaxial cell for rock but it does not work well for granular material due to the sleeve resistance on specimen deformation. Figure 3-1 to Figure 3-3 show stress-strain curve on broken rock carried out via the Hoek-Franklin Cell, and it is clear that the rubber sleeve affects the deformation of specimen. After point A, the axial stress was increased with high slope and did not follow the anticipated trend because rubber sleeve was resisting on the specimen lateral deformation. Probably, after some lateral deformation of specimen, the resistance of rubber sleeve on lateral deformation acts like extra confining pressure on specimen; hence, the actual confining pressure on specimen has been increased while oil pressure in cell is constant. As another possible reason, specimen can contact the Hoek cell wall due to the diametral deformation of specimen exceeding the internal dimensions of the cell. Triaxial tests results using Hoek cell is in Appendix (A).

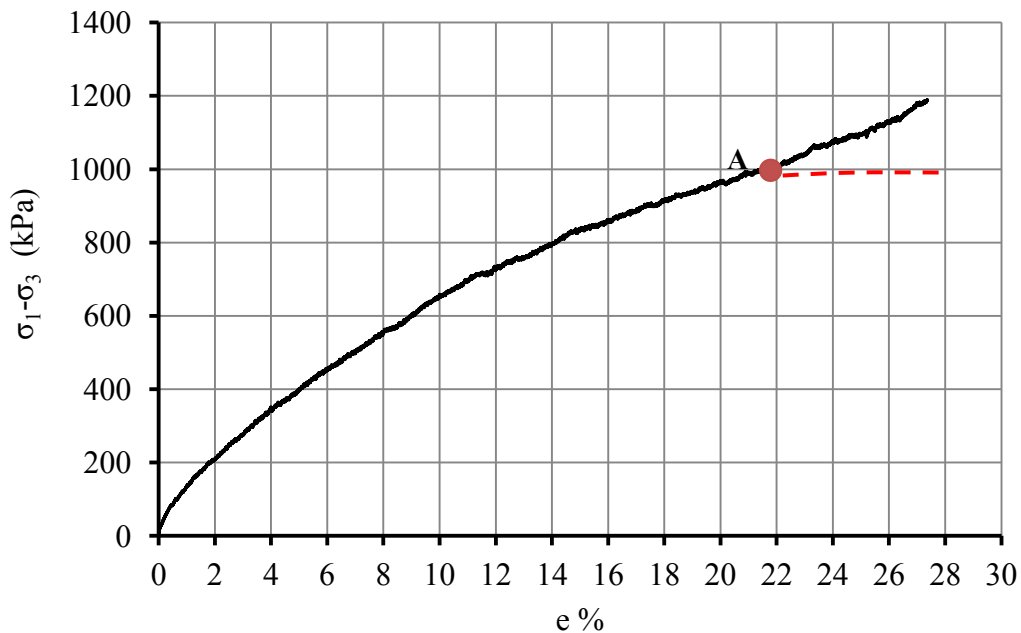


Figure 3-1- Triaxial test on broken sandstone by Hoek-Franklin Cell, with confining pressure set at 345 kPa

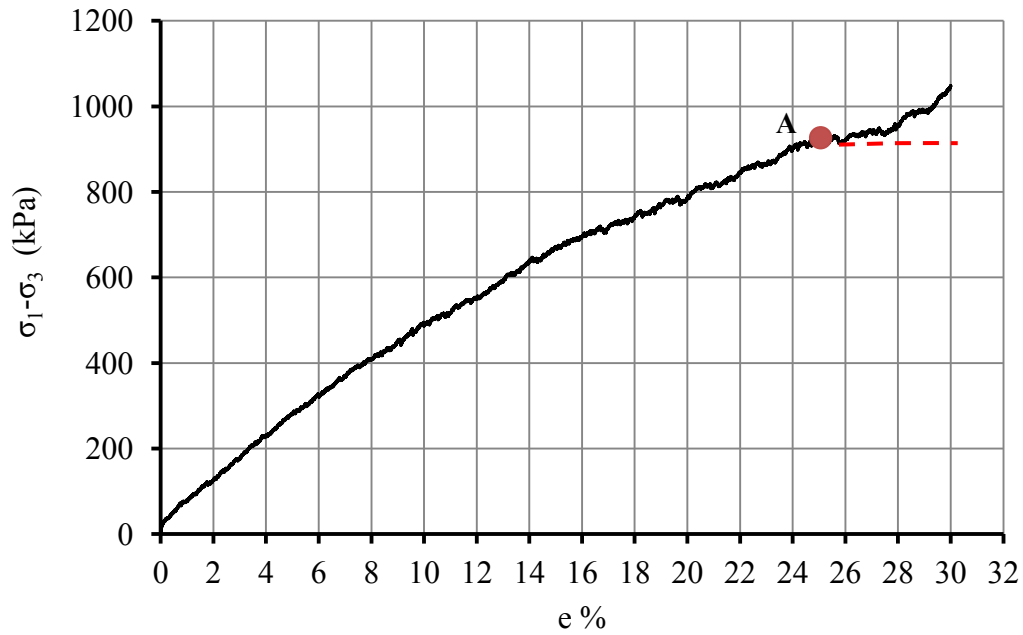


Figure 3-2- Triaxial test on broken sandstone by Hoek-Franklin Cell, with confining pressure set at 275 kPa

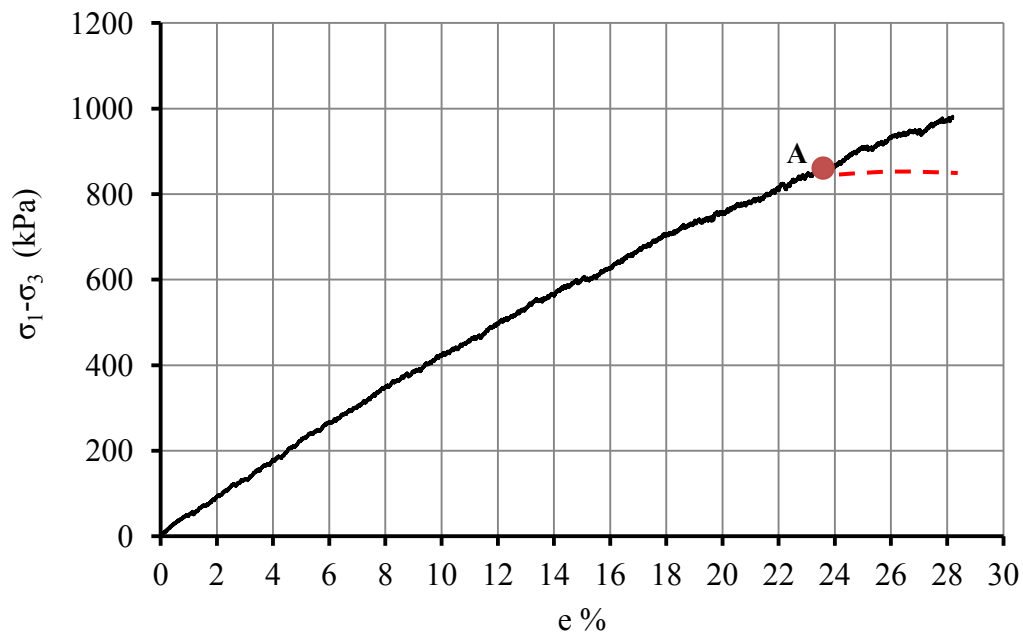


Figure 3-3- Triaxial test on broken sandstone by Hoek-Franklin Cell, with confining pressure set at 138 kPa

In this research, a soil triaxial cell was used as it is compatible with thin membranes to reduce the effect of the membrane on specimen deformation. Figure 3-4 and Figure 3-5 show the cell used and the triaxial test equipment that was set up to test broken rock in this research respectively.



Figure 3-4- The triaxial soil cell used in this research

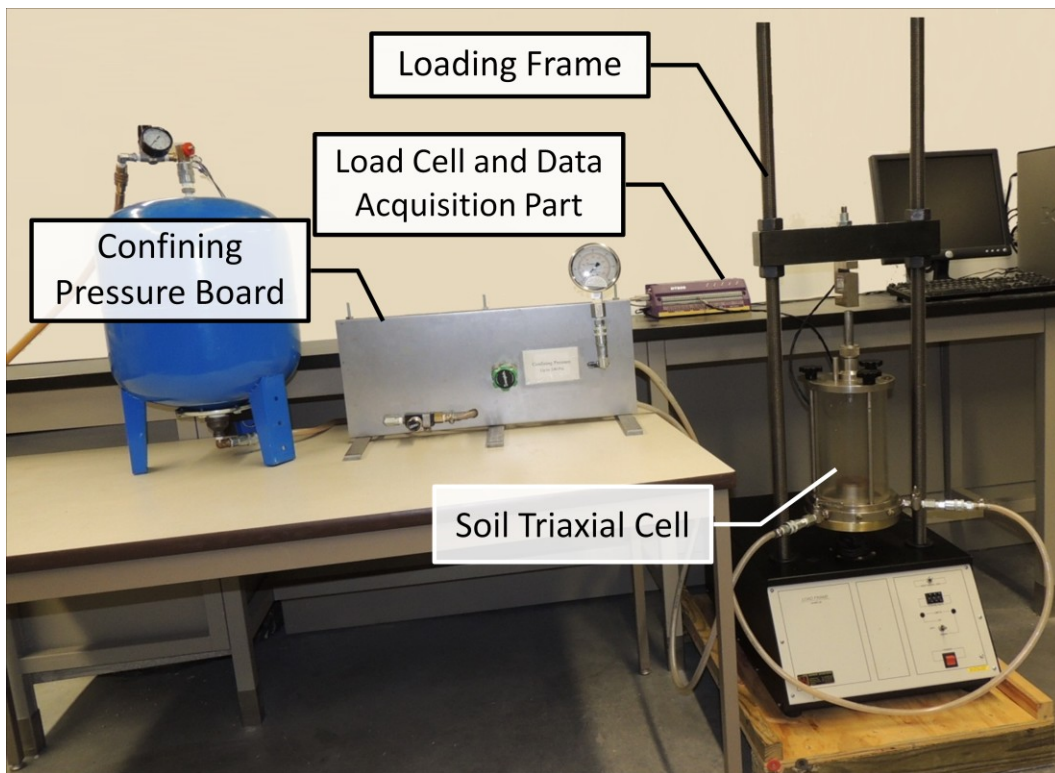


Figure 3-5- Triaxial test equipment for broken rock

3.2 Triaxial Testing Procedures and Specimen Preparing

In this research, the specimens used for the triaxial tests were broken sandstone generated by a rock jaw crusher with a gap of 1cm. The sandstone used in the crusher was homogenous sandstone with very fine grains. The homogeneity of this type of sandstone was a major reason to choose it in this research work. The density of intact sandstone was 2300 kg/m^3 . Three uniaxial compression tests were done on intact sandstone to determine the unconfined compressive strength. Figure 3-6 to Figure 3-8 show the result of the uniaxial compression tests on the intact sandstone. Figure 3-9 to Figure 3-11 show the failure mode of specimens after uniaxial compression test. Figure 3-11 illustrates the splitting failure mode on the specimen and the failure planes are almost parallel with the specimen axis. However, the failure plane is not close to the center of the specimen and specimen was split into many pieces under axial compression pressure. This type of failure mode may occur while the top and bottom of the specimen is not parallel. Therefore, the result of third test (Figure 3-11) was not used to calculate the uniaxial compressive strength of intact sandstone. By calculating the average of the first and second tests (Figure 3-9 and Figure 3-10), the uniaxial compressive strength of intact sandstone was calculated to be 32 MPa.

Based on conducted uniaxial compression tests on intact sandstone, the average of tangent young modules was calculated (at 50% of the intact rock strength) equal to 1950 MPa. In addition, Figure 3-12 and Figure 3-13 show the result of triaxial compression test on intact sandstone at 1 MPa and 3.45 MPa confining pressure respectively. Figure 3-14 and Figure 3-15 illustrate the failure mode after the tests. The failure mode of the specimen in Figure 3-14 shows the splitting failure on one side of the specimen, probably occurring because the top and bottom of specimen were not parallel. Therefore, the result of the presented triaxial test in Figure 3-14 was not used to analyze the mechanical properties of intact sandstone.

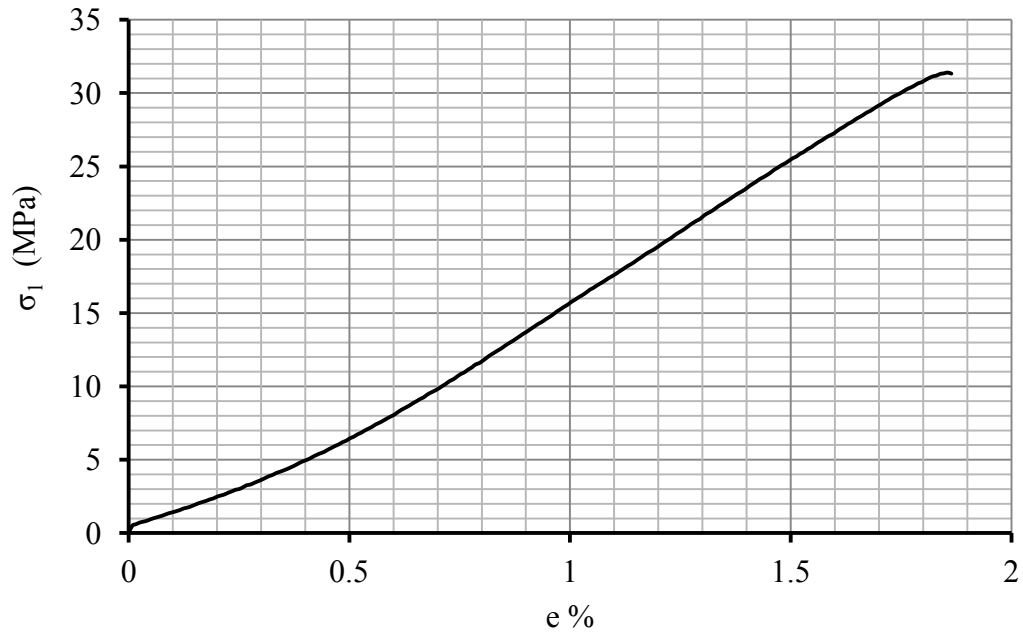


Figure 3-6- Uniaxial compression tests on the intact sandstone, $D=20\text{mm}$ and $L=46\text{ mm}$

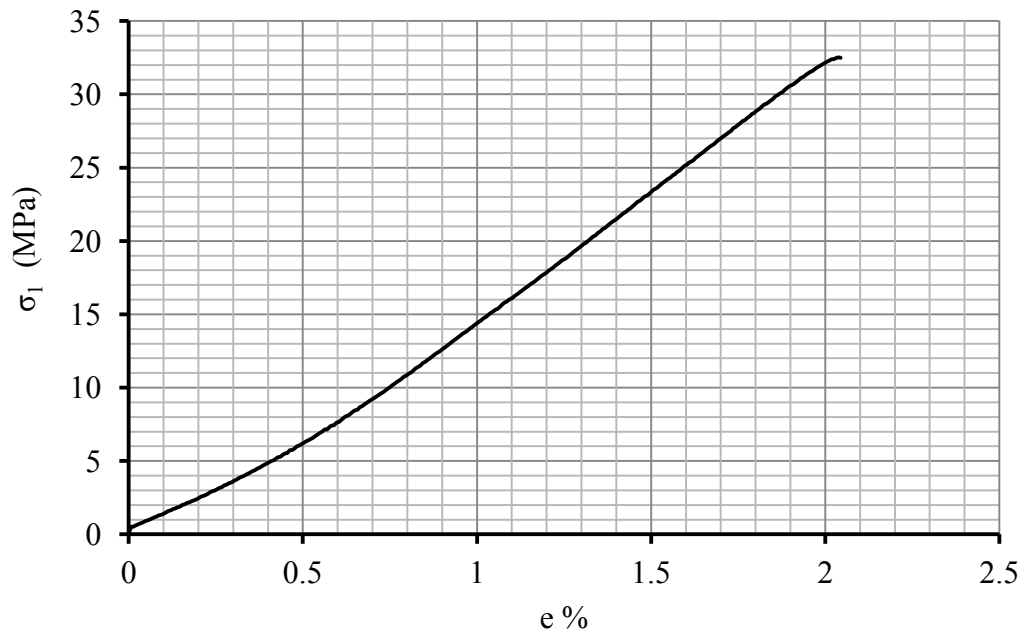


Figure 3-7- Uniaxial compression tests on the intact sandstone, $D=20\text{mm}$ and $L=45\text{ mm}$

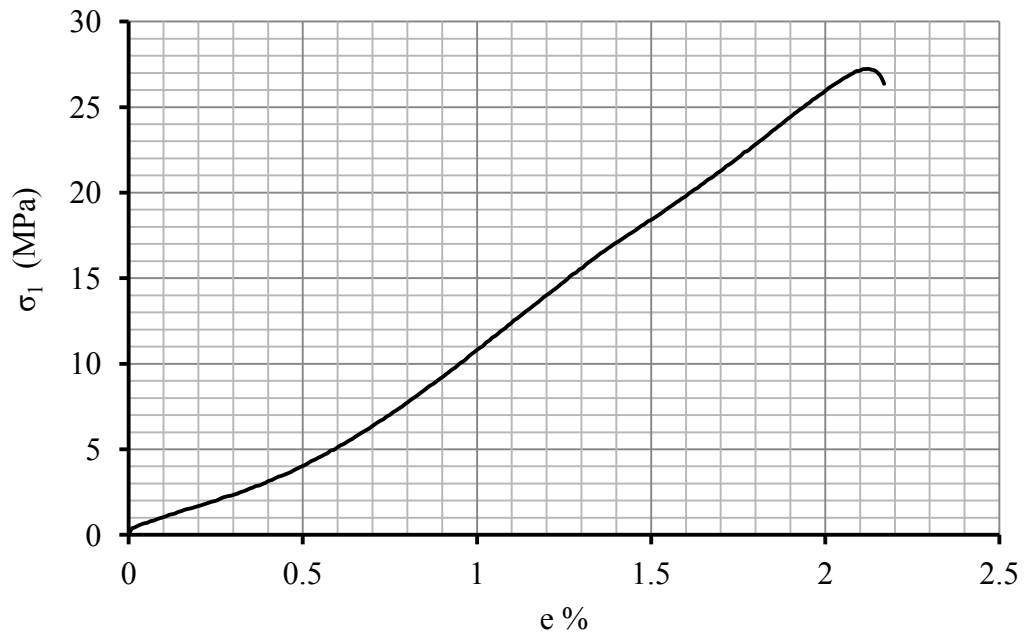


Figure 3-8- Uniaxial compression tests on the intact sandstone, $D=20\text{mm}$ and $L=40\text{ mm}$



Figure 3-9- Failure mode of the intact sandstone after uniaxial compression tests, $D=20\text{mm}$ and $L=46\text{ mm}$



Figure 3-10- Failure mode of the intact sandstone after uniaxial compression tests, $D=20\text{mm}$ and $L=45\text{ mm}$

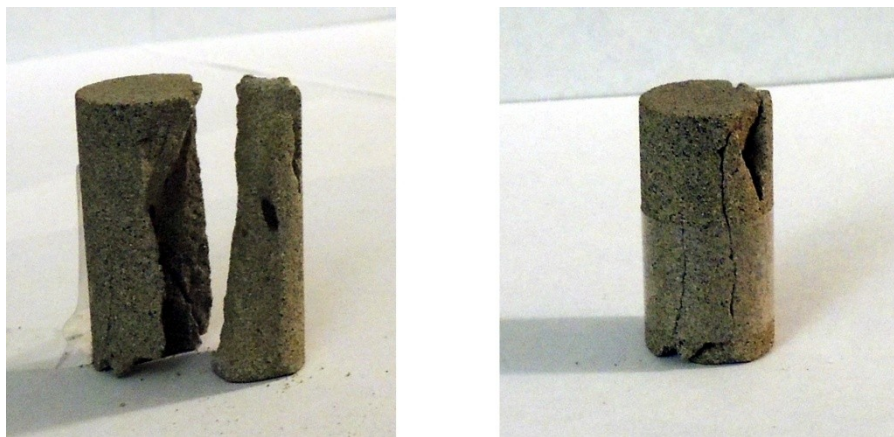


Figure 3-11- Failure mode of the intact sandstone after uniaxial compression tests, $D=20\text{mm}$ and $L=40\text{ mm}$

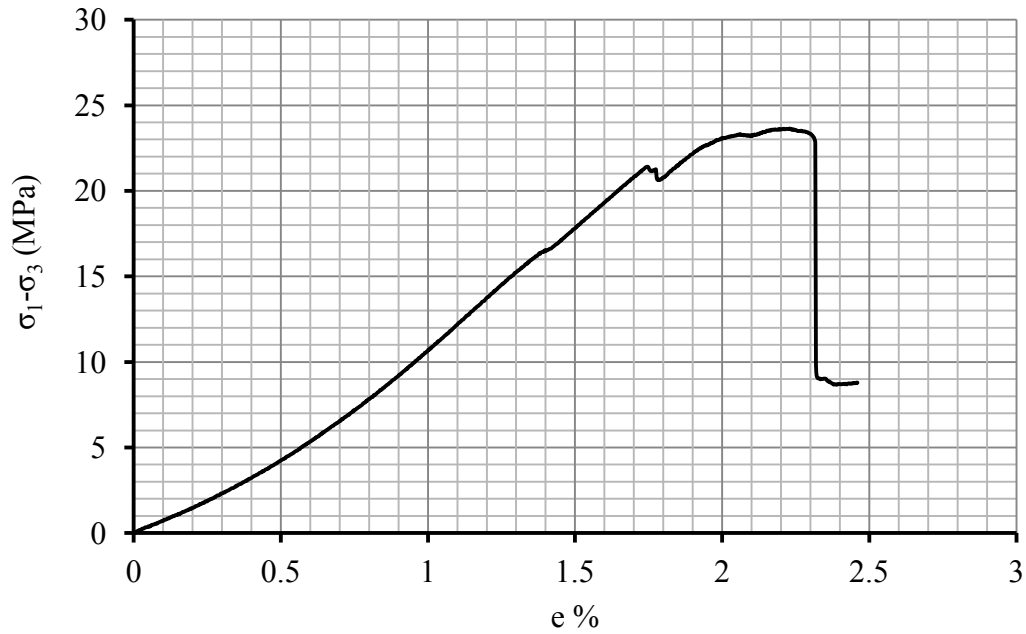


Figure 3-12- Triaxial compression tests on the intact sandstone, D=20mm, L=40mm and $\sigma_3=1$ MPa.

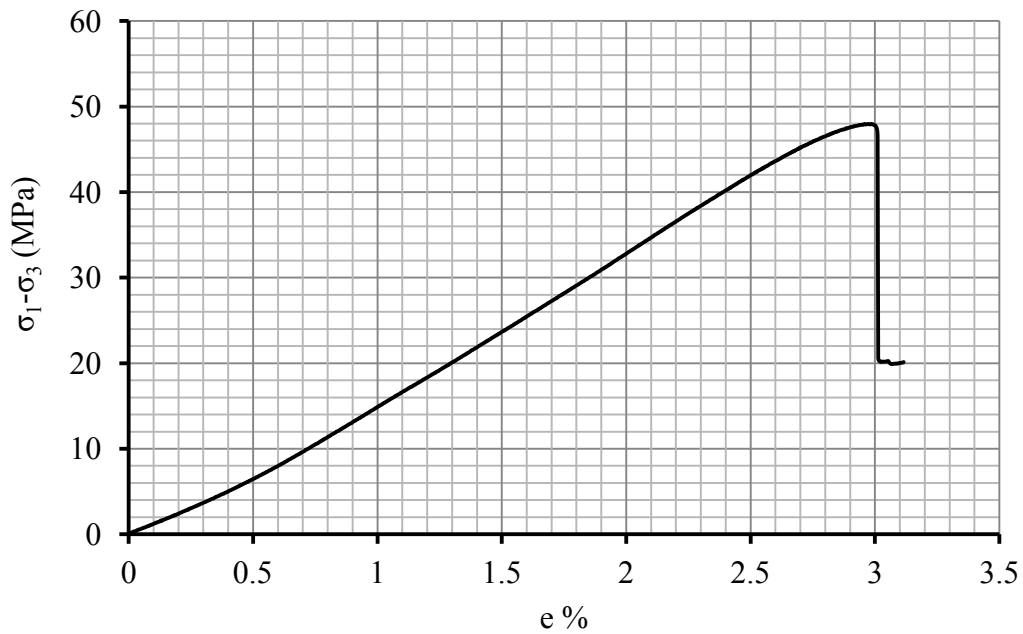


Figure 3-13- Triaxial compression tests on the intact sandstone, D=20mm, L=40mm and $\sigma_3=3.45$ MPa.



Figure 3-14- Failure mode of the intact sandstone after triaxial compression tests, D=20mm, L=40mm and $\sigma_3=1$ MPa.



Figure 3-15- Failure mode of the intact sandstone after triaxial compression tests, D=20mm, L=40mm and $\sigma_3=3.45$ MPa.

Table 3-2 shows a summary of acceptable results of the uniaxial and triaxial compression tests on intact sandstone. Figure 3-16 illustrates the relationship between minor principle stress and corresponding major principal stress at failure of intact sandstone. Equation (3-1) shows the best linear fit on σ_3 and σ_1 .

$$\sigma_1 = 5.5\sigma_3 + 32 \quad (3-1)$$

Researchers proposed Equation (3-2) to specify Coulomb criterion (Brady and Brown (2004)).

$$\sigma_1 = \frac{1 + \sin \phi}{1 - \sin \phi} \sigma_3 + \frac{2c \cos \phi}{1 - \sin \phi} \quad (3-2)$$

Where σ_1 is the major principal stress, σ_3 is the minor principal stress on critical failure plane, ϕ is the internal friction angle and c is cohesion coefficient.

Based on Equation (3-2), the internal friction angle and cohesion coefficient of intact sandstone was calculated by using Equation (3-3) and Equation (3-4), respectively.

$$\tan \psi = \frac{1 + \sin \phi}{1 - \sin \phi} \quad (3-3)$$

Substitution for $\tan \psi$ equal to 5.5 in Equation (3-2) gives the internal friction angle of intact sandstone to 43.8 degree.

$$5.5 = \frac{1 + \sin \phi}{1 - \sin \phi}$$

$$\phi = 43.8^\circ$$

$$\sigma_c = \frac{2c \cos \phi}{1 - \sin \phi} \quad (3-4)$$

Substitution for σ_c equal to 32 MPa in Equation (3-4) gives the cohesion coefficient of intact sandstone equal to 6.8 MPa.

$$32 = \frac{2c \cos 43.8}{1 - \sin 43.8}$$

$$c = 6.8$$

Figure 3-17 illustrates the Mohr-Coulomb failure envelope for intact sandstone. Based on Figure 3-17 the internal friction angle and cohesion coefficient of intact sandstone are 43.8 degree and 6.8 MPa, respectively.

Table 3-2- Summary of acceptable results of compression tests on intact sandstone

σ_3 (MPa)	σ_1 (MPa)
0	31.5
0	32.5
3.45	51

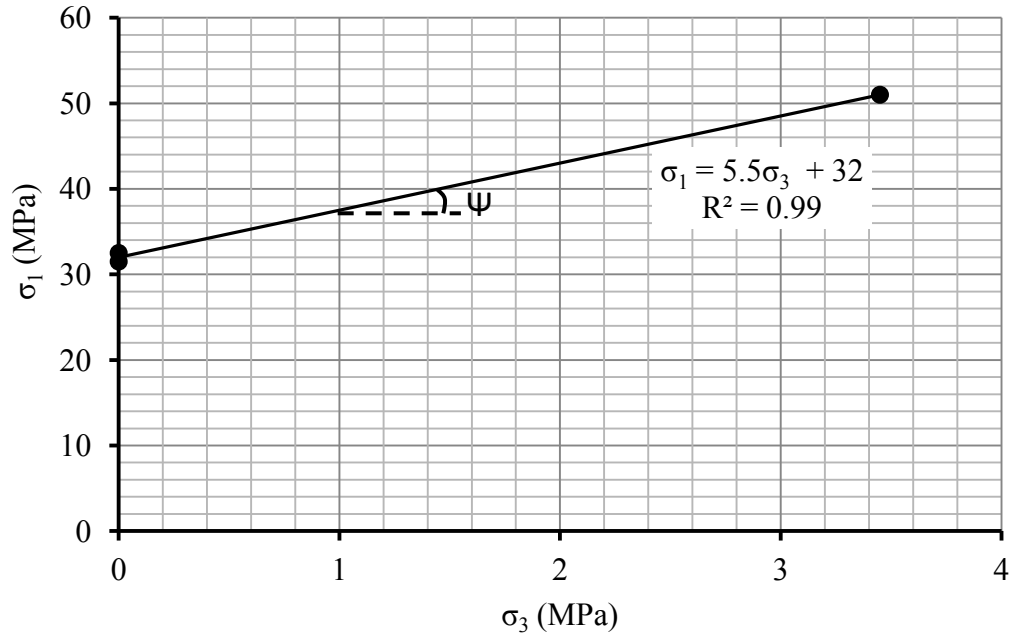


Figure 3-16- Linear relationship between confining pressure (σ_3) and ultimate strength (σ_1) of intact sandstone

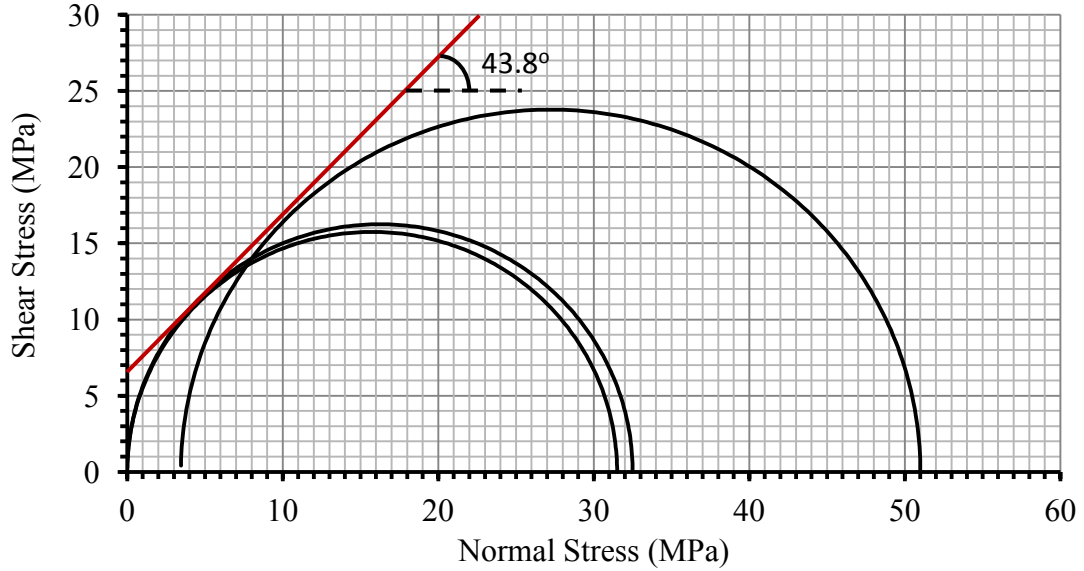


Figure 3-17- Mohr-Coulomb failure envelopes for intact sandstone

The constant parameter of Hoek-Brown criterion (m_i) of intact sandstone can be calculated by using the result of triaxial compression test. By substituting the result of triaxial compression test into the Hoek-Brown criterion, Equation (3-5) constant of Hoek-Brown criterion (m_i) was calculated equal to 11.

$$\sigma'_1 = \sigma'_3 + \sigma_c \left(m_i \frac{\sigma'_3}{\sigma_c} + 1 \right)^{0.5} \quad (3-5)$$

Where σ'_1 is the effective major principal stress, σ'_3 is the effective minor principal stress, σ_c is the uniaxial compressive strength of intact rock, and m_i is the constant parameters of the intact rock.

$$51 = 3.45 + 32 \left(m_i \frac{3.45}{32} + 1 \right)^{0.5}$$

$$m_i = 11$$

Table 3-3 shows a summary of physical and mechanical properties of tested intact sandstone.

Table 3-3- Summary of the physical and mechanical properties of sandstone

Property	Quantity
Density	2300 Kg/m ³
Young Modulus	1950 MPa
Uniaxial strength of Intact Rock	32 MPa
Internal Friction Angle of Intact Rock	44°
m_i	11

In this research, the following procedure was employed to determine the behavior of broken rock.

1. Crush sandstone via a rock jaw crusher.
2. Sieve the crushed rock to remove grains too small (<6 mm) and too big (>12 mm).
3. Determine the shape characteristics of specimens' particles through image analysis (Chapter 4 illustrates step 3).
4. Put the membrane in a mould. Figure 3-18 shows the mould used in the tests.
5. Fill the membrane with broken rock.
6. Vibrate it slowly at 60 hz to compact the broken rock.
7. Seal the top of the membrane.
8. Measure the exact height and diameter of the specimen at the top, middle and base with calipers.
9. Put the specimen inside the triaxial cell.
10. Fill the triaxial cell with water.
11. Increase the confining pressure gradually to the desired pressure.
12. Turn on the data acquisition system to record the applied stress and corresponding axial strain.
13. Apply the lateral pressure simultaneously.
14. Continue to apply axial force via the loading frame.

15. Adjust the confining pressure to create a constant confining pressure during the test.
16. After completing the test, release the axial force and confining pressure at the frame rate.
17. Drain the water from the triaxial cell.
18. Repeat the test on new specimens at different confining pressures.



Figure 3-18- Used mould in conducted tests.

3.3 Failed Tests Prematurely

Some of triaxial compression tests on broken rock failed prematurely because of problems during the test. The results of failed tests were not used in analyzing the triaxial test results to investigate the behavior of broken rock. The following problems were major reasons that some triaxial tests were failed prematurely.

1. Rubber membrane punctured by a sharp particle
2. Eccentric deformation of specimen

A sharp particle of a broken rock specimen probably would puncture the rubber membrane because of increasing the lateral diameter of the specimen during the triaxial test. If the membrane is punctured by a particle, the water will flow into the specimen. The result of the triaxial test is not valid if the rubber membrane is punctured by a sharp particle during the test because water flows into the specimen and decreases the frictional strength between particles. In addition, applying confining pressure on a specimen with a punctured membrane is impossible. Based on this research, the following signs can help researchers to determine when the membrane is punctured by a particle.

- Confining pressure suddenly decreases
- Air bubbles appear around the specimen during the test
- Visual appearances of water inside the membrane during the test
- Water inside the membrane after taking out the specimen

Monitoring the confining pressure is important in triaxial tests on broken rock to determine when the membrane is punctured by a sharp particle. However, sometimes the puncture in the membrane is very small and detecting a sudden decrease at confining pressure is impossible. In this case, after finishing the test and taking out the specimen, there is water inside the specimen, and the result of the test is not reliable because determining when water had flowed inside the

specimen and affected the frictional behavior of particles is impossible. Figure 3-19 illustrates a test in which the membrane was punctured by a sharp particle, and the confining pressure dropped suddenly. Figure 3-20 shows a test with very fine puncture on membrane by a sharp grain. Therefore, the confining pressure was not decreased suddenly but water was inside the membrane visually.



Figure 3-19- A punctured membrane with a sharp particle, with a sudden decrease at confining pressure after puncturing



Figure 3-20- A punctured membrane with a sharp particle, without a sudden decrease at confining pressure after puncturing

Eccentric deformation of specimen during the triaxial test is another problem that can affect the result. The result of a triaxial test with eccentric deformed specimen is not reliable because the applied force by the loading frame is not applied to the axial of the specimen. Therefore, the applied axial force by the frame cannot be used to calculate the maximum significant stress. Figure 3-21 shows a triaxial test with eccentric deformation of specimen. The reason for eccentric deformation of specimen during the triaxial test is poor specimen preparation. The top and bottom of specimen should be parallel and completely perpendicular to axial of specimen. The loading steel cap should be stay perpendicular to axial of specimen after emplacing it on the top of specimen. Information of the premature failed tests was presented in the Appendix (B).



Figure 3-21- An eccentric deformation of specimen in triaxial test on broken rock

3.4 Triaxial Test Results

Determining the ultimate axial strength of broken rock specimen from axial stress-strain graph is difficult because there are several critical points that can be considered as an ultimate strength point. Figure 3-22 shows the axial stress-strain graph for a specimen of broken rock. There are three points (A, B and C) that can be considered as a possible ultimate strength points. In this research, the first maximum point on the axial stress-strain graph (point A) was taken as the ultimate strength, and assumed after the first maximum point (point A), breakage of some particles may change the particle geometry of the specimen. The geometry of particles of specimen after first maximum point can be changed and be different from the geometry of specimen at the beginning of the test.

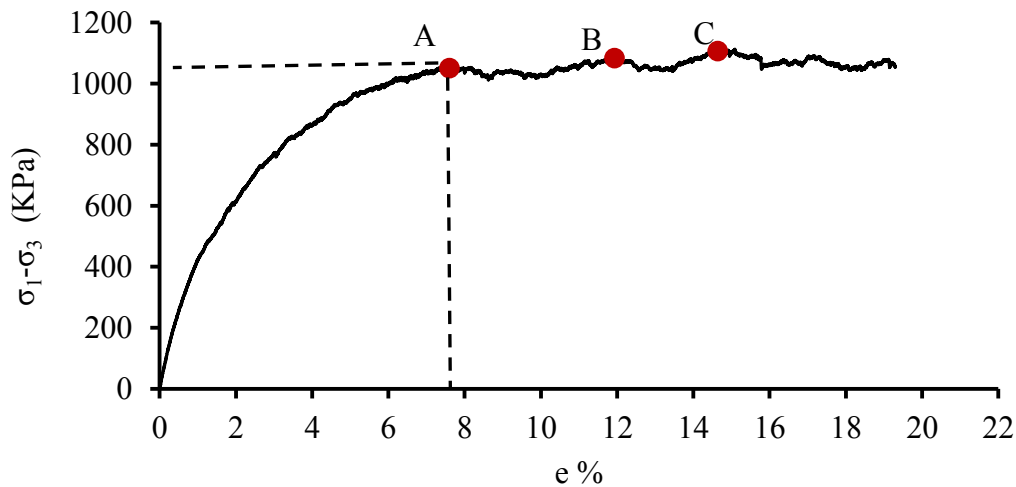


Figure 3-22- Axial stress-strain graph obtained from triaxial compression test on specimen of broken rock at confining pressure equal to 276 kPa

Monitoring the changes of cell pressure during the triaxial test is another parameter that can be useful to recognize the first maximum point on axial stress-strain graph. The deformation of specimen increase the cell pressure gradually, therefore operator release the pressure to have constant confining pressure during a triaxial test, but upon reaching the first maximum point on axial stress-strain graph, the cell pressure was unstable and needed more adjustment to be constant.

On the other hand, the first strength point of broken rock in triaxial test occurs when the cell pressure (confining pressure) starts to instability and needs more to be adjusted. Therefore, monitoring the change of confining pressure can be useful to recognize the first strength point of broken rock specimen in triaxial compression test.

Table 3-4 shows the summary of ultimate strength of each specimen that was determined by the mentioned method from the axial stress-strain graph of triaxial compression test on the specimen of broken rock. The details of axial stress-strain graph of triaxial tests are in Appendix (C).

Table 3-4- The ultimate strength of the specimens determined by triaxial tests

No.	σ_3 (kPa)	σ_1 (kPa)	e %	Onset of cell pressure instability per axial strain	Relative Density	Void Ratio
Test1	137.90	751.53	5.65	5.10	0.637	0.569
Test2	137.90	675.69	8.10	6.45	0.630	0.588
Test3	137.90	792.86	6.00	4.54	0.661	0.512
Test4	137.90	700.49	9.85	9.12	0.624	0.602
Test5	137.90	648.01	6.50	5.72	0.591	0.692
Test6	137.90	751.53	11.99	10.55	0.632	0.583
Test7	137.90	579.16	6.58	5.82	0.559	0.789
Test8	137.90	661.91	10.10	9.14	0.614	0.630
Test9	206.84	1068.69	6.04	5.05	0.637	0.569
Test10	206.84	923.94	5.93	5.60	0.602	0.662
Test11	206.84	1075.58	6.36	5.21	0.651	0.536
Test12	206.84	1013.53	6.20	5.80	0.616	0.622
Test13	206.84	930.79	5.65	5.61	0.584	0.712
Test14	275.79	1275.53	6.60	6.04	0.603	0.658
Test15	275.79	1206.58	7.80	7.15	0.593	0.685
Test16	275.79	1323.79	7.60	6.50	0.633	0.581
Test17	275.79	1137.64	7.97	7.82	0.576	0.735
Test18	34.47	290.66	6.31	6.00	0.602	0.661
Test19	34.47	243.45	4.91	4.85	0.584	0.713
Test20	34.47	307.67	5.71	5.04	0.660	0.515
Test21	34.47	206.96	6.11	5.90	0.624	0.601
Test22	34.47	219.99	8.71	8.14	0.629	0.591
Test23	68.95	419.37	6.37	6.05	0.616	0.622
Test24	68.95	441.97	7.64	7.14	0.634	0.578
Test25	68.95	479.10	6.80	6.80	0.647	0.545
Test26	68.95	440.63	11.20	10.70	0.640	0.563
Test27	68.95	390.26	6.11	4.04	0.632	0.583

In this research, the triaxial tests on broken rock show that recognizing the ultimate strength of broken rock is completely different from the compression test on intact rock. Figure 3-23 illustrates an example of compression test on intact rock. The ultimate strength of an intact rock is obviously clear, but determining the strength of broken rock by using triaxial compression test at low confining pressure is complicated and needs more discussion because there is more than one maximum point (for example point A, B and C in Figure 3-22) on the axial stress-strain graph.

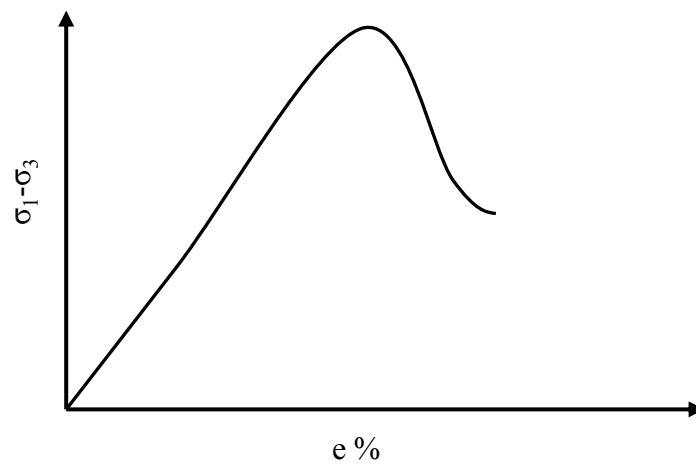


Figure 3-23- An example of compression test on intact rock

Monitoring the cell pressure can help with understanding the behavior of broken rock deformation; therefore in this research the onset of instability of cell pressure was noted and used as a sign to recognize the first maximum point on axial stress-strain graph. The results show that the maximum point on axial stress-strain graph occurs after cell pressure instability. The onset of cell pressure instability for each test is given in Table 3-4.

3.5 Membrane correction

In the triaxial test, a rubber membrane encloses the specimen to allow confining pressure to be applied by a fluid to the specimen. The behavior of the membrane affects the results because the axial and lateral strain of the specimen deforms the rubber membrane during the test. Mechanical properties of the membrane, the applied confining pressure, size of grains in the specimen, geometry of grains and thickness of the membrane all affect test results.

Many researchers have studied the effects of confining a membrane in triaxial tests; Henkel (1952), Bishop (1962), Duncan (1967), Frydman (1973), Baldi (1973), Molenkamp (1981), Ramana (1981), Rochelle (1988), Baxter (2000), Frost (2009) and Noor (2012). The errors that occurred were due to the mechanical properties of the membrane, type and grain size of the specimen, but were also seen as being negligible in some cases. ASTM D4767-11 (2011) recommends the correction of triaxial test results if the error due to the membrane represents more than 5% of the deviatoric stress.

Baldi (1973) and Molenkamp (1981) believed that membrane penetration into the void space between grains affects the measurement of the specimen's volume change in drained tests and the pore pressure in undrained tests. Molenkamp (1981) shows that membrane penetration is a function of confining pressure and elastic modulus of the membrane. Baldi (1973) also, demonstrated that particle shape has less effect on membrane penetration. In this research, the membrane penetration has been neglected because the triaxial tests are conducted at low confining pressure, to a maximum of 276 kPa, and the literature shows the membrane penetration is critical on the pore pressure in an undrained test. In the tests conducted here, the specimens were dry.

Henkel (1952), Bishop (1962) and Baxter (2000) recommended a method to determine the mechanical parameters of membranes in tension. This method has been based on stretching a one-inch wide loop of the membrane and measuring the relative axial deformation. Figure 3-24 shows the sketch of method. Where

Equation (3-6), (3-7) and (3-8) are the formulas used by the researchers in evaluating the parameters.

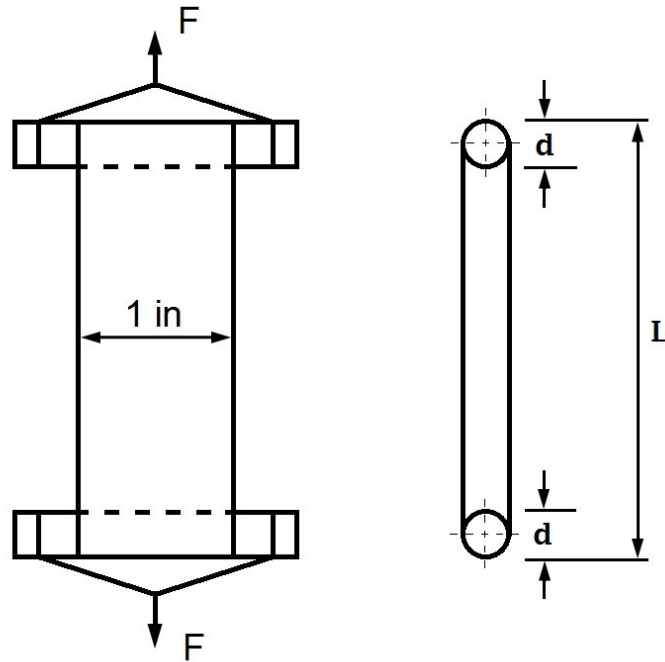


Figure 3-24- The sketch for measuring the extension modulus of a rubber membrane, after Bishop (1962)

$$L_m = 2(L - d - 2t) + \pi(d + t) \quad (3-6)$$

$$F_{in} = \frac{F}{2} \quad (3-7)$$

$$M = \frac{F_{in}}{\varepsilon} \quad (3-8)$$

Where F is axial force, d is the diameter of the bar, t is the membrane thickness, L is overall length of the membrane ring in the test, L_m is the mean length of the membrane, F_{in} is load per inch and M is the extension modulus of the membrane.

In the research in this thesis two types of membrane have been used, latex and neoprene/latex mixed membranes. Neoprene/latex mixed membranes had better performance in triaxial tests on broken rock because of its resistance to puncture by sharp grains. Figure 3-25 shows the stress-strain curve that has been determined by the mentioned method. In addition, Figure 3-26 illustrates Newton per meter curve of latex and neoprene/latex membranes.

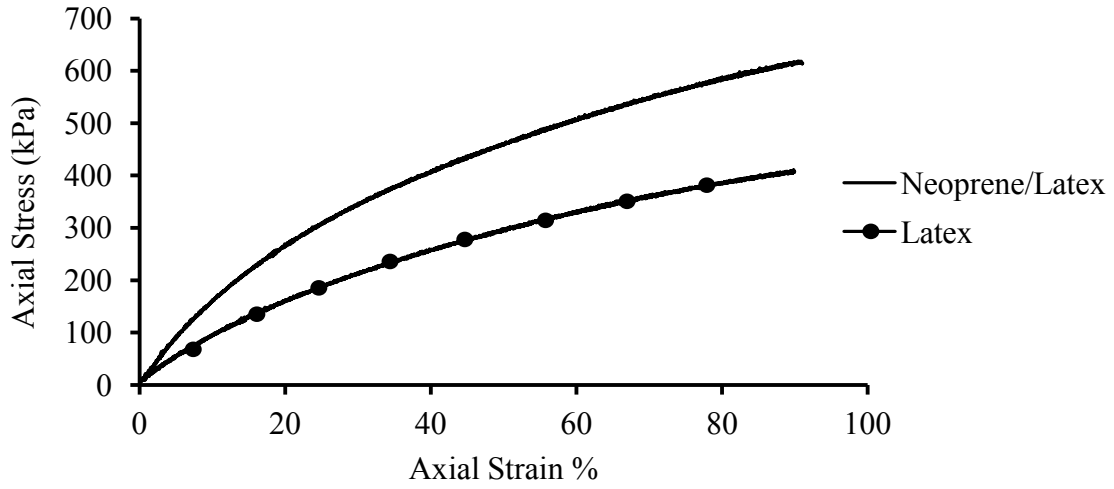


Figure 3-25- Stress- strain curve of rubber membranes

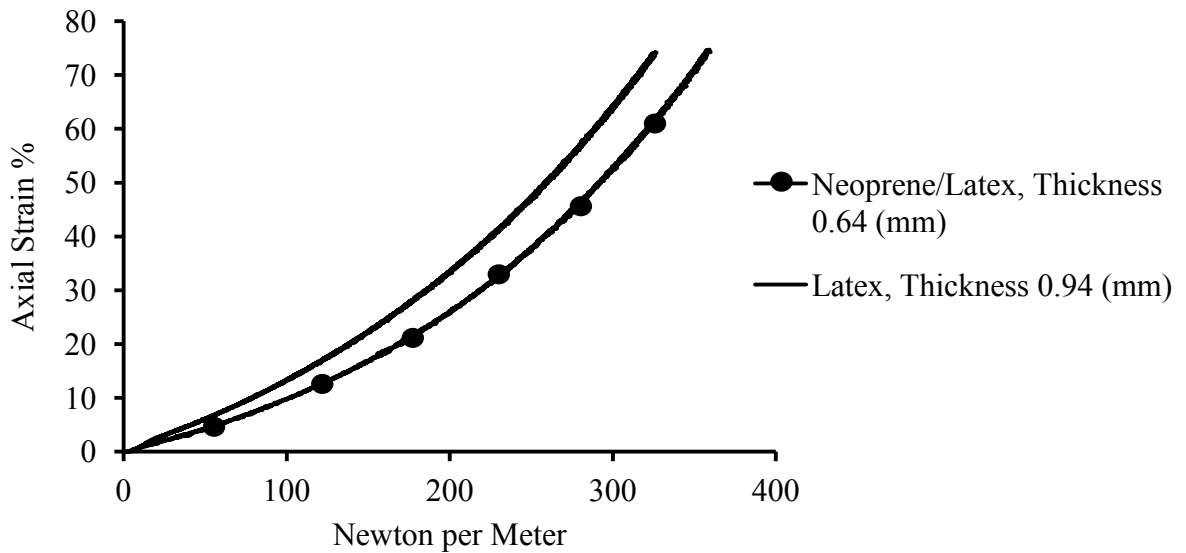


Figure 3-26- Newton per Meter curve for rubber membrane

To determine the membrane restraint correction, analytical methods have been developed based on specimen and membrane deformed shape. Henkel (1952), Rochelle (1988) and Baxter (2000) developed a compression shell theory to determine the deformation of rubber membranes where the membrane deforms like a cylindrical shell under axial compression and does not buckle during the test. Rochelle (1988) believed that at high confining pressure, sufficient pressure would hold the membrane tightly in contrast to the specimen; therefore, the membrane and specimen deform together with no buckling.

Henkel (1952) used hoop tension theory to calculate the lateral stress of the membrane in bulging deformation of specimens during triaxial tests. In buckling, the increasing diameter of the specimen causes circumferential tension in the membrane as the confining membrane resists lateral deformation of the specimen. The induced lateral tension in the membrane acts like an extra confining pressure around the specimen. For this reason, to correct the membrane error, the induced lateral tension in the membrane should be added to the cell confining pressure.

In this research, the lateral restraint of the rubber membrane has been calculated by three different methods; compression shell theory, hoop tension theory and numerical modeling.

1. Compression Shell Theory

Henkel (1952) explained when there is no buckling deformation, the membrane deforms like a cylindrical shell under axial compression, and the rubber correction can be calculated through Equation (3-9).

$$\sigma_r = \frac{\pi D M_c \varepsilon (1 - \varepsilon)}{A_0} \quad (3-9)$$

Where D is the initial diameter of the specimen, M_c is the compression modulus of the membrane (N per meter), ε is the axial strain of the specimen and A_0 is the initial area of the specimen.

Henkel (1952) and ASTM (2007) recommend subtracting the rubber correction factor from the major axial stress to calculate the correct deviatoric stress. Equation (3-10) shows the corrected deviatoric stress considering the membrane correction.

$$\text{Deviatoric.Stress} = \sigma_1 - \sigma_3 - \sigma_r \quad (3-10)$$

Figure 3-27 illustrates the correction for Neoprene/Latex and Latex membranes using Equation (3-9). To plot Figure 3-27, the initial diameter of the specimen was 0.07 meter and the average compression modulus of Neoprene/Latex and Latex membranes were 928.5 and 735.5 N/m respectively as shown Figure 3-26. It is clear that the maximum induced correction for Neoprene/Latex and Latex membranes in the conducted tests are less than 5% of peak strength, which is negligible.

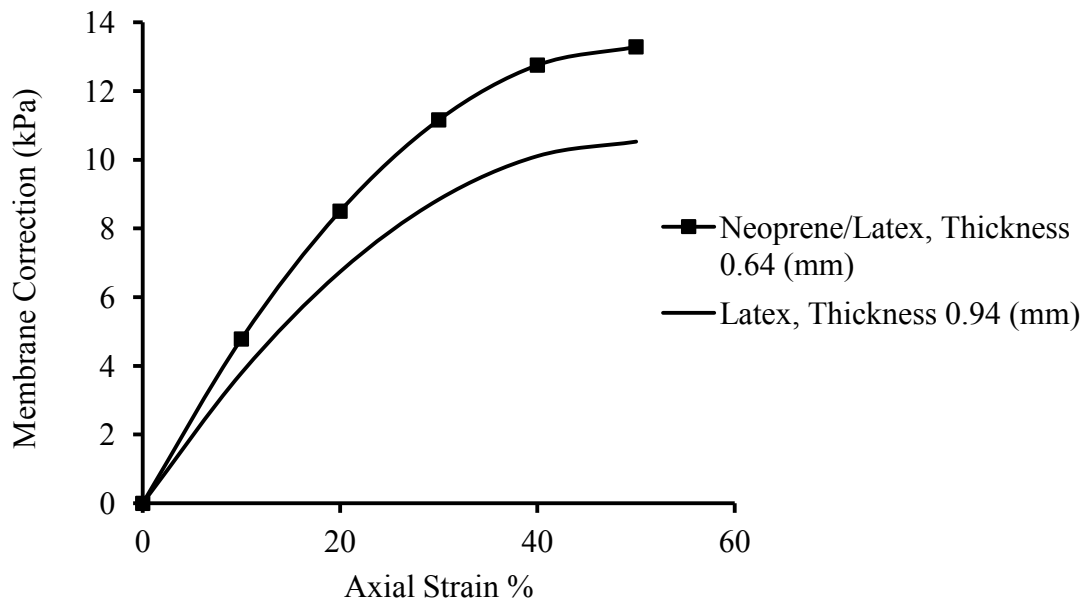


Figure 3-27- Lateral confining pressure correction through compression shell theory

2. Hoop Tension Theory

Henkel (1952) provided information about membrane error correction in buckling deformation of specimens while the membrane acts like a rubber belt to resist lateral deformation of the specimen. The induced lateral tension in the membrane functions as an increase in confining pressure for the specimen. Henkel (1952) introduced Equation (3-11) to calculate membrane error considering hoop tension theory in buckling deformation.

$$\sigma_r = \frac{2M(1-\sqrt{1-\varepsilon})}{D(1-\varepsilon)} \quad (3-11)$$

Where D is the initial diameter of the specimen, M is the compression modulus of the membrane (N/m), ε is the axial strain of the specimen.

Figure 3-28 shows the correction for Neoprene/Latex and Latex membranes through hoop tension theory. The maximum error is less than 5% of peak strength considering the test results reported in Appendix C.

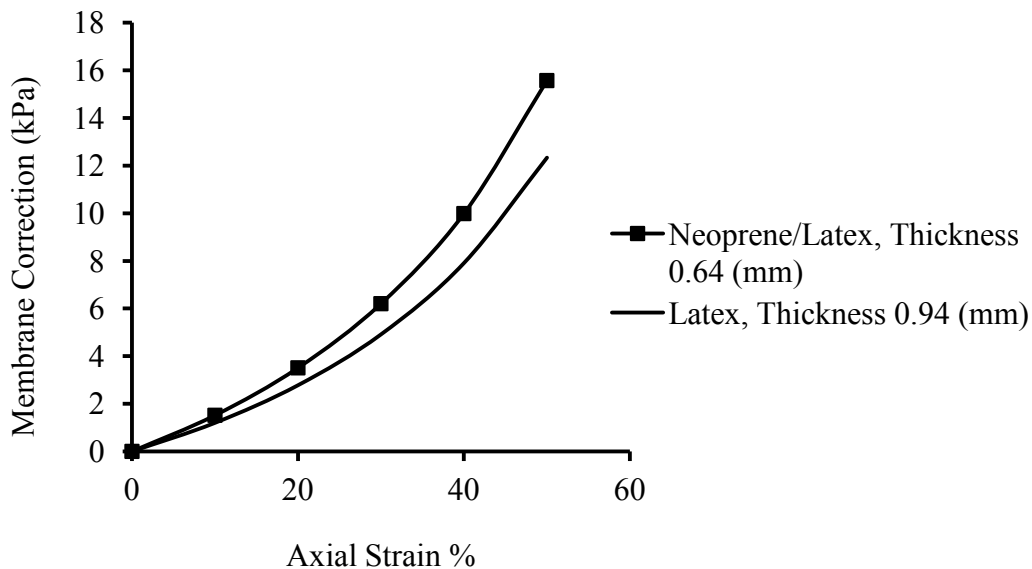


Figure 3-28- Lateral confining pressure correction through Hoop tension theory

3. Numerical modeling

In this research, a numerical model of the membrane was generated via ABAQUS to better understand the behavior of the membrane considering the shape of the specimen deformation. A cylindrical membrane was created with the actual dimensions of Neoprene/Latex membrane in the triaxial test. The stress-strain curve in Figure 3-25 was applied to the model and the model behavior assumed hyperelastic. The deformations of specimens are seen to be buckling in this research because of the low confining pressure; therefore, the buckling deformation of membrane was modeled using ABAQUS .

The following steps were done for membrane numerical modeling:

1. Generating the geometry of membrane
2. Assigning the mechanical properties
3. Applying the boundary conditions and load
4. Assigning the mesh to model
5. Running the model

The rubber membrane has a cylindrical geometry; therefore, it can be presented by an axisymmetric model. In an axisymmetric shape, the geometry of the shape has axial symmetry. Thus, the rotation of a section of the shape around an axis can generate the entire shape. In Figure 3-29, 360-degree rotation of the rectangle with respect to the axis can generate a cylindrical shape with a radius and thickness equal to r and t , respectively.

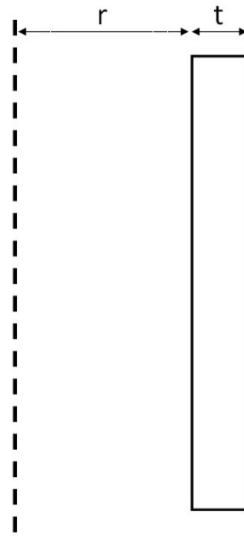


Figure 3-29- A section of membrane in a axisymmetric model

An axisymmetric model of membrane was built in ABAQUS by generating a section of membrane. The behavior of membrane was assumed hyperelastic behavior and the stress-strain data in Figure 3-25 for Neoprene/Latex membrane was assigned to modeled membrane.

The boundary conditions of model were determined based on the deformation of membrane in practice. In a compression triaxial test, the membrane height is going to be decreasing while the specimen is buckling; therefore, in the model the bottom boundary was restrained in both X and Y direction, but the upper boundary was restrained only in X direction and it could move in Y direction. Figure 3-30 illustrates the sketch of the boundary conditions.

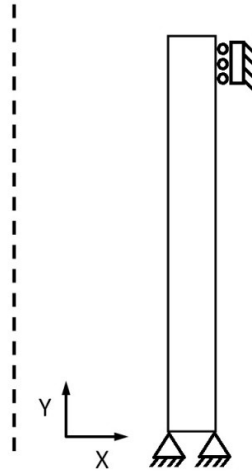


Figure 3-30- Boundary conditions of model

To apply the buckling deformation on the membrane a curved rigid part was pushed toward to the membrane. The rigid part does not have any deformation and there is no frictional resistance between the rigid part and membrane. When the rigid part is pushed toward membrane, the average of generated stress between rigid part and model is equivalent lateral stress due to membrane deformation. Figure 3-31 shows the interaction of rigid part and membrane.

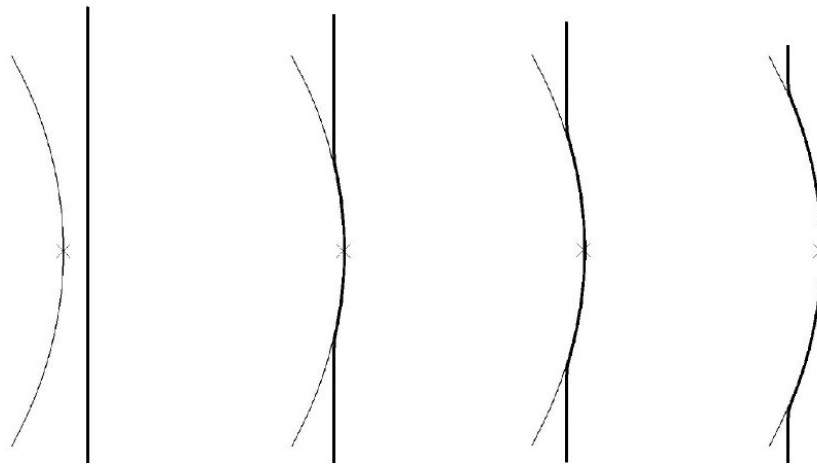


Figure 3-31- Deformation of membrane by pushing a rigid part

Figure 3-32 shows a 3D view of the deformed membrane that it is analogous to the specimen deformation in actual tests.

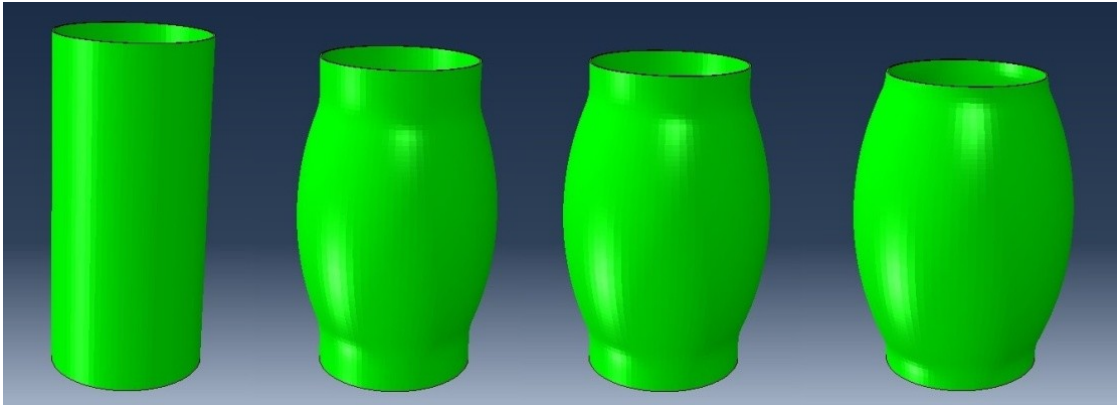


Figure 3-32- Membrane buckling in numerical modeling

Maximum of the lateral displacement of modeled membrane and average of the corresponding generated stress between rigid part and membrane was recorded as given in Figure 3-33 and Figure 3-34. ABAQUS recommends a four nodes linear element for axisymmetric modeling. After mesh generating and specifying the type of element on model, membrane model is ready to run.

Figure 3-33 illustrates the maximum lateral strain of the membrane and lateral correction stress. The maximum error is 8.62 kPa at a lateral strain of 50 percent. This calculation of error is an upper estimation for the error calculation because in tests conducted in this research the maximum lateral strain is less than 25 percent. Therefore, the error due to the rubber membrane is considered negligible in this research.

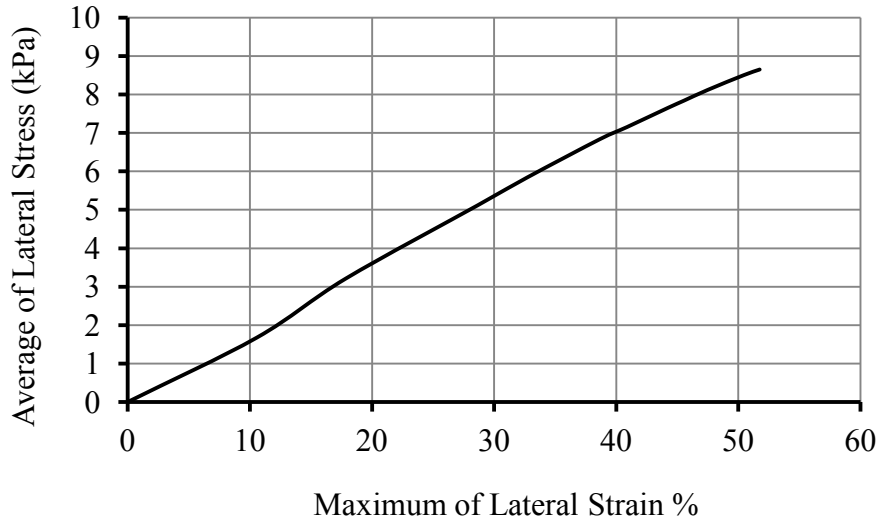


Figure 3-33- Average of lateral correction stress and maximum of lateral strain of membrane

Figure 3-34 shows the lateral displacement of the membrane and lateral correction stress. The lateral displacement of the membrane in the actual tests performed here was less than 0.03 m; therefore, the maximum membrane error was less than 8.62 kPa.

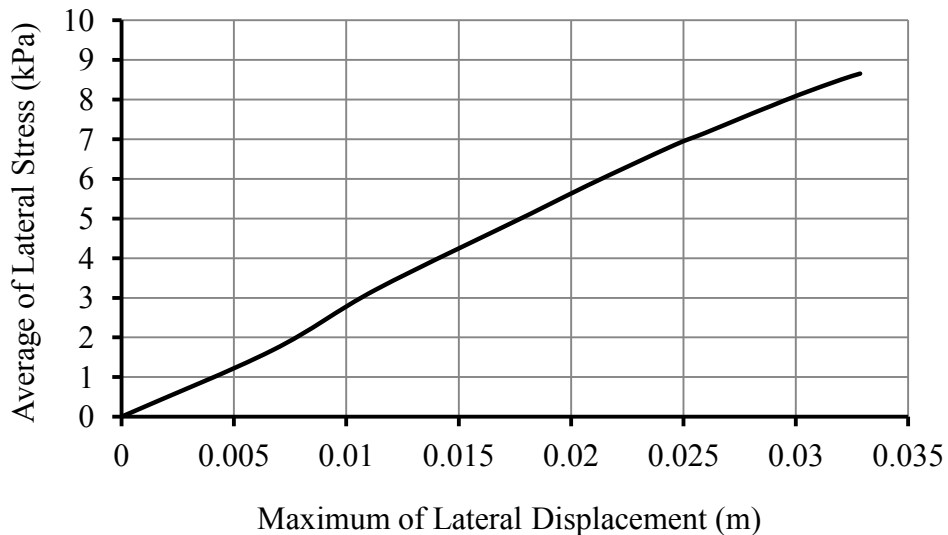


Figure 3-34- Average of lateral correction stress and maximum lateral displacement of membrane

3.6 Summary and Conclusions

This chapter contains the triaxial compression tests on the broken rock. The broken rock specimens were formed of crushed sandstone by a jaw crusher. The mechanical properties of the intact sandstone were determined by triaxial and uniaxial compression tests. The results show that the intact sandstone has a moderate strength with 32 MPa unconfined compressive strength.

The effect of the rubber membrane is very important in the triaxial test; therefore, the maximum error of the membrane was calculated by two analytical methods: Compression Shell Theory and Hoop Tension Theory. The specimen deformation in the triaxial tests was buckling deformation because of low confining pressure. Therefore, Hoop Tension Theory has better compatibility to determine the membrane error. In addition, the calculated error by Hoop Tension Theory is less than 5% of test results and is negligible. The rubber membrane numerical modeling also agrees with analytical modeling and the calculated error by numerical modeling is negligible.

In this research, the first strength point was assumed as peak strength of the specimens. A summary of the results is in Table 3-4. For each test, the confining pressure and corresponding axial strength were assumed as the minor and major principal stresses. The puncturing of the membrane by a sharp particle in the triaxial tests was an important problem. Therefore, a new rubber membrane that is more resistant to puncture (neoprene/latex mixed membrane) was used. The new membrane was better than the latex membrane but it did not solve the problem completely.

CHAPTER 4 : DETERMINING THE PARTICLE SHAPE CHARACTERISTICS OF SPECIMENS

Chapter 4 summarizes the code developed in this research to calculate the particle shape parameters by image processing. Form, angularity and texture are three parameters that describe the geometry of a particle. In addition, chapter 4 presents the method used to prepare representative samples for image processing, finally the calculated particle shape parameters of the specimens are available in this chapter.

4.1 Introduction

In this research, the behavior of broken rock at low confining pressure was investigated based on the geometry characteristics of particles. Therefore, determining the geometry characteristics of particles is an important part of the research. In experimental tests for this research, for each specimen, the geometry characteristics of particles was determined before the triaxial test. The particle geometry characteristics of specimens were calculated through the image processing technique by using a code developed in this research.

4.2 Developed code using MATLAB

Based on Equation (2-13) to (2-20) a code in MATLAB was developed to calculate the particle geometry characteristics of specimens. The particles photos were digital photo; therefore, the applied method was digital image processing method. Image processing is a part of signal processing and the developed methods in signal processing are used in image processing method. Generally, an image is a 2D signal with image parameters as the amplitude of the signal. Digital image is made of pixels and each pixel contains the image data based on image type. In this research, the photo of particle was an RGB image. An RGB image is a color image in which each pixel contains intensity of red, green and blue color.

The following steps should be carried out to calculate the geometry characteristics of particles through such an image processing technique. Thus, in the developed code in this research all of these steps have been followed.

1. Taking a photo of particles
2. Converting to binary
3. Preparing prior to analysis
4. Detecting the boundary of particle
5. Analyzing the particles

The first step to calculate the geometry characteristics is to take a high-resolution photo of particles. The particles photo is input data for image processing; therefore, its quality is very important. Improper light around the particles produces a shadow and consequently the boundary of the particle cannot be determined accurately by image processing. A photo box was built to provide the constant conditions of brightness for all pictures without any shadowing. Another important subject matter is the resolution of photo. The resolution of the photo should be adequate to recognize the boundary of the particle accurately by using image processing. Currently, most of the commercial cameras have enough resolution to take a high-resolution photo. However, the camera should be able to take photos with 100 pixels per diameter of particle (Masad (2007)). Figure 4-1 shows the designed photo box, and Figure 4-2 illustrates a photo that was taken in the photo box. Photos of specimens' particles are available in Appendix (D).

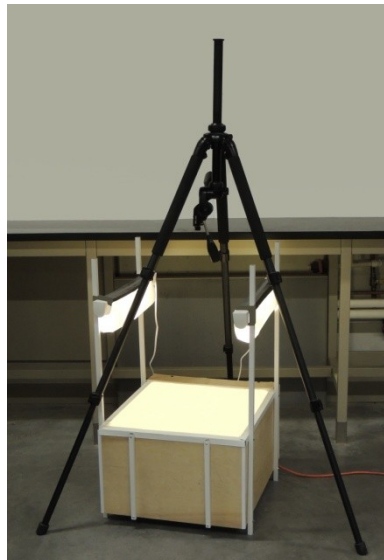


Figure 4-1- The photo box

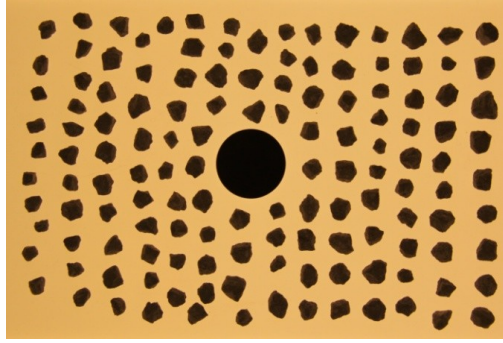


Figure 4-2- A photo that has been taken over the photo box

The Next step is converting the RGB photo to a binary photo because recognizing the boundary of a particle by using the binary photo is more accurate and easier. In the RGB photo, each pixel has three numbers to identify the color (each number is between 0 and 255, corresponding to the intensity of one color: Red, Green and Blue). Whereas, the pixel of a binary image can have one of two value (0 or 1). The white-black image is a useful type of binary image in which any white pixel has a value equal to 1 and black pixel correspond to 0. Recognizing the boundary pixels of a particle in a binary image is very simple. The boundary of a shape is where two pixels have different values in a binary image. Figure 4-3 shows an example of a binary image and the boundaries. To convert an RGB image, to a binary image any pixel that is white takes a value of 1 and other pixels take a value of 0.

1	1	1	1	1	1	1	1	1
1	1	1	1	1	1	1	1	1
1	1	1	1	0	1	1	1	1
1	1	1	0	0	0	1	1	1
1	1	0	0	0	0	0	1	1
1	1	1	0	0	0	1	1	1
1	1	1	1	0	1	1	1	1
1	1	1	1	1	1	1	1	1
1	1	1	1	1	1	1	1	1

Figure 4-3- An example of a binary image

Before determining the particle boundaries, some preparation is required on the converted binary photo:

1. Removing very small particles
2. Filling the holes inside particles

Some unwanted very small size particle such as dust may appear when taking particle photos. Very small size particles should be deleted from binary photos before analyzing the particles. The number of pixels per particle is a criterion that can be used to delete unwanted particles. Determining the threshold number of pixels is an experimental work and needs some attempts to find the best pixel number to delete unwanted small size particles. Figure 4-4 shows a created binary photo of the RGB Photo and deleted unwanted small particles.

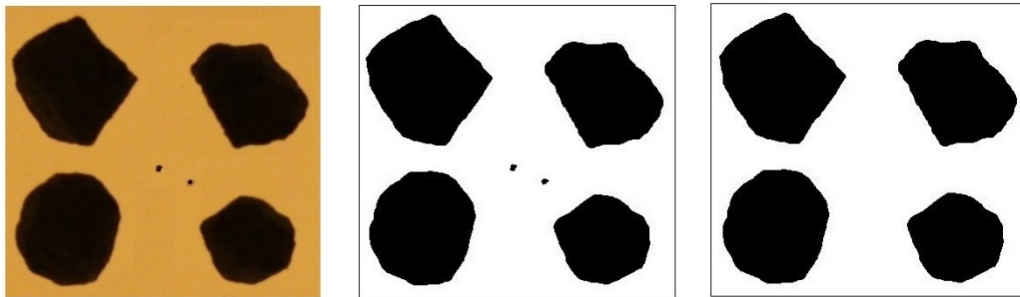


Figure 4-4- Steps of unwanted small particles deleting

In the converted binary image of an RGB image, some holes may appear inside the particles. The surface of particles is not smooth and the color intensity is changed on the surface of the particles; therefore, some pixels inside a particle may have white color in the converted binary image and this is seen like holes inside the particles. Before analyzing the particles to determine shape parameters, all holes inside particles should be filled. Thus, the value of any pixel inside a particle that is 1 should be changed to 0 to fill the holes inside the particles. Figure 4-5 illustrates the binary image and filling the hole inside a particle.

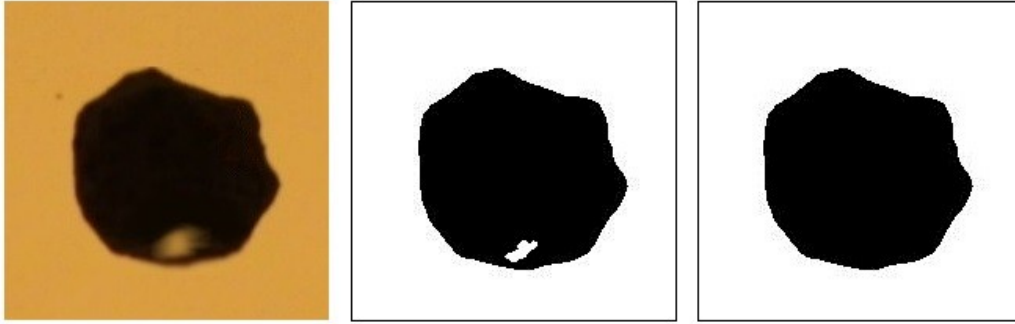


Figure 4-5-Filling the existing hole in a particle photo

After deleting very small particles and filling the existing holes inside the particles, the pixels in the boundary of the particles should be recognized. Boundary pixels are recognized in MATLAB based on the number of pixels in horizontal and vertical directions. For example, pixel (4, 6) is the 4th pixel in the horizontal direction and 6th pixel in vertical direction (Gonzalez (2004)). Therefore, the number of pixels in the horizontal and vertical directions can be considered as the corresponding x and y dimensions of a pixel, respectively in Cartesian Coordinates System. Equation (2-13) to (2-20) can be used in code developed in this research to determine the shape parameters of a particle using recognized boundary pixels. The developed code to determine the particle shape characteristics is available in Appendix (E). All particle geometry characteristics in Appendix (E) can be calculated from binary image except standard deviation of intensity (SD). To determine particle's standard deviation of intensity, the particle photo should be converted to gray image because the intensity of each pixel in the particle surface is important to calculate the standard deviation of intensity.

To determine the particles size distribution by using image processing method, the equivalent diameter of particle was calculated. The particle equivalent diameter is the diameter of a circle that has the same area with the particle. The determined particle size distribution through image processing results in bigger particle size compared with the sieve method. Because in the sieve method particles may be

stay at an angle on the sieve opening. Figure 4-6 shows an ellipsoid particle that cannot pass the sieve opening. Thus, particles size distribution using image processing requires a correction coefficient to describe particle size distribution with sieve analyzing. Janaka (2012) proposed a 0.86 correction coefficient to image processing result to determine the equivalent particles size distribution by the sieve method.

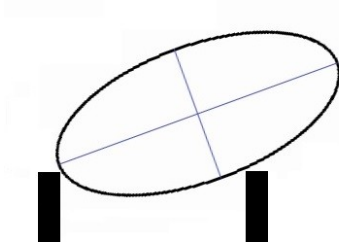


Figure 4-6- An example of a particle that cannot pass sieve while it is smaller than sieve opening

In this research, three sieve analyzing tests were done on three specimens with different form indexes to compare the results with the particle size distribution using image processing. Figure 4-7 to Figure 4-9 illustrate the particles size distribution determined using the image processing method and the sieve method for specimens that have a form index equal to 1.6, 2.4 and 2.7. The results show that the correction factor is relative to the form-index. Figure 4-7 shows that for specimens with a 1.6 form-index, the correction factor is 1. However, for specimens with a 2.4 and 2.7 form-index, the correction factor is 0.8 based on Figure 4-8 and Figure 4-9. Thus, for specimens with a form index smaller than 1.6, a correction factor equal to 1 was applied. For specimens with a form index bigger than 2.4, a correction factor equal to 0.8 was applied. Also, for specimens with a form index between 1.6 and 2.4, a correction factor between 1 and 0.8 was considered. The particle size distribution of specimens are in Appendix (F).

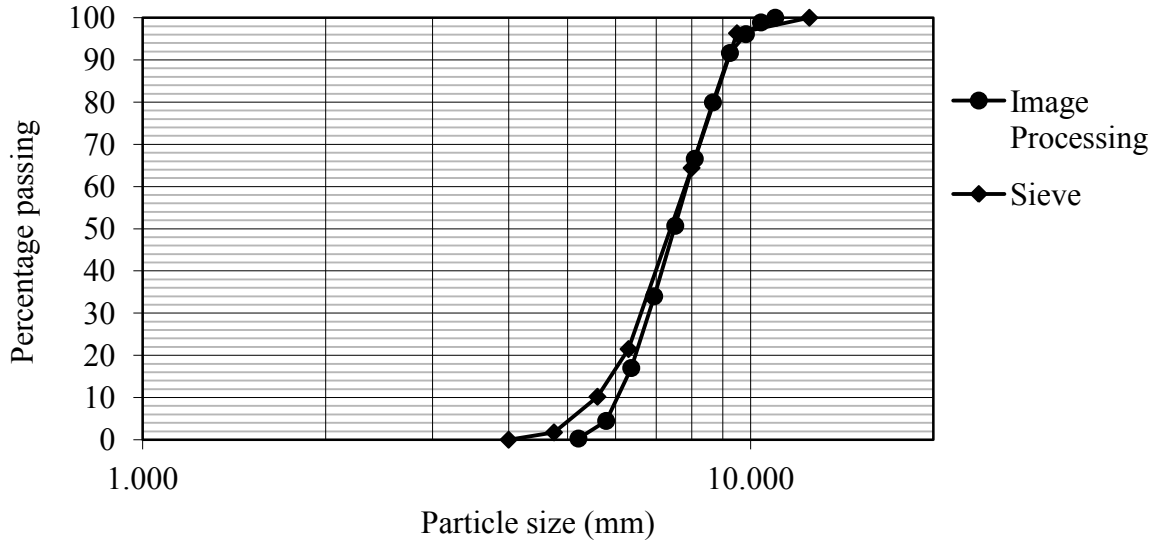


Figure 4-7-Size distribution of particles with form index equal to 1.6, using image processing method and sieve method

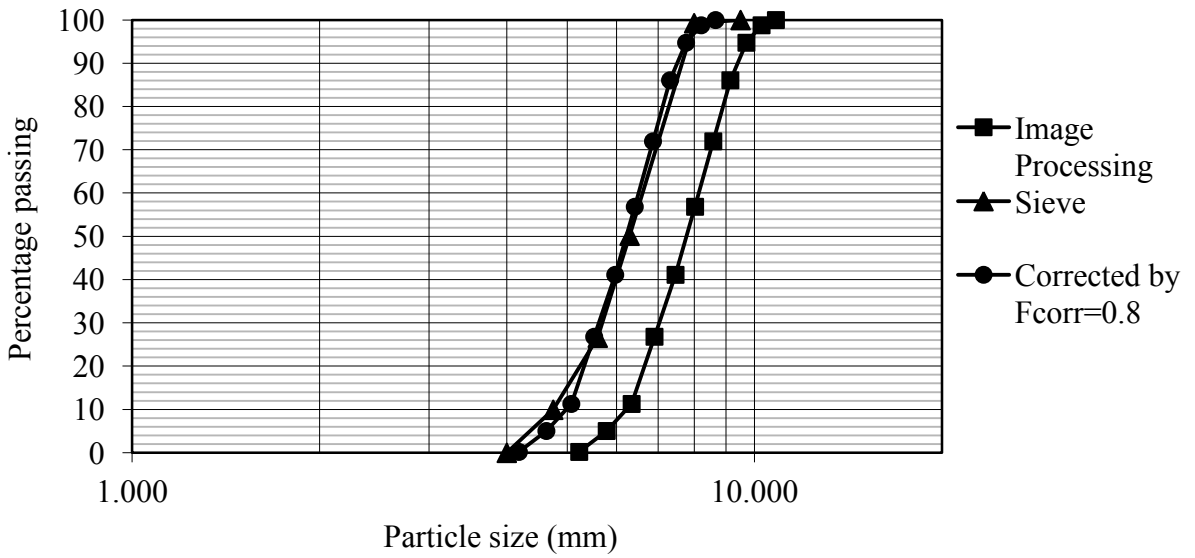


Figure 4-8-Size distribution of particles with form index equal to 2.4, using image processing method and sieve method

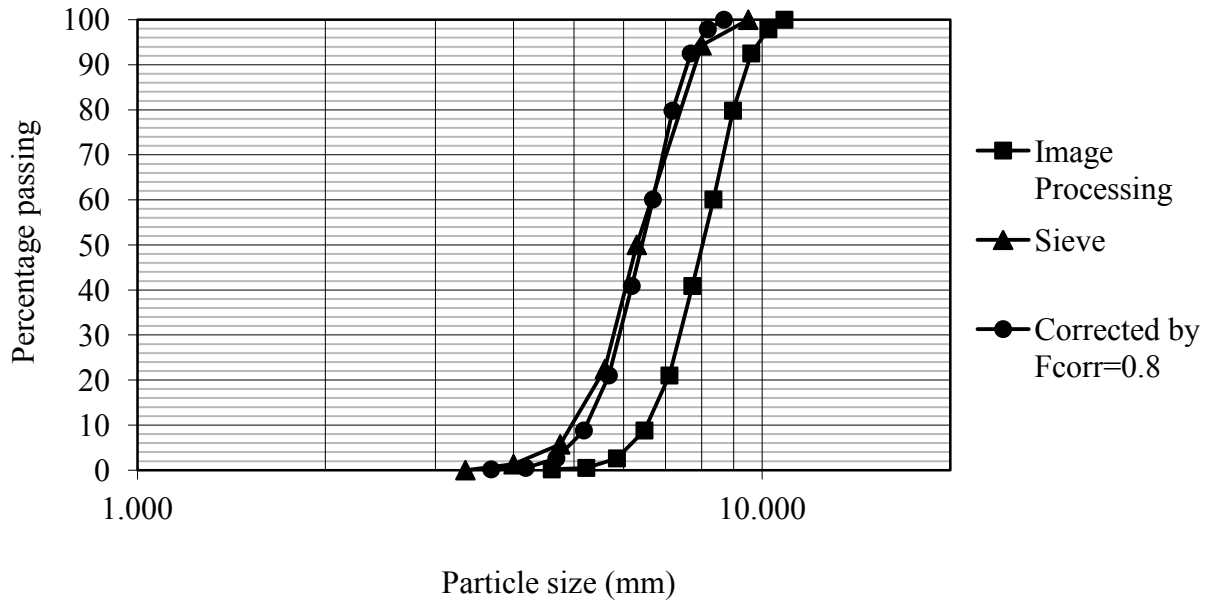


Figure 4-9- Size distribution of particles with form index equal to 2.7, using image processing method and sieve method

4.3 Representative sample of specimen

A method to determine the geometry characteristics of a specimen calculates the geometry characteristics of all particles of the specimen. However, this method is very time consuming and impractical because a specimen has many particles. Therefore, a representative part of the specimen should be separated from the specimen. The quartering method was carried out to separate the representative part of the specimen in this research. The quartering method has the following procedure (ASTM 447 (1972)).

- 1- Place the specimen on a clean and hard surface.
- 2- Quarter the specimen cone to four equal parts through pressing down the separator plate from the apex of the specimen cone
- 3- Choose two opposite quarters that are located diagonally
- 4- Mix two selected quarters together

- 5- Repeat steps 1 to 4; now the representative quarter of the primary specimen is ready

Figure 4-10 illustrates the representative quarter preparing steps. A high resolution photo was taken of the prepared representative part to calculate the geometry characteristics of the specimen.

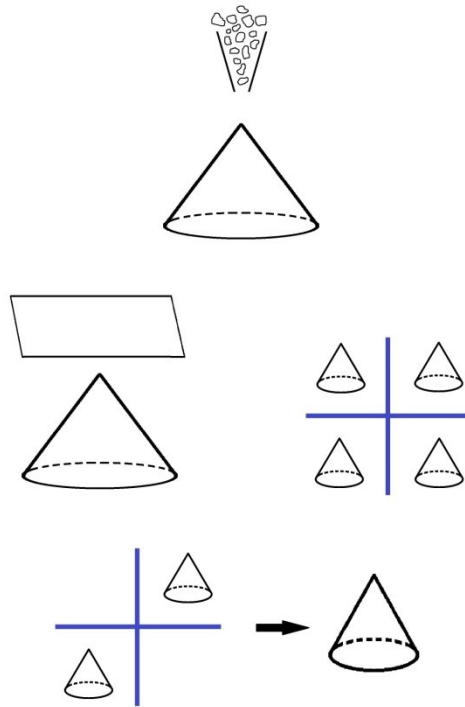


Figure 4-10- Representative part preparing steps

A representative sample should reflect precisely the characteristics of the larger population. Therefore, using the aforementioned method, the prepared representative quarter should present the geometry characteristics of the specimen. Figure 4-11 to Figure 4-14 show the geometry characteristics of a specimen calculated by two methods: the geometry characteristics of all particles of the specimen and the geometry characteristics of representative quarter particles. It is clear that the geometry characteristics for both methods are almost

equal and this demonstrates that the representative quarter can present the geometry characteristics of a specimen.

In this research, the geometry characteristics of a representative quarter of a specimen was calculated and assumed the representative quarter indicates the geometry characteristics of a specimen within an acceptable error.

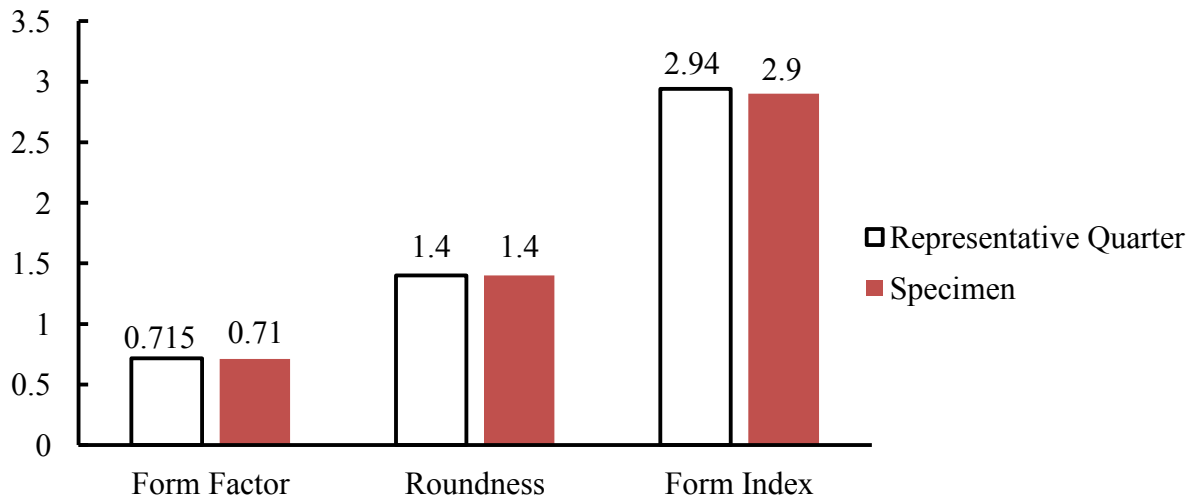


Figure 4-11- Form characteristics of representative quarter sample vs. specimen

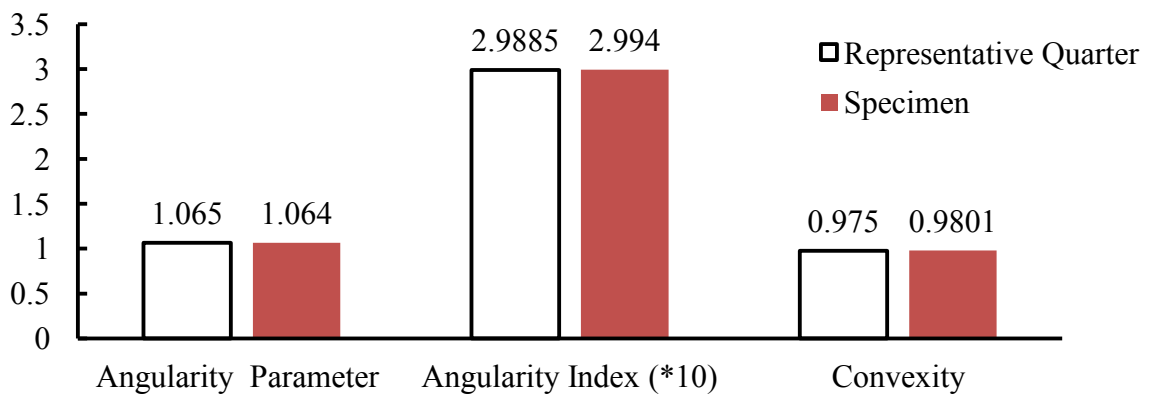


Figure 4-12- Angularity characteristics of representative quarter sample vs. specimen

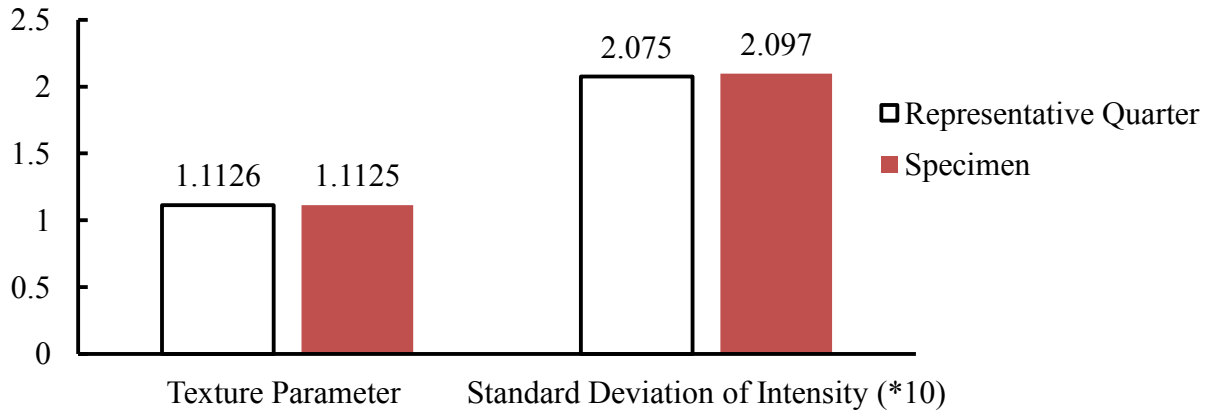


Figure 4-13- Texture characteristics of representative quarter sample vs. specimen

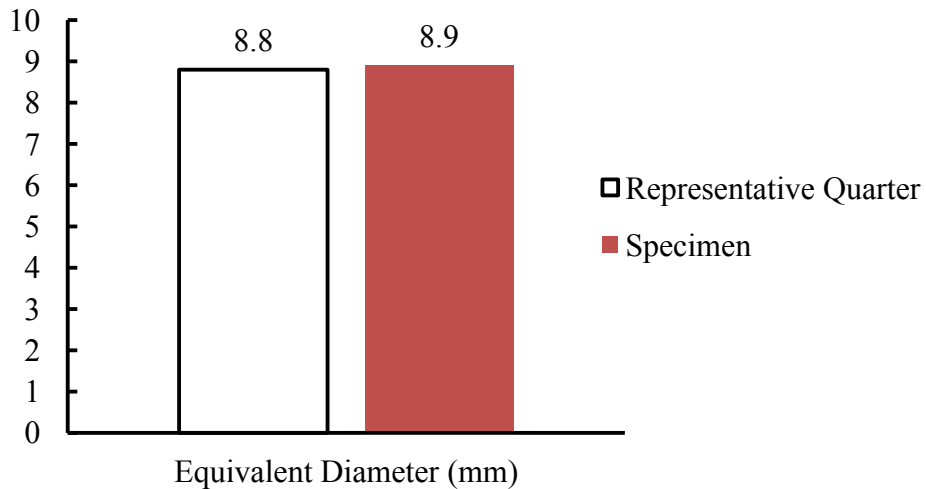


Figure 4-14- Equivalent diameter of representative quarter sample vs. specimen

4.4 Statistical analysis on the image processing results

Results of image processing require statistical analysis because the developed code calculates the geometry characteristics of all particles of the representative sample one by one, and eventually the geometry characteristics of a specimen should be described by only one number for each geometry characteristic despite the specimen having many particles.

An important consideration to statistical analysis is how a bin size is defined. Freedman (1981) introduced a method to calculate the appropriate number of bins for data analysis. There are three useful methods to determine the bin: the Freedman-Diaconis method, the Scott method and Sturges method. The Sturges' method does not work well for a large amount of data. Scott method works good for random sampling data. Figure 4-15, Figure 4-16 and Figure 4-17 show the form factor for Figure 4-2 particles. It is clear that the calculated mean values using the Freedman-Diaconis, Scott and Sturges methods are almost identical.

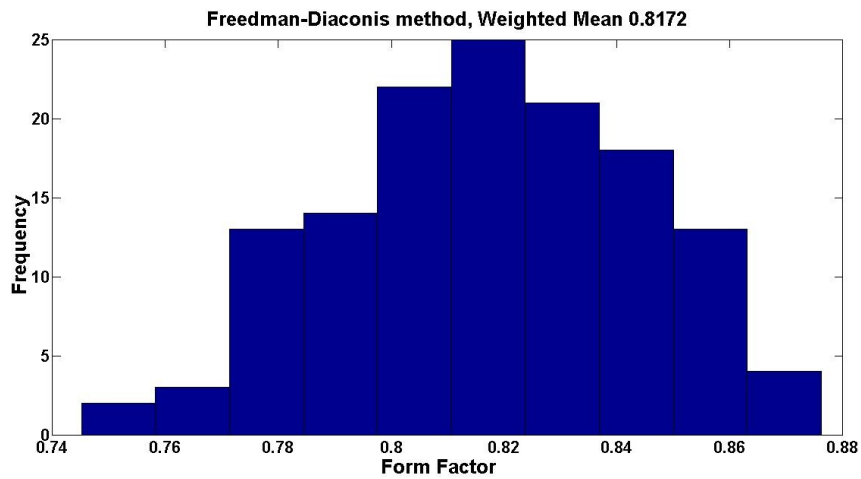


Figure 4-15- Form factor histogram calculated by Freedman-Diaconis method

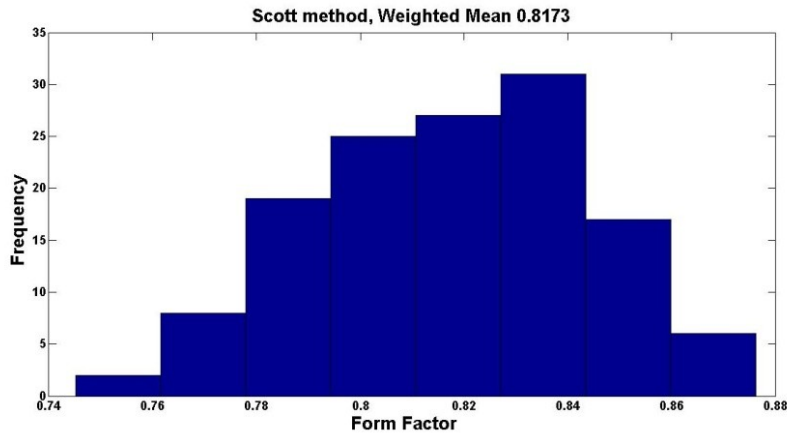


Figure 4-16- Form factor histogram calculated by Scott method

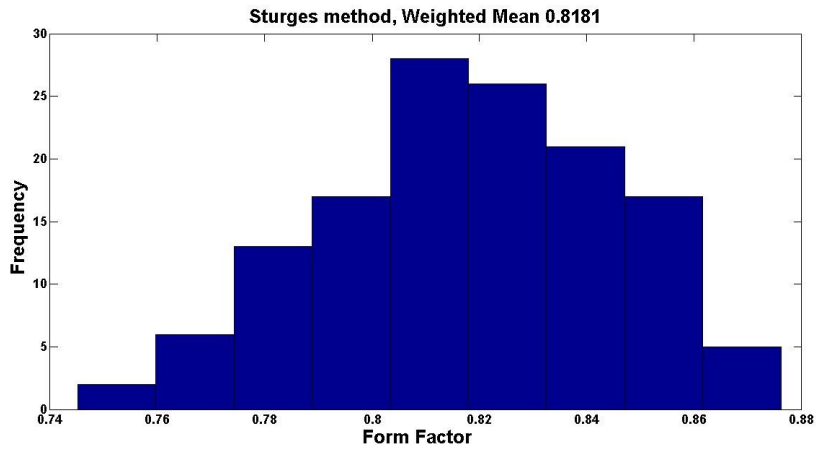


Figure 4-17- Form factor histogram calculated by Sturges method

The particles shape characteristics was calculated for each specimen and the summary of results is in Table 4-1. In addition, Table 4-2 shows average, minimum, maximum, standard deviation, range and variation of shape parameters of all specimens.

The results (Table 4-2) show following conclusions:

1. The texture-parameter and standard deviation of intensity (SD) of specimens are almost same because the specimens were only one broken rock type. Therefore, roughness parameters of specimens are almost same.
2. Form index and angularity index have better variability comparing with other shape parameters; therefore, form index and angularity index present better the particle geometry characteristics of crushed sandstone. Thus, form index and angularity index were used in broken rock behavior analyzing in Chapter 5.
3. Preparing a specimen with only one parameter variation was impossible. For example, form index from 1.534 in Test 1 changed to 3.081 in Test 2

but other parameters are not constant and angularity index changed from 16.398 to 29.042. The variation of all geometry parameters in specimens does not allow investigation the effect of geometry characteristics on the behavior of broken rock by comparing two individual specimens together; Therefore, some of specimens that have almost the same particles geometry parameters were collected to one group and the behavior of groups were compared to each other. Three groups of specimens were categorized (group A, B and C).The collected specimens in each group have almost same particle geometry parameters. Group (A) are specimens that have form index almost between 2.6 and 3. Specimens in group (A) have angularity index almost from 25 to 30. Specimens in group (B) have form index from 1.5 to 1.6 and angularity index from 15 to 20. Specimens in group (C) have form index range from 2 to 2.2 and angularity index range from 19 to 26. Table 4-3 to Table 4-5 show the categorized specimens in each group.

Table 4-6 is a summary of the specimen particles size that was determined of the particle size distribution graph in Appendix (F).

Table 4-1- The particles geometry of the specimens determined by image processing technique

No.	FI	FF	Roundness	AI	AP	Convexity	TP	SD
Test1	1.534	0.836	1.196	16.398	1.057	0.988	1.105	22.235
Test2	3.081	0.707	1.425	29.042	1.056	0.980	1.116	21.137
Test3	2.164	0.788	1.272	22.612	1.070	0.983	1.105	22.156
Test4	2.550	0.727	1.382	38.220	1.089	0.979	1.141	16.982
Test5	3.058	0.701	1.435	33.150	1.072	0.978	1.118	20.804
Test6	2.204	0.772	1.298	28.369	1.083	0.982	1.119	20.239
Test7	2.726	0.728	1.384	32.356	1.083	0.979	1.118	19.806
Test8	3.141	0.693	1.454	33.057	1.071	0.978	1.120	20.492
Test9	1.506	0.841	1.190	15.331	1.055	0.988	1.102	21.670
Test10	2.943	0.718	1.399	26.196	1.060	0.980	1.114	21.610
Test11	2.185	0.788	1.272	19.795	1.069	0.983	1.104	21.647
Test12	2.605	0.751	1.338	23.020	1.061	0.982	1.110	22.232
Test13	2.535	0.731	1.375	36.417	1.090	0.979	1.138	17.239
Test14	1.513	0.841	1.191	15.505	1.055	0.988	1.102	21.162
Test15	2.783	0.734	1.369	24.420	1.062	0.981	1.114	21.862
Test16	2.235	0.784	1.280	20.922	1.067	0.983	1.104	21.647
Test17	2.444	0.743	1.352	35.435	1.088	0.980	1.131	18.246
Test18	1.615	0.826	1.212	18.690	1.058	0.987	1.112	20.558
Test19	2.713	0.737	1.365	29.021	1.064	0.981	1.125	21.671
Test20	2.104	0.786	1.277	24.709	1.070	0.984	1.115	21.835
Test21	2.574	0.743	1.352	28.143	1.067	0.982	1.123	19.985
Test22	1.598	0.828	1.211	18.849	1.057	0.988	1.111	19.728
Test23	2.595	0.744	1.351	28.198	1.062	0.982	1.120	21.181
Test24	1.616	0.826	1.213	19.599	1.057	0.988	1.112	20.885
Test25	2.140	0.783	1.281	26.438	1.071	0.984	1.118	20.354
Test26	1.945	0.797	1.262	20.431	1.068	0.983	1.118	19.864
Test27	2.535	0.747	1.345	26.382	1.070	0.980	1.123	20.226

Table 4-2- Statistical parameters of particle geometry of the specimens

	FI	FF	Roundness	AI	AP	Convexity	TP	SD
Minimum	1.506	0.693	1.190	15.331	1.055	0.978	1.102	16.982
Maximum	3.141	0.841	1.454	38.220	1.090	0.988	1.141	22.235
Average	2.320	0.767	1.314	25.582	1.068	0.983	1.116	20.646
Standard Deviation	0.513	0.045	0.080	6.501	0.011	0.003	0.010	1.386
Range	1.635	0.148	0.264	22.889	0.035	0.010	0.039	5.253
Variation %	22.112	5.867	6.088	25.412	1.030	0.305	0.896	6.713

Table 4-3- Categorized specimens in group (A)

Group (A)	FI	AI
Test19	2.713	29.021
Test23	2.595	28.198
Test2	3.081	29.042
Test10	2.943	26.196
Test15	2.783	24.420
Mean	2.823	27.376

Table 4-4- Categorized specimens in group (B)

Group (B)	FI	AI
Test18	1.615	18.690
Test24	1.616	19.599
Test1	1.534	16.398
Test9	1.506	15.331
Test14	1.513	15.505
Mean	1.557	17.105

Table 4-5- Categorized specimens in group (C)

Group (C)	FI	AI
Test20	2.104	24.709
Test25	2.140	26.438
Test3	2.164	22.612
Test11	2.185	19.795
Test16	2.235	20.922
Mean	2.166	22.895

Table 4-6- A summary of the specimens particles size

No.	D ₆₀	D ₅₀	D ₁₀	F _{corr}
Test1	8.6	8.4	6.8	1.00
Test2	7.5	7.3	5.9	0.80
Test3	7.0	6.8	5.4	0.88
Test4	9.2	8.8	7.0	0.80
Test5	7.6	7.5	6.0	0.80
Test6	8.7	8.3	6.1	0.87
Test7	7.9	7.6	6.0	0.80
Test8	7.8	7.5	5.9	0.80
Test9	8.5	8.3	7.0	1.00
Test10	9.1	8.8	7.1	0.80
Test11	7.6	7.1	5.7	0.87
Test12	7.0	6.6	5.2	0.80
Test13	8.8	8.4	6.4	0.80
Test14	8.5	8.2	6.7	1.00
Test15	7.2	6.8	5.4	0.80
Test16	6.5	6.2	5.1	0.86
Test17	9.0	8.4	6.0	0.80
Test18	7.9	7.7	6.2	1.00
Test19	6.7	6.4	5.4	0.80
Test20	6.7	6.4	5.0	0.89
Test21	5.9	5.4	1.1	0.80
Test22	6.9	6.0	1.8	1.00
Test23	6.7	6.5	5.3	0.80
Test24	8.1	7.8	6.3	1.00
Test25	6.6	6.3	5.1	0.88
Test26	5.6	4.9	0.9	0.92
Test27	5.2	4.4	0.9	0.80

4.5 Comparing the specimens with actual Rockfill

To predict the behavior of actual Rockfill through using the laboratory test results, specimens should represent the actual broken rock. Preparing specimens with actual particle size distribution and practicing failure on them considering the large top size ($> 1\text{m}$) and wide particle size distribution of rockfills in mining and dam construction industry, is a challenging task. However, if a specimen of broken rock and actual Rockfill have parallel size distribution, the specimen and actual Rockfill will have the same contact points pattern between particles. Therefore, the behavior of the specimen can represent the behavior of the actual Rockfill. Figure 4-18 shows the contact points of two broken rock samples with parallel size distribution and different particle size.

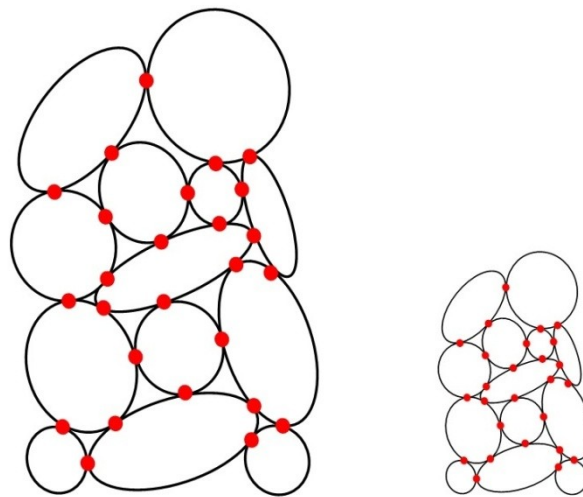


Figure 4-18- Conceptual figure of two broken rock specimens with the same contact points and parallel particle size distribution

The particle size distribution of actual broken rock is discussed under two categories:

- 1- Case study of some actual Rockfills
- 2- Size distribution of actual Rockfill based on production method

4.5.1 Case study of some actual Rockfill

The following projects are good examples to investigate the size distribution of actual Rockfill:

- Rockfill dams
- Overburden waste dumps in open pit mines
- Stockpiles in open pit mines
- Broken rock in block caving method

A large part of embankment dams are made of dumped Rockfill. Broken rock used in Rockfill dams must have enough shear strength to provide slope stability. Not only is the availability of broken rock at close distance to the dam an important parameter but also the size distribution of particles is taken into consideration in practice. Figure 4-19 shows size distribution of prepared specimens and actual Rockfill dams. Actual Rockfill size distribution data of Xiaolingtou dam, Charvak dam and Aswan dam have been collected from literature (Tao (2002), Goldin (2012) and Anderson (2012)).

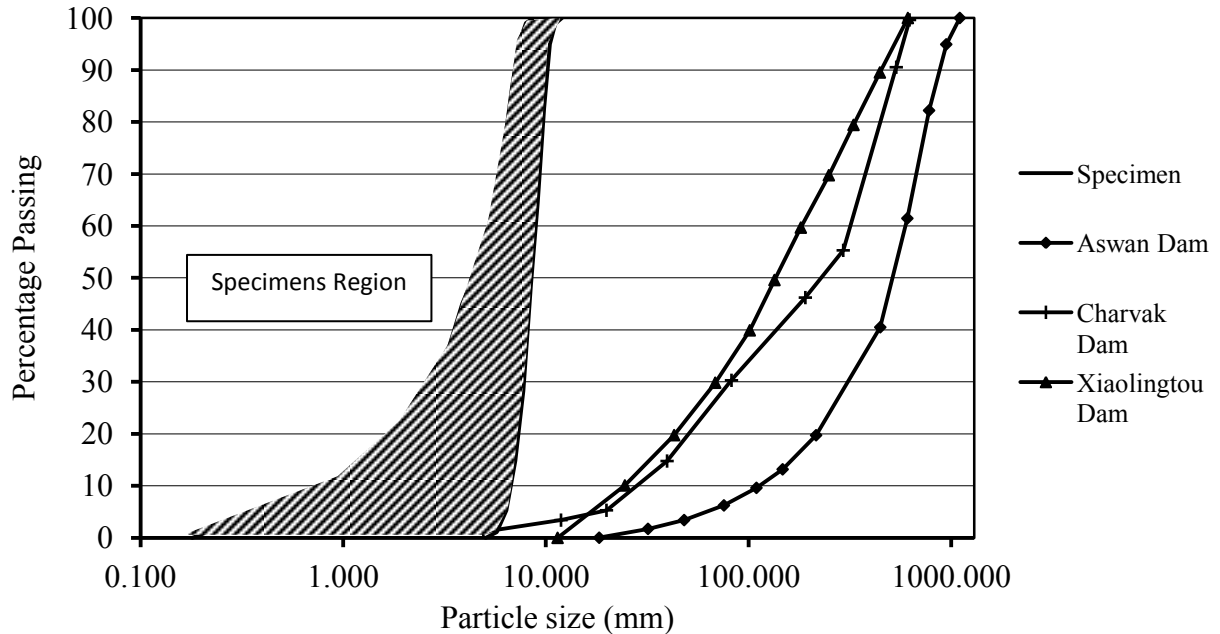


Figure 4-19- Size distribution of some actual Rockfill dams, this figure was adapted from Tao (2002), Goldin (2012) and Anderson (2012)

Based on Figure 4-19, broken rock in the mentioned dams has well graded distribution because of the wide range of particle sizes. In addition, the uniformity coefficient (C_u) of these dams is more than 4 and the coefficient of curvature (C_c) is less than 3. Figure 4-19 illustrates the size distribution of specimens. Comparing the size distribution of the specimen with the size distribution of real Rockfill dams shows they are almost parallel. Particle size distribution of the specimens and actual broken rock cannot be exactly parallel because scaling down the small size particles of actual Rockfill and large particles simultaneously with the same scaling factor is not useful. For example, Aswan dam particle size distribution is from 15 to 1150 mm. Scaling down with a scaling factor equal to 115 needs a specimen with size distribution from 0.1 to 10 mm, but 0.1 mm diameter particles do not reflect the expected geometry properties of the 15 mm size particles and behave like dust. Table 4-7 shows the size distribution parameters for actual dams.

Table 4-7- Size distribution parameters for actual dams

	D ₁₀ (mm)	D ₃₀ (mm)	D ₆₀ (mm)	C _u	C _c
Aswan High Dam	110	290	650	5.91	1.18
Charvak Dam	30	82	300	10.00	0.75
Xiaolingtou Dam	25	69	185	7.40	1.03

Another existing example of actual broken rock is overburden waste dumps in open pit mines. Size distribution of overburden waste dumps is different and depends on the production method, type of rock mass and alteration level. Mine waste dumps contain a wide range of particles from very fine particles like soil to large blocks like cobbles or boulders. Rock mass type and alteration level also affect the mechanical behavior of overburden wastes. Mechanical behavior of waste dumps with a substantial portion of very fine particles is different from waste dumps with no small particles. Because the mechanical behavior of broken rock is controlled by particles point to point contact. Figure 4-20 shows the particle size distribution of the overburden waste dumps for example (Habte (2012), Kusuma (2012), Hungr (2002) and Fox (2011)). The size distribution of the Brukunga mine waste dump is more compatible with the prepared specimen in this study because this waste dump does not have very fine particles compared to the other presented waste dumps in Figure 4-20.

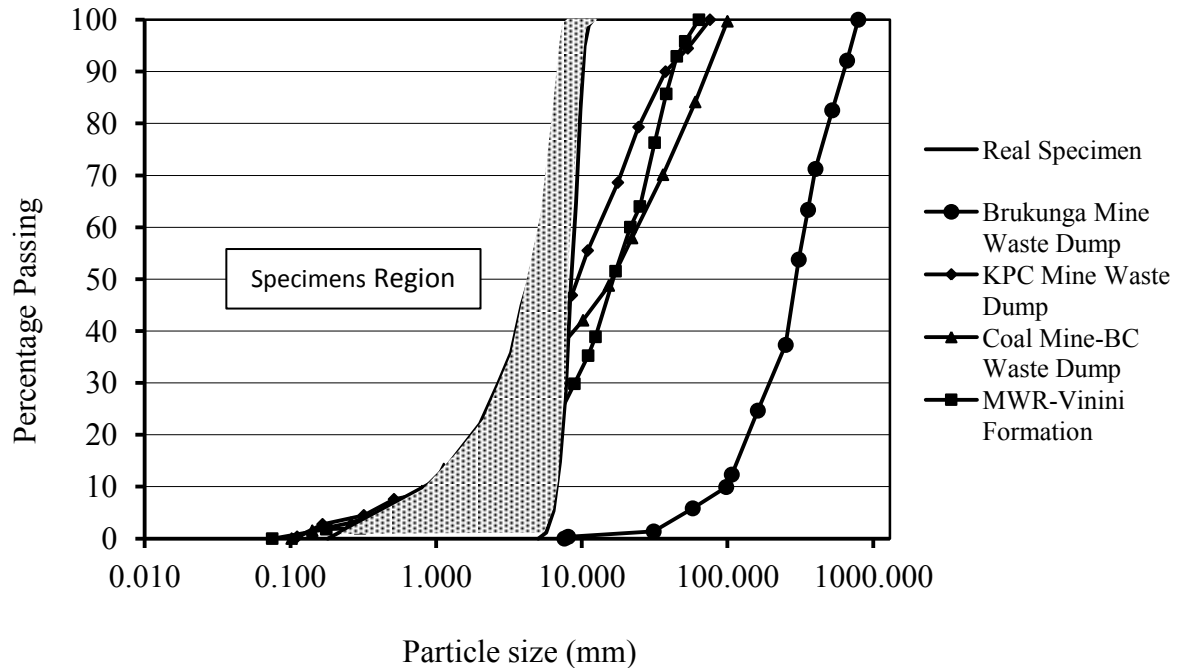


Figure 4-20- Size distribution of actual overburden waste dumps, this figure was adapted from Habte (2012), Kusuma (2012), Hungr (2002) and Fox (2011).

Table 4-8 presents the size distribution parameters of the discussed waste dumps. The uniformity coefficient for the Brukunga mine waste dump is close to the uniformity coefficient of the specimens. The prepared specimens in this research can represent a waste dump with less fine particles.

Table 4-8- Size distribution parameters for actual overburden waste dumps

	D_{10} (mm)	D_{30} (mm)	D_{60} (mm)	C_u	C_c
Brukunga Mine Waste Dump	99	198	347	3.50	1.14
KPC Mine Waste Dump	1.5	4.5	14.5	9.67	0.93
Coal Mine-BC Waste Dump	0.9	4.5	25	27.78	0.90
MWR-Vinini Formation	2	8.9	21.5	10.75	1.84

Figure 4-21 shows the size distribution of an ore stockpile (Pourghahramani (2010)). As seen, the application of a primary gyratory crusher in the mine site produced crushed ore with a uniformity coefficient of 3.5. The size distribution of

the specimens shows better match with the presented stockpile particle size distribution, in terms of parallel size distribution, compared to the example cases of Rockfill dams or waste dumps. Because specimens and ore stockpile both are crusher product.

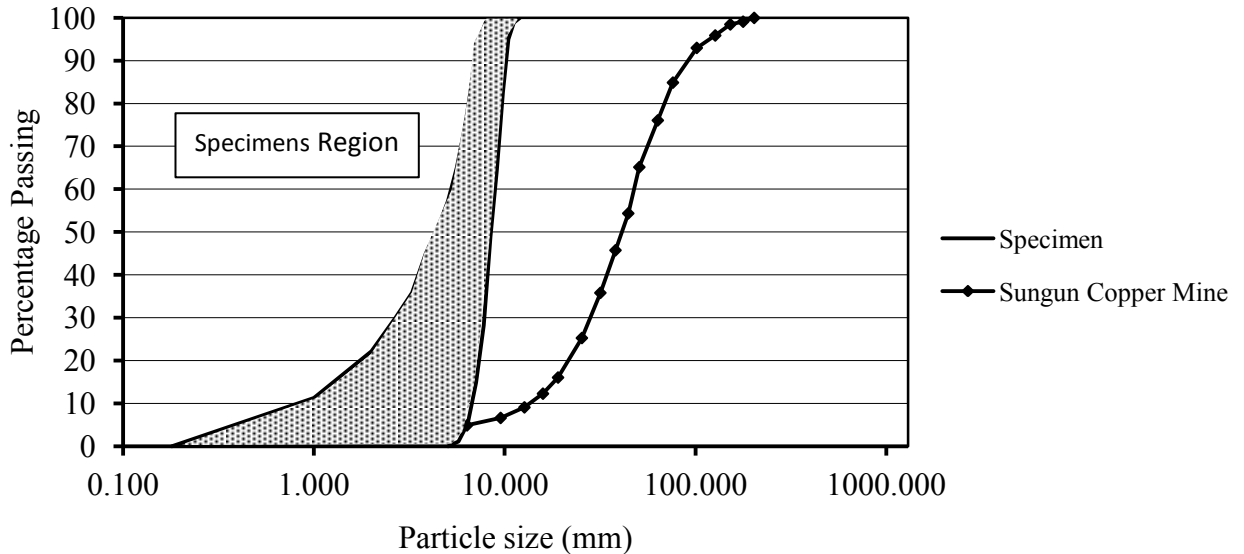


Figure 4-21- Particle size distribution of an actual mine stockpile, this figure was adapted from Pourghahramani (2010).

Another example for actual broken rock is the block caving extraction method. Block size distribution after primary fragmentation is broken down to a smaller size during movement in the draw columns. Therefore, secondary fragmentation has smaller particles than primary fragmentation because the rocks fail a couple of hundred meters to the draw points. Figure 4-22 illustrates the size distribution of actual block caving extraction at primary and secondary fragmentation (Butcher (2002) and Golder Associates (2012)). As seen in Figure 4-22 the prepared specimens' size distributions are highly compatible with addressed block caving particle size distribution examples. Meanwhile it should be pointed out that there is no guarantee that all block caving mines will have similar size distribution.

Primary and secondary fragmentation depends on cavability of rock mass, joints spacing, joints orientation, lateral confining pressure and draw point design; therefore as a result, block size distribution can be different for every mine.

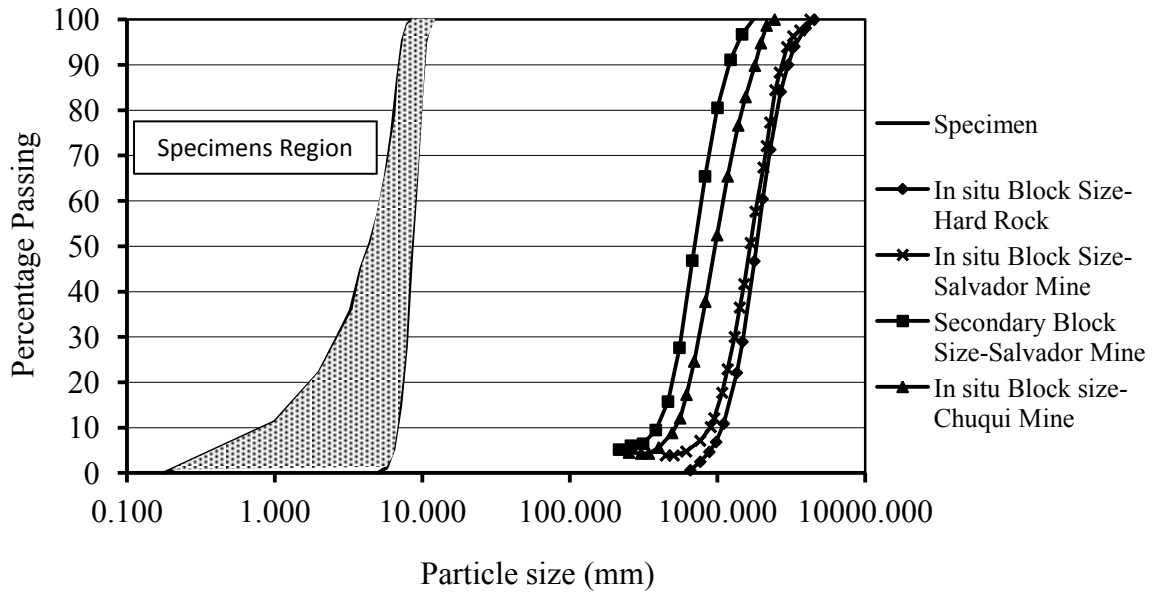


Figure 4-22- Primary and secondary fragmentation of actual block caving, this figure was adapted from Butcher (2002) and Golder Associates (2012).

Table 4-9 illustrates the size distribution parameters for an actual block caving method. The uniformity coefficient of fragmentation of presented block caving mines in Figure 4-22 is close to the uniformity coefficient of the specimen; and with a scaling factor equal to 50, the size distribution of the specimen can be scaled up to the actual block caving fragmentation of mine presented in Figure 4-22.

Table 4-9- Size distribution parameters for actual block caving

	D ₁₀ (mm)	D ₃₀ (mm)	D ₆₀ (mm)	C _u	C _c
In situ Block Size-Hard Rock	1096	1495	2022	1.84	1.01
In situ Block Size-Salvador Mine	899	1308	1850	2.06	1.03
Secondary Block Size-Salvador Mine	387	580	801	2.07	1.09
In situ Block size-Chuqui Mine	504	605	1065	2.11	0.68

4.5.2 Size distribution of actual Rockfill based on production method

The production method of broken rock affects the size distribution of particles. For example, in case of ore stockpiles, which usually experience one stage of primary crushing, the particle size distribution of the piles are dictated by the gap size and type of the crusher installed in the mine site. It has been suggested in the literature that, the size distribution of the crushed rocks by any crusher could be determined and predicted by one of the common particle size distribution functions such as Rosin-Rammler or Gaudin-Schuhmann distributions, Wills (2011) and Gupta (2006).

Hence, the compatibility of size distribution of the specimens with size distribution functions was investigated to find out whether or not the prepared specimens in this research present the actual broken rock produced by a mechanical crusher such as ore stockpile.

The Rosin-Rammler distribution suggests that the crusher products have the following distribution (Equation (4-1)).

$$100 - P = 100e^{-aX^b} \quad (4-1)$$

Where P is cumulative passing percentage, X is grain size, and b and a are constant parameters.

For better graphical presentation and easier calculation of the function parameters Equation (4-1) can be modified as Equation (4-2):

$$\log\left(\ln\left(\frac{100}{100-P}\right)\right) = b \log(X) + \log(a) \quad (4-2)$$

Based on Equation (4-2) the $\ln\left(\frac{100}{100-P}\right)$ and X have a linear relationship if collected data is presented in a Log-Log scale. Figure 4-23 to Figure 4-28 show Rosin-Rammler distribution of some prepared specimens in this research as some random examples. Obviously, they are linear and this means the specimens have Rosin-Rammler distribution.

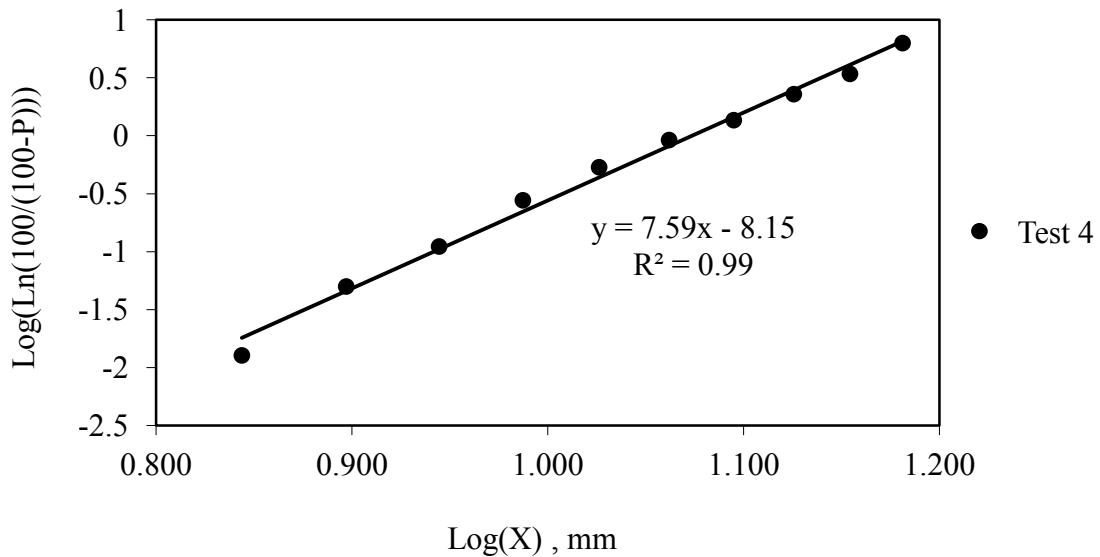


Figure 4-23- Rosin-Rammler distribution of the Test 4 specimen

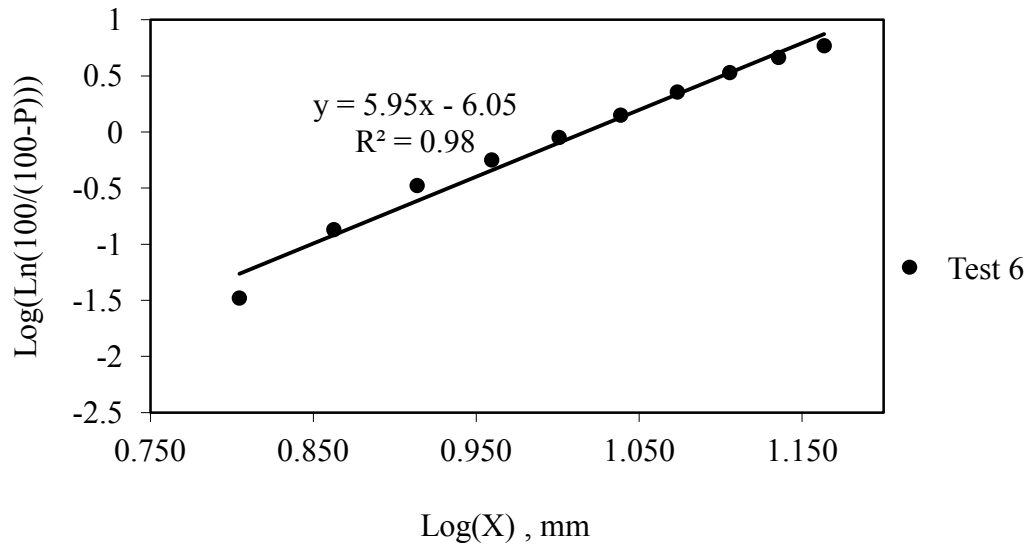


Figure 4-24- Rosin-Rammler distribution of the Test 6 specimen

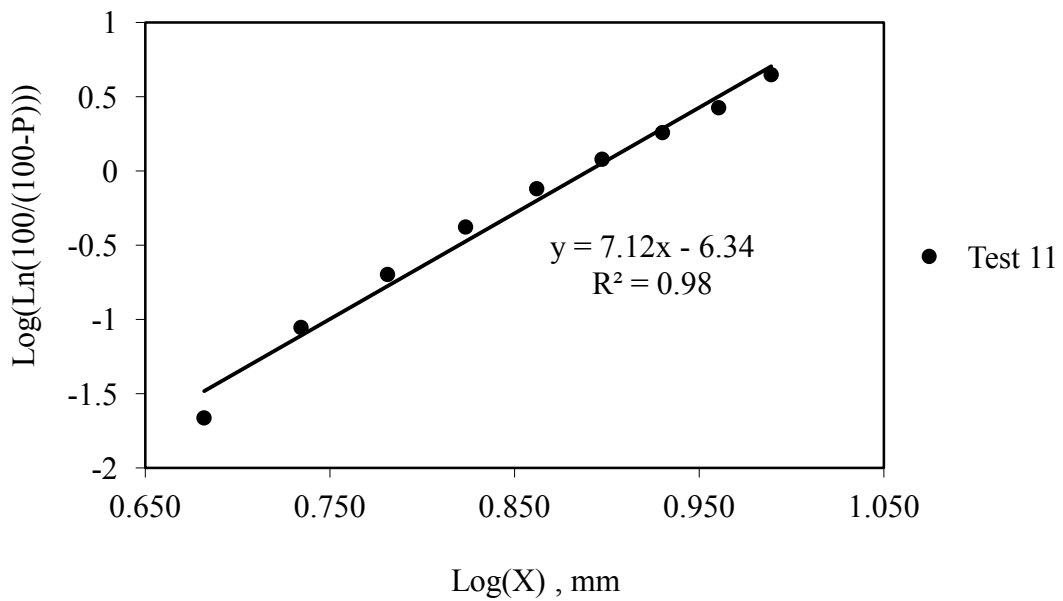


Figure 4-25- Rosin-Rammler distribution of the Test 11 specimen

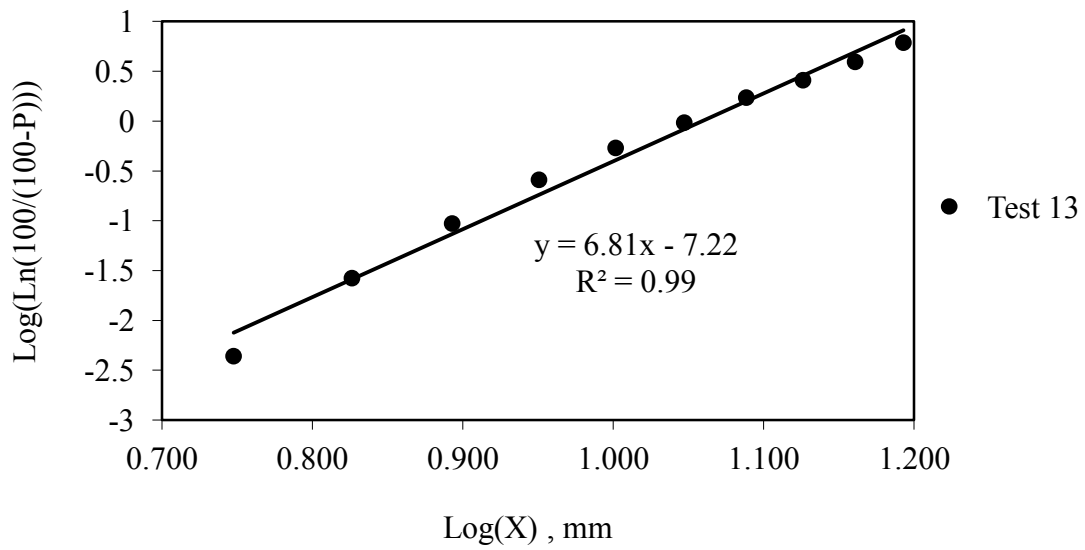


Figure 4-26- Rosin-Rammler distribution of the Test 13 specimen

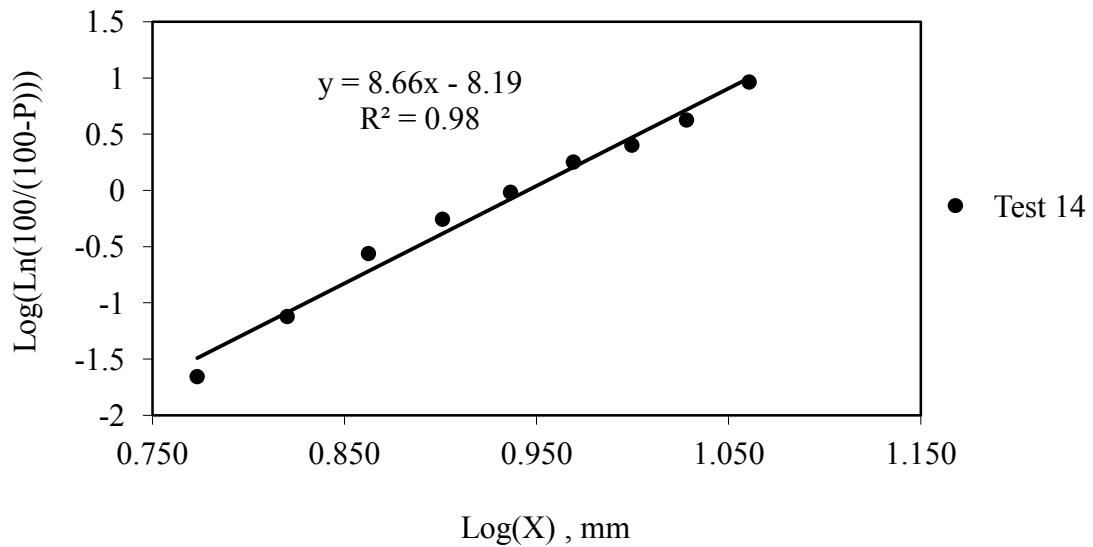


Figure 4-27- Rosin-Rammler distribution of the Test 14 specimen

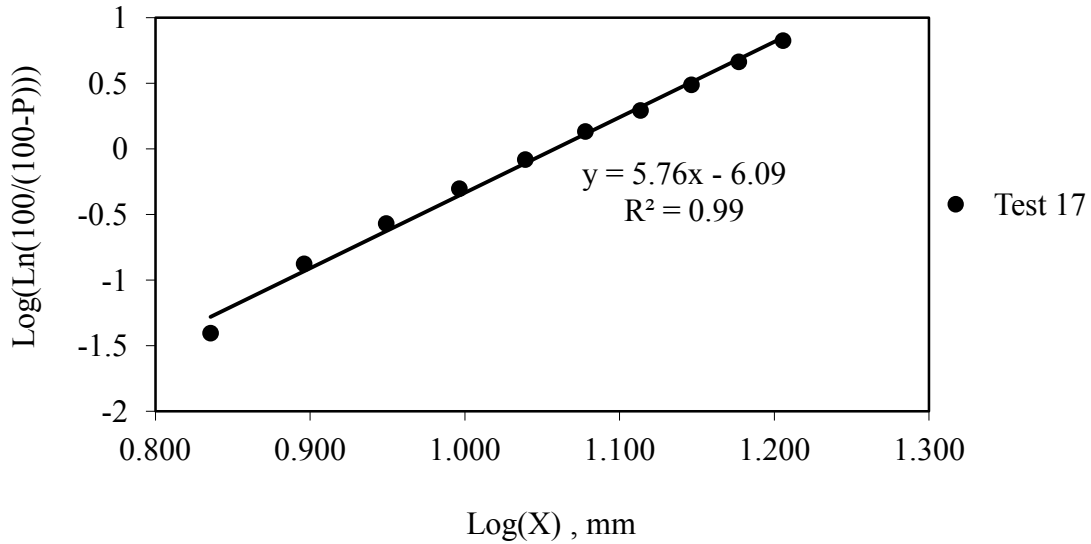


Figure 4-28- Rosin-Rammler distribution of the Test 17 specimen

Gaudin-Schuhmann distribution function is another method to present the distribution of crusher products. Equation (4-3) has been proposed for Gaudin-Schuhmann distribution.

$$P = 100 \left(\frac{X}{c} \right)^d \quad (4-3)$$

Where P is cumulative passing percentage, X is grain size, and c and d are constant parameters.

Equation (4-3) can be simplified as Equation (4-4):

$$\log(P) = d \log(X) + [\log(100) - d \log(c)] \quad (4-4)$$

Where P is cumulative passing percentage, X is grain size, and c and d are constant parameters.

Based on Equation (4-4), the P and X in a Log-Log scale graph should be linear if the given data follows this distribution. Figure 4-29 shows Gaudin-Schuhmann distribution function compatibility of some specimens as an example. However, size distributions of specimens are not linear in the full range of a Log-Log graph. The central and fine particle size section fits this function while the upper right side (coarse particles) is not following this function.

Comparing size distribution of specimens using Rosin-Rammler and Gaudin-Schuhmann formulas shows that the size distribution of specimens has better compatibility with the Rosin-Rammler distribution than Gaudin-Schuhmann.

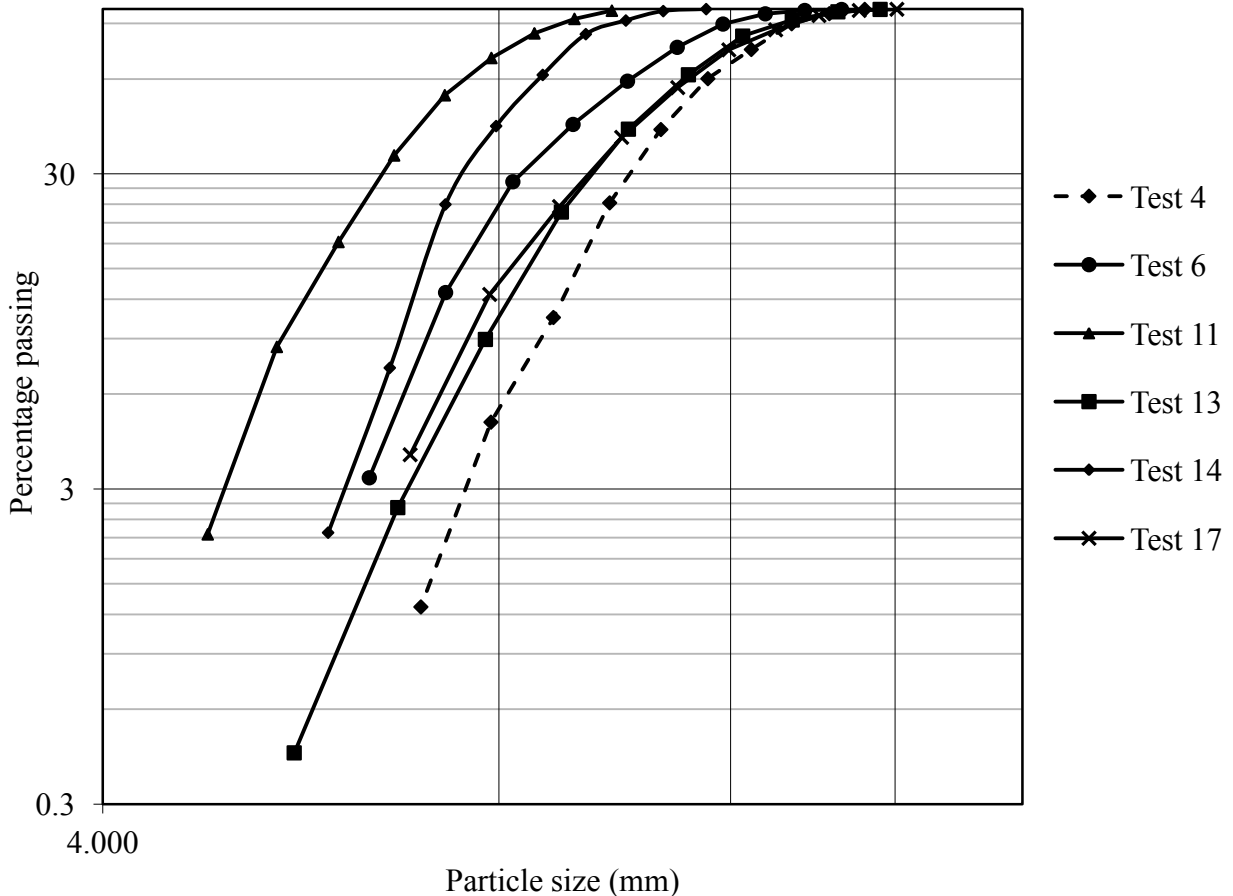


Figure 4-29- Gaudin-Schuhmann distribution of some specimens as an example

4.5.3 Shape characteristic of actual Rockfill

Shape and angularity of particles in the actual Rockfill have a wide range. Actual broken rock has a shape range from angular particles for crushed rock (by a crusher) to completely rounded particles (by movement in river). The following parameters affect the shape of actual broken rock.

- Rock type, weathering and alteration degree
- Joint sets, spacing and orientation of joints
- Production method (Comminution method)
- Abrasion by moving after breaking

Rock type and microstructures such as schistosity play an important role in the shape of particles especially for small size particles, but for large size broken blocks, the structure of rock mass is a significant parameter. For example, particles of crushed granite are more spherical than crushed gneiss or shales particles. Figure 4-30 and Figure 4-31 show the geometry of particles in Pradesh and Salma Rockfill dams respectively (Honkanadavar (2014)). Table 4-10 and Table 4-11 show the calculated shape characteristics of Figure 4-30 and Figure 4-31 by developed code in this research to determine the shape characteristics in the Pradesh and Salma Rockfill dams.

Figure 4-32 and Figure 4-33 illustrate the prepared Black-White photo by image processing code for Pradesh and Salma Rockfill dam respectively.



Figure 4-30- Shape of particles in the Pradesh Rockfill dam, this figure was adapted from Honkanadavar (2014).



Figure 4-31- Shape of particles in the Salma Rockfill dam, this figure was adapted from Honkanadavar (2014).

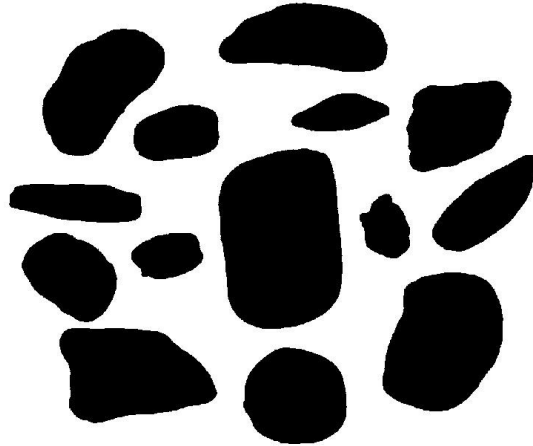


Figure 4-32- Black-White photo of particles in the Pradesh Rockfill dam

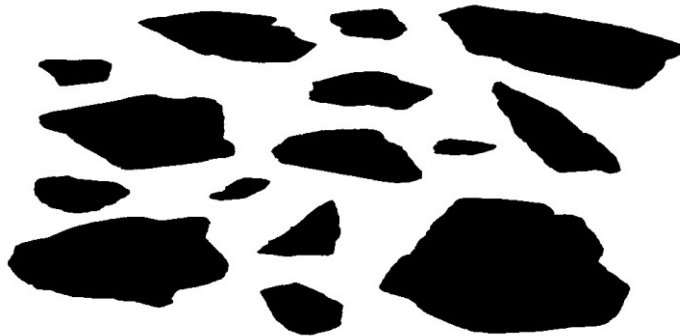


Figure 4-33- Black-White photo of particles in the Salma Rockfill dam

Based on Table 4-10 and Table 4-11, shape and angularity parameters for Pradesh and Salma dam is close to the shape and angularity of the prepared specimens in this research.

Table 4-10- Shape and angularity characteristics of Pradesh dam

	Average
angularity index	22.95
Angular-Parameter	1.05
Convexity	0.98
form factor	0.72
form index	2.76
Roundness	1.41

Table 4-11- Shape and angularity characteristics of Salma dam

	Average
angularity index	34.46
Angular-Parameter	1.09
Convexity	0.97
form factor	0.53
form index	4.70
Roundness	1.91

4.6 Summary and Conclusions

The image processing method is a powerful method to determine the geometry of a particle. Therefore, a code was developed by using MATLAB to determine the particle shape parameters by an image processing method. The working steps of the developed code are in this chapter. Particle photos are very important and it should be done in a photo box to have a photo without any possible shadow.

In addition, a representative part of the specimen was prepared and the accuracy of the representative part was compared with a specimen. Results show that the particle shape characteristics of the representative part are almost the same as the particle shape characteristics of the specimen; therefore, the representative quarter can represent the specimen. A summary of the specimens shape parameters is in Table 4-1.

In this chapter, the actual rockfill was investigated to find out whether the particle size distribution of the specimens is parallel with an actual rockfill size

distribution or not. If the specimen and actual rockfill have parallel size distribution, we can assume the behavior of specimen represents the actual rockfill. Based on Figure 4-19 to Figure 4-22 there are some actual rockfills with almost parallel size distribution to specimen size distribution. The specimens are a crusher product with Rosin-Rammler distribution; therefore, the specimens have better compatibility with an actual rockfill produced by a crusher. It should be clarified that the specimens in this research work have narrow range of particles size versus real-life size distribution for actual rock fill; therefore, the test results should be used carefully however, the specimen size distribution is almost Rosin-Rammler distribution and is parallel with some actual rock piles. In addition to size distribution, the void ratio of specimen and actual rock fill should be reasonable same.

Another important parameter is particle geometry of specimens and actual rockfill. The particle shape of two rockfill dams (Pradesh dam and Salma dam) was analyzed with code developed in this research. The results show that the particles shape characteristics of these dams (especially the Pradesh dam) have good compatibility with specimen geometry characteristics.

CHAPTER 5 : BEHAVIOR OF BROKEN ROCK BASED ON PARTICLES GEOMETRY

Chapter 5 contains the analysis of the triaxial tests results to understand the behavior of broken rock. The effect of angularity, form and texture of particles on the strength of broken rock are investigated. In addition, the shear strength of broken rock and the effect of water on the strength of broken rock are analyzed in this chapter.

5.1 Introduction

Triaxial tests were conducted on specimens of broken rock with different particle geometry at different confining pressures. The details of the procedure for conducted triaxial tests and the governed image processing method to determine the geometry of particles are in chapter 3 and chapter 4, respectively. This chapter presents the analysis of the results of the triaxial tests to investigate the effect of particles geometry on the strength of broken rock. The results of the triaxial tests indicate that the confining pressure and void ratio of broken rock have significant effect on the strength of broken rock.

5.2 Effect of confining pressure on the peak strength of broken rock

Researchers have proven the effect of confining pressure on the strength of rock. In the case of broken rock, the impact of confining pressure plays a more important role because the cohesion of broken rock is effectively zero and the frictional behavior of particles dominate the behavior of broken rock at low confining pressure. Based on the triaxial test results, the strength of broken rock and confining pressure have positive affinity. Figure 5-1 shows the results of the triaxial tests on the specimens of broken rock (a summary of results is available in Table 3-4). Increasing the confining pressure enhances the strength of broken rock. The linear relationship between confining pressure and strength of broken rock is inaccurate because the linear equation eventuates high unconfined compressive strength for broken rock (Figure 5-1).

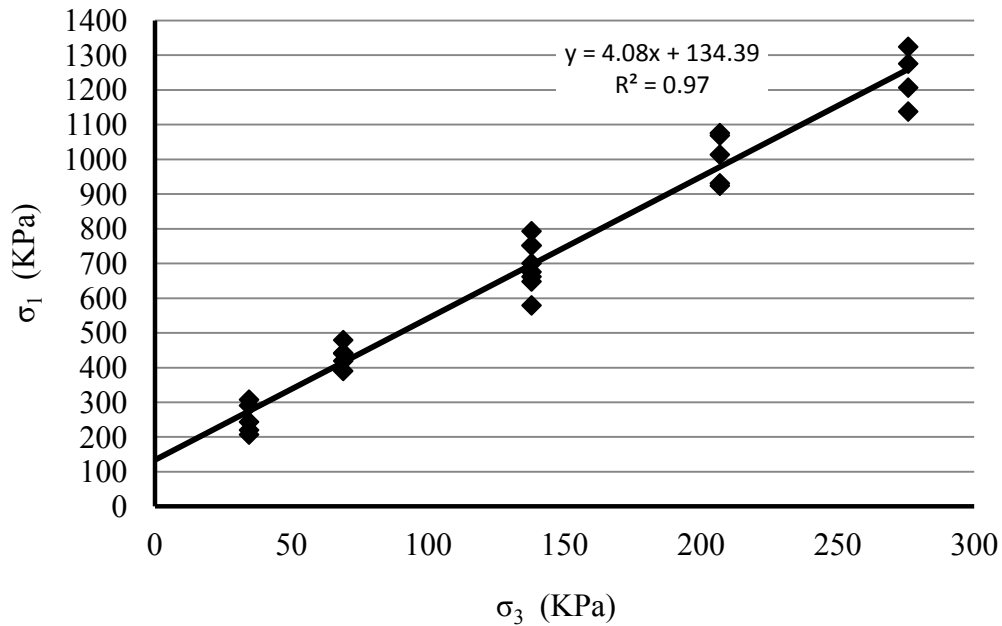


Figure 5-1- Linear function fitted on the triaxial tests data results high unconfined compressive strength for broken rock

Figure 5-2 illustrates another linear function fitted on the results of triaxial tests. This equation does not estimate high unconfined compressive strength for broken rock, but it also does not calculate the strength of broken rock accurately at low confining pressure (at confining pressure equal to 34.47 and 68.95 kPa). Therefore, the linear equation does not illustrate the relationship between confining pressure and strength of broken rock accurately. Figure 5-3 shows a power function that has been fitted on result of the triaxial tests. It is clear that power function not only estimates more accurately the strength of broken rock at low confining pressure but also does not determine high unconfined compressive strength for broken rock. Therefore, based on the results of the triaxial tests on broken rock, it could be argued that the power relationship between minor and major principle stress can better determine the behavior of broken rock. However, the following qualities of the conducted triaxial tests in this research should be considered when using the proposed power function for broken rock:

1. The unconfined compressive strength of intact rock was 32 MPa, which is almost moderate strength for an intact rock.
2. The range of confining pressure was from 34.47 to 275.79 kPa.
3. The maximum size of the specimen particles was 12 mm.

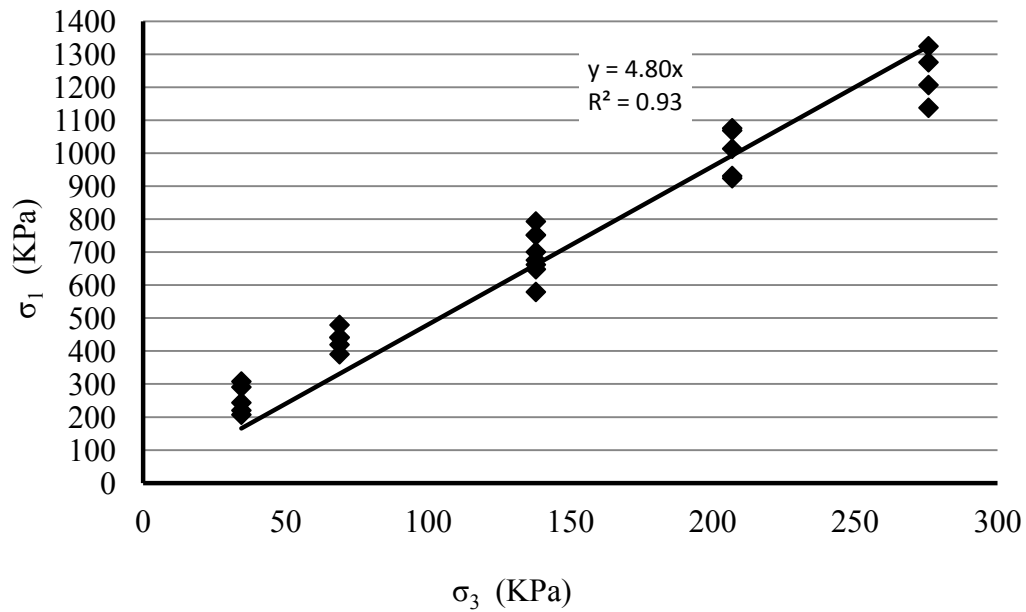


Figure 5-2- A linear function fitted on the triaxial tests data that cannot determine the strength of broken rock accurately at low confining pressure

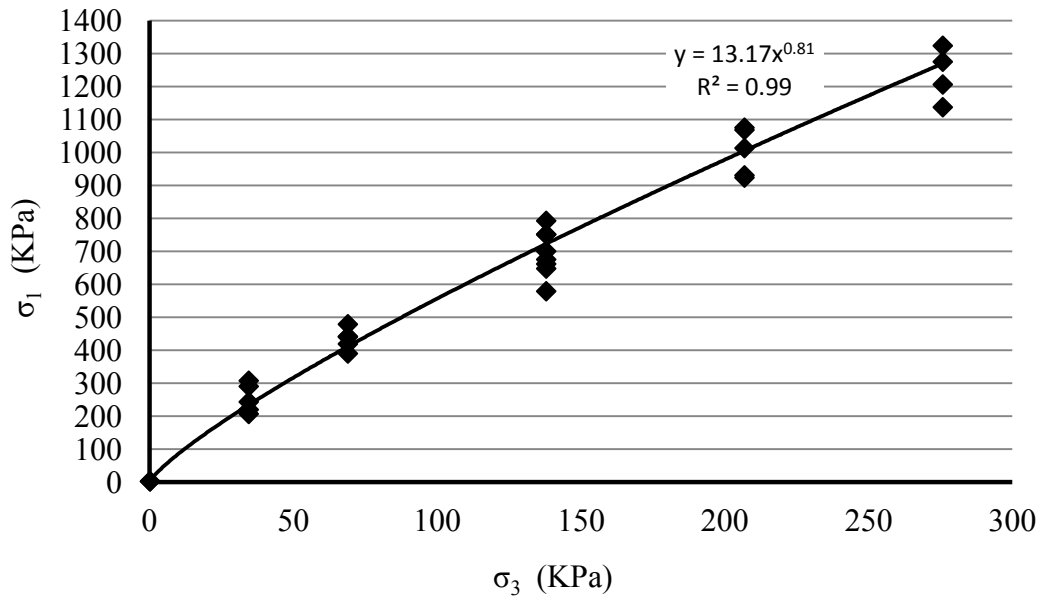


Figure 5-3- The power function fitted on the triaxial tests results can estimate more accurately the strength of broken rock

To investigate the effect of confining pressure on the strength of broken rock, in addition to triaxial tests, an unconfined compression test was conducted on a broken rock specimen. In this test, the specimen of broken rock was restricted with a very thin latex membrane (0.05 mm thickness). Figure 5-4 shows the prepared specimen for unconfined compression test and Figure 5-5 illustrates the test result. In this test, no confining pressure was applied and the latex membrane was very thin; however, the produced confining pressure by latex membrane can be calculated through Hoop tension theory. Figure 5-6 and Figure 5-7 show the emplaced specimen in the cell and the deformation of the specimen at the end of the test, respectively. The calculated graph in Chapter 3 (Figure 3-28) can be used to determine the produced lateral pressure by latex membrane in this test. The thickness of the latex membrane in the unconfined compression test was 18.8 times finer than latex membrane in Figure 3-28; therefore, the lateral pressure due to finer membrane will be 18.8 times smaller than the calculated pressure for the latex membrane in Figure 3-28. The calculated lateral pressure for the latex membrane in Figure 3-28 is equal to 2.78 kPa at 20% axial strain; therefore,

maximum lateral pressure at 20% axial strain for finer latex membrane in the unconfined compression test will be equal to 148 Pa.



Figure 5-4- Prepared specimen for unconfined compression test on broken rock

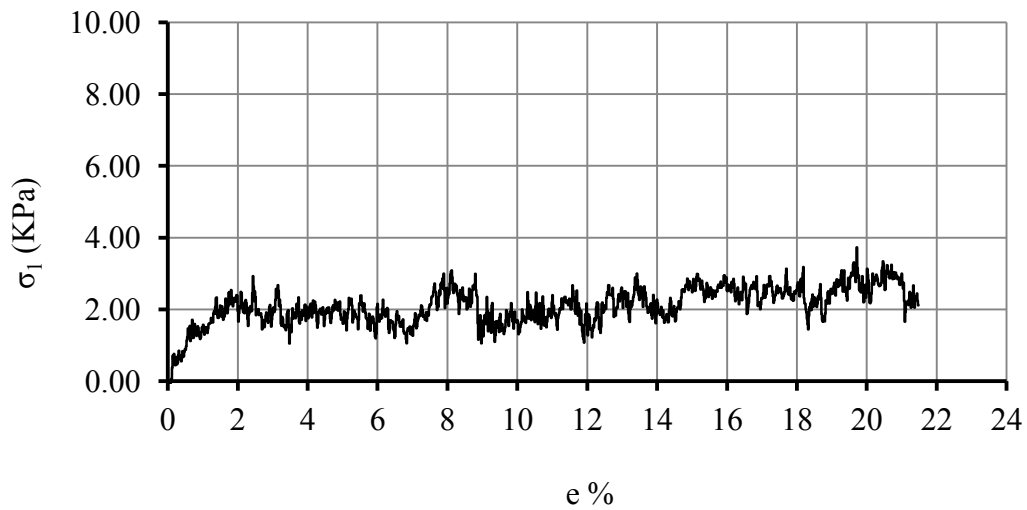


Figure 5-5- Result of unconfined compression test on broken rock



Figure 5-6- Specimen of broken rock before deformation

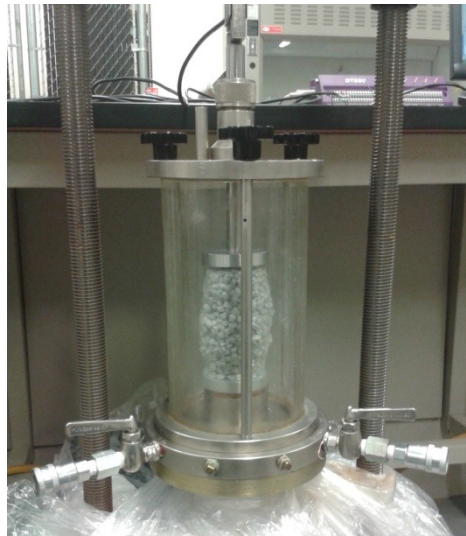


Figure 5-7- Buckling deformation of a broken rock specimen in unconfined compression test

The produced lateral confining pressure by membrane in the unconfined compression test was calculated 148 Pa at 20% axial strain while the strength of specimen was 2.5 kPa (Figure 5-5). Therefore, it can be argued that the strength of

broken rock is sensitive to confining pressure because a small confining pressure such as 148 Pa could result in 2.5 kPa strength for broken rock.

5.3 Effect of shape characteristics on the peak strength of broken rock

The shape characteristics of specimens were summarized in Chapter 4 in Table 4-1. In this research, all of the specimens were prepared from one rock type and all of the texture parameters (SD and TP) in Table 4-1 have almost the same value; therefore, the texture parameters in Table 4-1 do not have significant variation. In addition, the form index and angularity index were selected to investigate the effect of geometry of particles because form index and angularity index have reasonable variation to describe the form and angularity of the specimens compared to other parameters.

To investigate the effect of geometry of particles on the strength of broken rock three groups were specified from Table 4-1: Group (A), Group (B) and Group (C). The collected specimens in each group have almost the same shape characteristics. Table 5-1, Table 5-2 and Table 5-3 show the collected tests in group (A), group (B) and group (C), respectively.

Table 5-1- Categorized specimens in group (A)

Group (A)	σ_3 (kPa)	σ_1 (kPa)	Void Ratio	FI	AI
Test19	34.47	243.45	0.713	2.713	29.021
Test23	68.95	419.37	0.622	2.595	28.198
Test2	137.90	675.59	0.588	3.081	29.042
Test10	206.84	923.97	0.662	2.943	26.196
Test15	275.79	1206.58	0.685	2.783	24.420
Mean	-	-	0.654	2.823	27.376

Table 5-2- Categorized specimens in group (B)








Group (B)	σ_3 (kPa)	σ_1 (kPa)	Void Ratio	FI	AI
Test18	34.47	290.66	0.661	1.615	18.690
Test24	68.95	441.97	0.578	1.616	19.599
Test1	137.90	751.52	0.569	1.534	16.398
Test9	206.84	1068.67	0.569	1.506	15.331
Test14	275.79	1275.53	0.658	1.513	15.505
Mean	-	-	0.607	1.557	17.105

Table 5-3- Categorized specimens in group (C)

Group (C)	σ_3 (kPa)	σ_1 (kPa)	Void Ratio	FI	AI
Test20	34.47	307.67	0.515	2.104	24.709
Test25	68.95	479.10	0.545	2.140	26.438
Test3	137.90	792.86	0.512	2.164	22.612
Test11	206.84	1075.58	0.536	2.185	19.795
Test16	275.79	1324.12	0.581	2.235	20.922
Mean	-	-	0.538	2.166	22.895

To better understanding the concept of the calculated form index and angularity index for each specimen, the form index and angularity index of some sample particles were calculated and summarized in Table 5-4.

Table 5-4- Form index and angularity index of typical particles

No.	Particle Shape	FI	AI	Similar Group
1		4.39	24.14	-
2		3.31	34.26	Group (A)
3		3.19	21.39	-
4		2.24	24.01	Group (C)
5		1.91	18.62	-
6		1.59	16.96	Group (B)
7		1.48	19.05	-

The geometry parameter of group (A) is close to the geometry parameter of particle number 2 in Table 5-4. Group (B) and particle number 6 have almost the same shape characteristics. Finally, Group (C) and particle number 4 have almost the same geometry parameters. This type of comparison can provide better visual sense of the geometry parameters of Group (A), (B) and (C). Therefore, Group (B)

has more rounded and circular particles than Group (A). And Group (C) has more rounded particles than Group (A) and less rounded particles than Group (B). Figure 5-8 illustrates the best power function on group (A), (B) and (C).

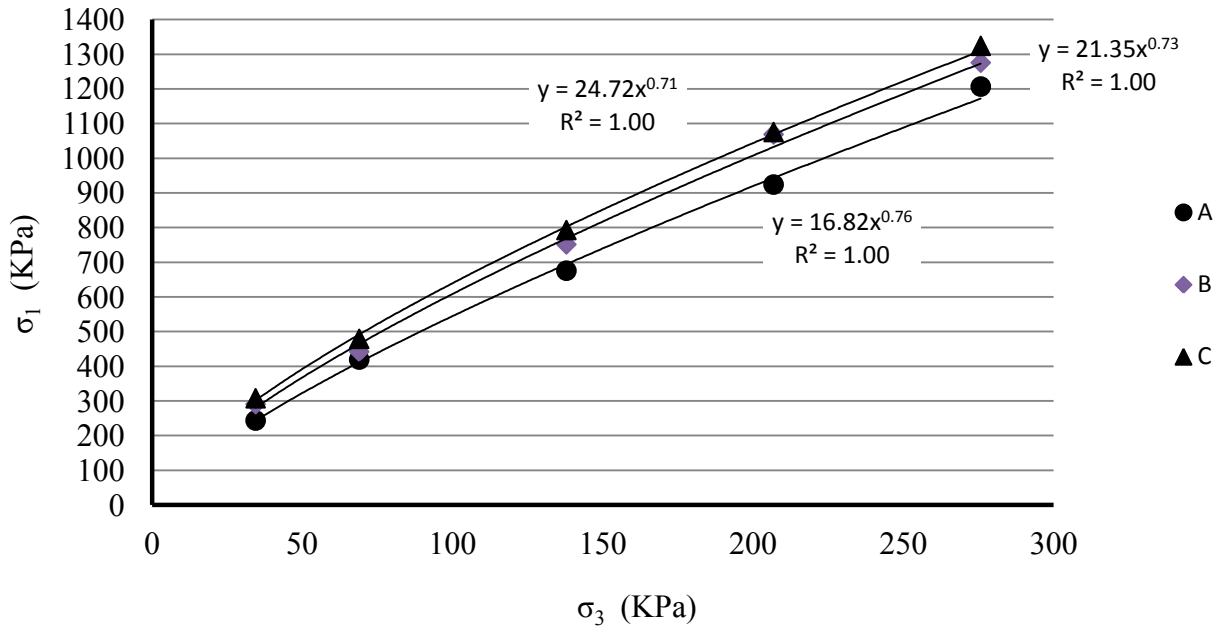


Figure 5-8- Fitted power function on group (A), (B) and (C) data

Equation (5-1) shows the power function proposed for tested broken sandstone in this research. Table 5-5 shows the power function parameters for Group (A), (B) and (C). In the next sections, the relationship between function parameters (α and β) and geometry parameters of Group (A), (B) and (C) was investigated.

$$\sigma_1 = \alpha \sigma_3^\beta \quad (5-1)$$

Table 5-5- Average of form-index and angularity-index of group (A), (B) and (C), and fitted power function parameters

No.	α	β	Average of Void Ratio	Average of FI	Average of AI
Group (A)	16.817	0.755	0.654	2.823	27.376
Group (B)	21.350	0.728	0.607	1.557	17.105
Group (C)	24.724	0.706	0.538	2.166	22.895

5.3.1 Effect of form index

Form index is a dimensionless parameter that describes the overall shape of a particle. The spherical particles have a form index equal to one but this parameter is bigger than that of an ellipsoid particle. In Figure 5-9 the average form index of each group versus the coefficient of fitted function (α) were plotted based on summarized data in Table 5-5. Also, Figure 5-10 illustrates the average form index versus power of fitted function (β). The tests results do not show a strong correlation between fitted function parameters (α and β) and average of form-index of group because the square error (R^2) is not close to 1 in Figure 5-9 and Figure 5-10. Therefore, these results do not show definitive conclusions on the effect of form index on the fitted function parameters (α and β) and consequently on the strength of broken rock.

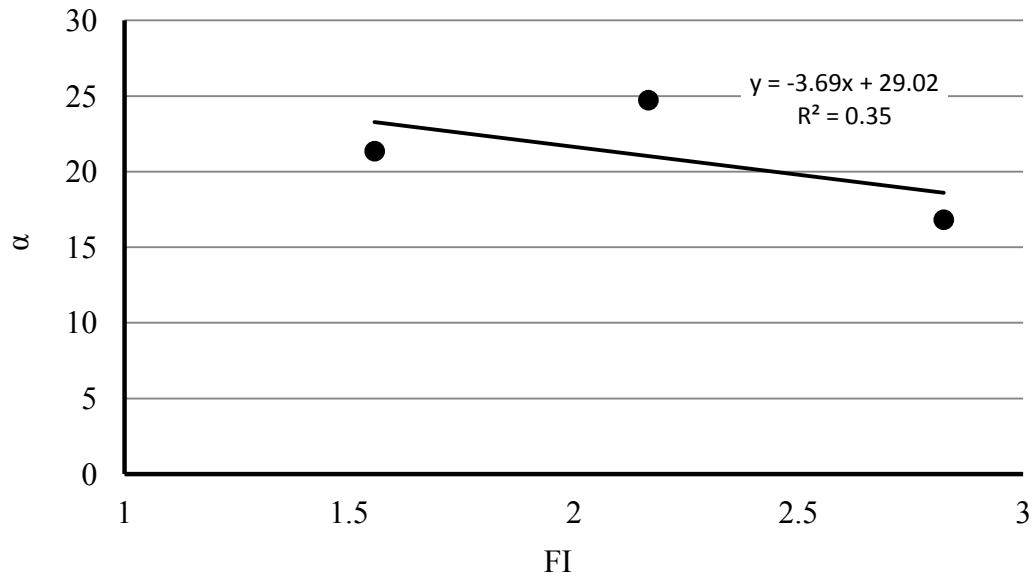


Figure 5-9- Average of form index of group (A), (B) and (C) versus fitted function parameter (α)

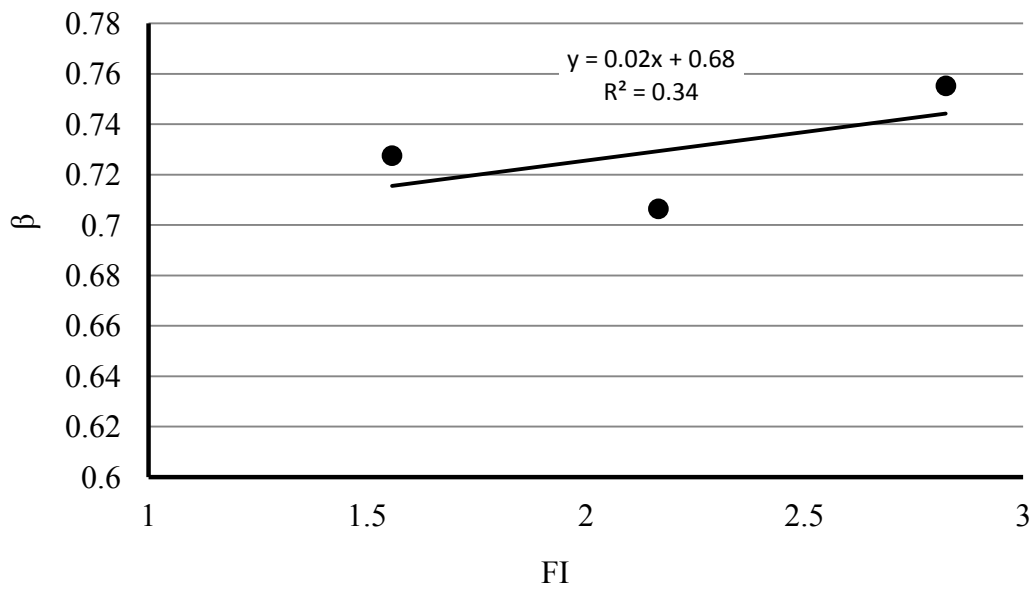


Figure 5-10- Average of form index of group (A), (B) and (C) versus fitted function parameter (β)

5.3.2 Effect of angularity index

Figure 5-11 and Figure 5-12 show the average angularity index of group (A), (B) and (C) versus fitted function parameters α and β , respectively. The correlation between the angularity index and α and β is not strong; therefore, the summarized results in this section do not illustrate a strong relationship between angularity index and strength of broken rock. Figure 5-13 depicts the relationship between the ratio of form index to angularity index and normalized strength of broken rock by confining pressure. The illustrated data in Figure 5-13 is group (A), (B) and (C) together. The correlation between $\frac{FI}{AI}$ and $\frac{\sigma_1}{\sigma_3}$ is better than the correlation

between the form index and α or β . In addition, the correlation between $\frac{FI}{AI}$ and $\frac{\sigma_1}{\sigma_3}$ is better than the correlation between the angularity index and α or β ;

however, it does not prove a relationship between $\frac{FI}{AI}$ and $\frac{\sigma_1}{\sigma_3}$.

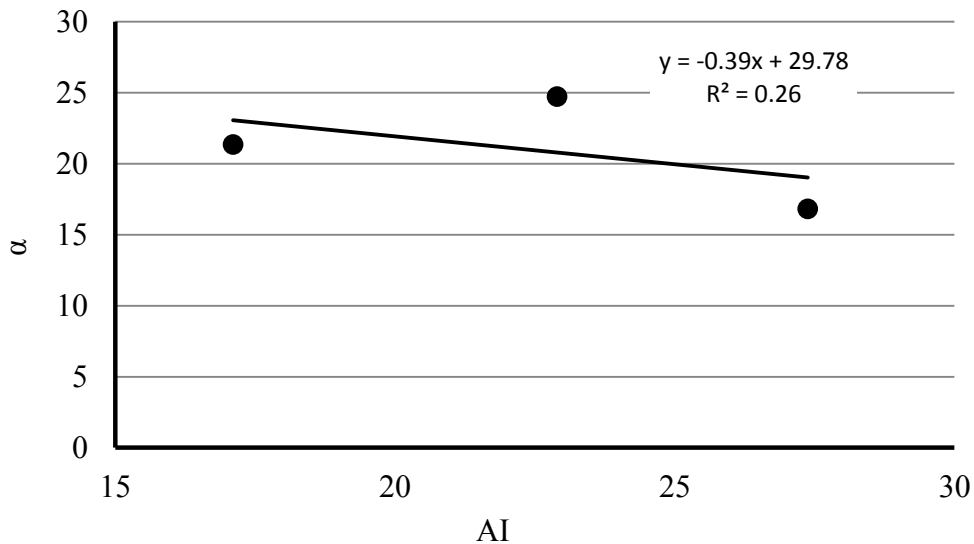


Figure 5-11- Average of angularity index of group (A), (B) and (C) versus fitted function parameter (α)

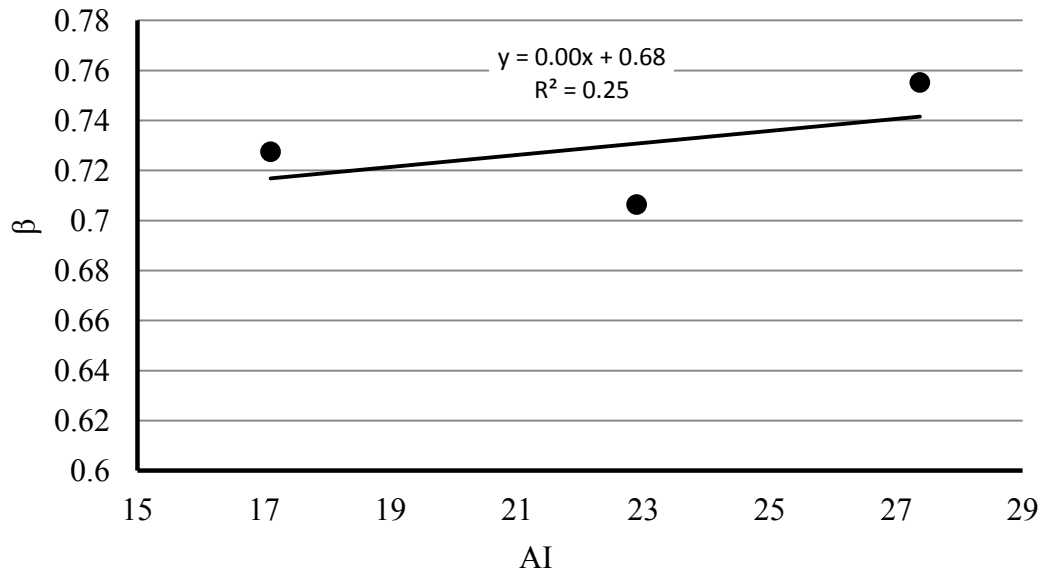


Figure 5-12- Average of angularity index of group (A), (B) and (C) versus fitted function parameter (β)

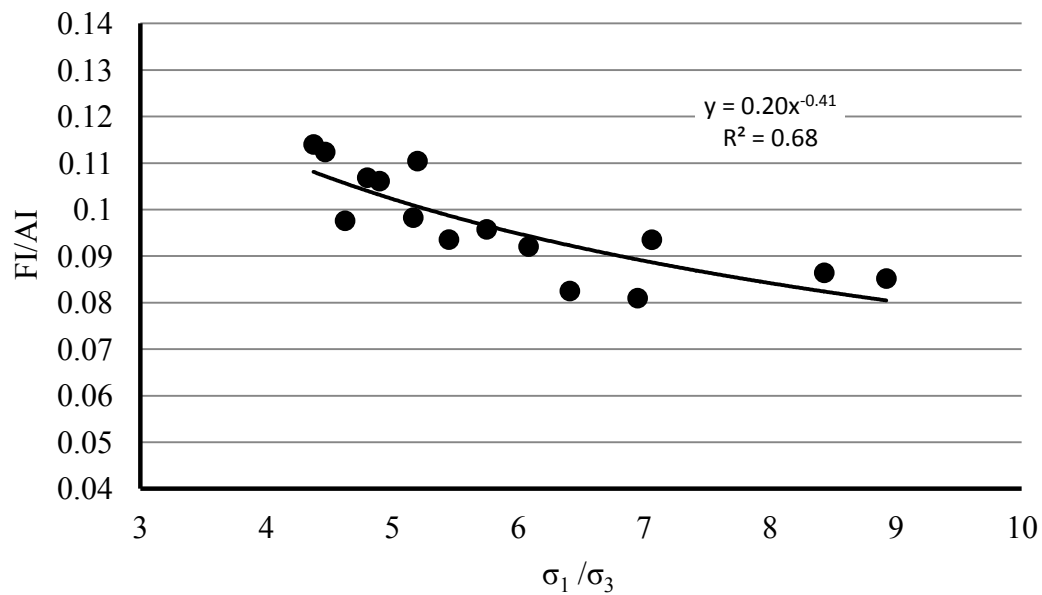


Figure 5-13-Ratio of broken rock strength to confining pressure versus ratio of form index to angularity index

5.3.3 Effect of Void ratio

The void ratio of a specimen is the ratio of the void space between particles to the volume of particles. To determine the void ratio of a broken rock specimen, it is assumed that the particles are completely solid and the void space inside the intact rock was not taken in to account. The void ratio can be calculated by using Equation (5-2).

$$e = \frac{V_v}{V_s} \quad (5-2)$$

Where V_v is the volume of void spaces between particles and V_s is the volume of solids (particles).

The specimen's void ratio during triaxial compression test is changed; therefore, in this research the initial void ratio of the specimen was calculated and used to plot the figures. Figure 5-14 and Figure 5-15 show the correlation between the average void ratio of groups (A, B and C) and coefficients (α and β) of the fitted functions in Figure 5-8.

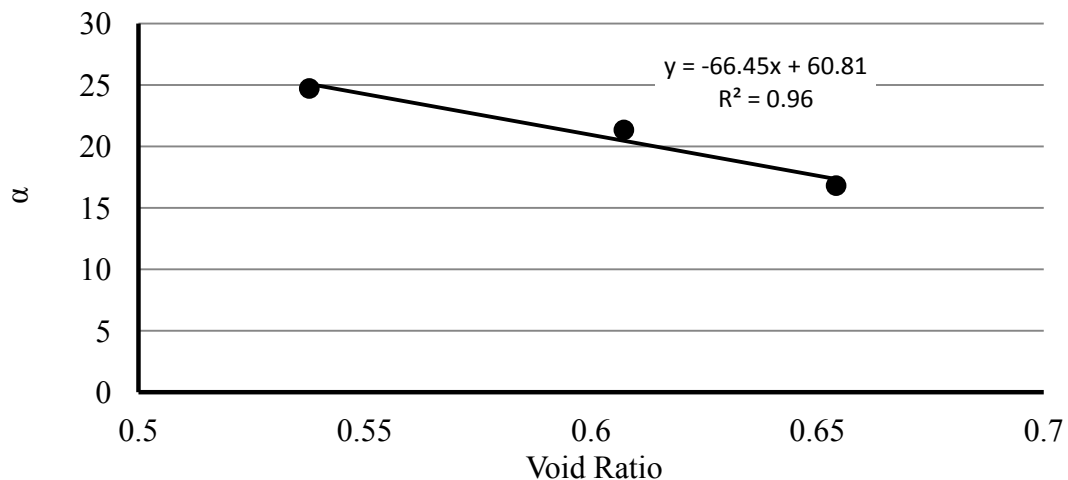


Figure 5-14- Relationship between void ratio and fitted function parameter (α)

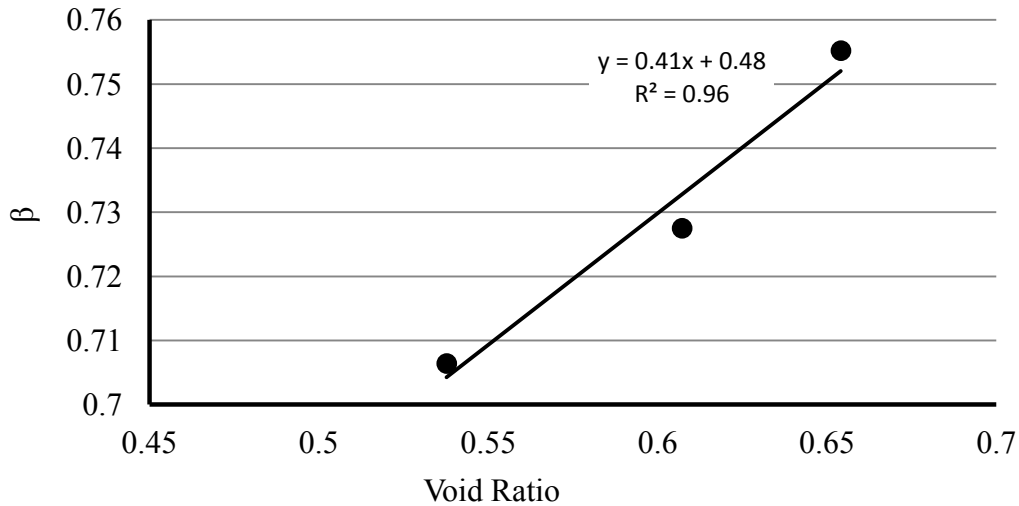


Figure 5-15 Relationship between void ratio and fitted function parameter (β)

It is clear that the void ratio of specimens and coefficient α have the strong correlation. Increasing the void ratio decreases the coefficient α while the void ratio and coefficient β have the direct relationship. The variation of β in group (A), (B) and (C) is very small (from 0.70 to 0.75); therefore it can be concluded that the void ratio and strength of broken rock have negative affinity. Decreasing of void ratio increases the strength of broken rock. The effect of void ratio on the strength of broken rock does make sense because void ratio is a feature of specimen density and the effect of density on the strength of rock is clear; hence, the correlation between void ratio and strength of broken rock is important.

The void ratio of specimen not only has a correlation with the coefficient of Equation (5-1) but it also has good correlation with the strength of specimen. Figure 5-16 illustrates the relationship between the void ratio of specimen with the strength of specimen at different confining pressures. It is clear the void ratio has negative affinity with the specimen strength. Increase of void ratio decreases the strength of specimen. The void ratio of the specimen also has negative affinity with the density of specimen; therefore, the density of specimen and strength of specimen has a direct relationship at different confining pressures.

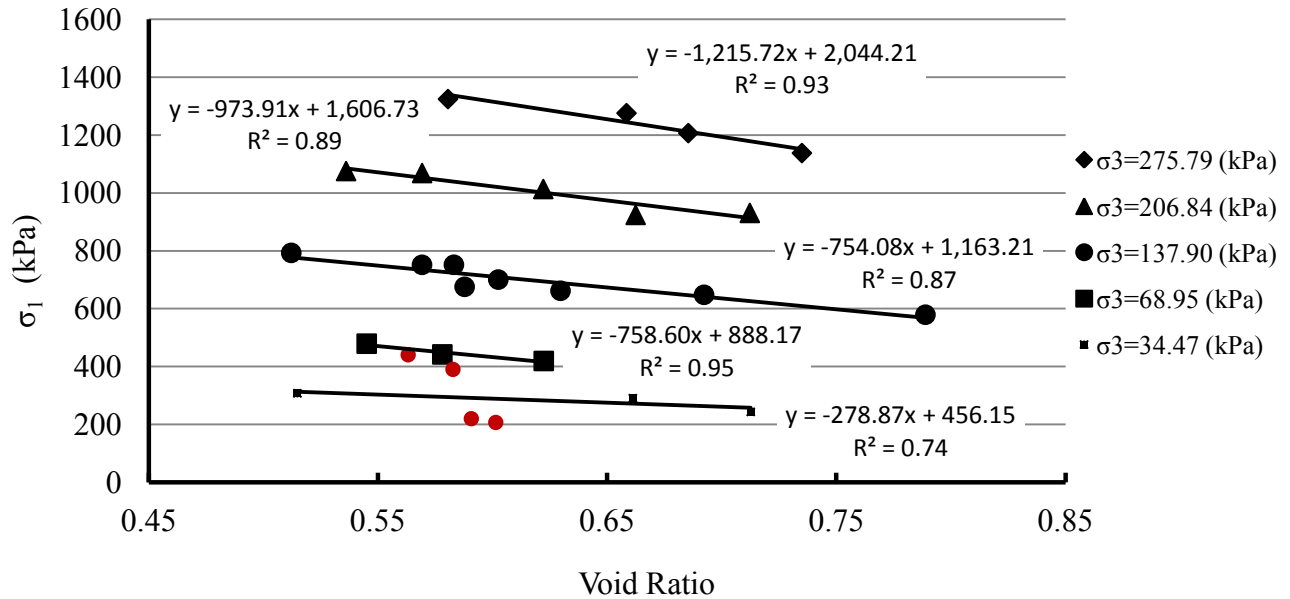


Figure 5-16- Relationship between void ratio and strength of broken rock at different confining pressure

Figure 5-16 was plotted with the results of all triaxial tests except tests No. 21, 22, 26 and 27 (the four red points in Figure 5-16). These tests (No. 21, 22, 26 and 27) have around at least 20% fine particles (2 to 0.18 mm) while other specimens do not have fine particles. Generally, in broken rock, very small particles behave like dust and a layer of fine particles between bigger particles does not allow the big particles contact with each other and consequently reduces the strength of broken rock. The specimen strength of tests No. 21, 22, 26 and 27 are almost 5% less than specimens with the same geometry parameters and confining pressure. In addition, tests No. 21, 22, 26 and 27 show that maybe the effect of fine particles is more important at lower confining pressure because tests No. 21 and 22 have greater strength decrease than tests No. 26 and 27. It is clear that further research is needed as these four tests are not adequate to make conclusion about the effect of fine particles on the strength of broken rock.

5.4 Shear strength of broken rock

Based on Coulomb-Navier failure criterion, the shear strength of material has two components: cohesion and friction. Equation (5-3) expresses the conventional Coulomb-Navier strength criterion.

$$\tau = c + \sigma_n \tan \phi \quad (5-3)$$

Where τ is shear strength, σ_n is normal stress on the failure plate, C is the cohesion coefficient and ϕ is the internal friction angle of the material.

Equation (5-4) and (5-5) indicate, respectively, the shear stress and normal stress on a plate that has angle θ between normal line on plat and major principal stress.

$$\tau = \left(\frac{\sigma_1 - \sigma_3}{2} \right) \sin 2\theta \quad (5-4)$$

$$\sigma_n = \left(\frac{\sigma_1 + \sigma_3}{2} \right) + \left(\frac{\sigma_1 - \sigma_3}{2} \right) \cos 2\theta \quad (5-5)$$

Where σ_1 is major principal stress and σ_3 is minor principal stress.

Substituting Equation (5-4) and (5-5) into Equation (5-3) gives Equation (5-6).

$$C = \left(\frac{\sigma_1 - \sigma_3}{2} \right) [\sin 2\theta - \cos 2\theta] - \left(\frac{\sigma_1 + \sigma_3}{2} \right) \tan \phi \quad (5-6)$$

To calculate the more likely failure angle, the optimum point of Equation (5-6) should be calculated when $\frac{\partial C}{\partial \theta} = 0$. This results Equation (5-7).

$$\tan 2\theta = \frac{-1}{\tan \phi} \quad (5-7)$$

Where θ is the more likely failure angle.

Using trigonometry, Equation (5-8) and (5-9) are other equations to determine the failure angle.

$$\sin 2\theta = \frac{1}{\sqrt{1 + \tan^2 \phi}} \quad (5-8)$$

$$\cos 2\theta = \frac{-\tan \phi}{\sqrt{1 + \tan^2 \phi}} \quad (5-9)$$

Substituting Equation (5-8) and (5-9) into Equation (5-6) gives Equation (5-10).

$$2C = \sigma_1 \left(\sqrt{1 + \tan^2 \phi} - \tan \phi \right) - \sigma_3 \left(\sqrt{1 + \tan^2 \phi} + \tan \phi \right) \quad (5-10)$$

The cohesion between particles for granule material is zero; for this reason, the cohesion coefficient for coulomb failure is zero ($c=0$), and Equation (5-10) is simplified to Equation (5-11).

$$\frac{\sigma_1}{\sigma_3} = \frac{\sqrt{1 + \tan^2 \phi} + \tan \phi}{\sqrt{1 + \tan^2 \phi} - \tan \phi} \quad (5-11)$$

By using Equation (5-11), the internal friction angle for granule material can be calculated based on the principal major and minor stresses that are determined through triaxial tests. Table 5-6 shows the computed internal friction angles by using Equation (5-11).

Table 5-6- The calculated internal friction angle from result of triaxial tests

No.	σ_3 (kPa)	σ_1 (kPa)	ϕ (deg)
Test1	137.90	751.52	43.63
Test2	137.90	675.59	41.38
Test3	137.90	792.86	44.73
Test4	137.90	700.49	42.15
Test5	137.90	648.01	40.47
Test6	137.90	751.77	43.63
Test7	137.90	579.16	37.98
Test8	137.90	661.91	40.93
Test9	206.84	1068.67	42.51
Test10	206.84	923.97	39.36
Test11	206.84	1075.58	42.64
Test12	206.84	1013.51	41.38
Test13	206.84	930.79	39.52
Test14	275.79	1275.53	40.13
Test15	275.79	1206.58	38.90
Test16	275.79	1324.12	40.94
Test17	275.79	1137.63	37.57
Test18	34.47	290.66	51.99
Test19	34.47	243.45	48.76
Test20	34.47	307.67	52.99
Test21	34.47	206.96	45.60
Test22	34.47	219.99	46.81
Test23	68.95	419.37	45.86
Test24	68.95	441.97	46.90
Test25	68.95	479.10	48.45
Test26	68.95	440.63	46.84
Test27	68.95	390.26	44.41

Figure 5-17 illustrates the peak shear strength and corresponding normal stress at the most possible failure plane calculated by triaxial test results. It is clear that the relationship between shear strength and normal stress is a non-linear relationship.

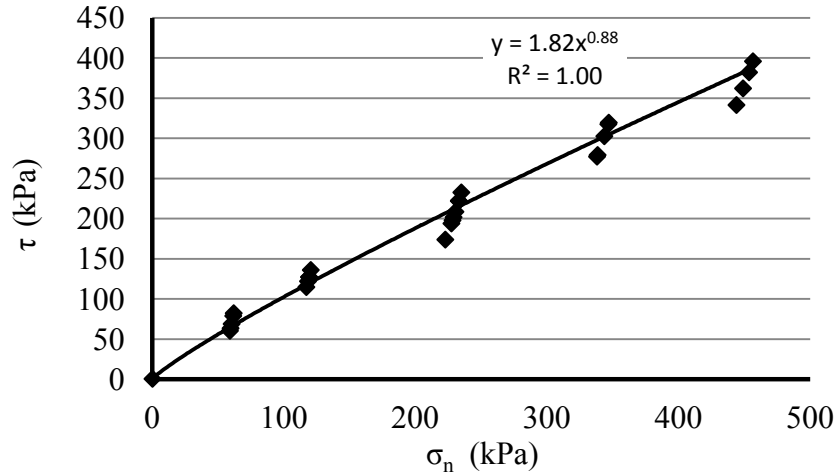


Figure 5-17- Shear strength of broken rock calculated by triaxial test results

Figure 5-18 shows the relationship between internal friction angle and confining pressure. The internal friction angle of broken rock and confining pressure have negative affinity. An increase in confining pressure decreases the effective internal friction angle of broken rock. Figure 5-19 illustrates the relationship between effective internal friction angle and confining pressure for three categorized group (A, B and C).

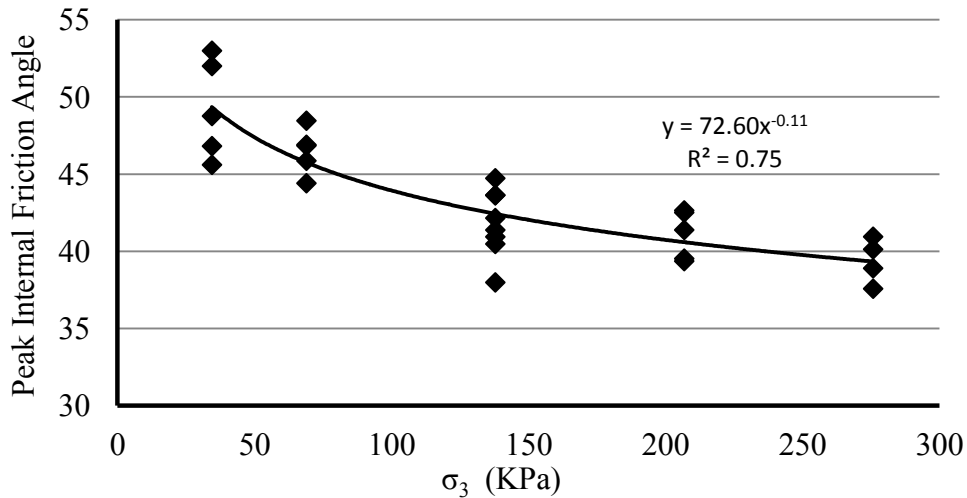


Figure 5-18- Relationship between peak internal friction angle and confining pressure

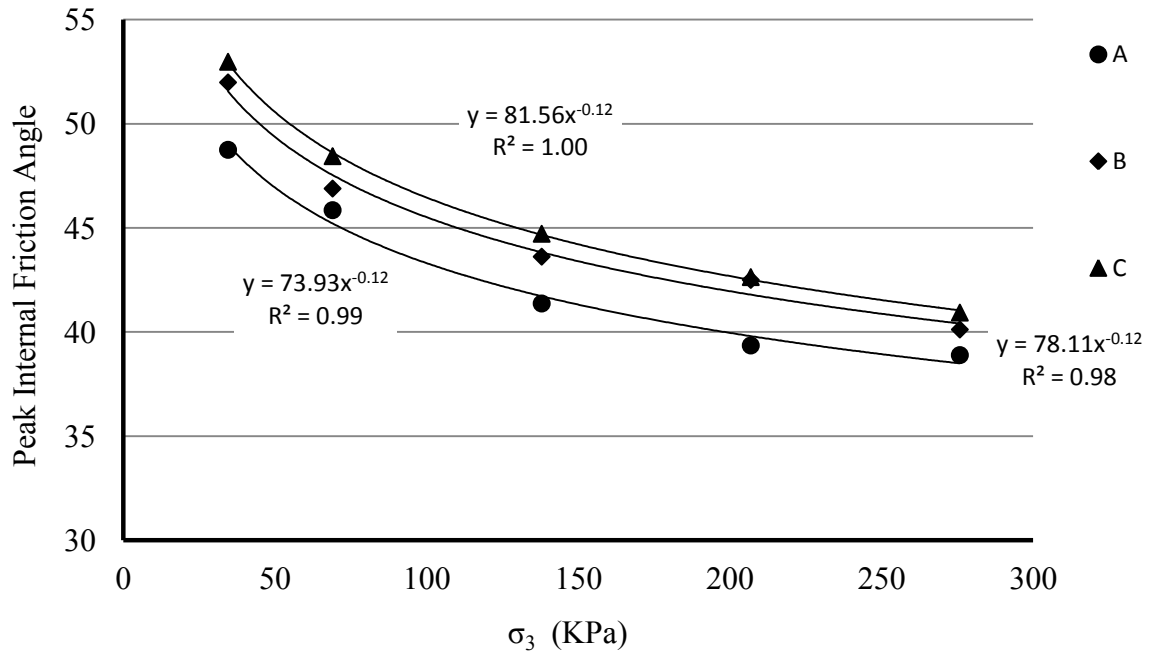


Figure 5-19- Relationship between peak internal friction angle and confining pressure for group (A), (B) and (C) separately

Figure 5-20 shows the correlation between internal friction angle and ratio of form-index to angularity-index. The correlation between this ratio and internal friction angle is better than the correlation between form index and broken rock strength parameters.

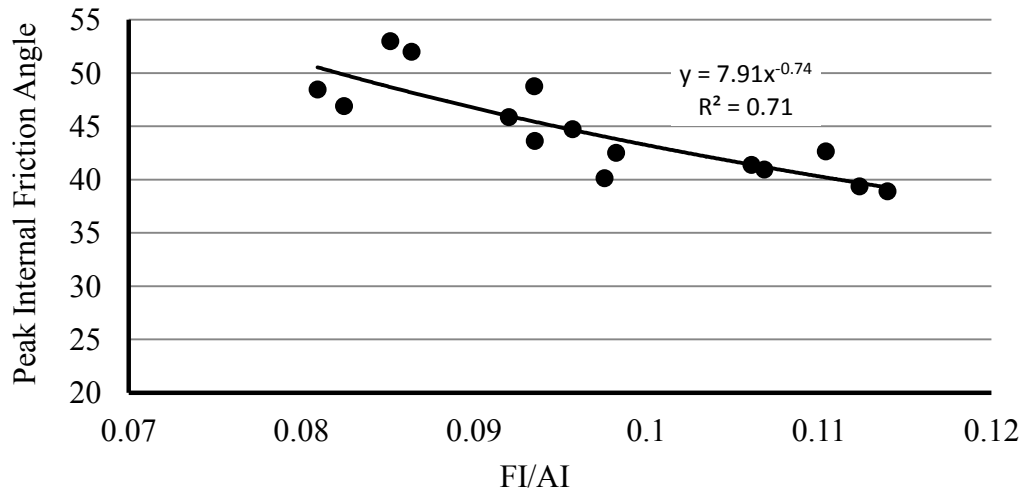


Figure 5-20- Relationship between peak internal friction angle and ratio of form index to angularity index

The void ratio of specimen and calculated internal friction angle through triaxial test results have good correlation. Figure 5-21 depicts the relationship between internal friction angle and void ratio of specimen at different confining pressures. Figure 5-21 illustrates that the dense broken rock material has a bigger internal friction angle than loose material.

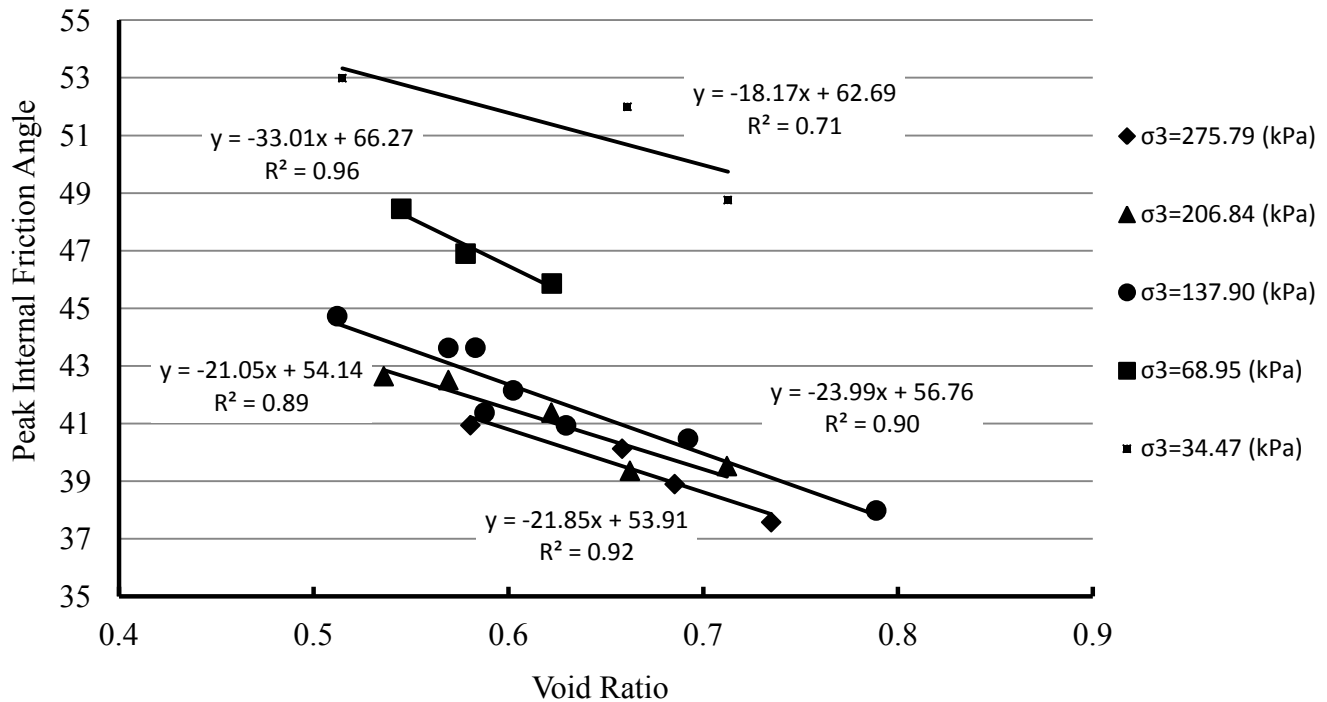


Figure 5-21- Relationship between peak internal friction angle and void ratio

5.5 Effect of water on the strength of broken rock

In many geotechnical projects, there is water in rock from groundwater or seasonal rain. Water has a significant effect on the strength of rock. In this section, the influence of water on the strength of broken rock is investigated in two categories: the effect of pore pressure on the strength of broken rock and the effect of water on the strength of particles.

5.5.1 Effect of pore pressure on the strength of broken rock

Pore pressure increases the effective stress resulting in a decrease in the effective strength of broken rock. Most failure criteria are based on the effective stress and increasing the effective stress increases a failure likelihood. Equation (5-12) expresses the increase of effective stress due to pore pressure. Figure 5-22 shows the effect of pore pressure on the strength of broken rock. The history of slope failure in rainy seasons demonstrates that water decreases the strength of rock.

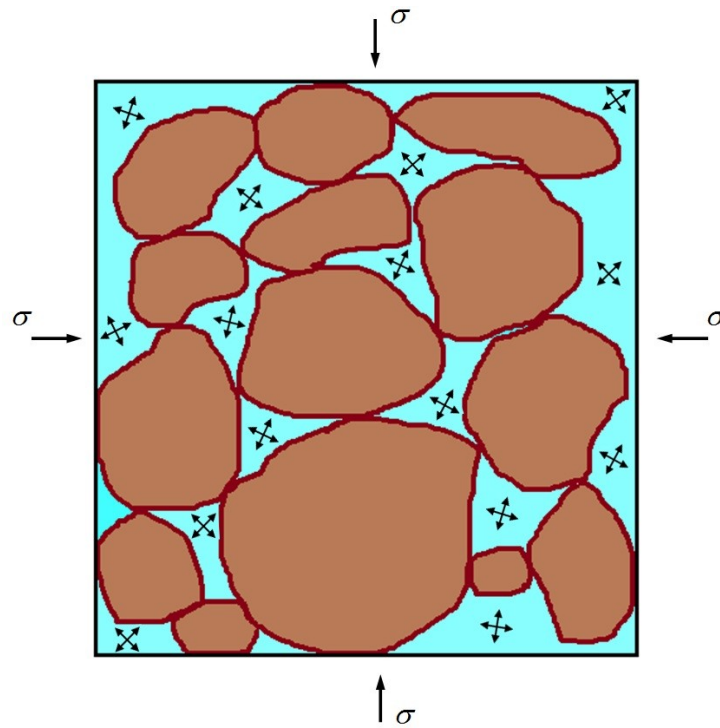


Figure 5-22- Sketch of pore pressure in the broken rock

$$\sigma' = \sigma + u \quad (5-12)$$

Where σ' is the effective stress, σ is total stress and u is pore pressure.

Figure 5-23 illustrates how the pore pressure can reduce the effective stress and change the stable stress situation to an unstable situation based on Mohr-Coulomb failure criterion.

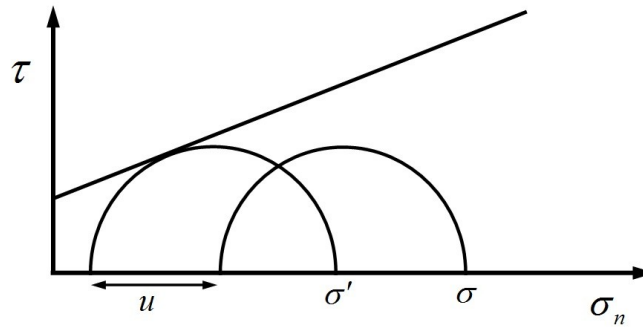


Figure 5-23- Effect of pore pressure based on Mohr-Coulomb criterion

5.5.2 Effect of water on the strength of particles

Not only does the pore pressure of water reduce the strength of broken rock but effectively decreases the strength by decreasing the frictional parameters of the particles. Figure 5-24 and Figure 5-25 show the axial stress-strain curve for broken sandstone in two different conditions: with unsaturated particles and saturated particles, respectively. For both tests, the confining pressure and geometry parameters and size distribution of particles were the same. The strength of broken sandstone with saturated particles is almost 30 percent less than the strength of broken sandstone with unsaturated particles although the tests were performed drained.

This means, water decreases the frictional strength between particles and reduces the strength of particles for breakage; consequently, water decreases the strength of broken rock even without pore pressure. Determining how much water impacts the strength of broken rock requires further testing and study.

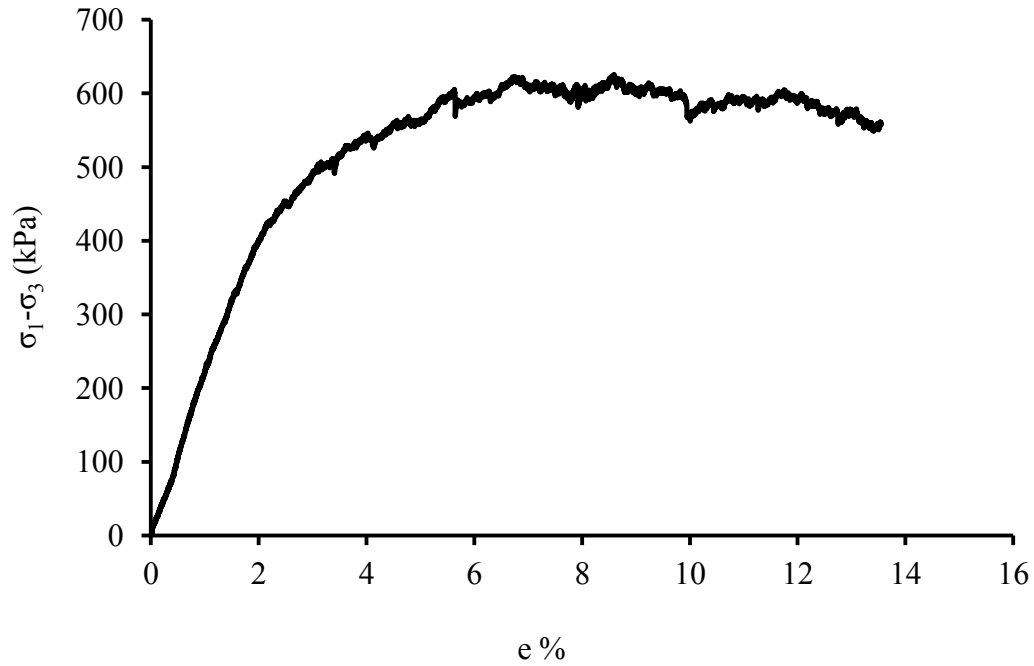


Figure 5-24- Axial stress-strain curve for unsaturated broken sandstone, at a confining pressure of 138 kPa

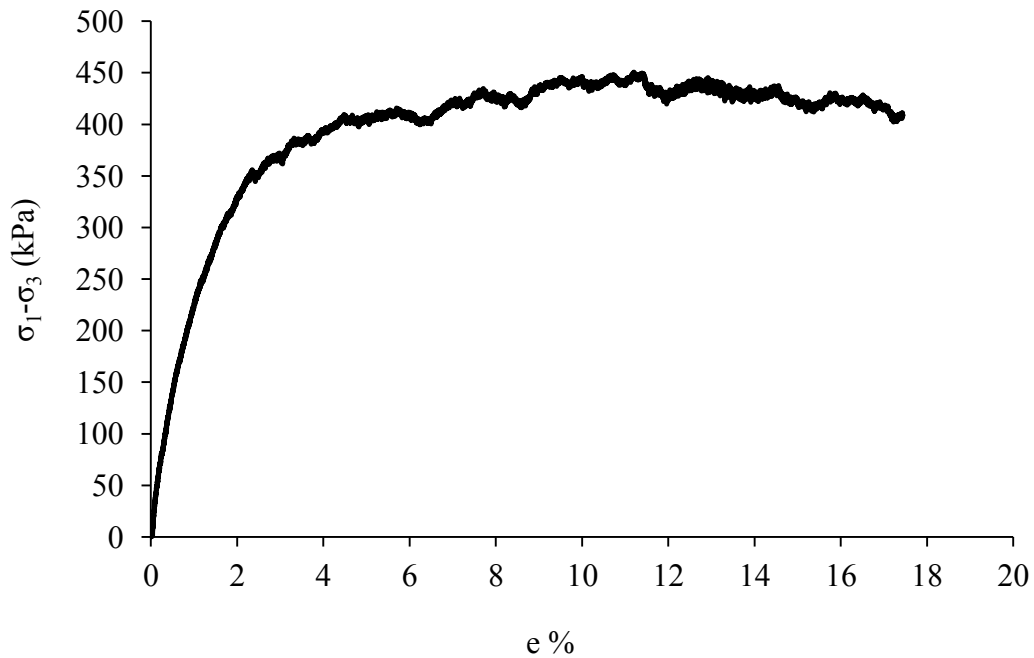


Figure 5-25- Axial stress-strain curve for saturated broken sandstone, at a confining pressure of 138 kPa

5.6 Summary and Conclusions

In this chapter, the triaxial test results were investigated to find out the effect of particle shape characteristics on the behavior of broken rock. It was expected that the confining pressure would have the most significant effect on the strength of broken rock; therefore, the relationship between confining pressure and strength of broken rock was determined with a nonlinear function. The correlation between confining pressure and strength of broken rock is very strong because broken rock is formed of discrete particles and confining pressure affects the contact force between particles.

To investigate the impact of particles shape on the strength of broken rock, three groups (Group (A), (B) and (C)) from specimens that have almost the same particle shape characteristics were specified. Thus, all tests in each group have almost the same particles shape parameters, but the particle shape parameters of group (A), (B) and (C) are different. Therefore, the relationship between the particle shape parameters of groups and coefficients of fitted equations was investigated. The correlation between particle shape parameters (form index and angularity index) is not strong, possibly because of the small range in particle shape parameters variation in specimens. But the correlation between void ratio and coefficients of fitted equations (α and β) is strong. There is a better correlation between $\frac{FI}{AI}$ and $\frac{\sigma_1}{\sigma_3}$ that can show a relationship between particle geometry and strength of broken rock.

The calculated shear strength by triaxial test results show that relationship between shear strength and corresponding normal stress is nonlinear. Peak internal friction angle and confining pressure have negative affinity, also the internal friction angle and void ratio of broken rock have negative affinity, and an increase in void ratio decreases the peak internal friction angle.

The triaxial test on the saturated broken rock shows that water decreases the strength of broken rock even without pore pressure; therefore, effect of water on

the strength of broken rock needs further research. The change of pore pressure in an unsaturated rock and buoyancy effects of water in a rock can explain the influence of the water without pore pressure on the strength of a rock.

CHAPTER 6 : CONCLUSION AND DISCUSSION

Chapter 6 provides the discussion and conclusion of the thesis. The scientific and industrial contributions of the research are highlighted in this chapter. In addition, Chapter 6 contains recommendations for future work in modeling the behavior of broken rock.

6.1 Summary of Research

The behavior of broken rock plays significant role in geomechanical design. Backfill design, waste dumps, rockfill engineering and slope stability indicate the significance of broken rock. There are many previous studies on the behavior of broken rock that indicate the geometry of particles play a significant role in the strength of broken rock; however, there are few comprehensive study to investigate the strength of broken rock using the geometry of particles.

Three independents parameters can describe completely the geometry of a particle: Form, Angularity and Texture. Form describes the overall shape of a particle. Particles are similar to triangles, circles, quadrangles or other shapes. Angularity expresses the variations at the apexes of each fragment and texture describes the surface roughness and inequality at such a scale that it does not affect the overall shape. In this research, these three parameters were used to describe the geometry of a particle. The image processing technique is a well-known method to determine the geometry of a particle. Using the selected equations in Chapter 4 from high-resolution photos, the geometry of a particle can be quantified. The image processing technique was conducted on all particles of the representative part of each specimen and the average of geometry parameters for the representative parts used to indicate the geometry of the entire specimen.

The triaxial test method was chosen to determine the strength of broken rock because this method provides acceptable conditions for specimen deformation without impressing any preset failure plane on the specimen. The applied confining pressures in this research were set low to ensure the frictional behavior of particles dominates the behavior of broken rock. Figure 6-1 shows the research workflow.

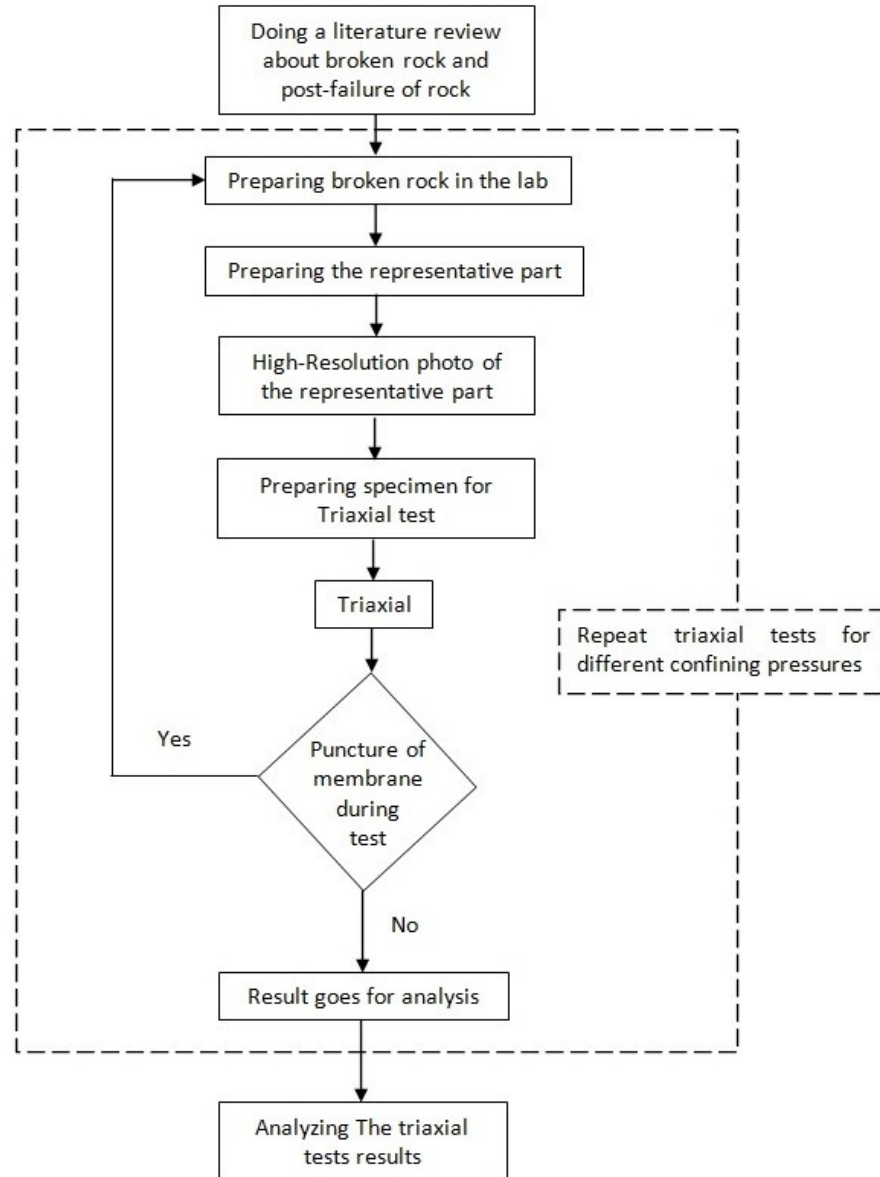


Figure 6-1- Workflow of this research

The effect of the rubber membrane on the triaxial test results was investigated by analytical and numerical methods. The maximum correction confining pressure was calculated by Compression Shell and Hoop Tension Theories where the numerical modeling of the rubber membrane agreed with analytical results.

6.2 A review on the behavior of broken rock

The behavior of broken rock is a complex problem in which many parameters play a role. Different mechanisms between completely discrete particles finally determine the behavior of broken rock. A combination of the following mechanisms controls the behavior of broken rock.

1. Sliding resistance between particles
2. Rotating resistance of particles
3. Breakage of particles

During broken rock deformation, sliding, rolling and breakage can be started and stopped several times. For example, sliding can happen between two particles while another particle is rolling and other particles are broken. These mechanisms can be changed in a moment and a particle sliding may start rolling or breakage; therefore, the combination of behavior mechanisms can be changed several times during broken rock deformation. Thus, modeling the behavior of broken rock can be complex and difficult. In the following section some of important features of broken rock behavior are concluded.

6.2.1 Frictional behavior of broken rock

The frictional resistance of broken rock is affected by two parts: Sliding particles on the each other and Rolling resistance between particles. Based on the Amontons laws (Feda (1982)), the friction strength is independent of size of contact area and is directly affected by normal stress. An important source to create normal stress on the contact surface of particles is lateral pressure; therefore, this may explain why broken rock is very sensitive to confining pressure. Marsal (1969) and (1973) illustrates that in broken rock, the average of frictional resistance on the surface of particles is a proportion of average contact force. Marsal introduced Equation (6-1) and believed that the coefficient of friction depends on the normal force on the contact surfaces.

$$\bar{R} = \frac{\bar{\mu}}{\sqrt{1 + \bar{\mu}^2}} \bar{P} \quad (6-1)$$

Where \bar{R} is the average of frictional resistance on the surface of particles, \bar{P} is the average contact force and $\bar{\mu}$ is the average coefficient of friction on the contact surfaces.

Concerning rotating resistance between particles, Marsal showed that the shape of particles and the number of contacts between particles are significant parameters on the rolling resistance. The ellipsoid and angular particles can show more rotating resistance than spherical particles because they have more difficulty in rotating while particles are confined with each other.

6.2.2 Void ratio and strength of broken rock

Void ratio is an aspect of density and it makes sense that density and strength have relationship. Therefore, the void ratio and strength of broken rock can have an inverse relationship. Broken rock with low void ratio presents more density and higher strength. Mogami (1969) introduced Equation (6-2) and (6-3) to calculate the internal friction angle of broken rock through direct shear box test and triaxial compression test, respectively:

$$\sin \phi = \frac{k}{1 + e} \quad (6-2)$$

$$\sin \phi = \frac{k_1}{2(1 + e) + k_1} \quad (6-3)$$

Where ϕ is internal friction angle, k and k_1 are constant parameters, and e is void ratio

In the proposed equations by Mogami, the internal friction angle has an inverse relationship with void ratio. Therefore, the dense broken rock has a larger internal friction angle and higher shear strength than loose broken rock based on Mogami equations. The triaxial test results in this research show an inverse relationship between void ratio and strength of broken rock.

The distribution of void spaces between solid particles has been investigated in applied mathematics as the packing problem. Gray (1968), Donev (2007) and Delaney (2010) show that the shape of particles plays an important role on the packing fraction. The packing density or packing fraction is determined by using Equation (5-4):

$$D_p = \frac{V_p}{V_T} \quad (6-4)$$

Where V_p is the volume of solid particles and V_T is total volume of container

Delaney (2010) illustrated that packing density is decreased by increasing the aspect ratio of particles. Figure 6-2 shows the relationship between the aspect ratio of particles and packing density at different oblate. Delaney used Equation (6-5) to define the shape of particles:

$$\left(\frac{x}{a}\right)^m + \left(\frac{y}{b}\right)^m + \left(\frac{z}{c}\right)^m = 1 \quad (6-5)$$

Where a , b and c are the radius at x , y and z direction, respectively, and m is shape parameter that defines the curvature of the particle.

Table 6-1 shows the 2D particle geometry at different aspect ratios and different shape parameters (m).

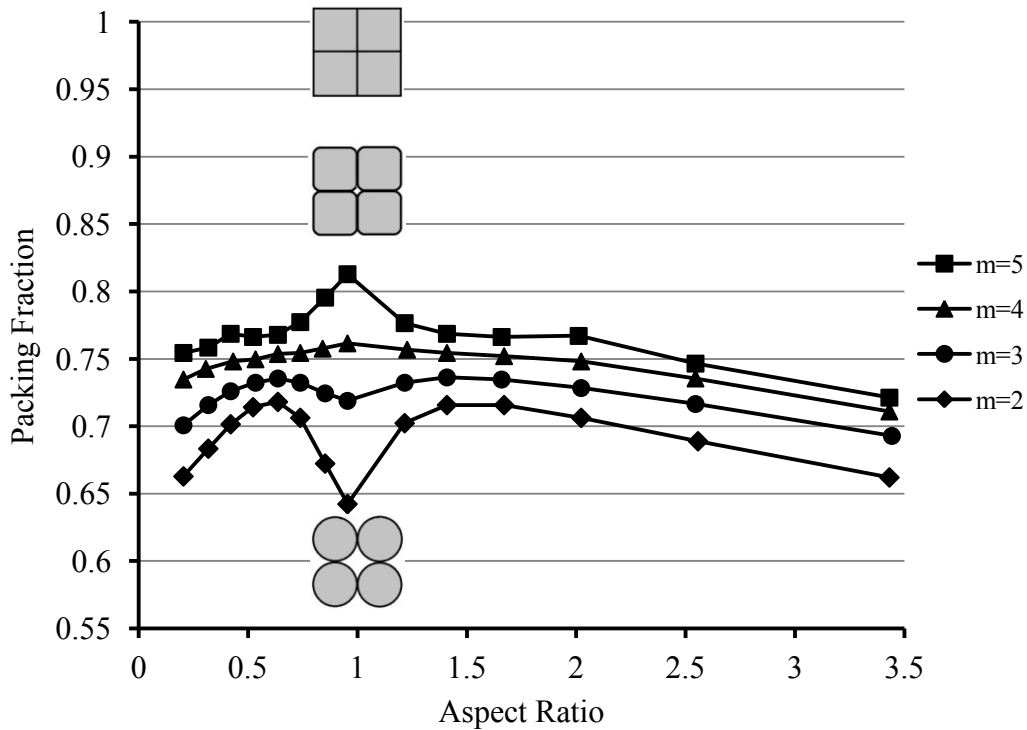






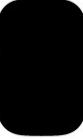




Figure 6-2- Relationship between the aspect ratio of particles and packing density at different shape parameters (m), this figure was adapted from Delaney (2010).

The packing density is very sensitive to shape parameters (m) at aspect ratio equal to one. The geometry of particles that have aspect ratio equal to one, change from spherical to cubic shape by increasing the shape parameter (m) value from 2 to infinity. Therefore, the packing density changes sharply from 0.63 to 1 by changing the geometry from spherical to cubic shape at aspect ratio equal to one.

Table 6-1- 2D particle geometry at different aspect ratios and different shape parameters (m).

		Aspect Ratio		
		1.5	2	2.5
m	2			
	2.8			
	4			

All figures in Table 6-1 were analyzed with code developed for this research using MATLAB, and form index and angularity index of the figures were determined. The results show that form index has a direct relationship with the aspect ratio of particles. In addition, angularity index has a positive affinity with shape parameter (m). Figure 6-3 illustrates the relationship between form index and aspect ratio at different shape parameter (m). It is clear that there is direct relationship between form index and aspect ratio; therefore, it can be argued that an increase in form index affects the packing density and decreases it.

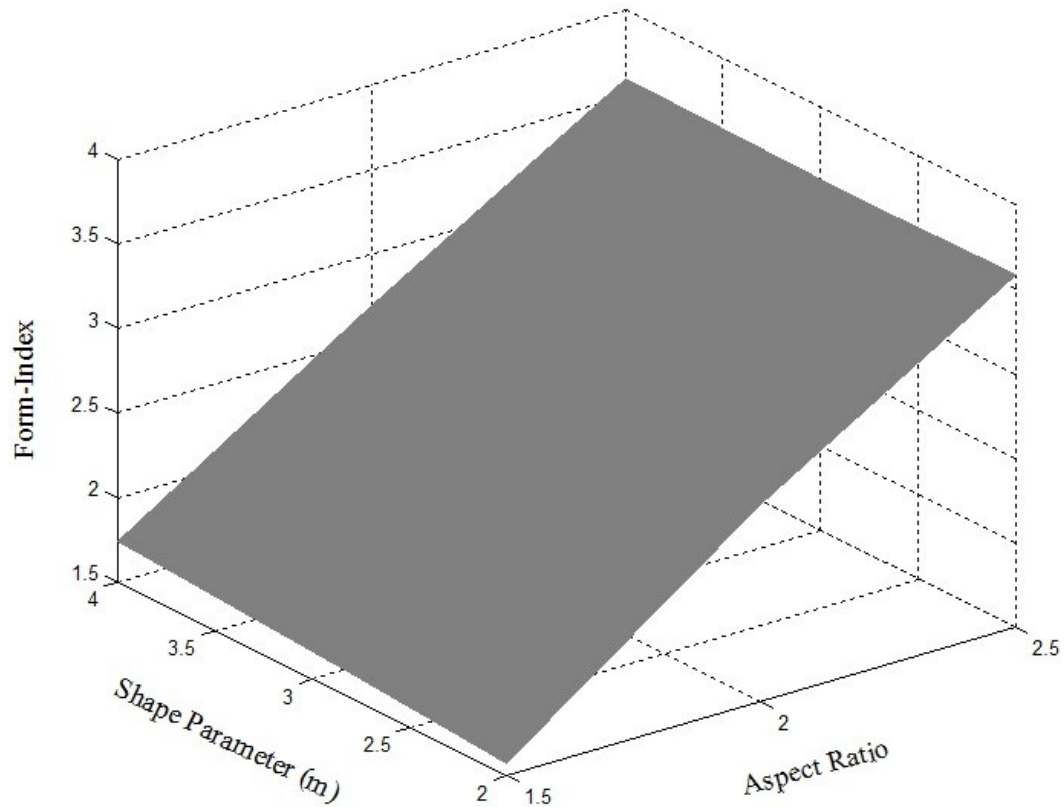


Figure 6-3- Relationship between form index and aspect ratio at different shape parameter (m)

Figure 6-4 shows the relationship between angularity index and shape parameter (m). The angularity index and shape parameter (m) have positive affinity. Therefore, based on Figure 6-2, an increase in angularity index can increase the packing density.

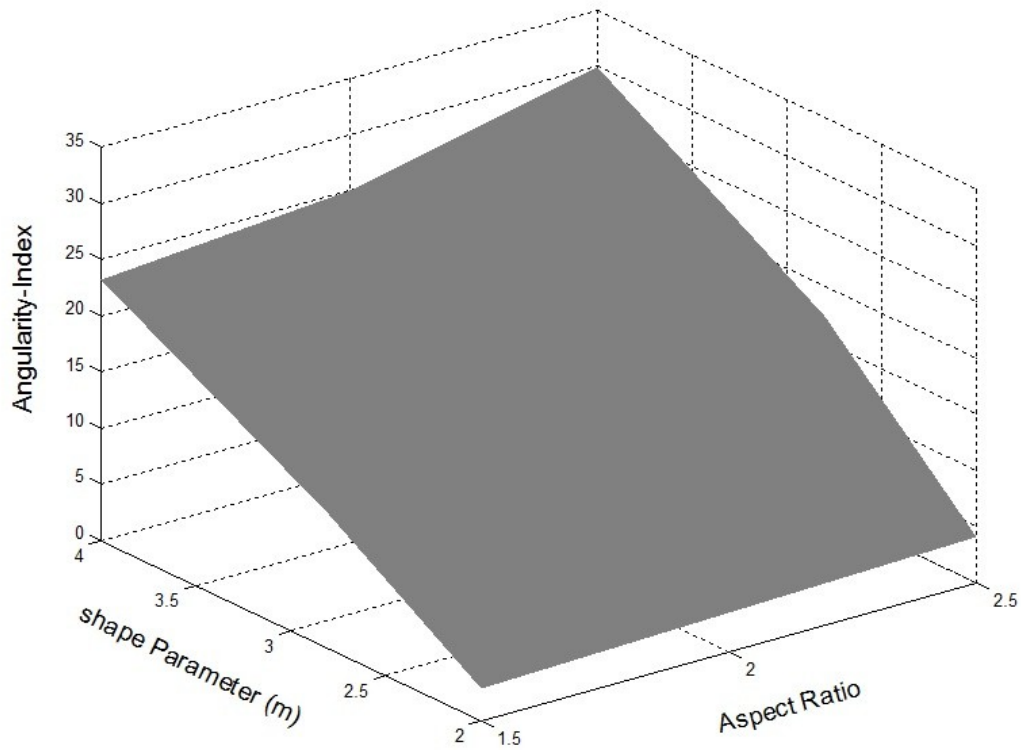


Figure 6-4- Relationship between angularity index and shape parameter (m) at different aspect ratio

On the other hand, the void ratio of broken rock and packing density are related. If the particles are completely solid in broken rock, then the volume of particles and volume of solids are equal ($V_p=V_s$), and Equation (6-6) expresses the relationship between void ratio of broken rock and packing density. Therefore, the form index and angularity index can affect the void ratio of broken rock. An increase in form index can decrease packing density and consequently increases the void ratio, while angularity index increase may decrease the void ratio of broken rock:

$$D_p = \frac{1}{1+e} \quad (6-6)$$

Where D_p is the packing density and e is void ratio of broken rock

6.2.3 Dilation of broken rock

The tendency of granule material such as broken rock to dilation is an important behavior that is observed on broken rock deformation. The volume of broken rock is expanded under compressive loading. The particles of broken rock can show different behavior. For example, particles can slide on the surface, roll on the other particle, or break to different parts. These behaviors define the volume change of broken rock and consequently the dilation under compressive loading. The volume deformation of broken rock is affected by packing and geometry of particles. Therefore, dilation of broken rock is a function of particles geometry and packing of broken rock. On the other hand, the strength of broken rock is a function of confining pressure, dilation and void ratio (Equation (6-7) and (6-8));

$$\text{Dilation} = f_1(\text{Geometry, Packing}) \quad (6-7)$$

$$\sigma_{1p} = f_2(\sigma_3, \text{Dilation, void Ratio}) \quad (6-8)$$

Therefore, particle geometry (form index and angularity index) will affect the strength of broken rock. Figure 6-5 is a conceptual figure that illustrates the relationship between the ratio of major to minor principle stress and confining pressure. It also shows the relationship between dilation angle and confining pressure.

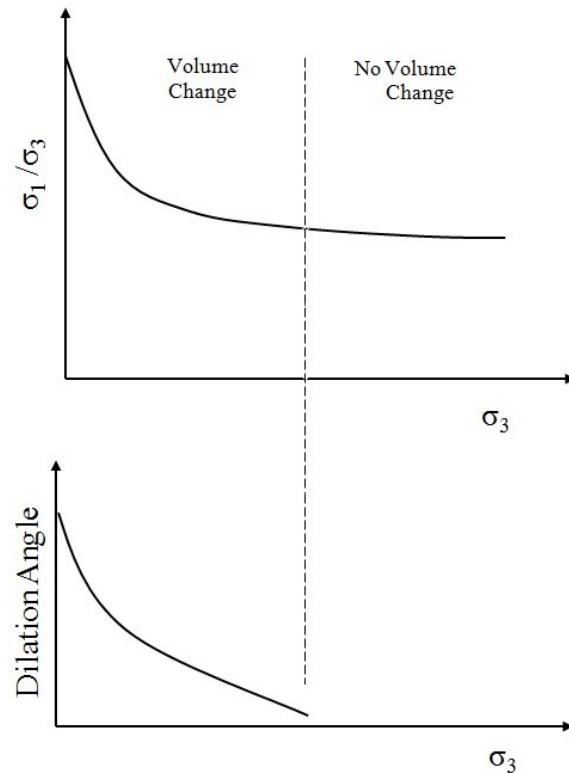


Figure 6-5- Conceptual figure shows the relationship between dilation angle and confining pressure

The effect of particle geometry parameters on the strength of broken rock is expected whereas the impact of particles shape on the dilation of broken rock is certain. However, the results of conducted triaxial compression tests on the broken rock in this research do not show a strong relationship between particle geometry characteristics and the strength of broken rock. The following reasons explain why the results of tests in this research cannot quantify the strength of broken rock as a function of particle shape while the effect of particle shape on the strength of broken rock is a matter of common sense.

1. The summarized shape characteristics of specimens in Table 4-1 show that the parameters range are small. Therefore, the shape parameters of specimens do not have substantial difference with each other to detect a

difference in the test results. The texture of specimens (texture parameter and standard deviation of intensity) is almost the same because all of the specimens were prepared from one broken rock type. Preparing specimens of different rock types may result in a difference in the texture of broken rock specimen.

The specimens were prepared of crushed rock; therefore, the particles had limited shape and angularity. For example, preparing a specimen with spherical particles and another specimen with ellipsoid particles was impossible in practice while the source of all crushed particles was one rock type that was crushed by one type of crusher.

2. There are too many measured variables for each specimen. Void ratio, form, angularity, texture, size of particles and confining pressure were measured variables for each specimen. Whereas, preparing some specimens with only one variable change was impossible. For example, preparing some specimens with different angularity but constant void ratio, form, particles size and texture was impossible. Therefore, detecting the effect of angularity change on the test results while the other parameters were not constant was impossible. Considering the small range of shape parameters, this problem is very important. The effects of different variables were mixed together and detecting the effect of each variable on the test result was difficult. The confining pressure was the only variable that was completely controlled in each test.
3. The specimens were prepared of sandstone with 32 MPa unconfined compressive strength. Because its grains were very fine, and we can assume it is a continuous rock and thus neglect the effect of grains in particles. An intact rock with 32 MPa unconfined compressive strength is a moderate strength rock. The strength of intact sandstone can be another reason. The effect of particle shape on the broken rock with strength particles is greater than effect on moderate and weak particles. However,

the particles formed of high strength intact rock may have more sharp corners to puncture the rubber membrane and more problems in the triaxial test.

4. Another reason can be the number of conducted triaxial tests. More tests may better determine the effect of particle shape on the strength of broken rock. Not only is determining the particle shape characteristics of each specimen by image processing time consuming, but premature failed tests are another problem in triaxial test on broken rock. Rubber membrane punctured by a sharp particle was an important problem in the triaxial test on broken rock. A new membrane made of mixed neoprene and latex was used that was more resistant to puncture than a latex membrane but preventing puncturing by sharp particles was difficult.
5. The errors in experimental tests can be another reason to reduce the detected effect of particles shape characteristics on the strength of broken rock while the variation range of particles shape parameters in the specimens are small. The source of error can be a measurement error, equipment accuracy error, rubber membrane error and image processing error.
6. The particles shape characteristics can have multiple impacts on the strength of broken rock. For example, an increase in the form index of a particle may increase the strength of a broken rock by enhancing the particle rolling resistance. On the other hand, an increase in the form index of a particle can decrease the packing density and increase the void ratio, and finally it can decrease the strength of broken rock. Therefore, the deterministic discussion about the effect of particle shape on the strength of broken rock is difficult and a probabilistic discussion may work better.

6.3 Conclusions

Triaxial tests have been conducted on specimens of broken rock at different confining pressures, and the results were analyzed to investigate the effect of particles shape characteristics on the strength of broken rock. The results show that confining pressure and void ratio have a significant effect on the strength of broken rock while particle shape characteristics can affect frictional resistance of particles and void ratio of broken rock. Results during the course of this research are summarized below.

- Membrane pressure correction, based on Compression Shell Theory, for Neoprene/Latex and Latex membranes was less than 5% of axial strength and is negligible.
- Membrane pressure correction, calculated by Hoop Tension Theory, for Neoprene/Latex and Latex membranes was less than 5% of axial strength and is negligible.
- Calculated lateral membrane correction by numerical modeling for Neoprene/Latex and Latex membranes is low and negligible.
- The representative part, a quarter of the specimen and prepared through the method mentioned in Chapter 4, presents the geometry of sandstone particles with acceptable error.
- To determine the particle size distribution through image processing, a correction coefficient should be applied. The value of the correction coefficient depends on the form-index of particles.
- The specimens have a Rosin-Rammler distribution.
- Increasing the confining pressure enhances the strength of broken rock; this agrees with previous work. However, the relationship between confining pressure and strength of broken rock is nonlinear.

- The strength of broken rock is very sensitive at confining pressure. In an unconfined compression test on broken rock, a small lateral pressure (148 Pa) by very fine latex membrane results in 2.5 kPa axial strength.
- Results show a relationship between $\frac{FI}{AI}$ and $\frac{\sigma_1}{\sigma_3}$ but the correlation is not strong enough to prove a relationship.
- The void ratio and strength of broken rock have negative affinity. An increase in void ratio decreases the strength of broken rock.
- The internal friction angle and confining pressure have negative affinity; therefore, increasing the confining pressure decreases the internal friction angle.
- The internal friction angle and void ratio have negative affinity. An increase in void ratio decreases the internal friction angle.
- Water decreases the frictional strength between particles and reduces the strength of particles for breakage; consequently, water decreases the strength of broken rock even without pore pressure.
- The form-index of particle may have a direct relationship with the void ratio of broken rock and decreases the strength of broken rock while an increase in form-index may increase the strength of broken rock with more rolling resistance.

6.4 Contributions of PhD Research

The main contribution of this research to the body of knowledge is a better understanding of the effect of particle shape parameters on the behavior of broken rock. Another major aspect of this study is specifying existing problems in the triaxial test on broken rock for further research. In addition, the code developed by using MATLAB can be employed to determine the shape parameters of

particles in future research. The results of this study can be useful for some actual design projects:

- Determining the stability of a mine waste dump
- Determining the stability of a mine bench of very weak rock mass
- Improving the production scheduling of caving extraction methods in underground mines
- Reducing the support cost in underground structures with a better understanding of the behavior of broken rock

6.5 Recommendations for Future Research

This study was limited by some assumptions and constraints. The following recommendations could help to better understand the behavior of broken rock and provide feasible methods for industrial applications.

- In this research, the image processing technique was used on a 2D photo of particles to determine the geometry of particles while the geometry of particles is a 3D property in reality; therefore, in future work defining the 3D geometry of particles will help to accurately predict broken rock behavior.
- Control of the geometry of artificial particles is high while the shape of actual broken rock is limited by rock type and crushing method; Therefore, triaxial tests on the artificial particles with different shapes can help to determine the behavior of broken rock.
- Research on the effect of particle shape parameters on packing density and void ratio can help to determine the effect of particle shape on the strength of broken rock.
- Probabilistic analysis of particle shape effect on the strength of broken rock may be better than deterministic analysis because particle shape has multiple impacts on the behavior of broken rock.

- Water decreases the frictional strength between particles and decreases the strength of broken rock even without pore pressure. Determining the effect of water on the broken rock strength decreases, requires more testing and further study.
- Previous work shows that the post peak behavior of rock depends on the behavior of broken rock particles after failure; therefore, the investigation on broken rock particle behavior can explain the post peak behavior for rock mass. In this research, the void ratio and strength of broken rock have good correlation. Whereas, the void ratio of rock after failure can be very low. A research about deformation and void ratio change of rock mass after failure can help to better understanding the post peak behavior of a rock mass.
- Investigation the behavior of rail ballast is a good research topic for further research on the strength of broken rock. The initial rail ballast (granite) material is an angular particle; therefore, it can be shaped rounded by using ball mill. The behavior of initial angular ballast and the secondary rounded ballast can be compared to better understanding the effect of shape parameters on the strength of rail ballast.

BIBLIOGRAPHY

- [1] Al-Rousan, T., Masad, E., Tutumluer, E., and Pan, T. (2007). Evaluation of Image Analysis Techniques for Quantifying Aggregate Shape Characteristics. *Construction and Building Materials*, 21 978–990.
- [2] Al-Rousan, T. M. (2004). Characterization of Aggregate Shape Properties Using a Computer Automated System Thesis, Texas A&M University, College Station, Pages 229.
- [3] Arasan, S., Hasiloglu, A. S., and Akbulut, S. (2010). Shape Properties of Natural and Crushed Aggregate using Image Analysis. *International Journal of Civil and Structural Engineering, Volume 1, No 2*, 221-233.
- [4] ASTM. (1972). Test Sieving Methods-447 A. baltimore
- [5] ASTM. (1995). Standard Test Method for Unconfined Compressive Strength of Intact Rock Core Specimens-D2938-95.
- [6] ASTM. (2003). Standard Test Method for Unconsolidated-Undrained Triaxial Compression Test on Cohesive Soils-D2850.
- [7] ASTM. (2004). Standard Test Method for Triaxial Compressive Strength of Undrained Rock Core Specimens Without Pore Pressure Measurements-D2664-04.
- [8] ASTM. (2007). Standard Test Method for Unconsolidated-Undrained Triaxial Compression Test on Cohesive Soils-D2850-03a.
- [9] ASTM. (2008). Standard Practices for Preparing Rock Core as Cylindrical Test Specimens and Verifying Conformance to Dimensional and Shape Tolerances-D4543-08.
- [10] ASTM. (2011). Standard Test Method for consolidated-Undrained Triaxial Compression Test for Cohesive Soils- D4767-11.
- [11] ASTM. (2011). Standard Test Method for Consolidated Drained Triaxial Compression Test for Soils-D7181-11.
- [12] ASTM. (2011). Standard Test Method for Consolidated Undrained Triaxial Compression Test for Cohesive Soils-D4767-11.
- [13] Baldi, G. and Nova, R. (1973). Membrane Penetration Effects in Triaxial Testing. *Journal of Geotechnical Engineering*, 110 (3), 403-420.
- [14] Barrett, P. J. (1980). The shape of rock particles, a critical review. *Sedimentology*, 27, 291–303.

- [15] Bawden, W. F. (2010). Rock Mechanics Conference Invited Presentation Thoughts on Quantitative Field Scale Characterization of Post-failure Rock Mass Conditions and their Influence on Underground Mine Design. in *44th US Rock Mechanics Symposium and 5th U.S.-Canada Rock Mechanics Symposium*. Salt Lake City, UT: American Rock Mechanics Association (ARMA)
- [16] Baxter, D. Y. (2000). Mechanical Behavior of Soil Bentonite Cutoff Walls. Thesis, Virginia Polytechnic Institute and State University, Blacksburg, Pages 392.
- [17] Bieniawski, Z. T. (1967). Mechanism of brittle fracture of rock, Part I, II and III. *Int. J. Rock Mech. Min. Sci.*, 4 14.
- [18] Bieniawski, Z. T. (1967). Stability concept of brittle fracture propagation in rock. *Engineering Geology*, 2 (3), 14.
- [19] Bieniawski, Z. T. (1968). The effect of specimen size on compressive strength of coal. *Int. J. Rock Mech. Min. Sci.*, 5 17.
- [20] Bieniawski, Z. T. (1968). Propagation Of Brittle Fracture In Rock. in *Symposium on Rock Mechanics (USRMS)*. Austin, TX: American Institute of Mining, Metallurgical, and Petroleum Engineers Inc., pp. 20.
- [21] Bieniawski, Z. T., Denkhaus, H. G., and Vogler, U. W. (1969). Failure of fractured rock. *Int. d. Rock Mech. Min. Sci.*, 6 23.
- [22] Bishop, A. W. and Henkel, D. J. (1962). *Measurement of Soil Properties in the Triaxial Test*. Edward Arnold LTD, London.
- [23] Brace, W. F. (1963). A note on brittle crack growth in compression. *Journal of Geophysical Research*, 68 (12), 5.
- [24] Brady, B. H. G. and Brown, E. T. (2004). *Rock Mechanics for underground mining*. Springer,
- [25] Butcher, R. J. (2002). A scoping study method for determining the viability of block caving a hard rock orebody. *Bulletin of Canadian Institute of Mining, Metallurgy and Petroleum*, 95 (N° 1058),
- [26] Cai, M., Kaiser, P. K., Tasaka, Y., and Minami, M. (2007). Determination of residual strength parameters of jointed rock masses using the GSI system. *International Journal of Rock Mechanics & Mining Sciences*, 44 19.
- [27] Cai, M., Kaiser, P. K., Tasaka, Y., and Minami, M. (2007). *Peak and residual strengths of jointed rock masses and their determination for engineering design*. in Proceedings of Proc. 1st Canada-U.S. Rock Mech. Symp., Vancouver,
- [28] Carter, T. G., Diederichs, M. S., and Carvalho, J. L. (2007). A unified procedure for Hoek-Brown prediction of strength and post yield behaviour for rockmasses at the extreme ends of the rock competency scale. in *11th congress of the International society for rock mechanics*. NG Portugal, pp. 4.

- [29] Carter, T. G., Diederichs, M. S., and Carvalho, J. L. (2008). Application of modified Hoek-Brown transition relationships for assessing strength and post yield behaviour at both ends of the rock competence scale. *The Journal of The Southern African Institute of Mining and Metallurgy*, 108 14.
- [30] Carvalho, J. L., Carter, T. G., and Diederichs, M. S. (2007). An approach for prediction of strength and post yield behaviour for rock masses of low intact strength. in *1st Can-US Rock Mech.Symp.* Vancouver, British Columbia, Canada pp. 8.
- [31] Crowder, J. J. and Bawden, W. F. (2006). The estimation of post peak rock mass properties: numerical back analysis calibrated using In situ instrumentation data. *roscience*, pp. 22.
- [32] Crowder, J. J. and Coulson, A. L. (2006). The field-scale rock mechanics laboratory: estimation of post peak parameters and behaviour of fractured rock masses
in *The 41st U.S. Symposium on Rock Mechanics (USRMS)*. Golden, Colorado: American Rock Mechanics Association (ARMA)
- [33] Delaney, G. W. and Cleary, P. W. (2010). The packing properties of superellipsoids. *EPL (Europhysics Letters)*, 89 (3), 34002.
- [34] Diederichs, M. S., Carvalho, J. L., and Carter, T. G. (2007). A modified approach for prediction of strength and post yield behaviour for high GSI rockmasses in strong, brittle ground. in *1st Can-US Rock Mech.Symp.* Vancouver, British Columbia, Canada pp. 8.
- [35] Donev, A., Connelly, R., Stillinger, F. H., and Torquato, S. (2007). Hypoconstrained Jammed Packings of Nonspherical Hard Particles: Ellipses and Ellipsoids. *Phys. Rev. E*, 75 (5), 35.
- [36] Duncan, J. M. and Seed, H. B. (1967). Corrections for Strength Test Data. *Journal of the soil mechanics and foundations divisions*, 93 (SM5), 121-137.
- [37] Farmer, I. W. (1968). *Engineering behaviour of rocks*. Chapman and Hall, New York,
- [38] Fedaa, J. (1982). *Mechanics of Particulate Materials*. Elsevier Science Publishing Company, New York,
- [39] Fletcher, T., Chandan, C., Masad, E., and Sivakumar, K. (2003). Aggregate Imaging System (AIMS) for Characterizing the Shape of Fine and Coarse Aggregates. in *82nd Transportation Research Board Annual Meeting*. Washington, D.C., pp. 31.
- [40] Fox, Z. P. (2011). Critical State, Dilatancy and Particle Breakage of Mine Waste Rock. Thesis, Colorado State University, Fort Collins,

- [41] Freedman, D. and Diaconis, P. (1981). On the histogram as a density estimator:L 2 theory. *Zeitschrift für Wahrscheinlichkeitstheorie und Verwandte Gebiete*, 57 (4), 453-476.
- [42] Frost, J. D. and Evans, T. M. (2009). Membrane Effects in Biaxial Compression Tests. *Journal of Geotechnical and Geoenvironmental Engineering*, 135 (7), 986-991.
- [43] Frydman, S., Zeitlen, J. G., and Alpan, I. (1973). The Membrane Effect in Triaxial Testing of Granular Soils. *ASTM*, 1 (1), 37-41.
- [44] Fumagalli, E. (1969). Tests on Cohesionless Materials for Rockfill Dams. *Journal of Soil Mechanics & Foundations Div.*, 95 (1), 313-330.
- [45] Gates, L. L. (2010). Experimental Evaluation of New Generation Aggregate Image Measurement System. Thesis, Texas A&M University, College Station, Pages 237.
- [46] GolderAssoc. (2012). Pre-feasibility Block Cave Mine Design - Iron Cap Deposit. Golder Associates Ltd,
- [47] Gonzalez, R. C., Woods, R. E., and Eddins, S. L. (2004). *Digital Image Processing Using MATLAB*.
- [48] Gray, W. A. (1968). *The Packing of Solid Particles*. Chapman & Hall, London,
- [49] Griffith, A. A. (1921). The phenomena of rupture and flow in solids. *Philosophical Transactions of the Royal Society of London*, A 221 163–198.
- [50] Gupta, A. and Yan, D. (2006). Mineral processing design and operation: an introduction. *Elsevier*,
- [51] Habte, K. and Bocking, K. (2012). Co-Disposal Practices in Mine Waste Management. Golder Associates,
- [52] Hajiabdolmajid, V. R. (2001). Mobilization of strength in brittle failure of rock. Thesis, Queen's University, Kingston, Canada, Pages 268.
- [53] Henkel, D. J. and Gilbert, G. D. (1952). The Effect Measured of the Rubber Membrane on the Triaxial Compression Strength of Clay Samples. *Géotechnique* 3(1), 20-29.
- [54] Hobbs, D. W. (1966). A study of the behaviour of a broken rock under triaxial compression, and its application to mine roadways. *Int. J. Rock Mech. Min. Sci.*, 3 33.
- [55] Hobbs, D. W. (1970). The behavior of broken rock under triaxial compression. *Int J Rock Mech Min. Sc*, 7 23.
- [56] Hoek, E. (1964). Fracture of Anisotropic Rock. *Journal of the South African Institute of Mining and Metallurgy*, 64 23.

Bibliography

- [57] Hoek, E. (1965). Rock fracture under static stress conditions. Thesis, Cape Town, Cape Town, South Africa, Pages 229.
- [58] Hoek, E. (1966). Rock Mechanics - an introduction for the practical engineer. *Mining Magazine*, 67.
- [59] Hoek, E. (1980). Empirical strength criterion for rock masses. *J. Geotech. Engng Div.*, 106 22.
- [60] Hoek, E. (2001). Rock mass properties for underground mines. *Society for Mining, Metallurgy, and Exploration (SME)*, 21.
- [61] Hoek, E. and Brown, E. T. (1997). Practical estimates of rock mass strength. *Int. J. Rock Mech. Min. Sci.*, 34 (8), 22.
- [62] Hoek, E., Kaiser, P. K., and Bawden, W. F. (1995). *Support of underground excavations in hard rock*. A.A. Balkema, Rotterdam, Netherlands ; Brookfield, VT, USA,
- [63] Holtz, W. G. and Gibbs, H. G. (1956). Triaxial Shear Tests on Pervious Gravelly Soils. *Journal of the Soil Mechanics and Foundations Division*, 82 (1), 22.
- [64] Honkanadavar, N. P., Kumar, N., and Ratnam, M. (2014). Modeling the behaviour of alluvial and blasted quarried rockfill materials. *Geotechnical and Geological Engineering*, 32 1001-1015.
- [65] Hudson, J. A. and Harrison, J. P. (1997). *Engineering rock mechanics*. Elsevier Science, Kidlington,
- [66] Hungr, O., Dawson, R., Kent, A., Campbell, D., and Morgenstern, N. R. (2002). Rapid flow slides of coal-mine waste in British Columbia, Canada. *Geological Society of America Reviews in Engineering Geology*, XV 191-208.
- [67] Hussaini, M. A. (1970). Influence of end restraint and method of consolidation on the drained triaxial compressive strength of crushed Napa basalt. Waterways Experiment Station, Vicksburg, pp. 70.
- [68] Hussaini, M. A. (1971). Plane strain and triaxial compression tests on crushed napa basalt. Waterways Experiment Station, Vicksburg,
- [69] Hussaini, M. A. (1983). Effect of particle size and strain conditions on the strength of crushed basalt. *Canadian Geotechnical Journal*, 20 (4), 12.
- [70] Janaka, G. H. A., Kumara, J., Hayano, K., and Ogiwara, K. (2012). Image Analysis Techniques on Evaluation of Particle Size Distribution of Gravel. *Int. J. of GEOMATE*, 3 (1), 290-297.
- [71] Janoo, V. C. (1998). Quantification of Shape, Angularity, and Surface Texture of Base Course Materials. US Army Corps of Engineers, Cold Regions Research & Engineering Laboratory, pp. 29.

- [72] Joseph, T. G. (2000). Estimation of the post-failure stiffness of rock. Thesis, University of Alberta, Edmonton, Canada, Pages 536.
- [73] Joseph, T. G. and Barron, K. (2003). The post-failure characteristics of rock. *CIM Bulletin*, 96, N° 1070 9.
- [74] Kolbuszewski, J. J. and Frederick, M. R. (1963). *The significance of particle shape and size on the mechanical behaviour of granular materials*. in Proceedings of European Conference on Soil Mechanics and Foundation Engineering, Wiesbaden, pp. 253-263.
- [75] Kovrizhnykh, A. M. (2000). Numerical modeling of rock failure. *Journal of Mining Science*, 36 (2), 8.
- [76] Kuo, C.-Y. and Freeman, R. B. (2000). Imaging Indices for Quantification of Shape, Angularity, and Surface Texture of Aggregates. *Transportation Research Record: Journal of the Transportation Research Board*, 1721 57-65.
- [77] Kusuma, G. J., Shimada, H., Sasaoka, T., Matsui, K., and Nugraha, C. (2012). Physical and Geochemical Characteristics of Coal Mine Overburden Dump, Related to Acid Mine Drainage Generation. *Memoirs of the Faculty of Engineering, Kyushu University*, 72 (2), 23-38.
- [78] Lee, K. L. and Farhoomand, I. (1967). Compressibility And Crushing Of Granular Soil In Anisotropic Triaxial Compression. *Canadian Geotechnical Journal*, 4 (1), 68-86.
- [79] Liang, Z. Z. (2008). Three Dimensional Numerical Modelling of Rock Failure Process. Thesis, North-western University, China,
- [80] Lindström, H. (2010). Rock Property Measurements Using Image Processing. Thesis, KTH Royal Institute of Technology Stockholm, Pages 32.
- [81] Little, D., Button, J., Jayawickrama, P., Solaimanian, M., and Hudson, B. (2003). Quantify Shape, Angularity and Surface Texture of Aggregates Using Image Analysis and Study Their Effect on Performance. Texas Transportation Institute, The Texas A&M University System, College Station, Texas,
- [82] Marsal, R. j. (1969). Frictional Resistance of Granular Soils. in *Seventh International Conference on Soil Mechanics and Foundation Engineering*. Mexico
- [83] Marsal, R. j. (1969). Shear Strength of Rockfill Sample. in *Seventh International Conference on Soil Mechanics and Foundation Engineering*. Mexico
- [84] Marsal, R. j. (1969). A statistical Model of Granular Materials. in *Seventh International Conference on Soil Mechanics and Foundation Engineering*. Mexico
- [85] Marsal, R. J. (1973). Mechanical Properties of Rockfill. *Embankment Dam Engineering*, 12.

Bibliography

- [86] Marschi, N. D., Chan, C. K., and Seed, H. B. (1972). Evaluation of Properties of Rockfill Materials. *Journal of the Soil Mechanics and Foundations Division*, 98 (1), 20.
- [87] Martin, C. D. (1993). The strength of massive Lac du Bonnet Granite around underground openings. Thesis, University of Manitoba, Winnipeg, Manitoba, Canada, Pages 304.
- [88] Martin, C. D. and Chander, N. A. (1994). The progressive fracture of Lac du Bonnet granite. *Int. J. Rock. Mech. Min. Sci. & Geomech.*, 31 (6), 13.
- [89] Masad, E. (2001). Review Of Imaging Techniques For Characterizing The Shape of Aggregates Used in Asphalt Mixes. in *International Center for Aggregates Research 9th Annual Symposium: Aggregates - Concrete, Bases and Fines*. Austin, Texas
- [90] Masad, E. (2003). The Development of a Computer Controlled Image Analysis System for Measuring Aggregate Shape Properties. National Cooperative Highway Research Program NCHRP-IDEA Project 77, Transportation Research Board, National Research Council, Washington, D.C, Final Report, pp. 113.
- [91] Masad, E., Al-Rousan, T., Button, J., Little, D., and Tutumluer, E. (2007). Test Methods for Characterizing Aggregate Shape, Texture, and Angularity. National Cooperative Highway Research Program, WASHINGTON, D.C., NCHRP Report 555,
- [92] Masad, E., Olcott, D., White, T., and Tashman, L. (2001). Correlation of Fine Aggregate Imaging Shape Indices with Asphalt Mixture Performance. Transportation Research Record 1757. Transportation Research Board, National Research Council, Washington, D.C, pp. 148-156.
- [93] Masad, E. A., Little, D. N., Tashman, L., Saadeh, S., Al-Rousan, T., and Sukhwani, R. (2003). Evaluation of Aggregate Characteristics Affecting HMA Concrete Performance. Texas Transportation Institute, Texas,
- [94] Mogami, T. (1969). *On the Angle of Internal Friction of Rockfill Materials*. in Proceedings of Contributions and Discussions on Mechanical Properties of Rockfill and Gravel Materials, Mexico
- [95] Mogi, K. (1971). Fracture of flow of rocks under high triaxial compression. *Journal of Geophysical Research*, 76 (5), 15.
- [96] Molenkamp, F. and Luger, H. J. (1981). Modelling and minimization of membrane penetration effects in tests on granular soils. *Géotechnique*, 31 (4), 471-486.
- [97] Moraes, R. (2011). Numerical codes used to model failure in large fractured scale and jointed rock slopes in hydropower projects. in *6th international conference on dam engineering*. C.Pina, E.Portela, pp. 18.

- [98] Noor, M. J., Nyuin, J. D., and Derahman, A. (2012). A graphical method for membrane penetration in triaxial tests on granular soils. *Journal - The Institution of Engineers, Malaysia*, 73 (1), 23-30.
- [99] Park, N. (2006). Discrete element modeling of rock fracture behavior: fracture toughness and time-dependent fracture growth. Thesis, University of Texas, Austin, Pages 292.
- [100] Pourghahramani, P., Azimi, E., and Asadlo, D. (2010). Effect of ore type on the Sungun SAG mill performance and finding a resolution for increasing circuit throughput. Sahand University of Technology, Faculty of Mining Engineering,
- [101] Price, A. M. (1979). The effect of confining pressure on the post-yield deformation characteristics of rocks. Thesis, University Of Newcastle-Upon-Tyne, Pages 285.
- [102] Rajendra, P. T. and Rao, K. S. (2006). Post failure behaviour of a rock mass under the influence of triaxial and true triaxial confinement. *Engineering Geology*, 84 18.
- [103] Ramana, K. V. and Raju, V. S. (1981). Constant-Volume Triaxial Tests to Study the Effects of Membrane Penetration. *ASTM*, 4 (3), 117-122.
- [104] Ribacchi, R. (2000). Mechanical Tests on Pervasively Jointed Rock Material: Insight into Rock Mass Behaviour. *Rock Mech. Rock Engng.*, 33 (4), 24.
- [105] Rochelle, P. L., Leroueil, S., Trak, B., Leroux, L. B., and Tavenas, F. (1988). Observational Approach to Membrane and Area Corrections in Triaxial Tests. *ASTM*, 715-731.
- [106] Sainsbury, B., Pierce, M., and Ivars, D. M. (2008). Simulation of rock mass strength anisotropy and scale effects using a Ubiquitous Joint Rock Mass (UJRM) model. in *Proceedings of the 1st international FLAC/DEM symposium on numerical modelling*, C. D. a. P. Cundall, Ed. Minneapolis Itasca Consulting Group, pp. 10.
- [107] Stefanizzi, S., Barla, G., Kaiser, P. K., and Grasselli, G. (2008). Numerical modeling of rock mechanics tests in layered media using a finite / discrete element approach. in *The 12th International Conference of International Association for Computer Methods and Advances in Geomechanics (IACMAG)*. Goa, India: I, pp. 6.
- [108] Swift, G. A. (2007). Characterization of Coarse Aggregate Angularity Using Digital Image Processing. Thesis, University of Missouri, Columbia, USA, Pages 82.
- [109] Tutumluer, E., Rao, C., and Stefanski, J. A. (2000). Video Image Analysis of Aggregates. FHWA-IL-UI-278, Civil Engineering Studies UILU-ENG-2000-2015, University of Illinois Urbana-Champaign, Urbana, IL, Final Project Report, pp. 162.

Bibliography

- [110] Valley, B., Suorineni, F. T., and Kaiser, P. K. (2010). Numerical analyses of the effect of heterogeneities on rock failure process. in *44th US Rock Mechanics Symposium and 5th U.S.-Canada Rock Mechanics Symposium*. Salt Lake City: American Rock Mechanics Association, ARMA, pp. 10.
- [111] Van, M. (2008). Numerical modelling of brittle fracture and step-path failure: from laboratory to rock slope scale. Thesis, Simon Fraser University, Pages 331.
- [112] Villeneuve, M. C., Diederichs, M. S., Kaiser, P. K., and Frenzel, C. (2009). Constitutive model for numerical modelling of highly stressed heterogeneous massive rocks at excavation boundaries. in *Proceedings of the 3rd CANUS Rock Mechanics Symposium*. Toronto, Canada, pp. 14.
- [113] Wang, L., Lane, D. S., Lu, Y., and Druta, C. (2009). Portable Image Analysis System for Characterizing Aggregate Morphology. *Journal of the Transportation Research Board*, 3-11.
- [114] Wang, L. B., Park, J. Y., and Mohammad, L. N. (2003). Quantification of Morphology Characteristics of Aggregate From Profile Images. in *82nd Transportation Research Board Annual Meeting*. Washington, D.C., pp. 23.
- [115] Wawersik, W. R. and Brace, W. F. (1971). Post-Failure Behavior of a Granite and Diabase. *Rock Mechanics*, 3 25.
- [116] Wills, B. A. (2011). *Wills' mineral processing technology: an introduction to the practical aspects of ore treatment and mineral* Butterworth-Heinemann,
- [117] Wu, S. (2009). Computational simulation of strain localization: from theory to implementation. Thesis, Louisiana Tech University, Lafayette,
- [118] Yeggoni, M., Button, J. W., and Zollinger, D. G. (1994). Influence of Coarse Aggregate Shape And Surface Texture on Rutting of Hot-Mix Concrete. Texas Transportation Institute Report 1244-6, Texas A&M University, College Station, TX,

APPENDIX A

TRIAXIAL TESTS USING HOEK CELL

In the following, triaxial tests on broken rock specimens are provided. The Hoek-Franklin cell was employed to apply the confining pressure. The stress-strain graphs given in Figure A-1 to Figure A-5 have noise because the generated noise by loading frame electromotor affected the load cell; therefore, the recorded data had noise. An extra metal shield around the loading frame electromotor solved the problem and the rest of tests result in figure A-6 to figure A-9 does not have noise.

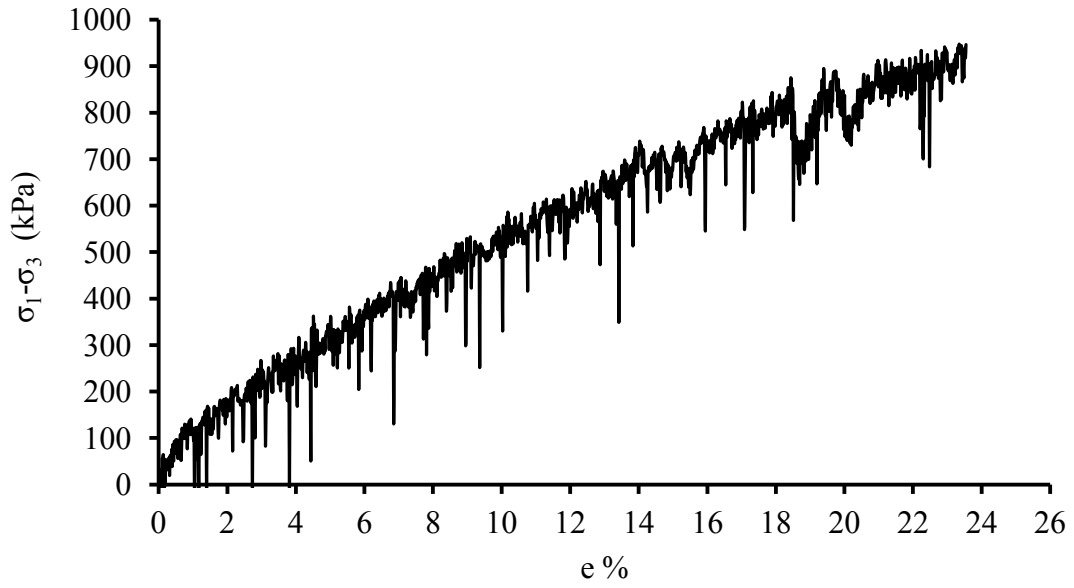


Figure A-1- Triaxial test on broken rock by Hoek-Franklin Cell, with confining pressure set at 414 kPa

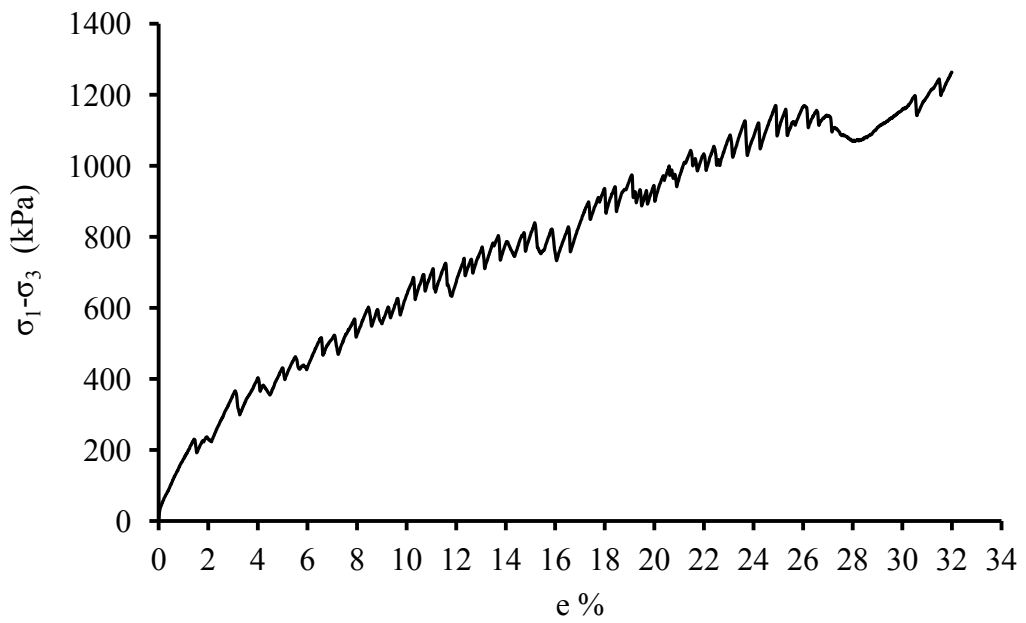


Figure A-2- Triaxial test on broken rock by Hoek-Franklin Cell, with confining pressure set at 690 kPa

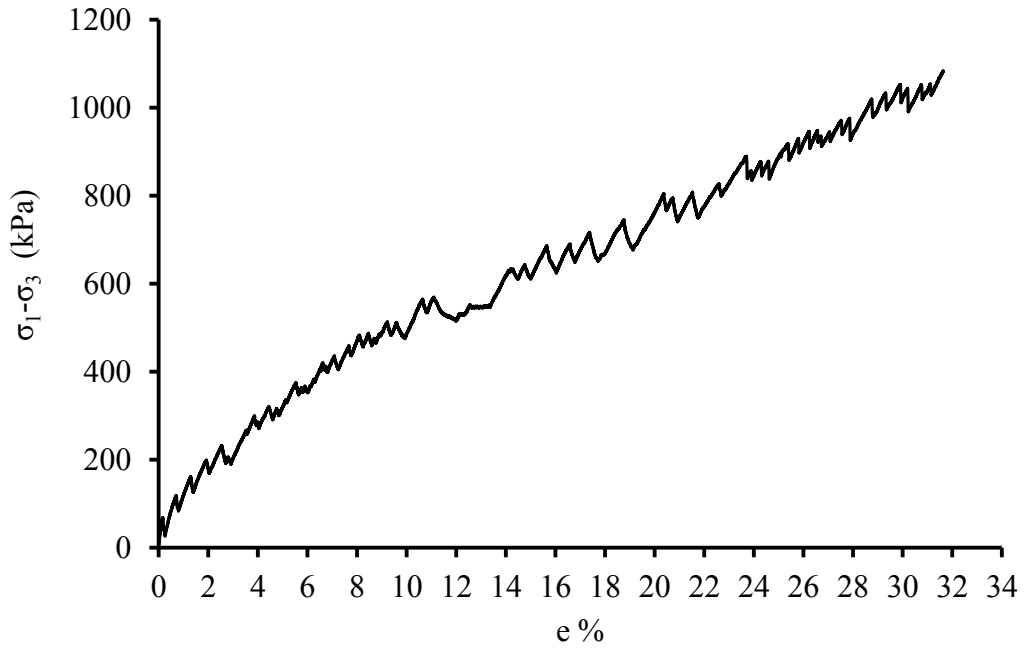


Figure A-3- Triaxial test on broken rock by Hoek-Franklin Cell, with confining pressure set at 345 kPa

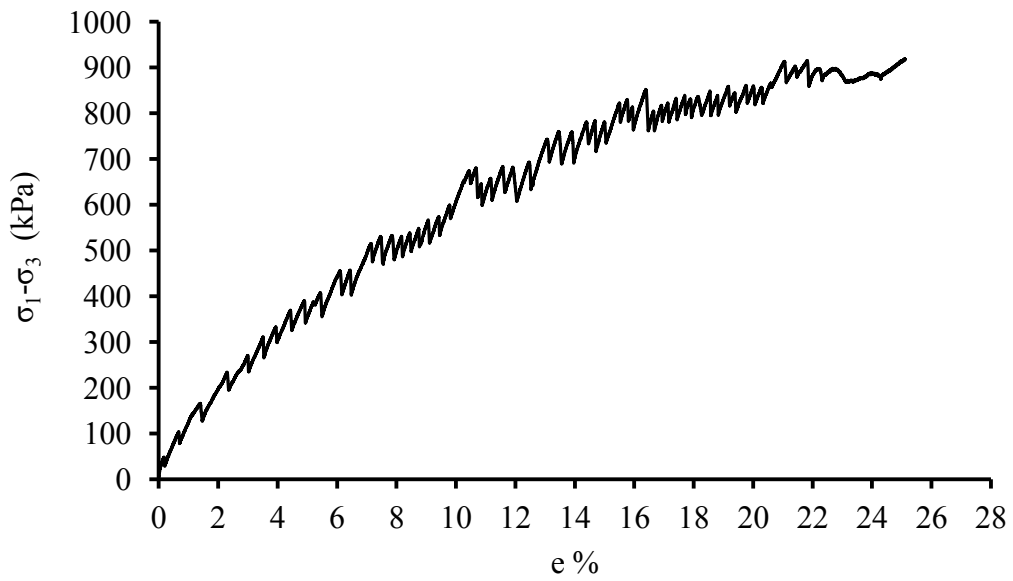


Figure A-4- Triaxial test on broken rock by Hoek-Franklin Cell, with confining pressure set at 620 kPa

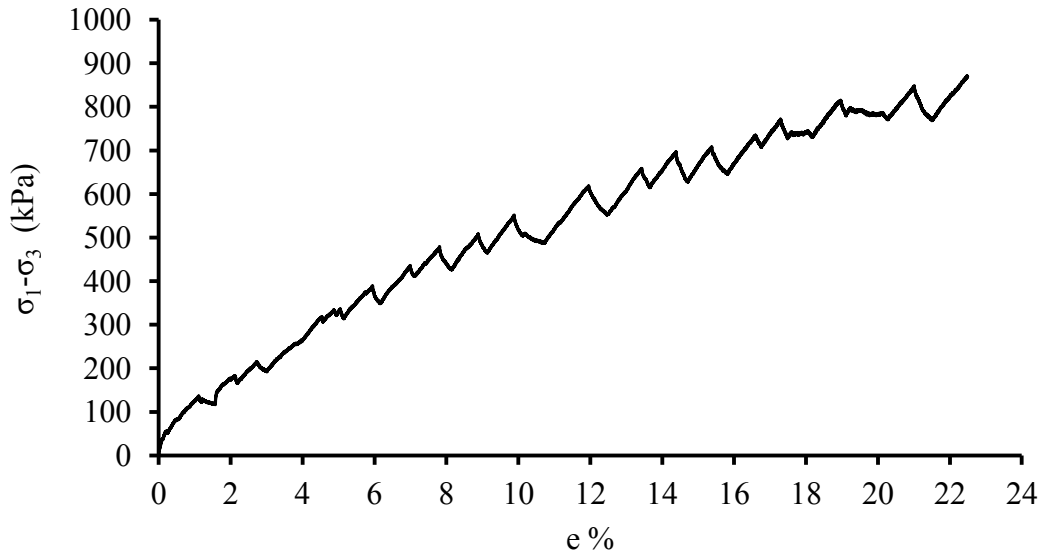


Figure A-5- Triaxial test on broken rock by Hoek-Franklin Cell, with confining pressure set at 345 kPa

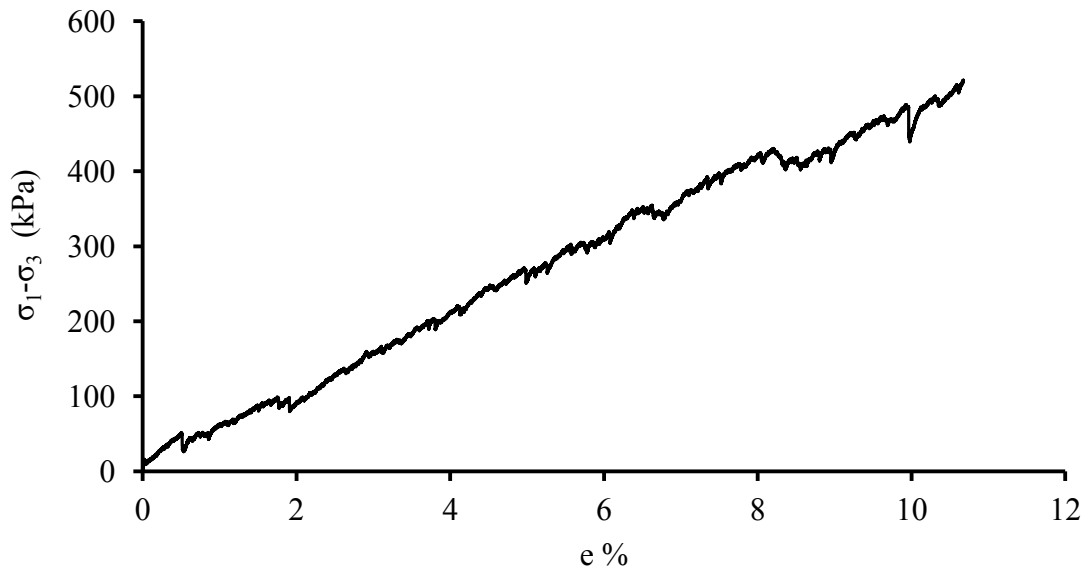


Figure A-6- Triaxial test on broken rock by Hoek-Franklin Cell, with confining pressure set at 207 kPa

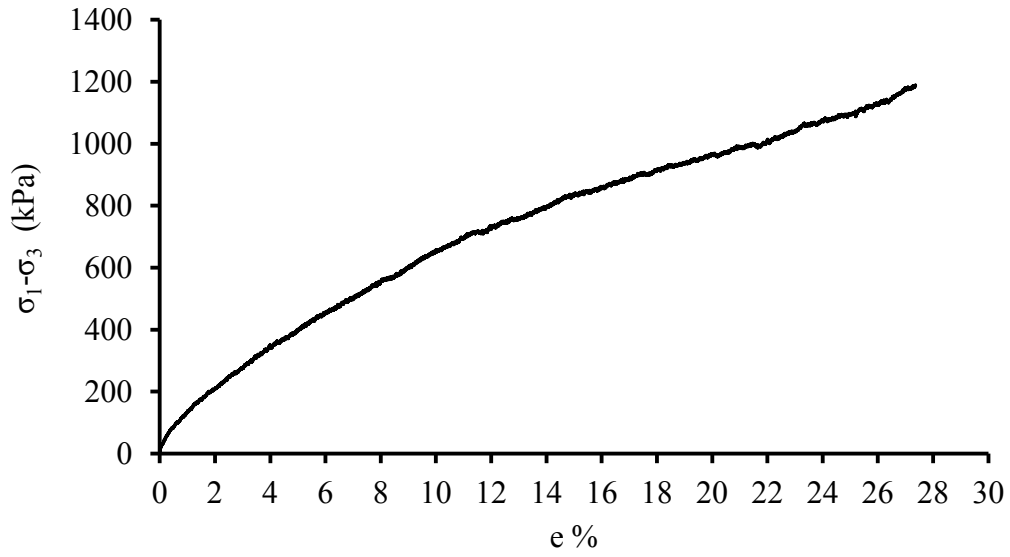


Figure A-7- Triaxial test on broken rock by Hoek-Franklin Cell, with confining pressure set at 345 kPa

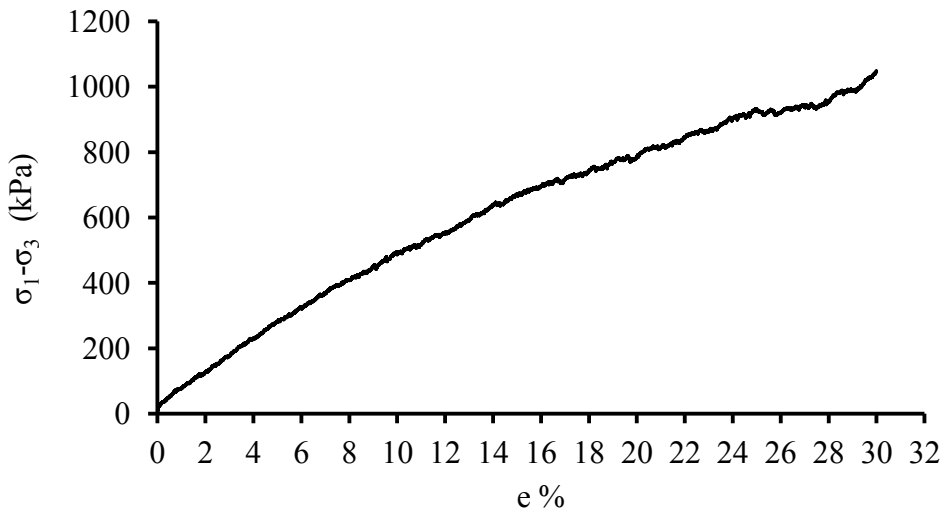


Figure A-8- Triaxial test on broken rock by Hoek-Franklin Cell, with confining pressure set at 275 kPa

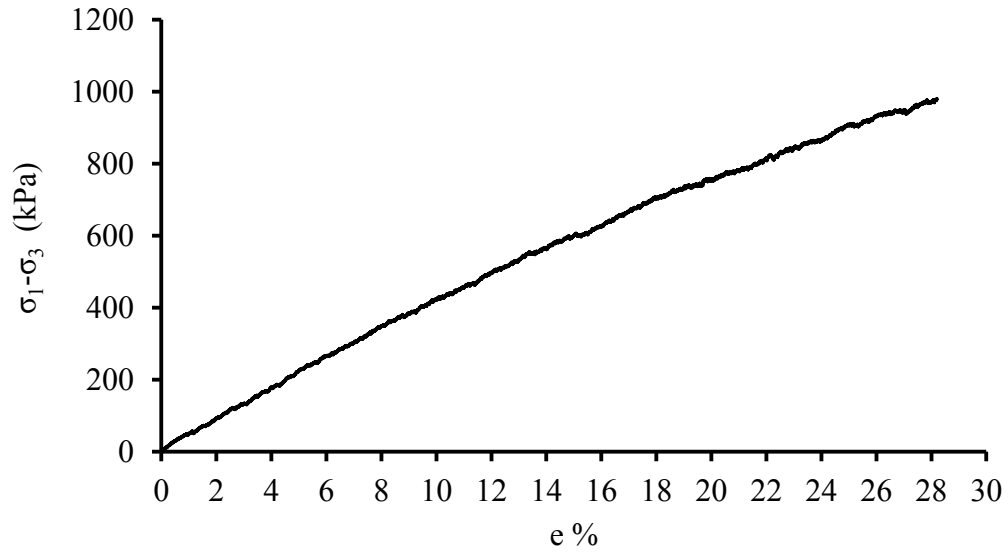


Figure A-9- Triaxial test on broken rock by Hoek-Franklin Cell, with confining pressure set at 138 kPa

APPENDIX B

PREMATURELY FAILED TESTS

The prematurely failed tests because of puncture in membrane during test or eccentric deformation of specimen are provided in this Appendix. The soil cell was employed to apply confining pressure transferred by water. The following data was neglected. Table B-1 is summary of particle shape characteristics of specimens and reason of failure.

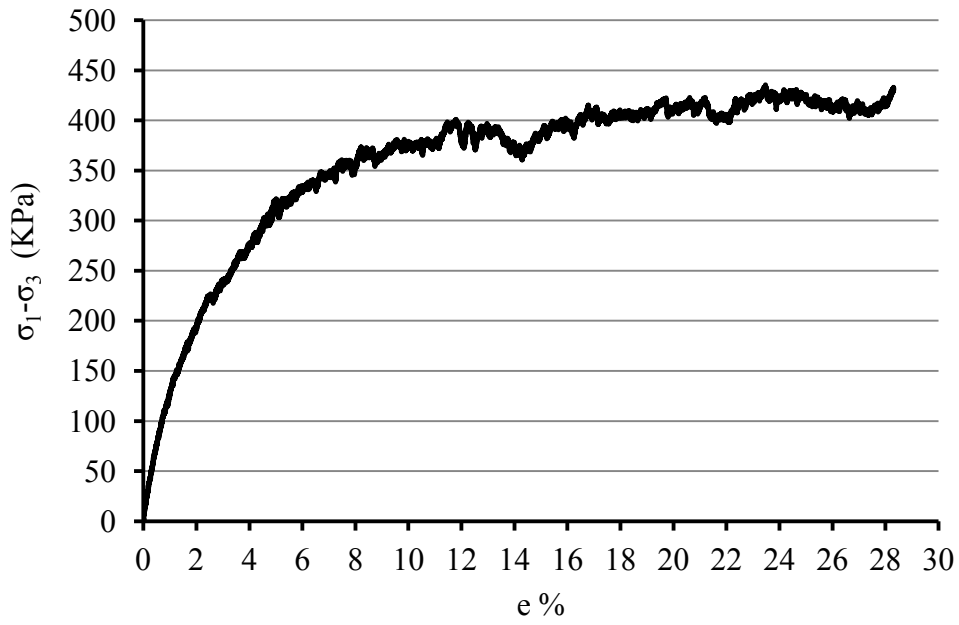


Figure B-1- Prematurely Failed test (Test F1), $\sigma_3 = 68.95$ kPa

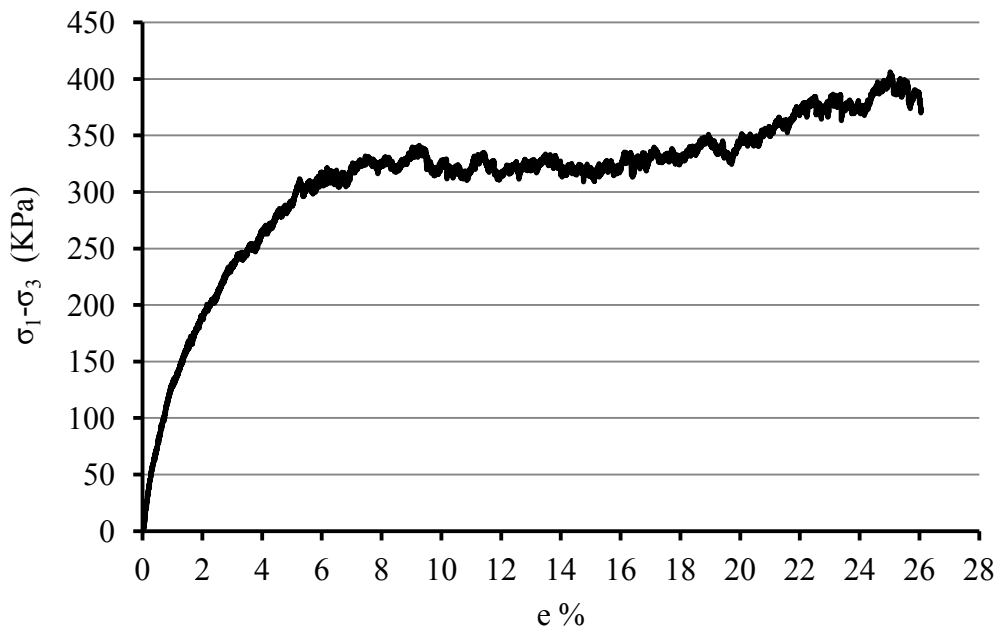


Figure B-2- Prematurely Failed test (Test F2), $\sigma_3 = 68.95$ kPa

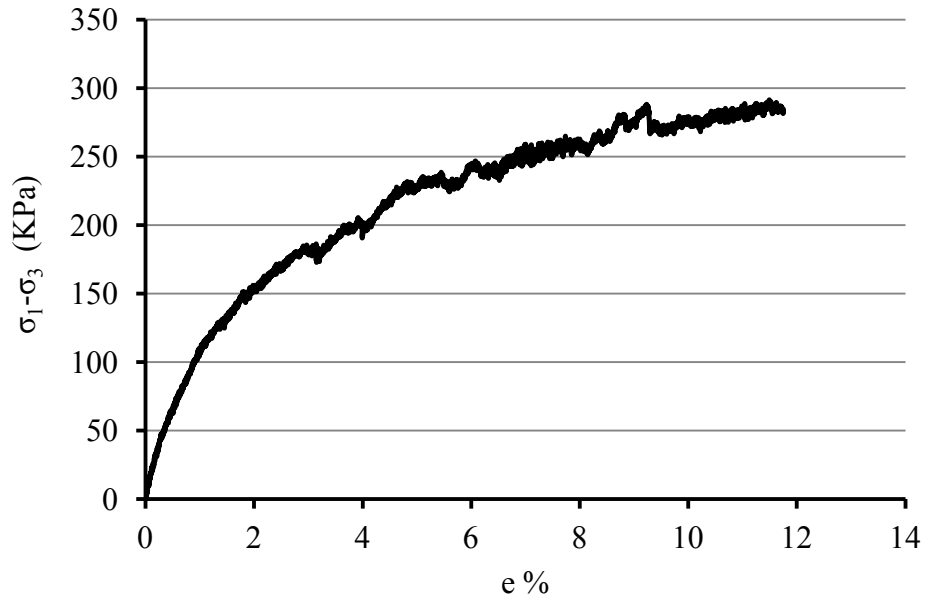


Figure B-3- Prematurely Failed test (Test F3), $\sigma_3 = 68.95$ kPa

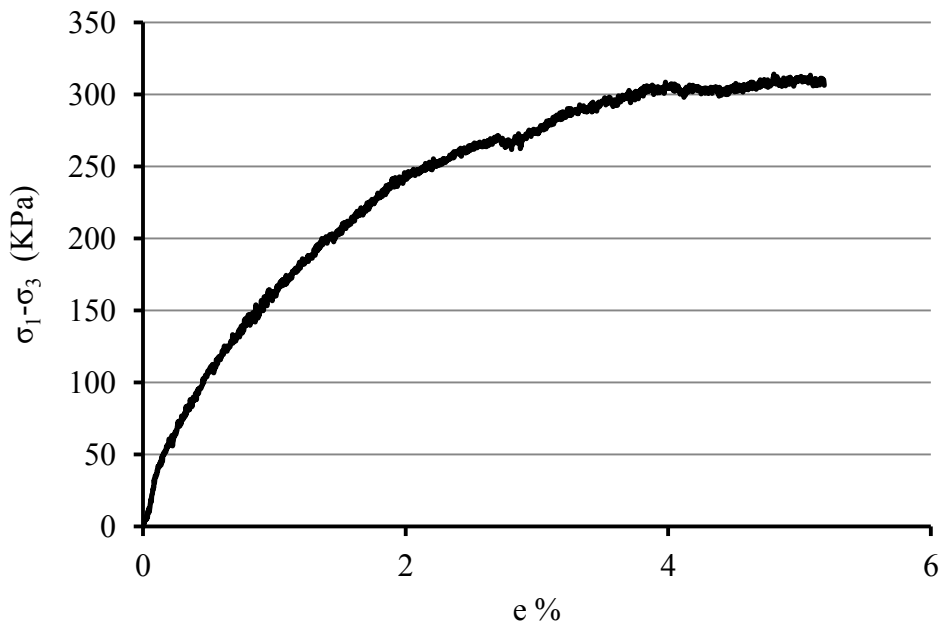


Figure B-4- Prematurely Failed test (Test F4), $\sigma_3 = 68.95$ kPa

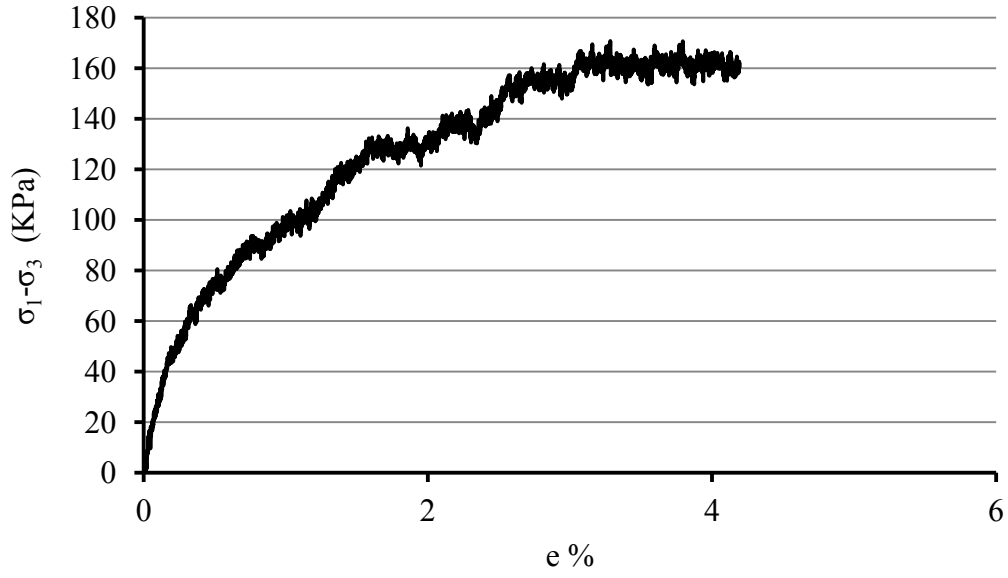


Figure B-5- Prematurely Failed test (Test F5), $\sigma_3 = 34.47$ kPa



Figure B-6- Prematurely Failed test (Test F6), $\sigma_3 = 34.47$ kPa

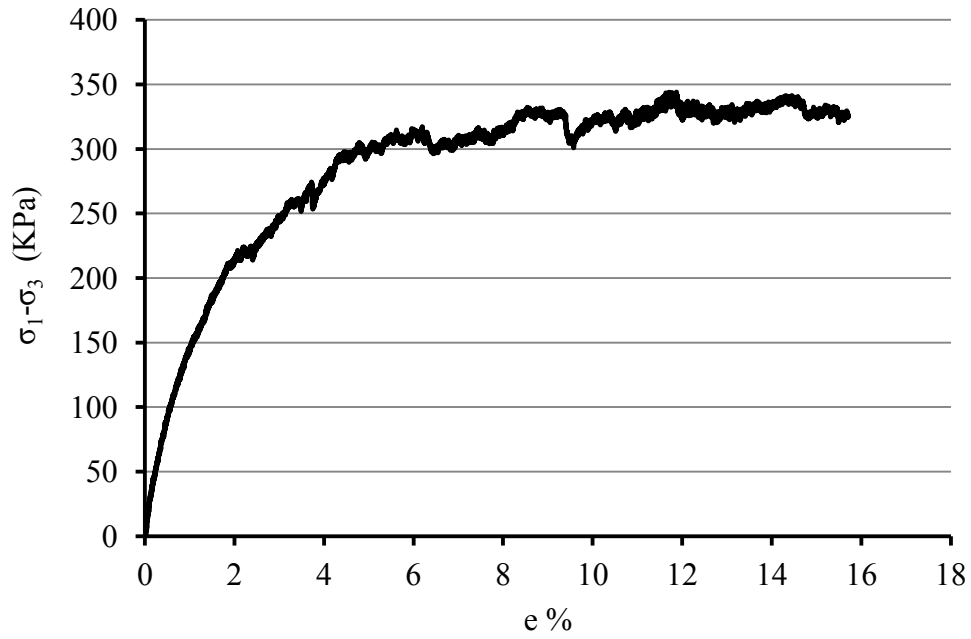


Figure B-7- Prematurely Failed test (Test F7), $\sigma_3 = 137.90$ kPa

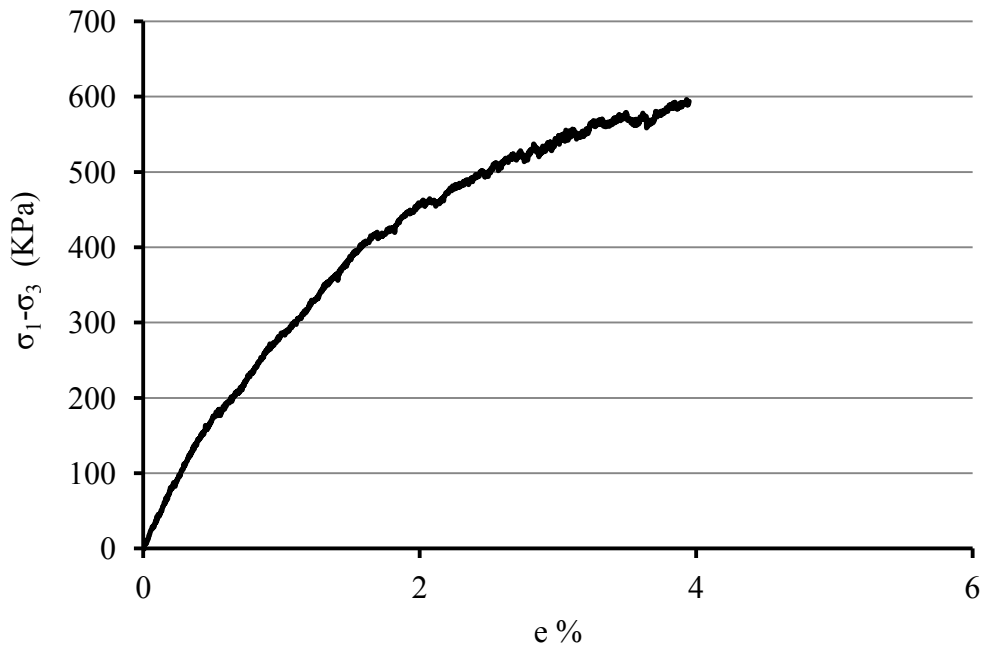


Figure B-8- Prematurely Failed test (Test F8), $\sigma_3 = 137.90$ kPa

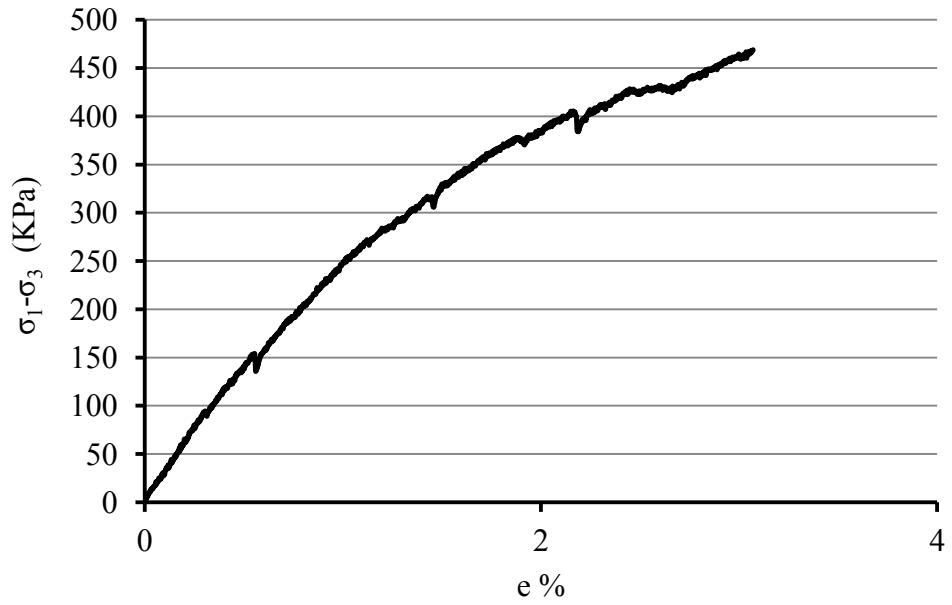


Figure B-9- Prematurely Failed test (Test F9), $\sigma_3 = 137.90$ kPa

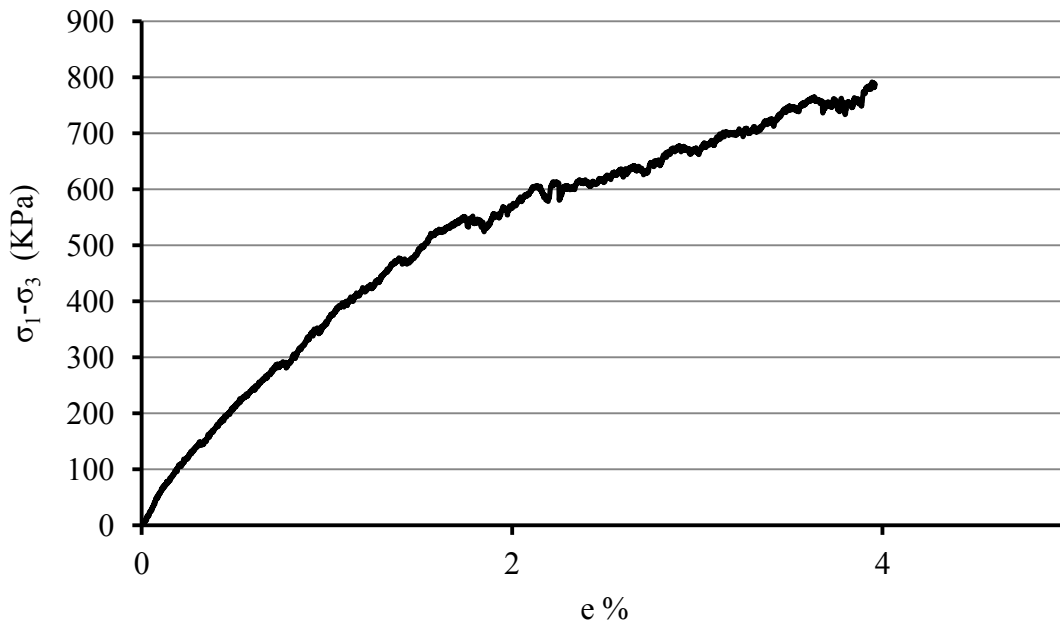


Figure B-10- Prematurely Failed test (Test F10), $\sigma_3 = 275.79$ kPa

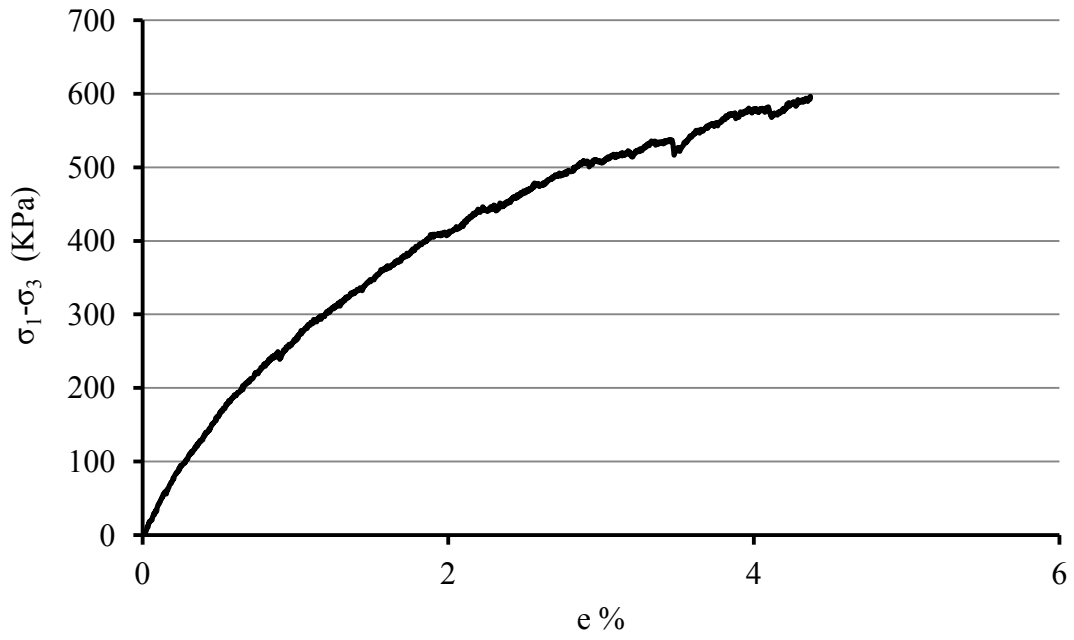


Figure B-11- Prematurely Failed test (Test F11), $\sigma_3 = 275.79$ kPa

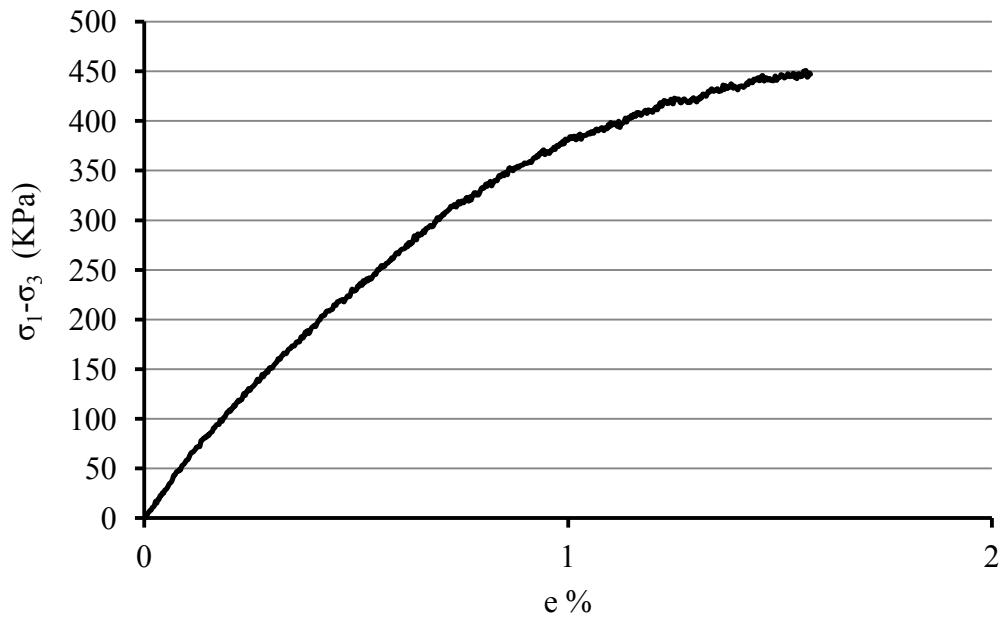


Figure B-12- Prematurely Failed test (Test F12), $\sigma_3 = 275.79$ kPa

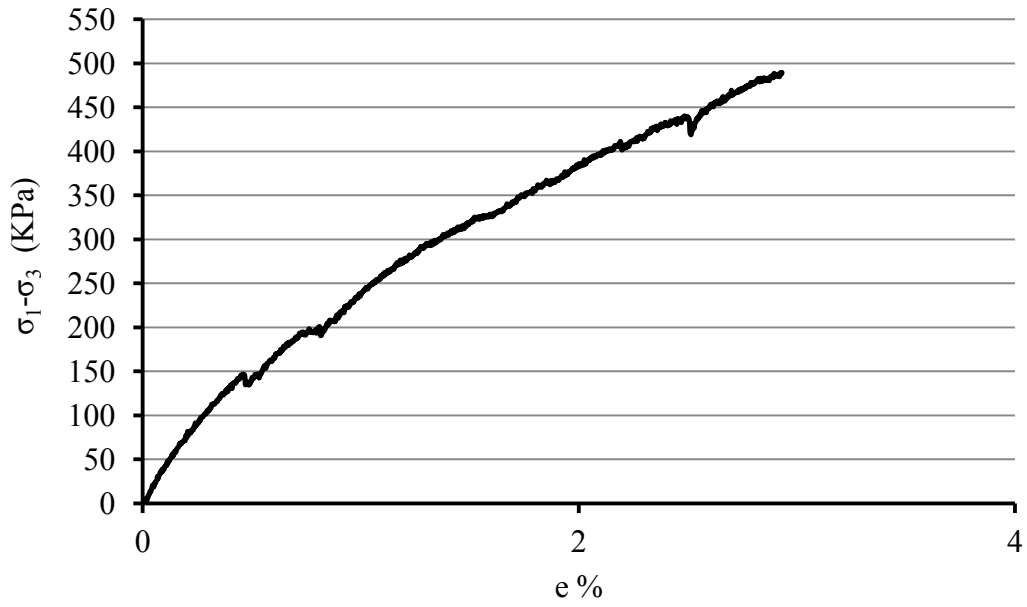


Figure B-13- Prematurely Failed test (Test F13), $\sigma_3 = 275.79$ kPa

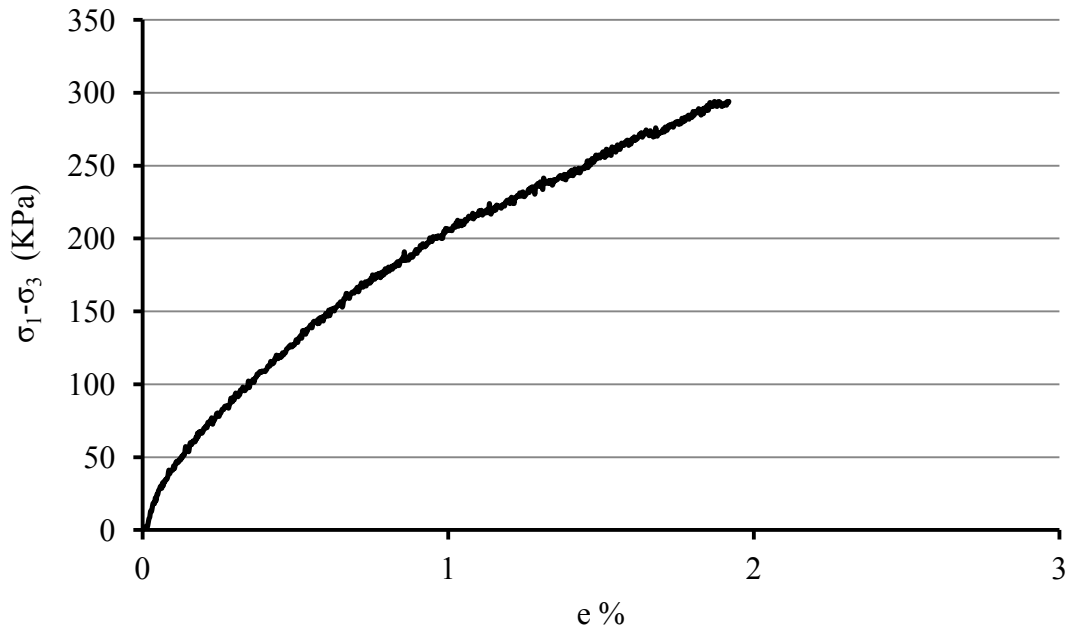


Figure B-14- Prematurely Failed test (Test F14), $\sigma_3 = 275.79$ kPa

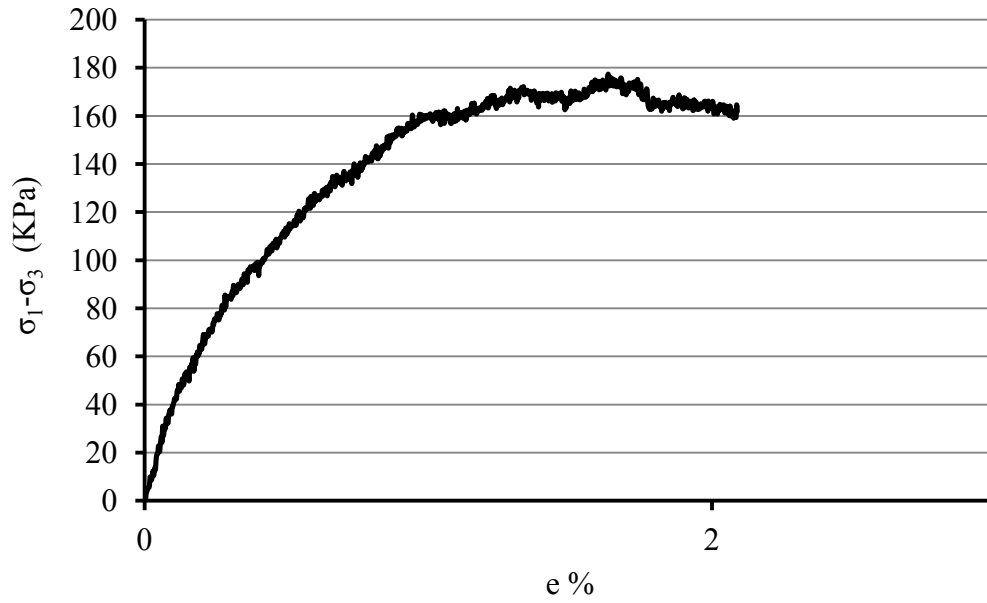


Figure B-15- Prematurely Failed test (Test F15), $\sigma_3 = 206.84$ kPa

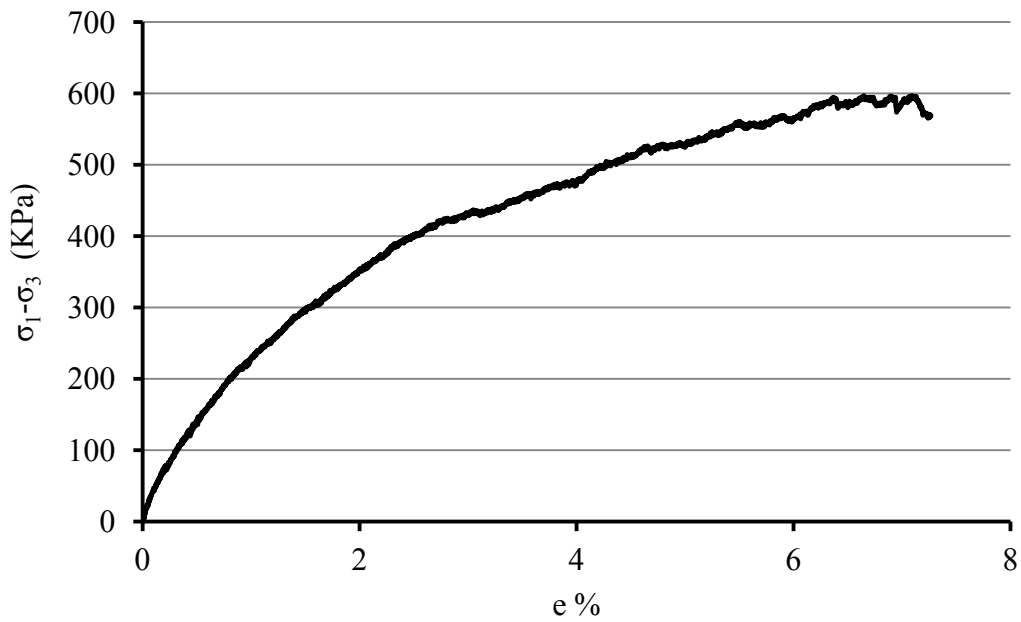


Figure B-16- Prematurely Failed test (Test F16), $\sigma_3 = 206.84$ kPa

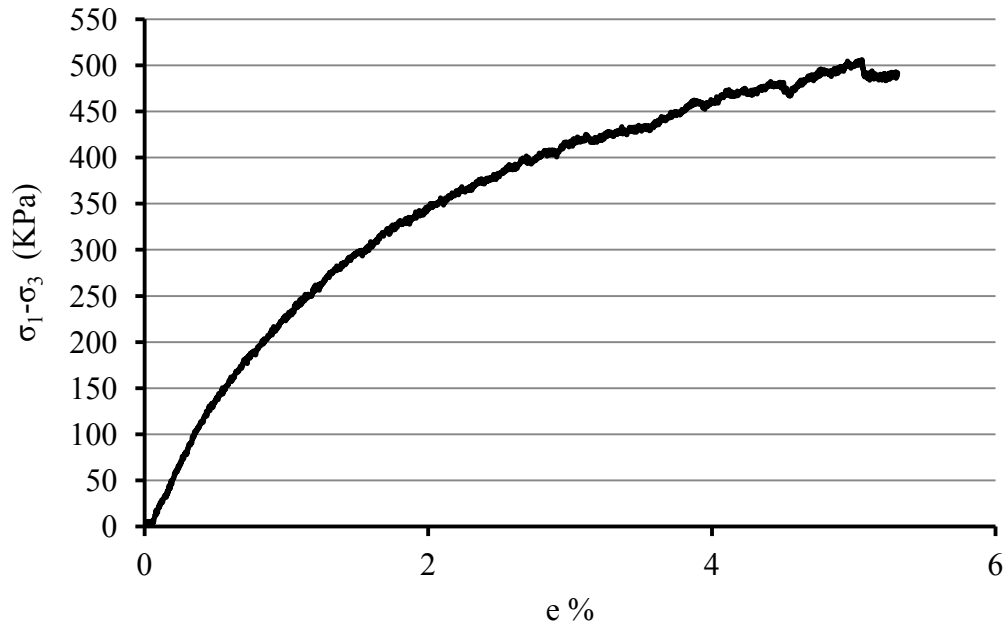


Figure B-17- Prematurely Failed test (Test F17), $\sigma_3 = 206.84$ kPa

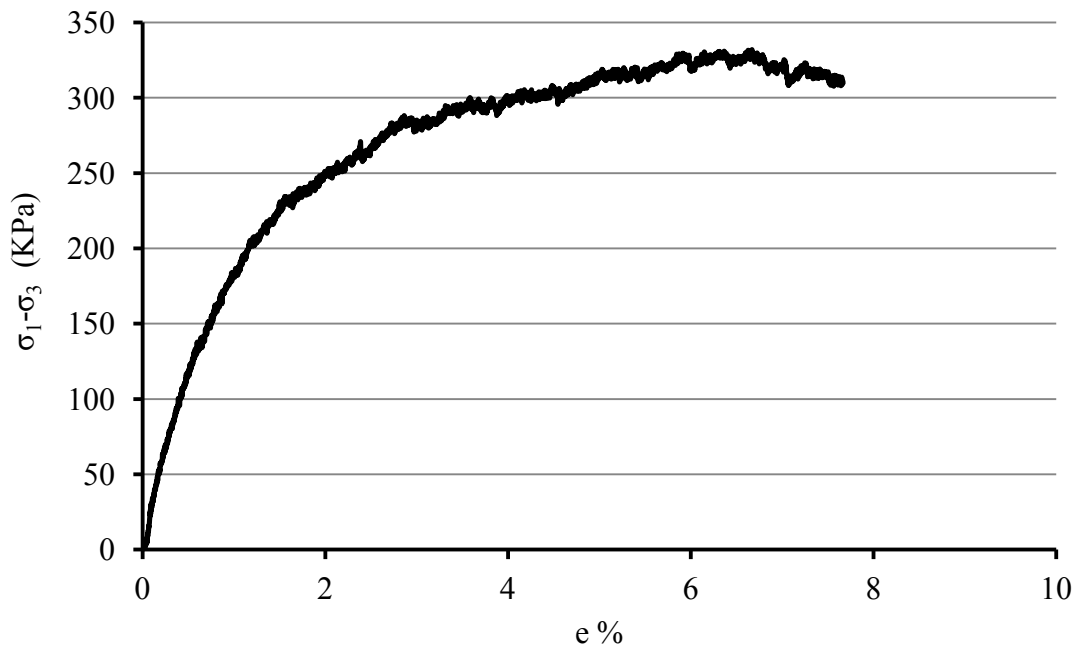


Figure B-18- Prematurely Failed test (Test F18), $\sigma_3 = 206.84$ kPa

Table B-1- Summary of specimens shape parameters and reason of premature failure

No.	FI	FF	Roundness	AI	AP	Convexity	TP	SD	Reason of Premature Failure - Comments
Test-F1	2.488	0.750	1.341	30.545	1.075	0.981	1.119	20.675	Eccentric deformation
Test-F2	2.483	0.749	1.342	31.160	1.079	0.980	1.120	20.161	Eccentric deformation and puncture
Test-F3	2.569	0.738	1.365	37.115	1.082	0.980	1.123	19.557	Membrane Puncture
Test-F4	2.369	0.765	1.315	28.745	1.068	0.983	1.113	20.636	Membrane Puncture
Test-F5	2.488	0.754	1.335	28.789	1.071	0.982	1.114	20.108	Membrane Puncture-In this test the confining pressure was applied by air Pressure
Test-F6	2.521	0.747	1.346	34.064	1.074	0.981	1.120	19.090	Membrane Puncture-In this test the confining pressure was applied by air Pressure
Test-F7	2.377	0.762	1.319	30.332	1.075	0.983	1.115	19.749	Membrane Puncture
Test-F8	2.608	0.741	1.358	31.379	1.075	0.981	1.118	20.732	Membrane Puncture
Test-F9	2.141	0.782	1.282	27.974	1.078	0.983	1.114	20.205	Membrane Puncture
Test-F10	2.520	0.760	1.321	22.122	1.061	0.983	1.107	21.825	Membrane Puncture
Test-F11	2.088	0.799	1.255	19.028	1.066	0.985	1.100	22.351	Membrane Puncture
Test-F12	2.720	0.732	1.373	32.473	1.057	0.982	1.126	20.815	Membrane Puncture
Test-F13	1.655	0.821	1.221	21.360	1.057	0.987	1.114	19.508	Membrane Puncture
Test-F14	2.542	0.751	1.337	27.213	1.062	0.983	1.117	20.705	Membrane Puncture
Test-F15	2.484	0.747	1.343	38.366	1.064	0.983	1.131	18.221	Eccentric deformation
Test-F16	2.068	0.776	1.294	37.277	1.077	0.983	1.131	18.580	Membrane Puncture
Test-F17	2.100	0.784	1.279	28.964	1.070	0.984	1.124	19.273	Membrane Puncture
Test-F18	2.518	0.750	1.338	30.143	1.063	0.982	1.121	20.218	Eccentric deformation and puncture

APPENDIX C

TRIAXIAL TESTS ON BROKEN SANDSTONE

This appendix contains the results of the triaxial tests performed on broken sandstone samples.

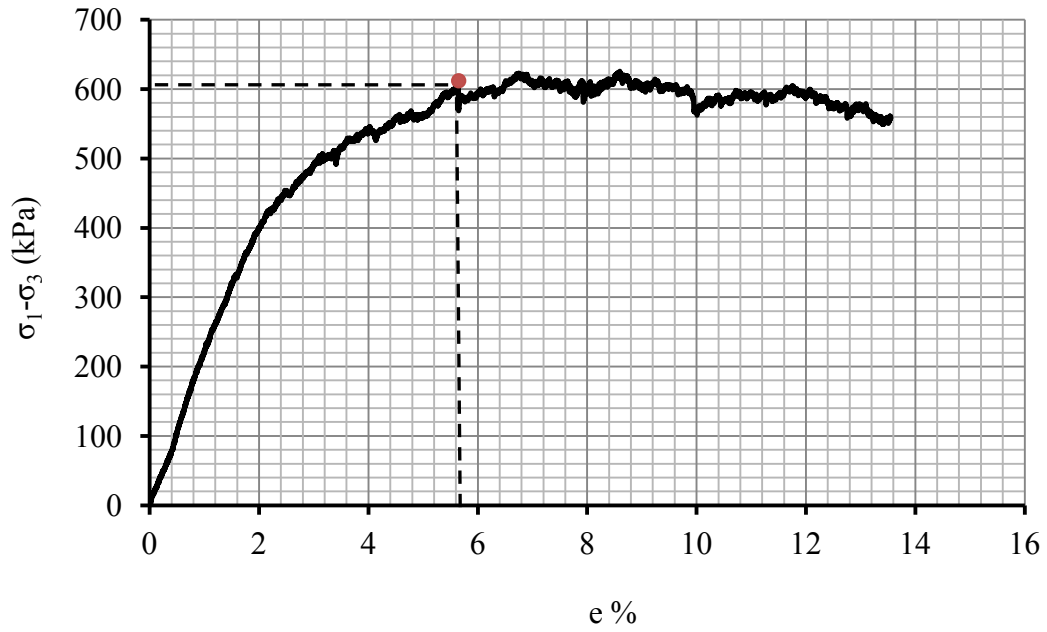


Figure C-1- Result of triaxial test (Test 1), Confining pressure is equal to 137.90 kPa.

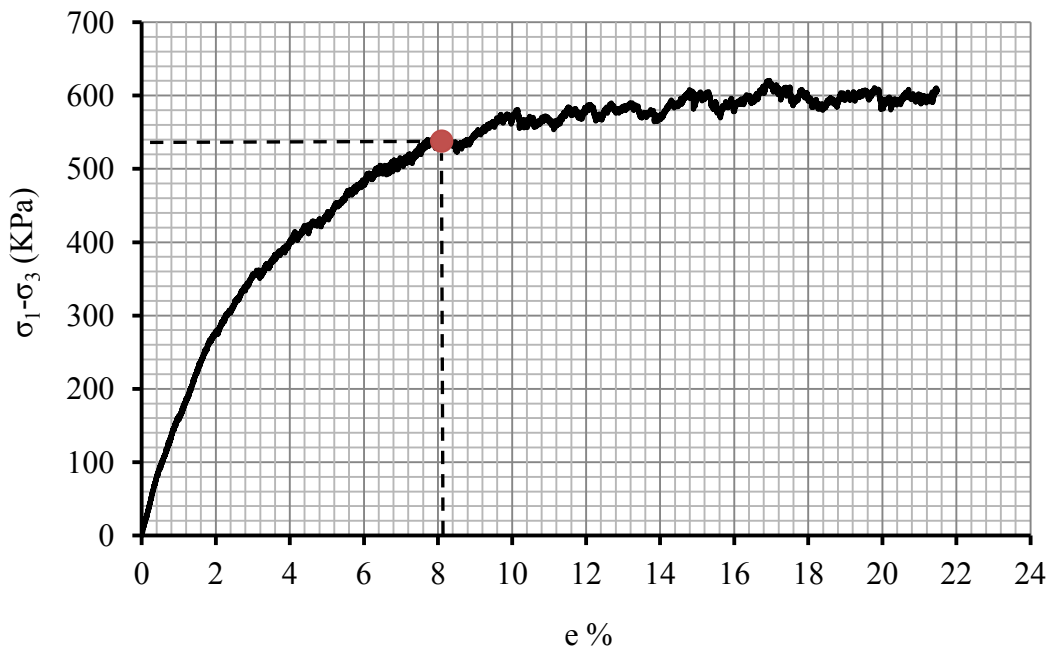


Figure C-2- Result of triaxial test (Test 2), Confining pressure is equal to 137.90 kPa.

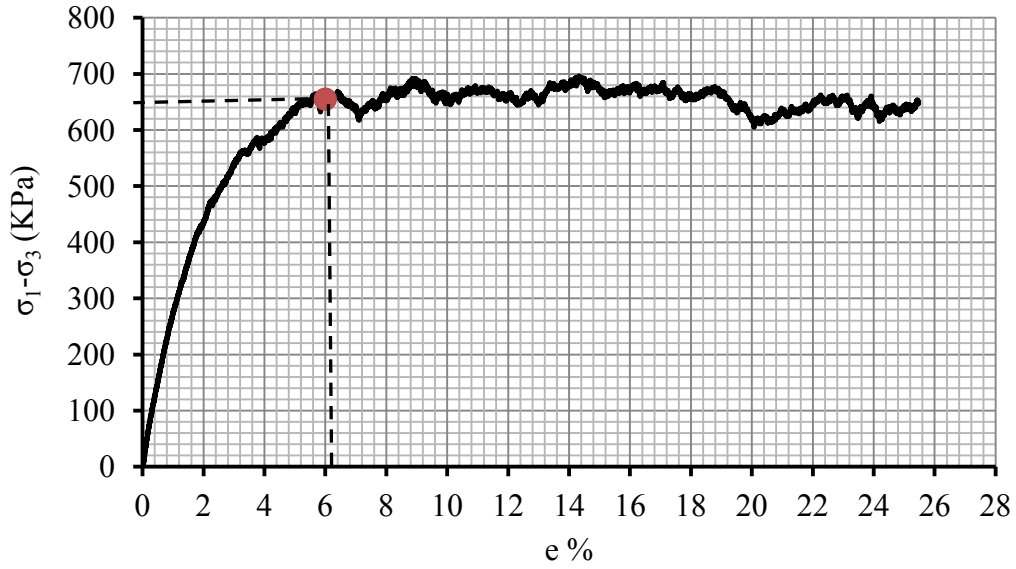


Figure C-3- Result of triaxial test (Test 3), Confining pressure is equal to 137.90 kPa.

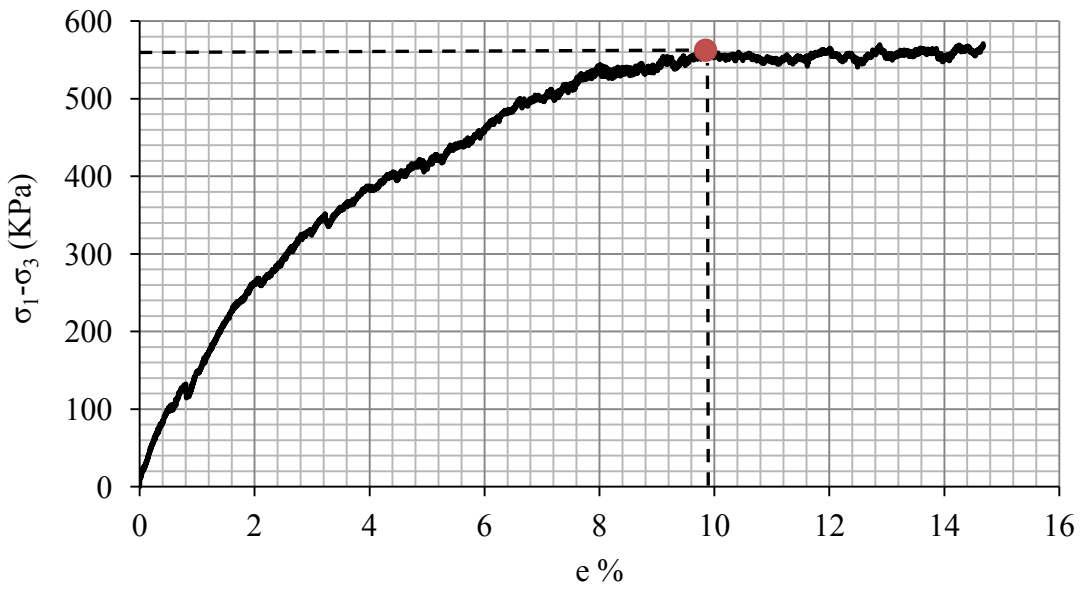


Figure C-4- Result of triaxial test (Test 4), Confining pressure is equal to 137.90 kPa.

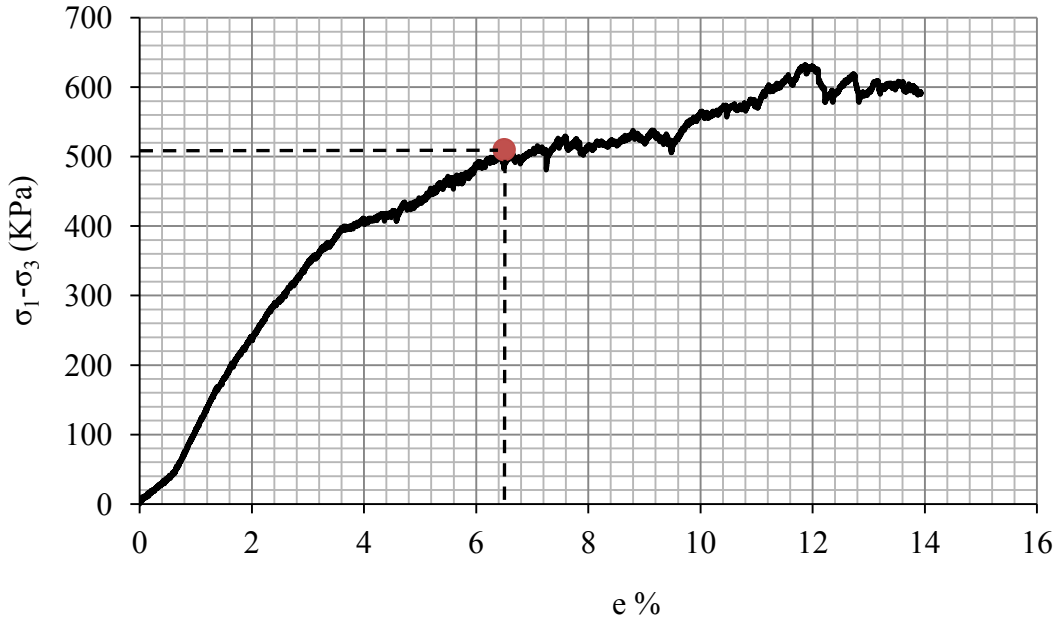


Figure C-5- Result of triaxial test (Test 5), Confining pressure is equal to 137.90 kPa.

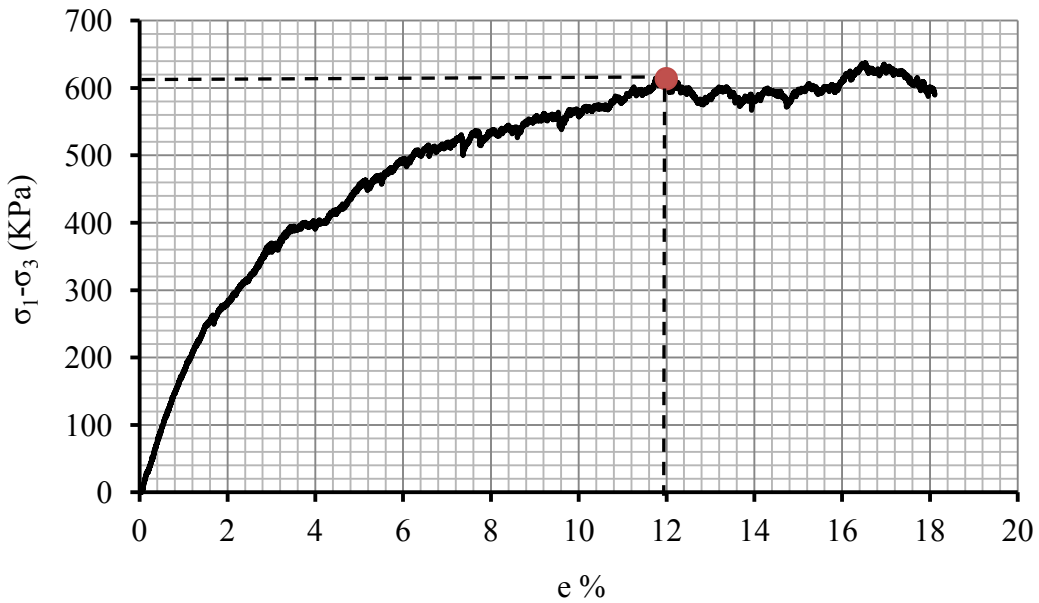


Figure C-6- Result of triaxial test (Test 6), Confining pressure is equal to 137.90 kPa.

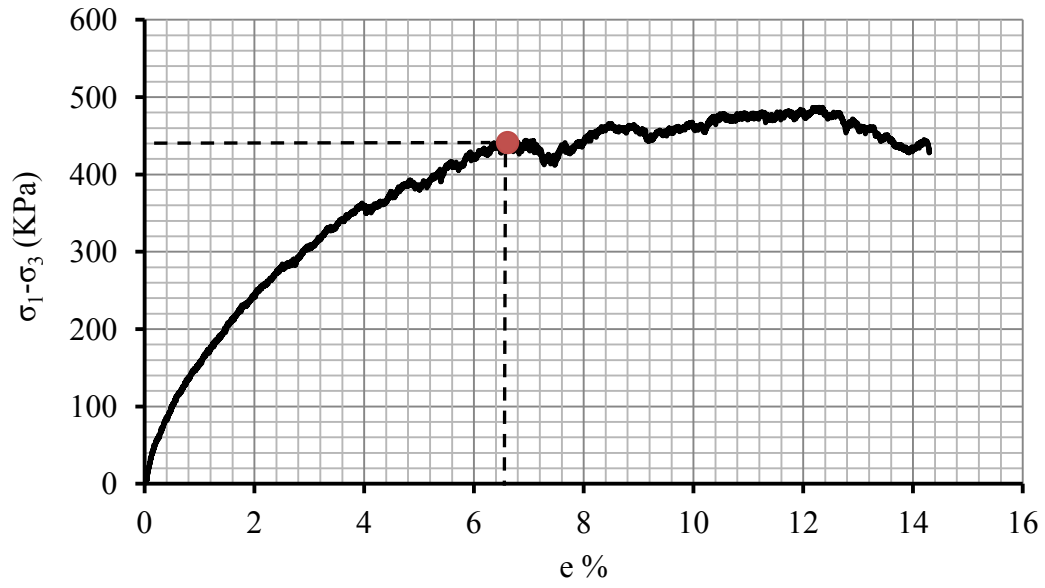


Figure C-7- Result of triaxial test (Test 7), Confining pressure is equal to 137.90 kPa.

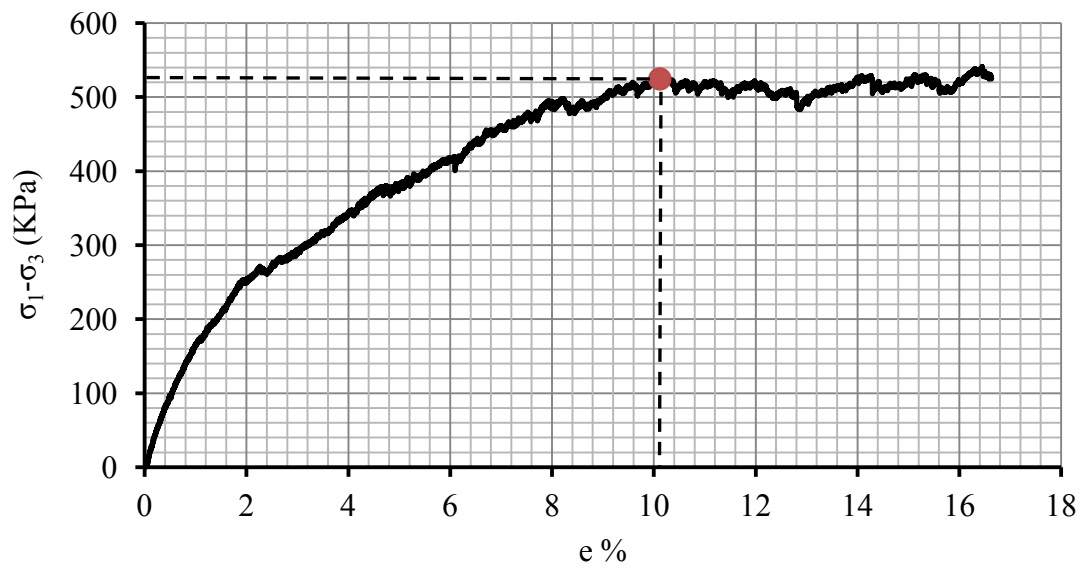


Figure C-8- Result of triaxial test (Test 8), Confining pressure is equal to 137.90 kPa.

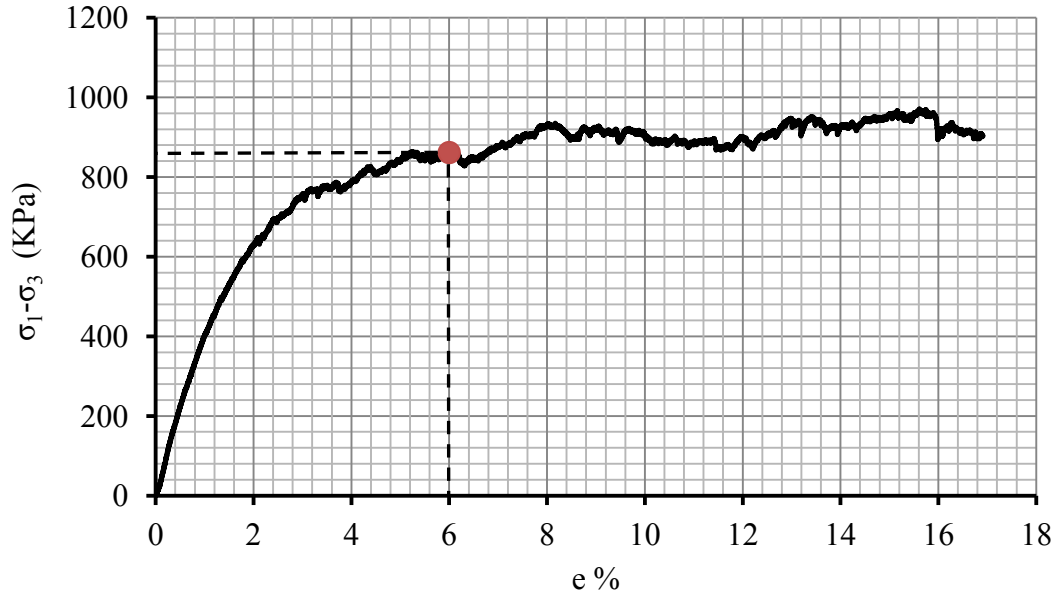


Figure C-9- Result of triaxial test (Test 9), Confining pressure is equal to 206.84 kPa.

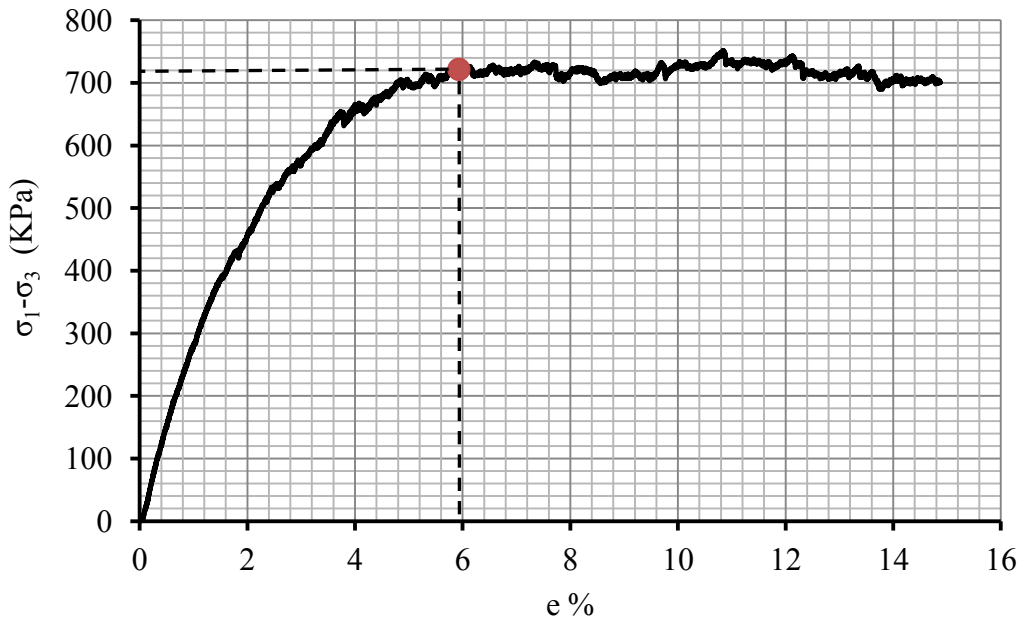


Figure C-10- Result of triaxial test (Test 10), Confining pressure is equal to 206.84 kPa.

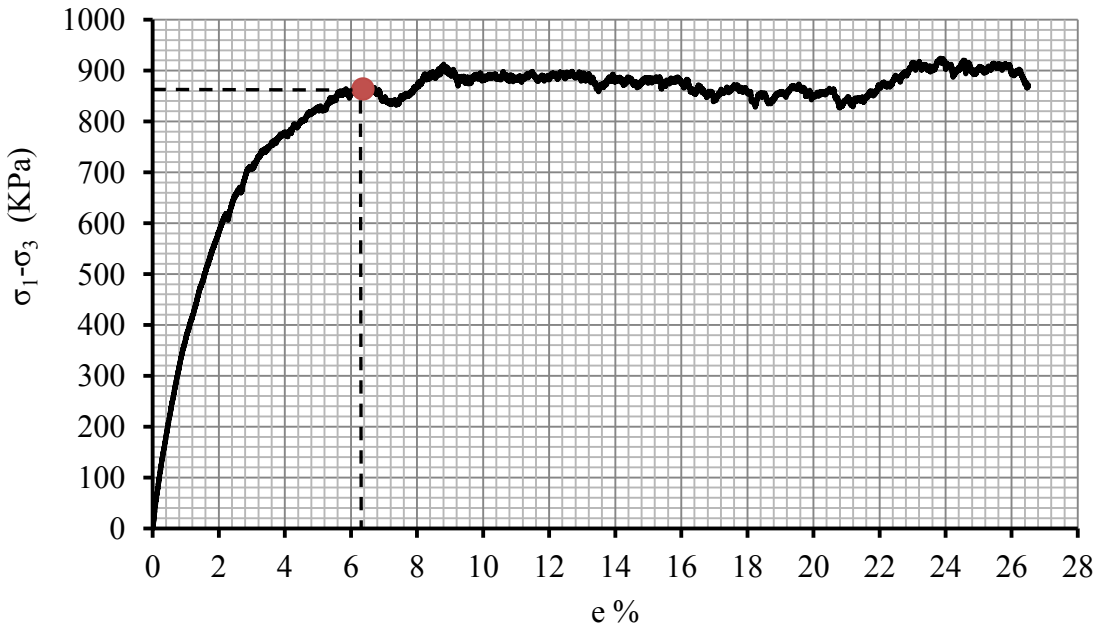


Figure C-11- Result of triaxial test (Test 11), Confining pressure is equal to 206.84 kPa.

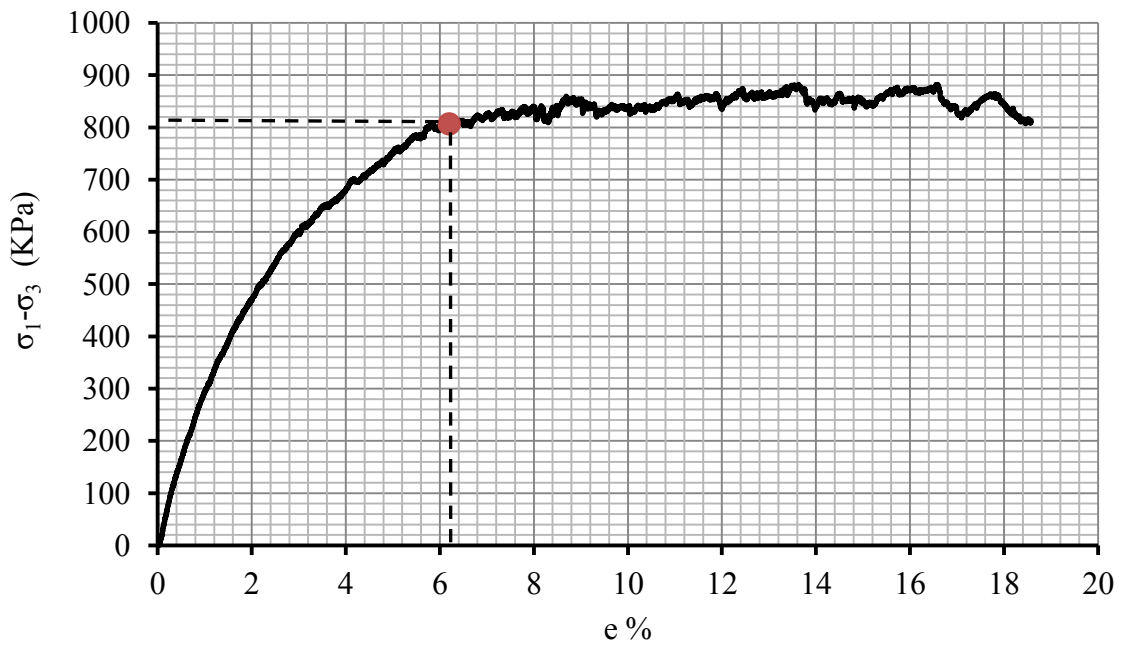


Figure C-12- Result of triaxial test (Test 12), Confining pressure is equal to 206.84 kPa.

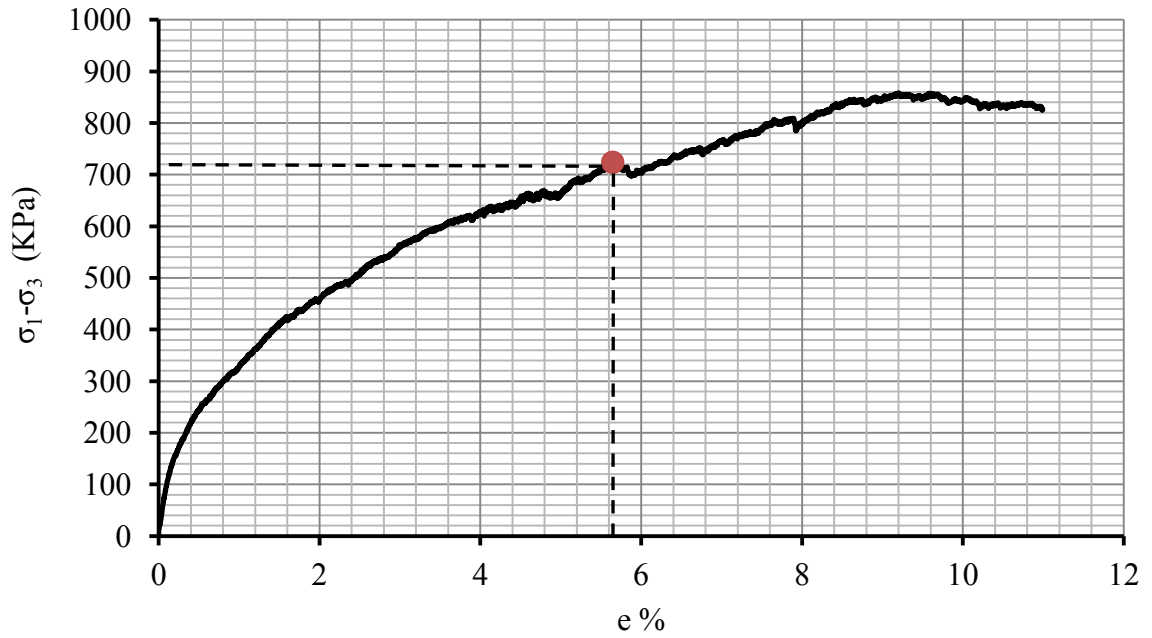


Figure C-13- Result of triaxial test (Test 13), Confining pressure is equal to 206.84 kPa.

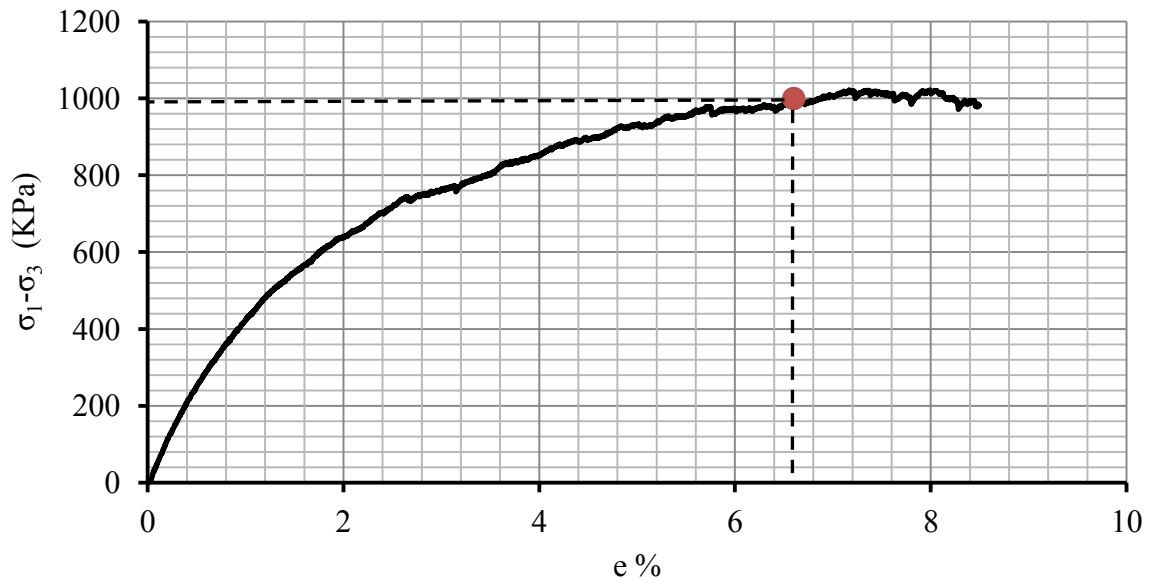


Figure C-14- Result of triaxial test (Test 14), Confining pressure is equal to 275.79 kPa.

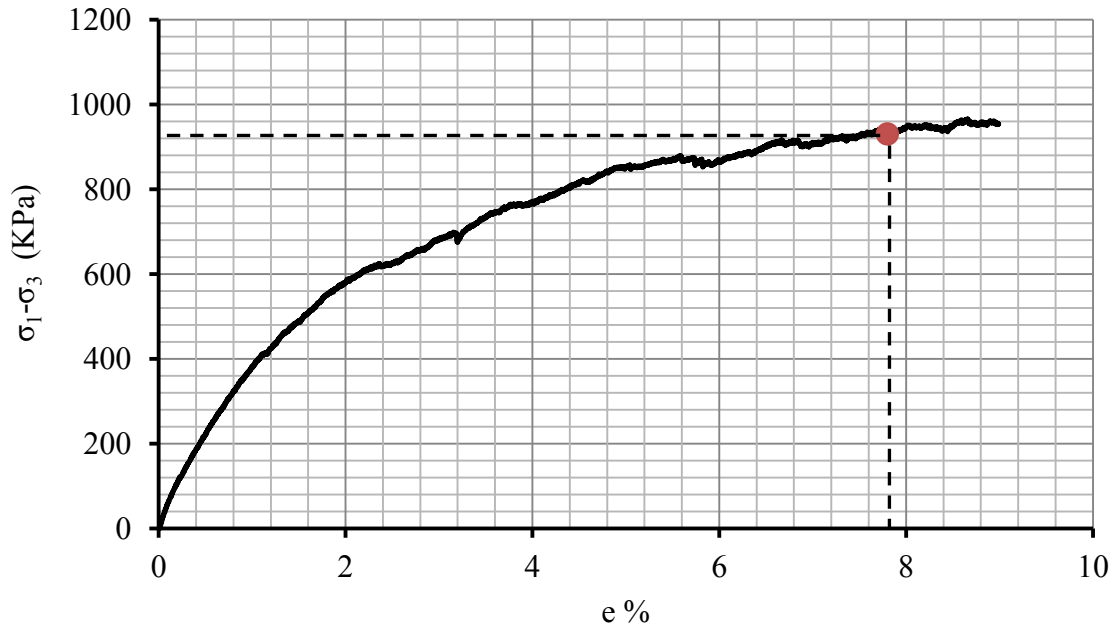


Figure C-15- Result of triaxial test (Test 15), Confining pressure is equal to 275.79 kPa.

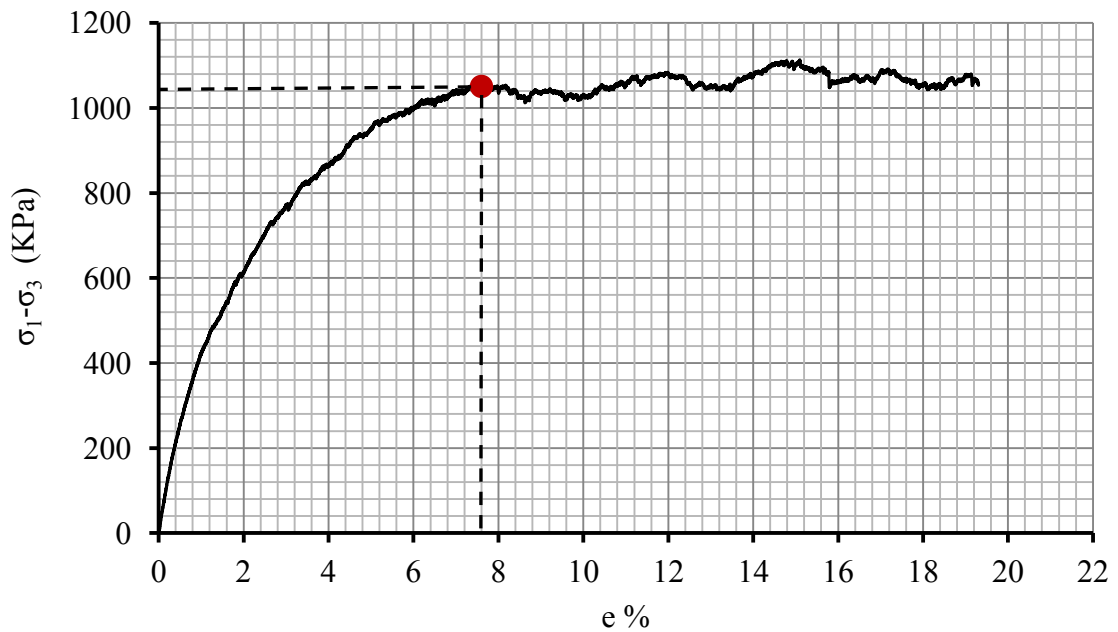


Figure C-16- Result of triaxial test (Test 16), Confining pressure is equal to 275.79 kPa.

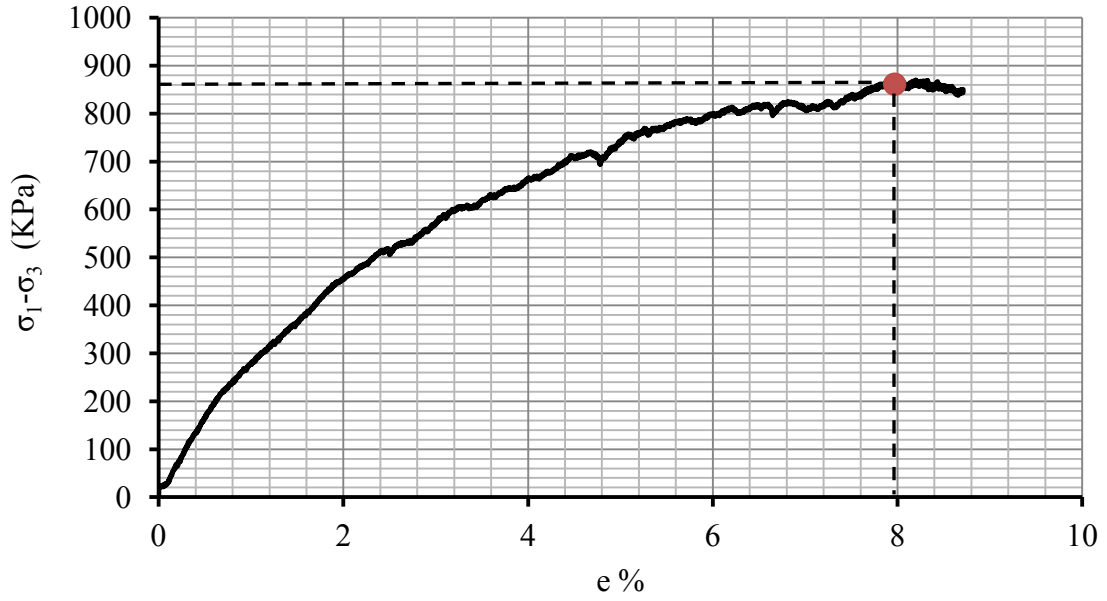


Figure C-17- Result of triaxial test (Test 17), Confining pressure is equal to 275.79 kPa.

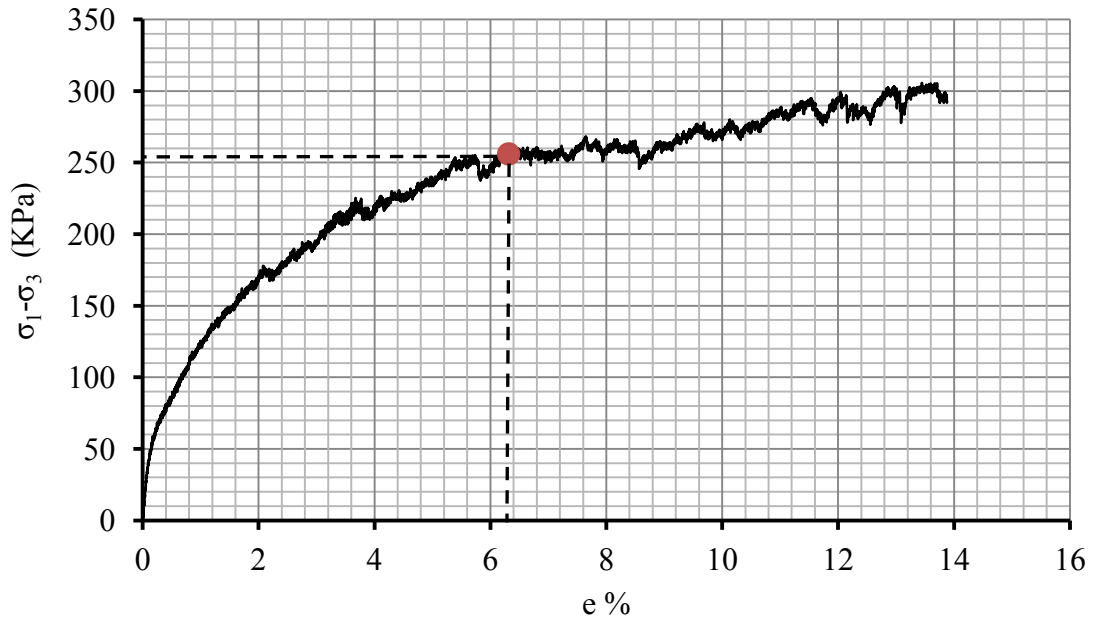


Figure C-18- Result of triaxial test (Test 18), Confining pressure is equal to 34.47 kPa.

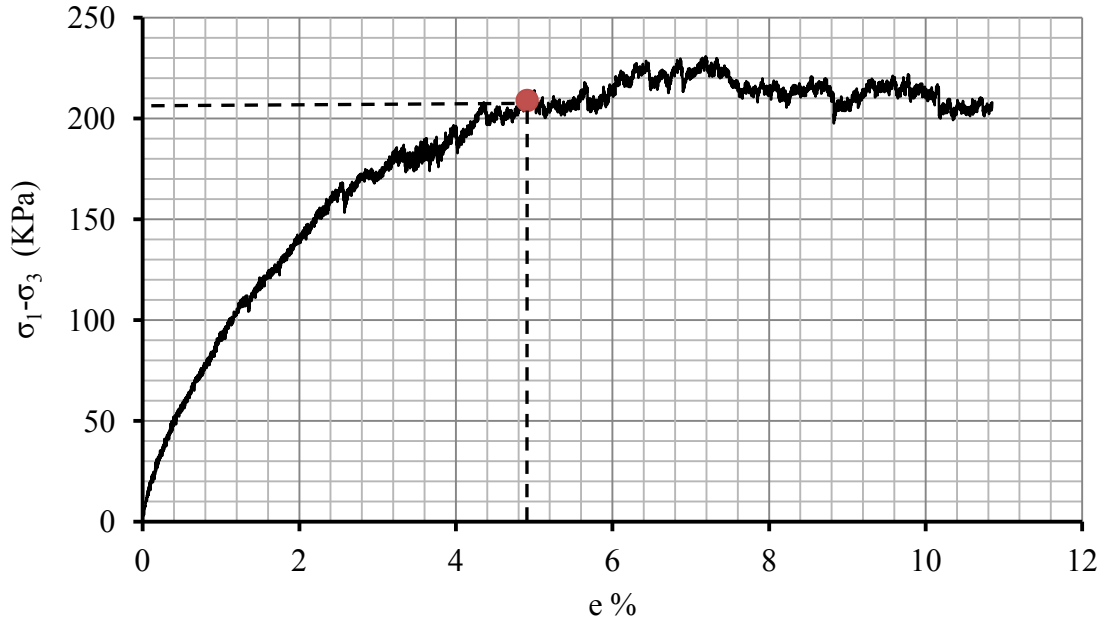


Figure C-19- Result of triaxial test (Test 19), Confining pressure is equal to 34.47 kPa.

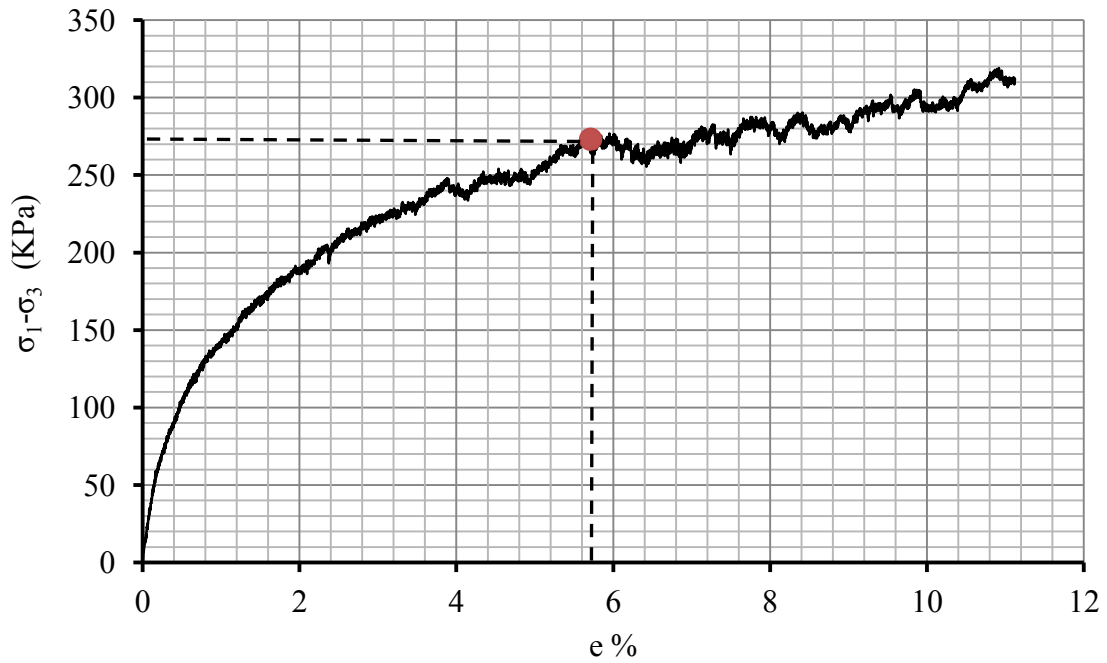


Figure C-20- Result of triaxial test (Test 20), Confining pressure is equal to 34.47 kPa.

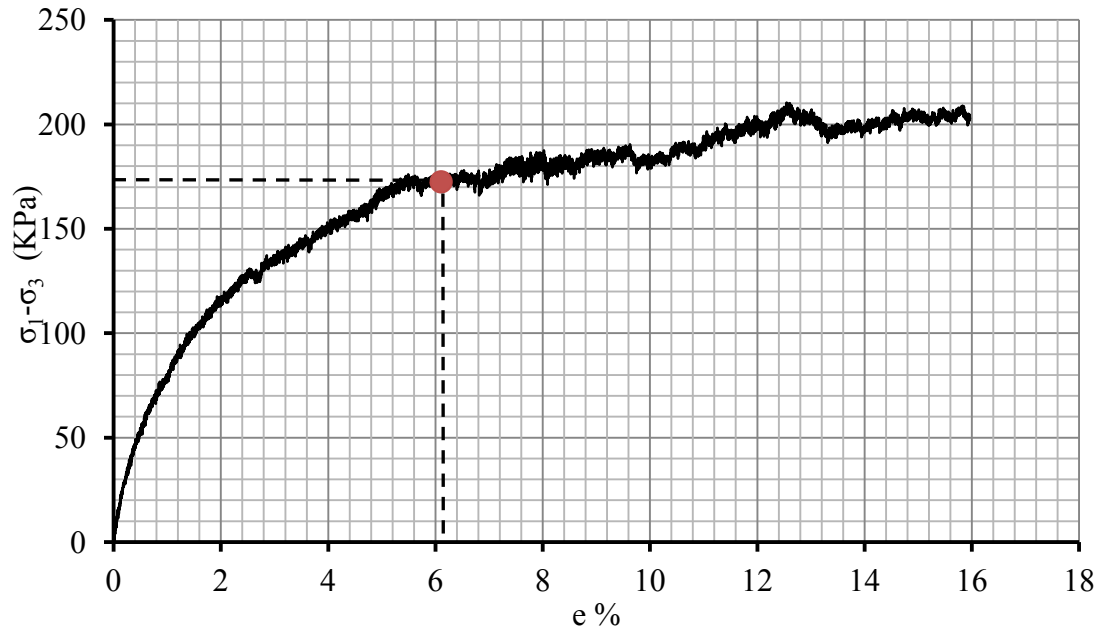


Figure C-21- Result of triaxial test (Test 21), Confining pressure is equal to 34.47 kPa.

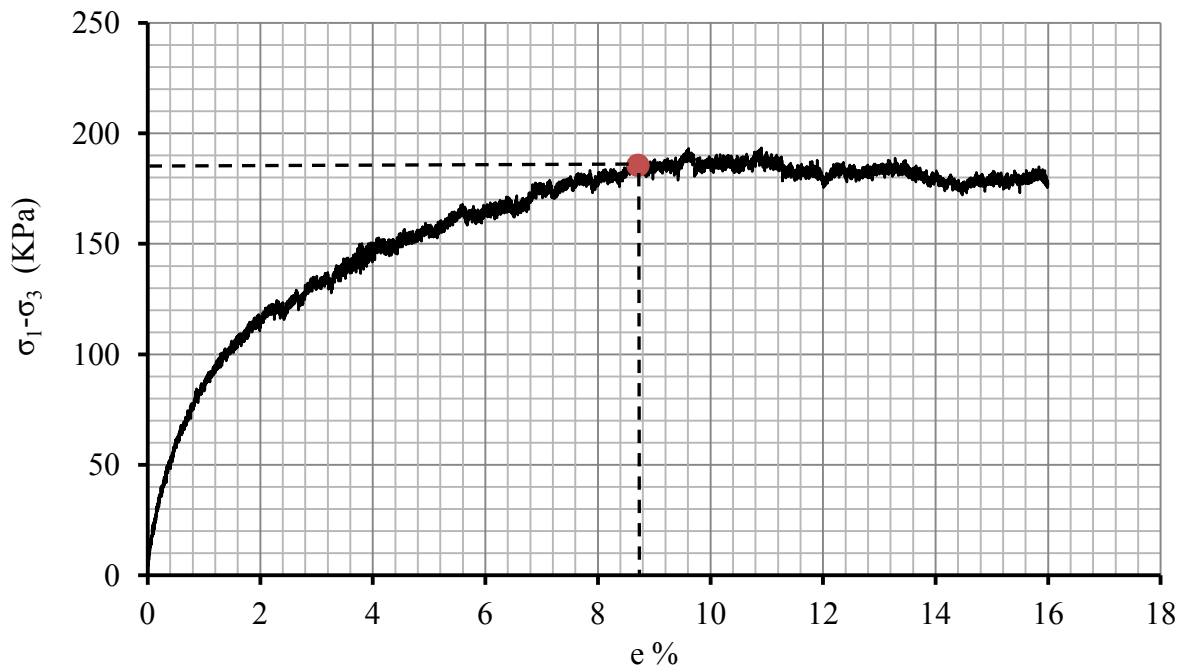


Figure C-22- Result of triaxial test (Test 22), Confining pressure is equal to 34.47 kPa.

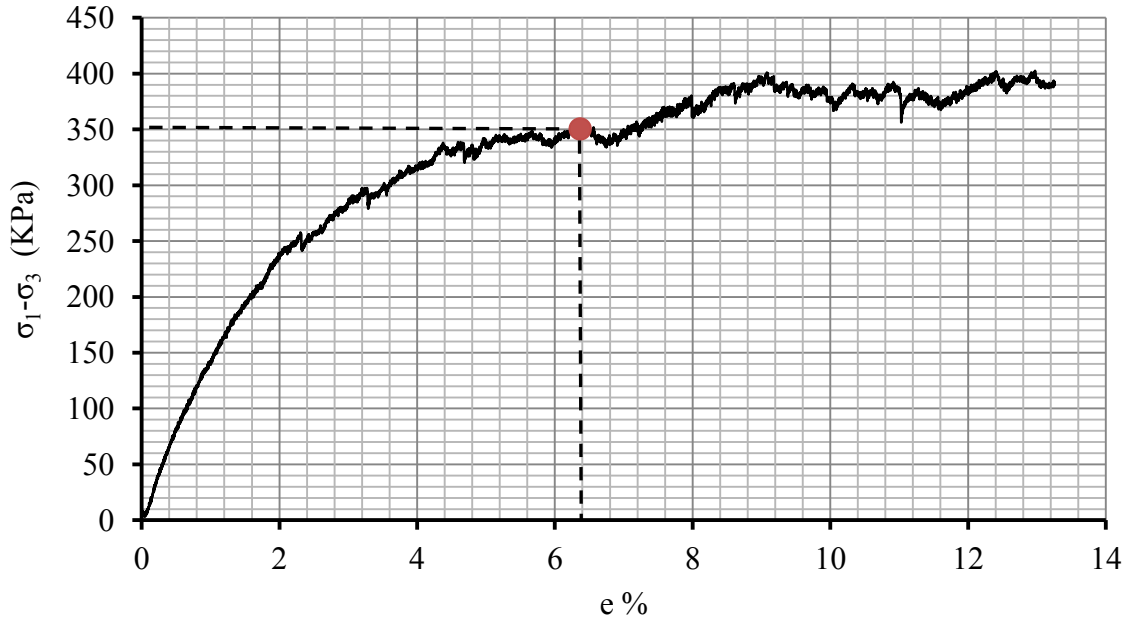


Figure C-23- Result of triaxial test (Test 23), Confining pressure is equal to 68.95 kPa.

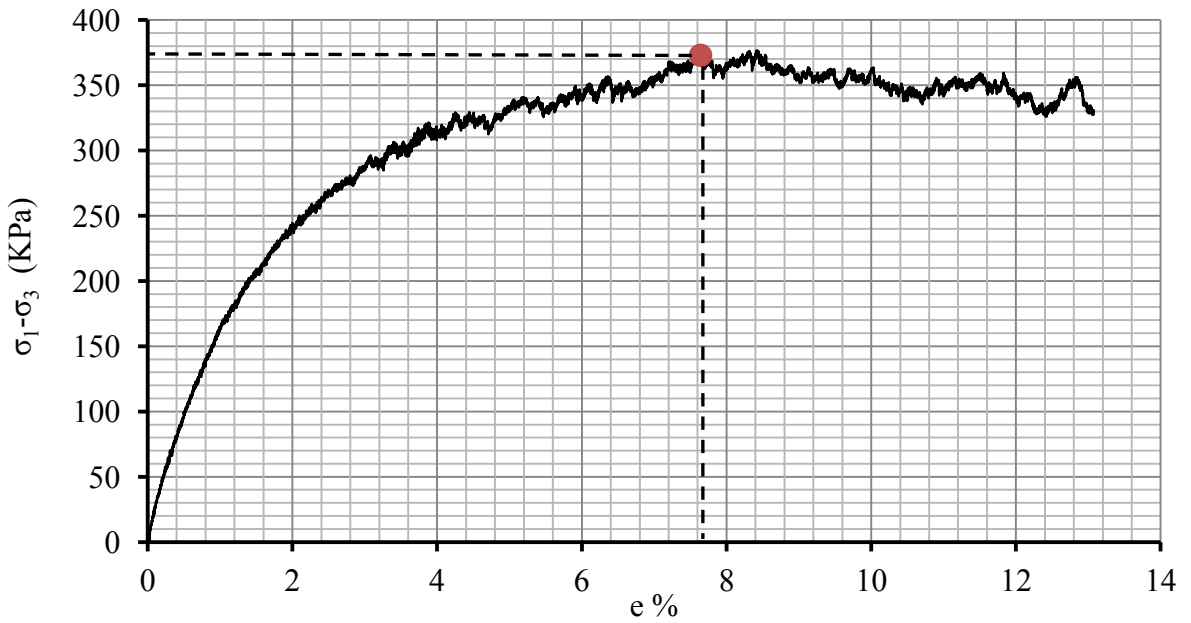


Figure C-24- Result of triaxial test (Test 24), Confining pressure is equal to 68.95 kPa.

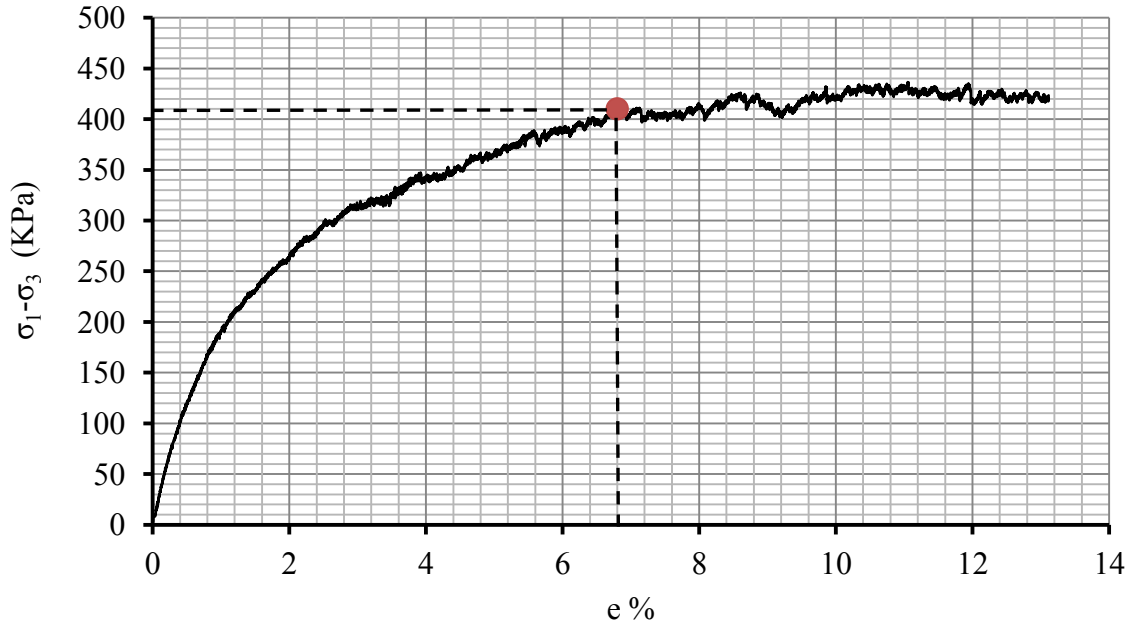


Figure C-25- Result of triaxial test (Test 25), Confining pressure is equal to 68.95 kPa.

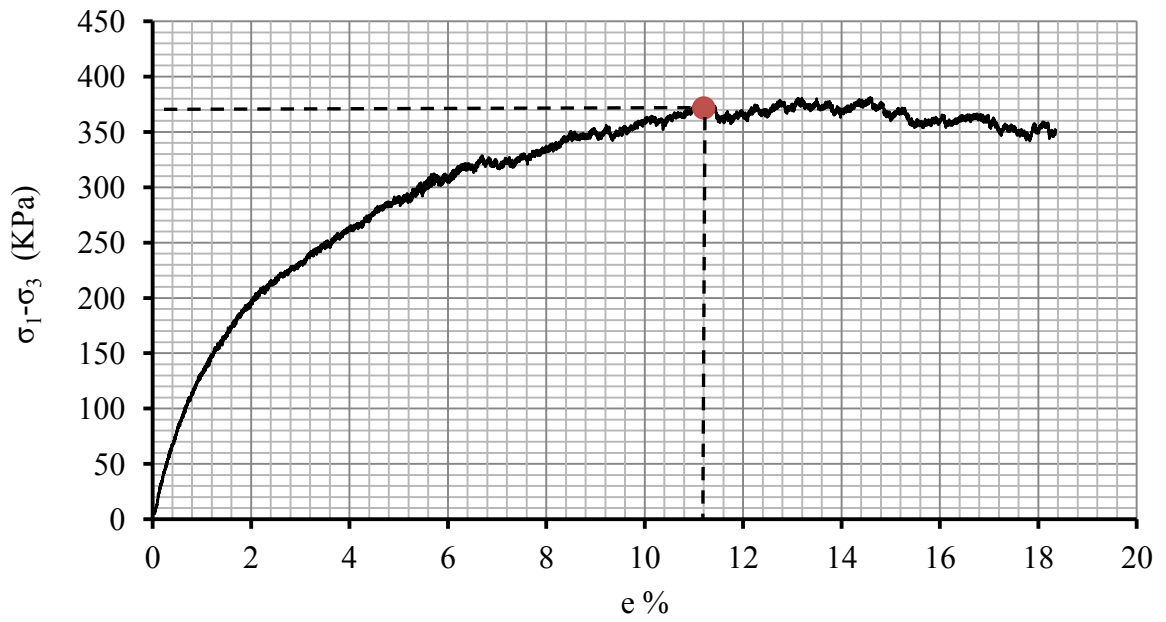


Figure C-26- Result of triaxial test (Test 26), Confining pressure is equal to 68.95 kPa.

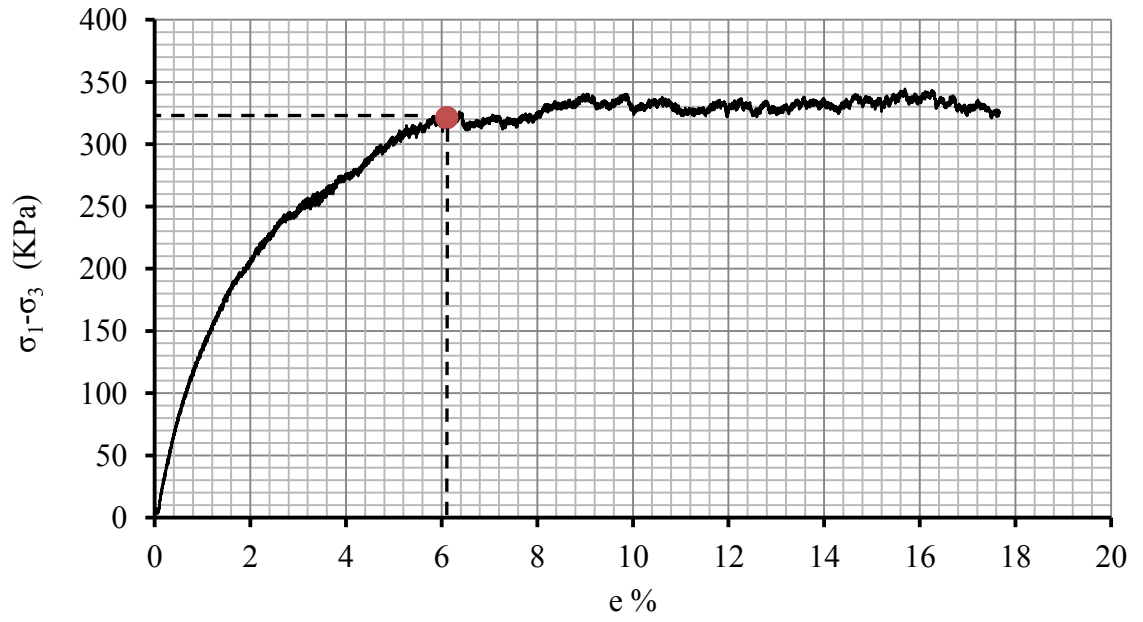


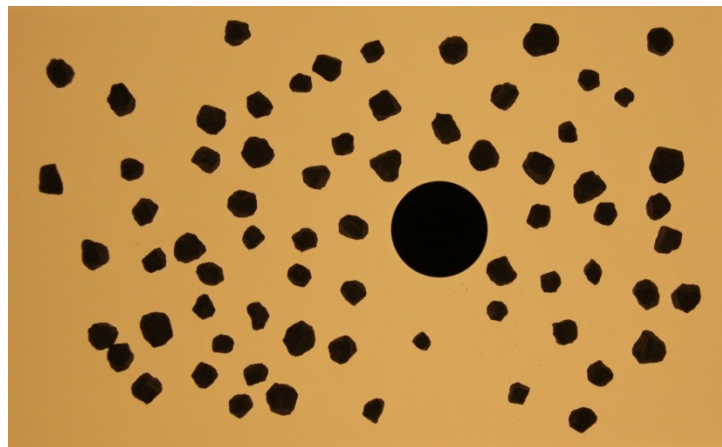
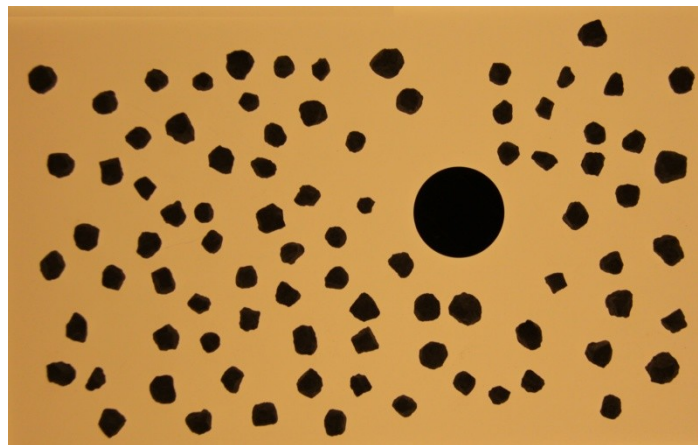
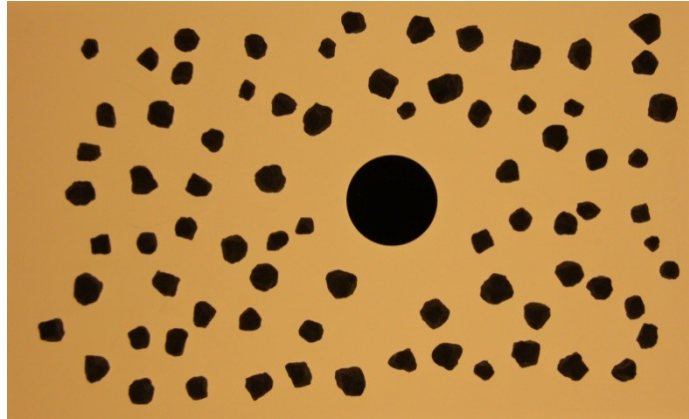
Figure C-27- Result of triaxial test (Test 27), Confining pressure is equal to 68.95 kPa.

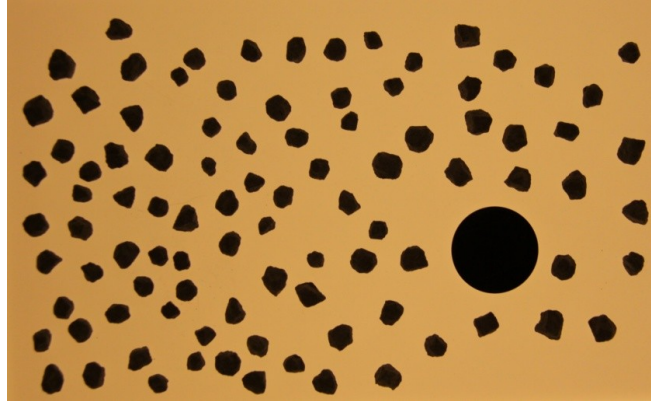
APPENDIX D

SECIMENS PARTICLES

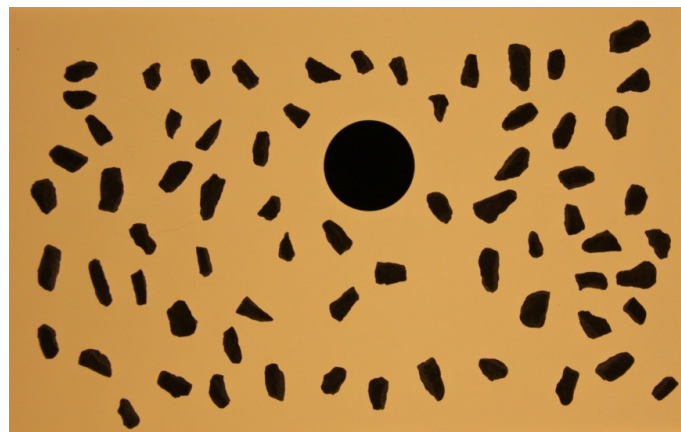
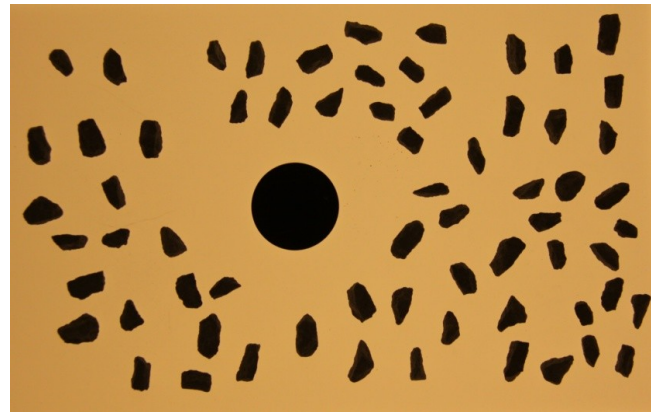
This Appendix contains the photo of specimens' particles.

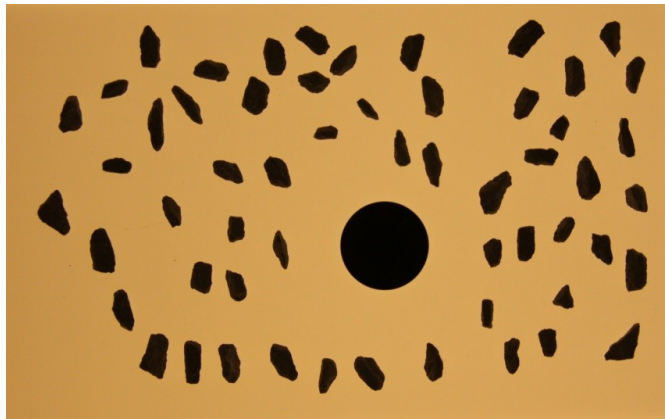
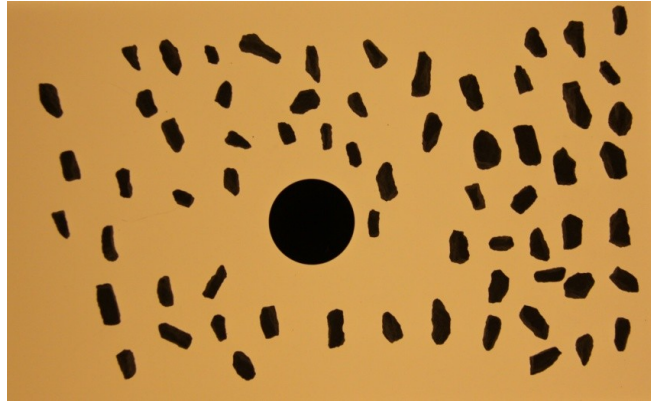
Particles of Test 1:



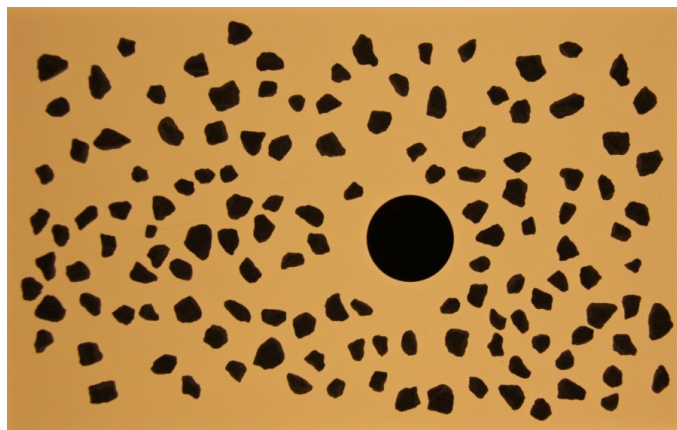


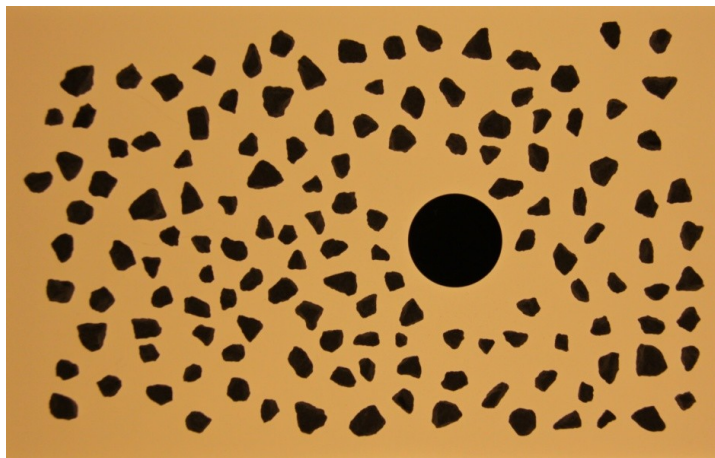
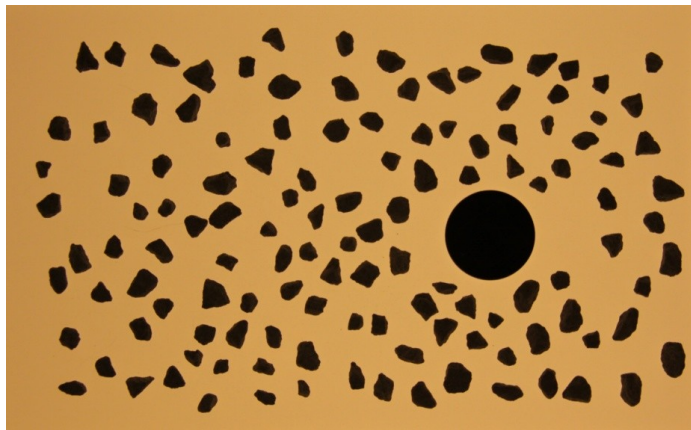
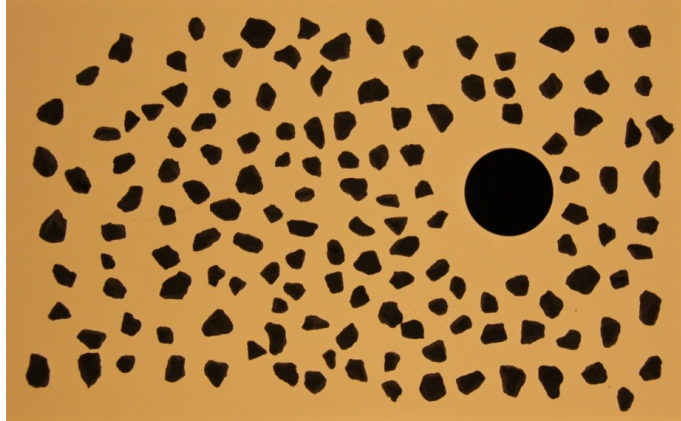
Particles of Test 2:



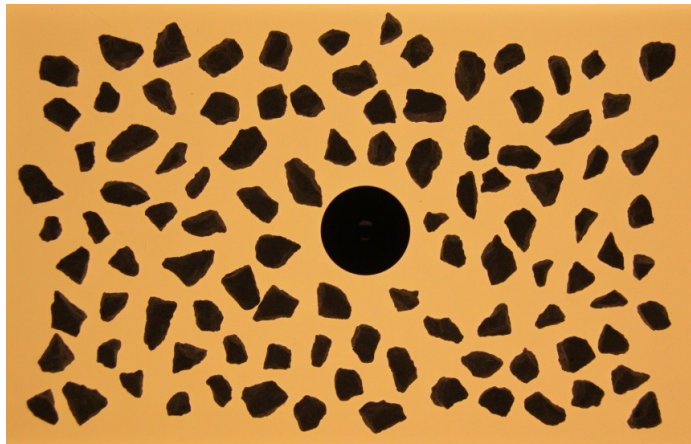
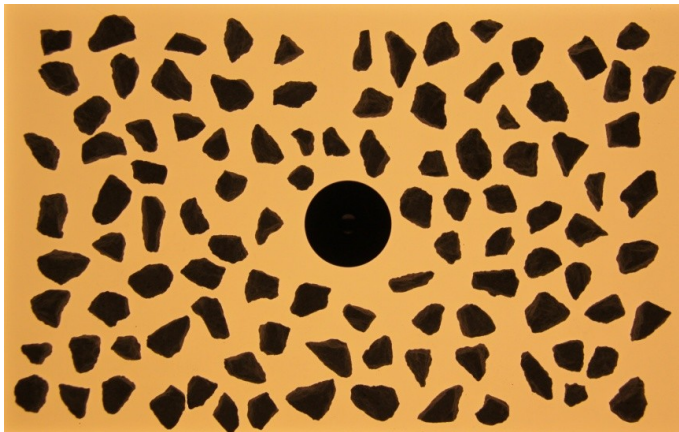
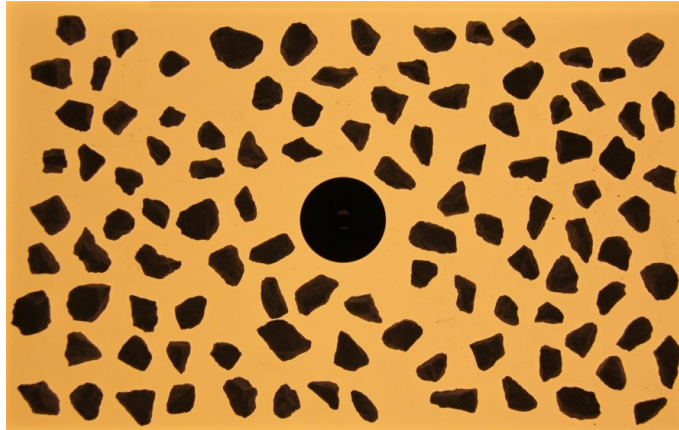


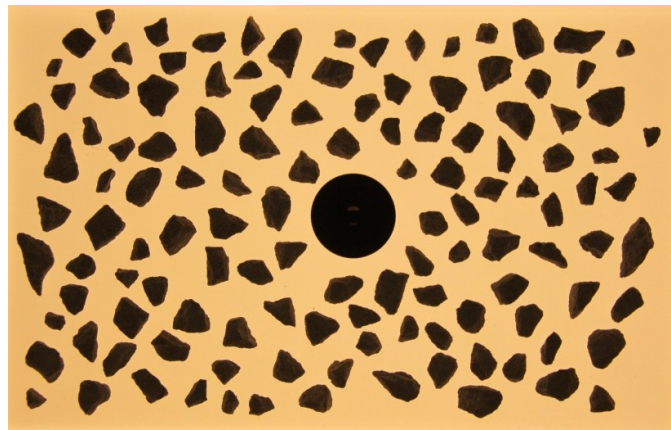
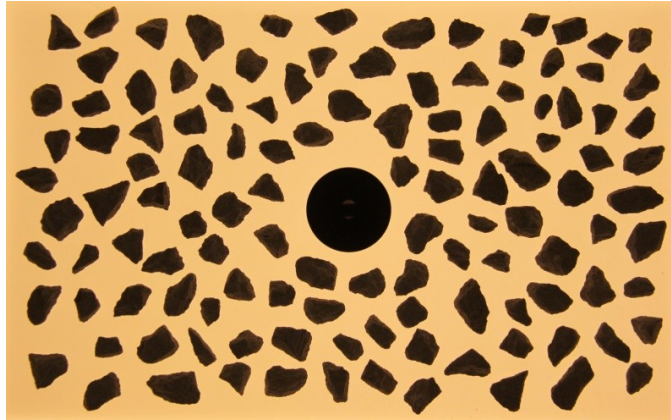
Particles of Test 3:



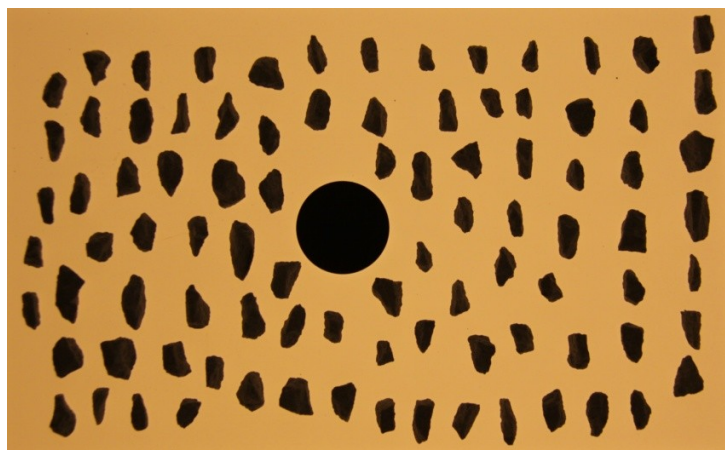


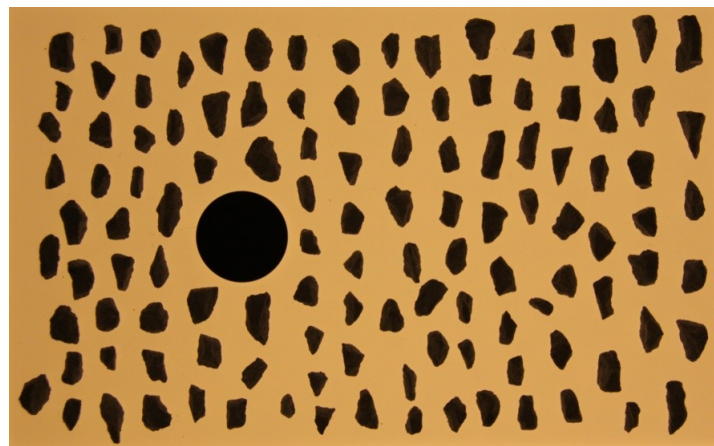
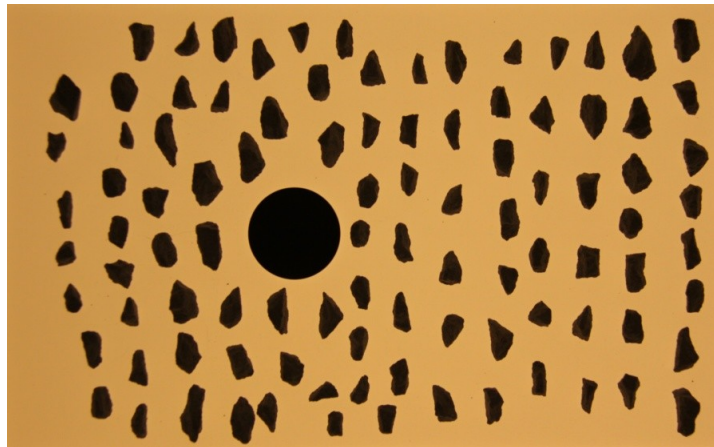
Particles of Test 4:

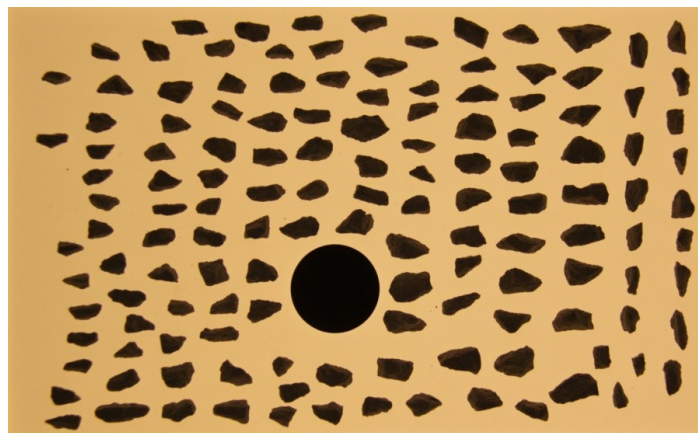
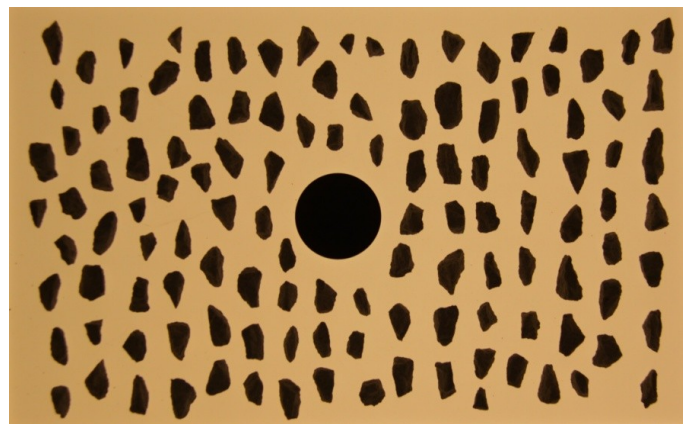
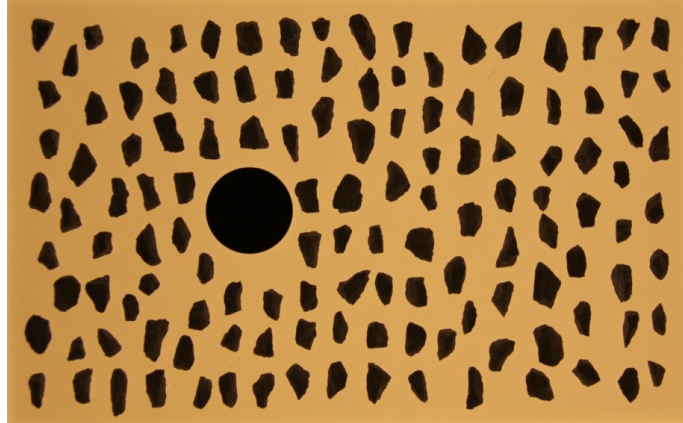




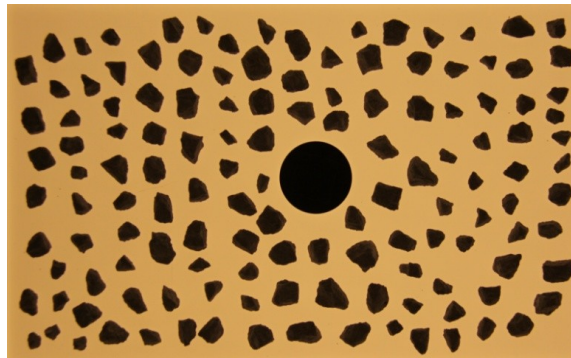
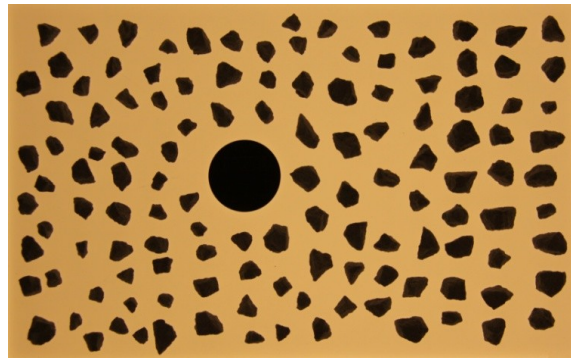
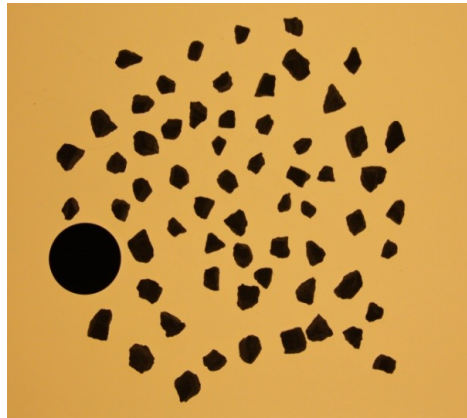
Particles of Test 5:

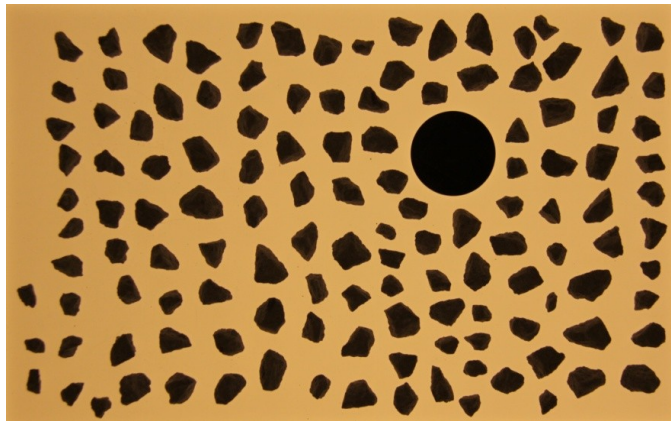
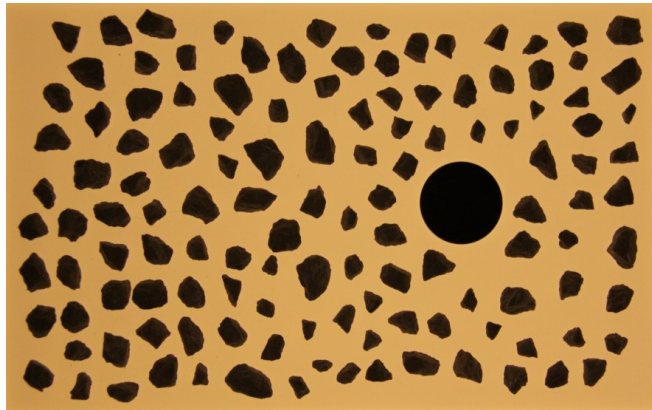
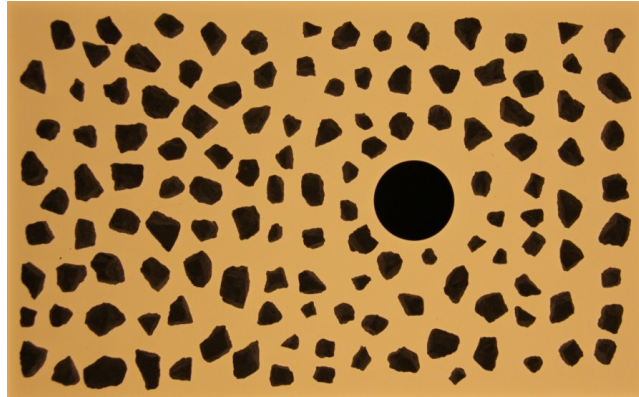




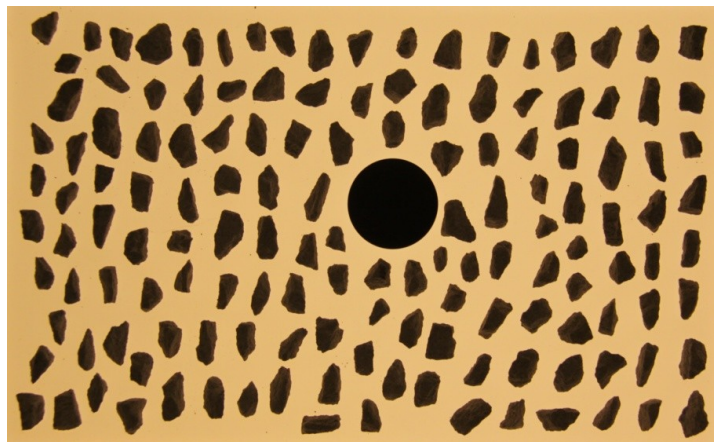
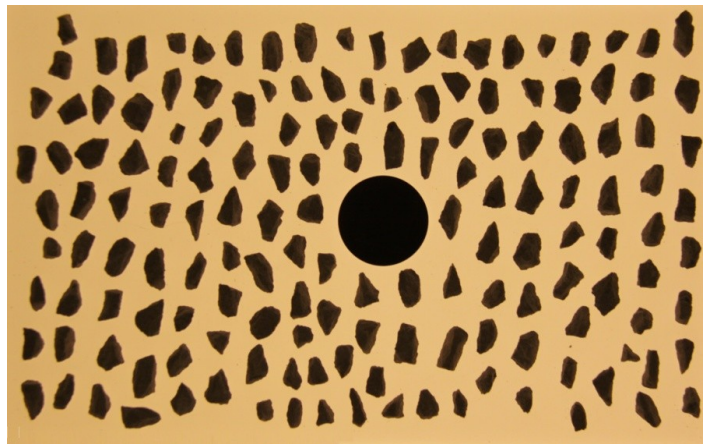
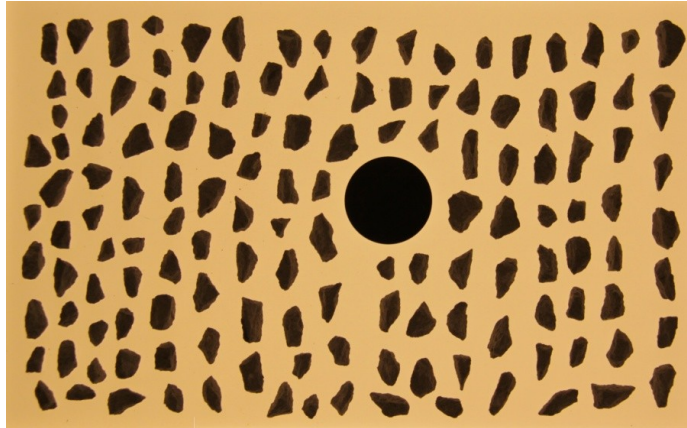


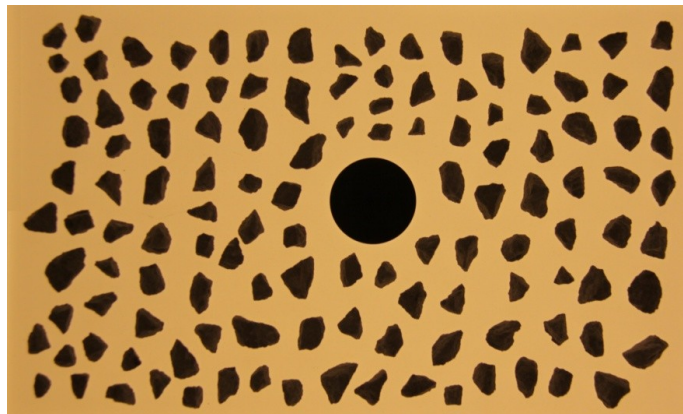
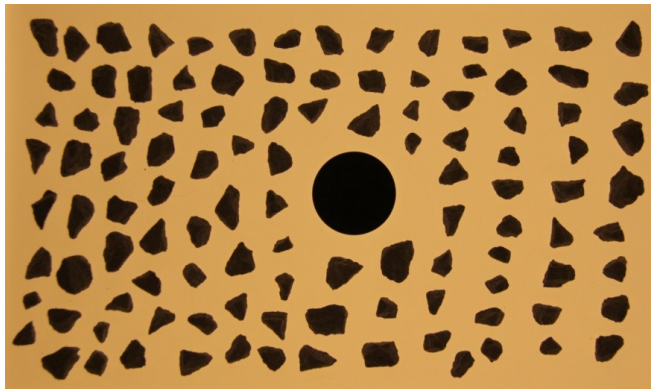
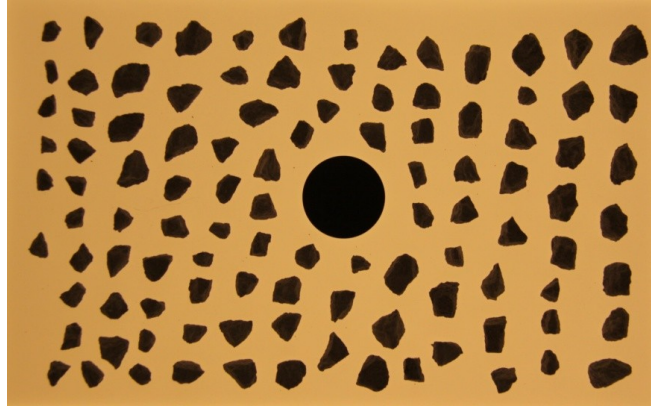
Particles of Test 6:



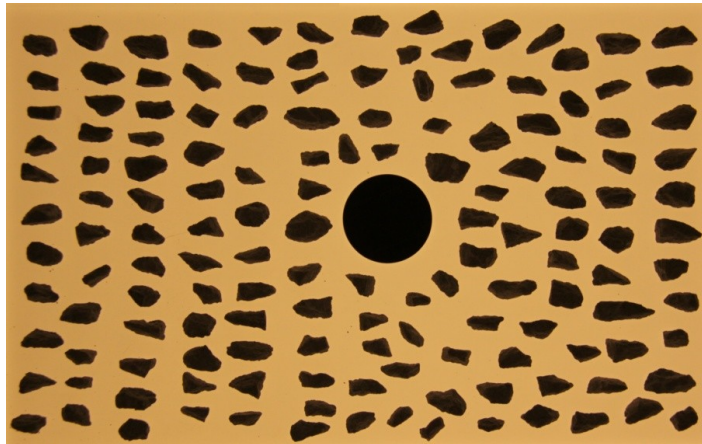
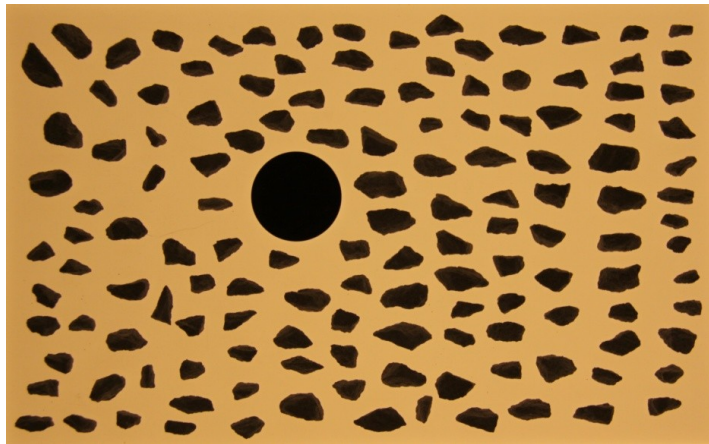
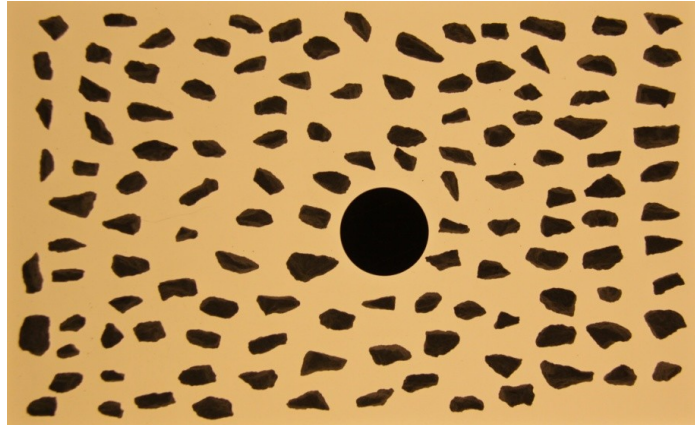


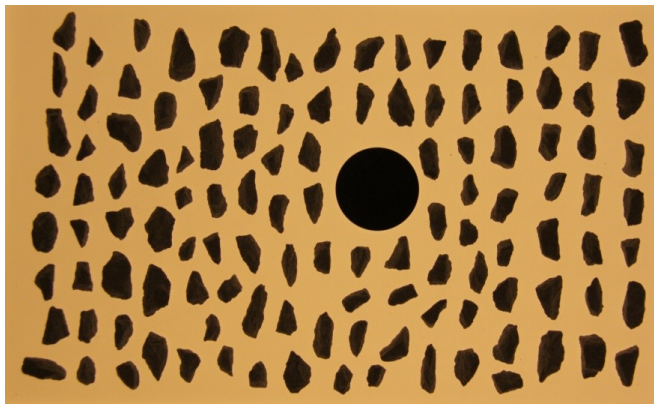
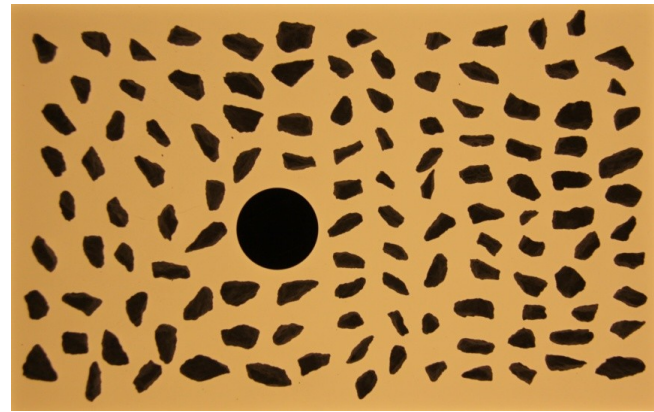
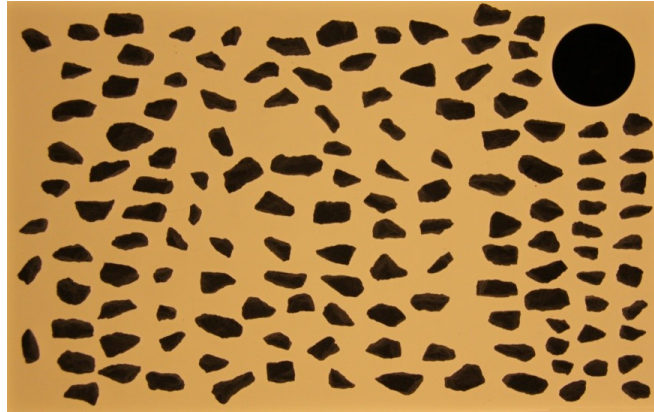
Particles of Test 7:

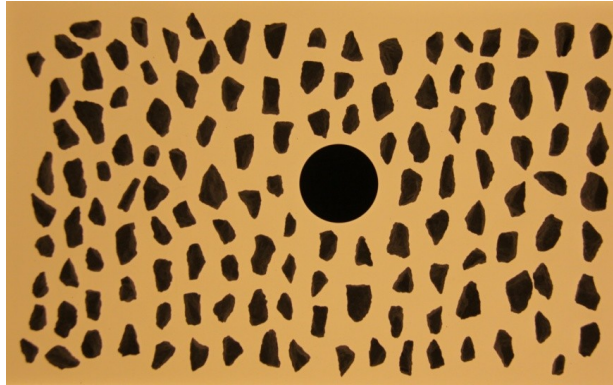




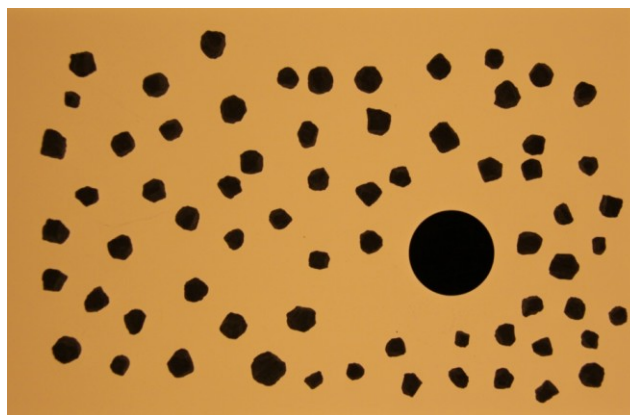
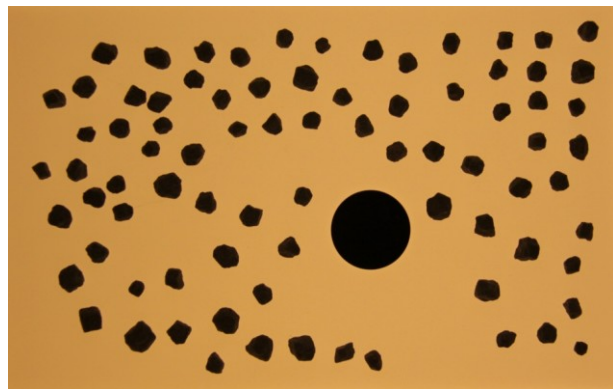
Particles of Test 8:

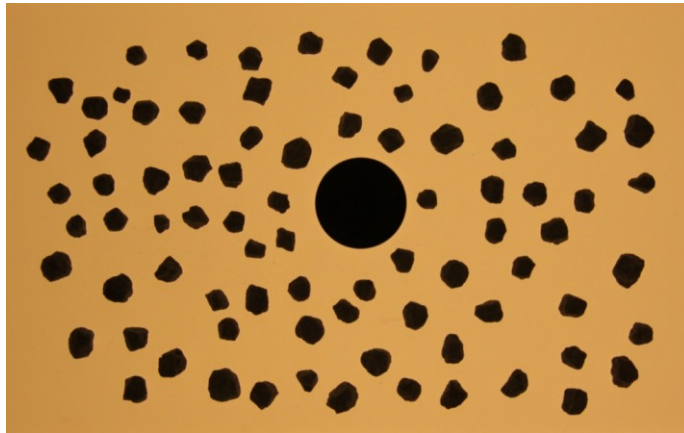
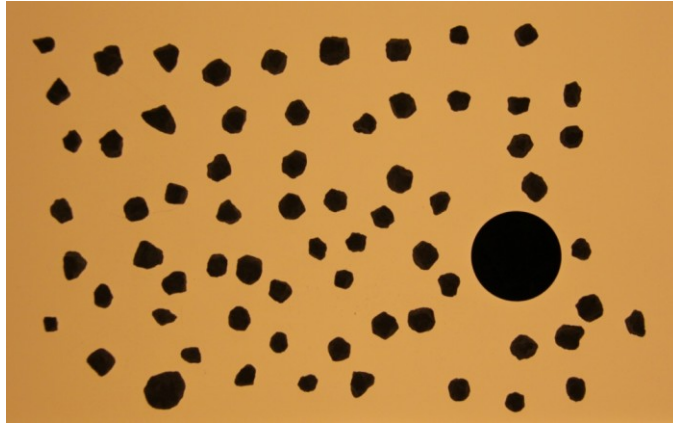




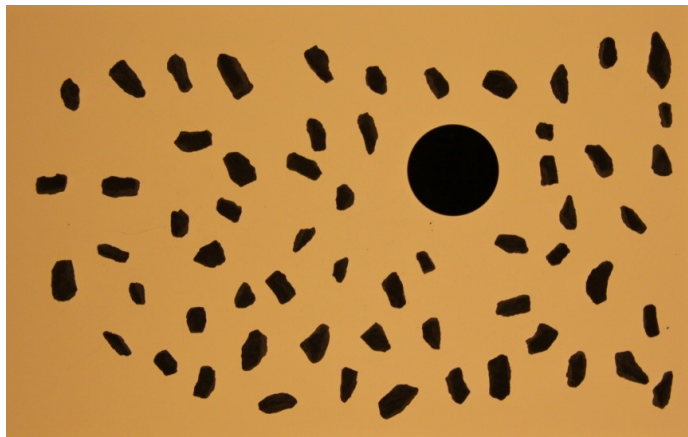


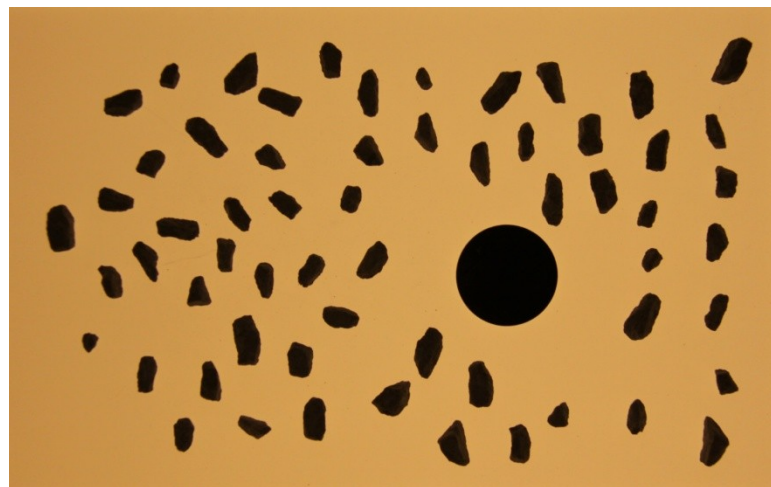
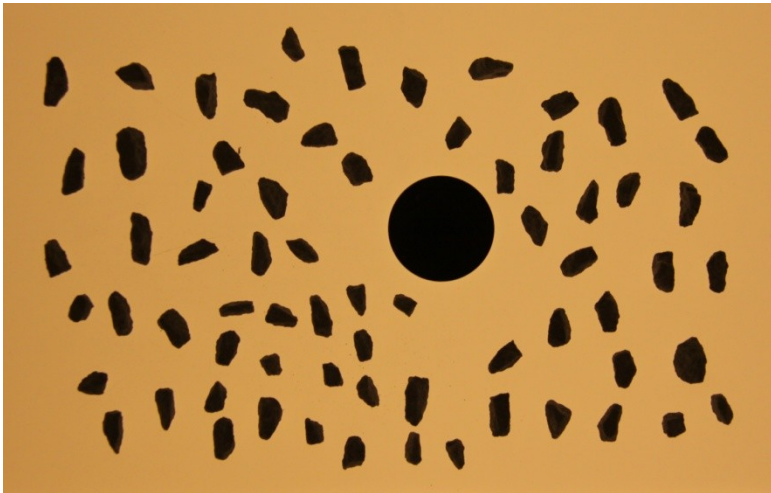
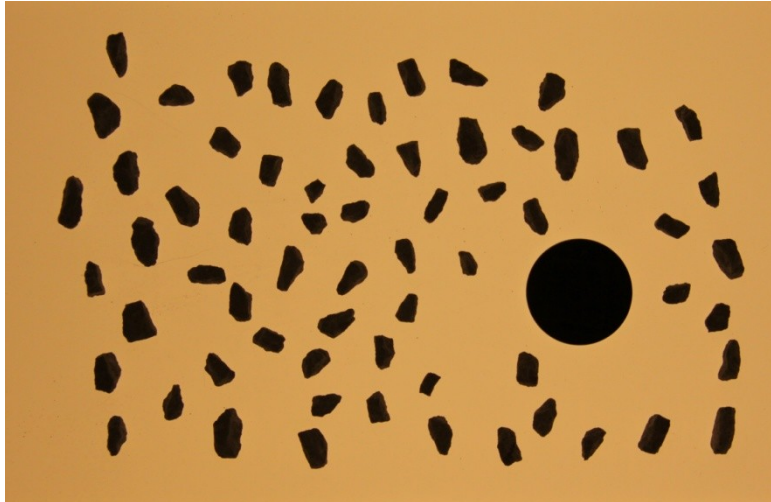
Particles of Test 9:

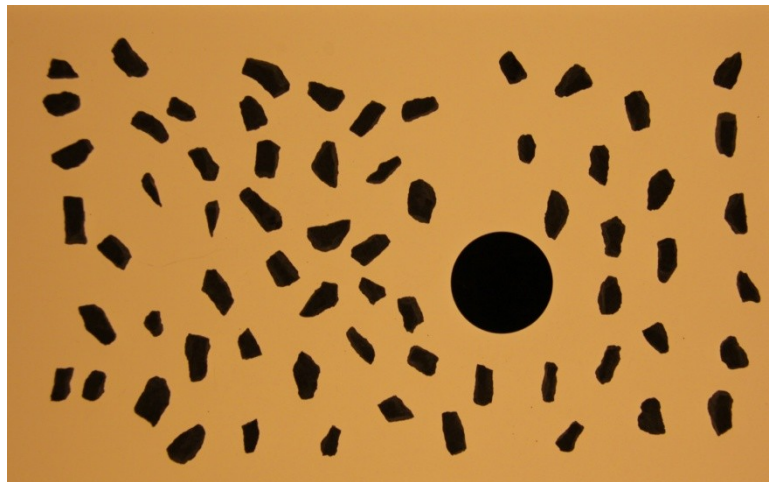
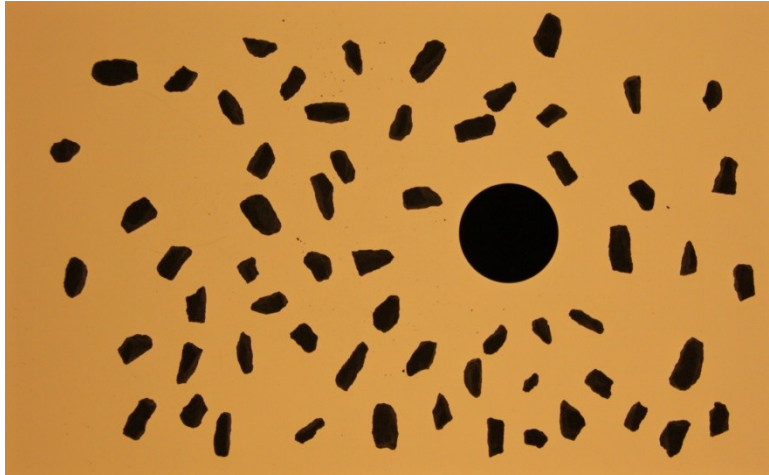




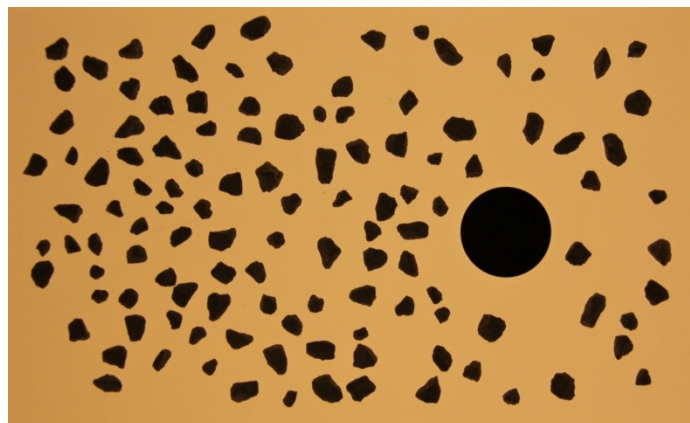
Particles of Test 10:

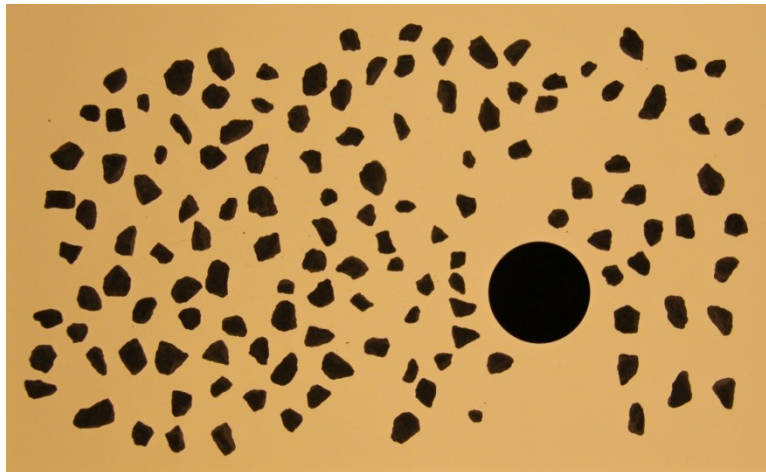
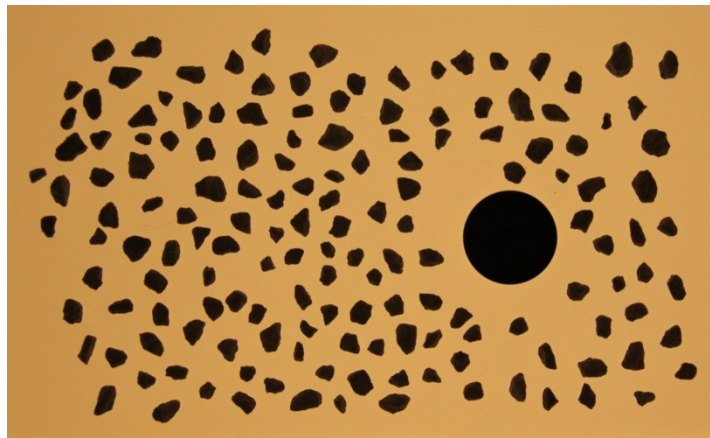
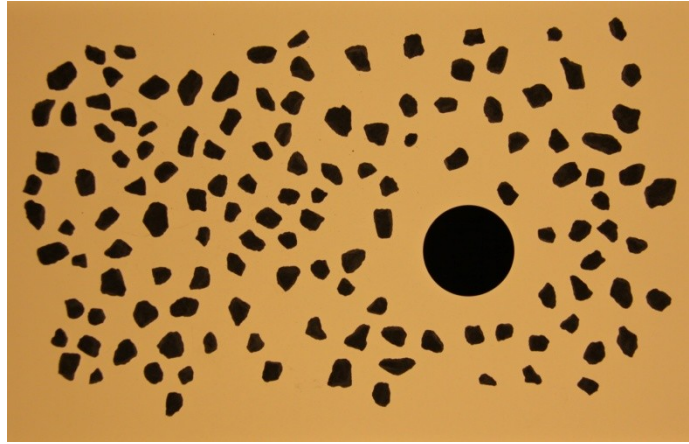


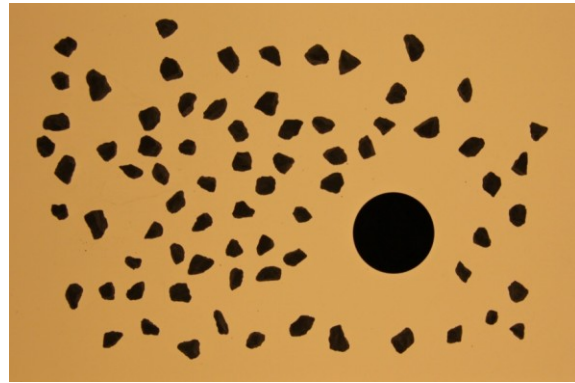
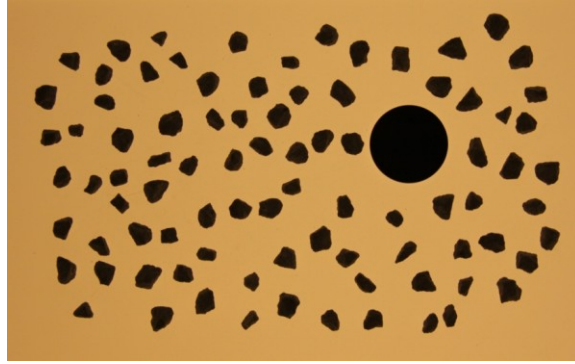




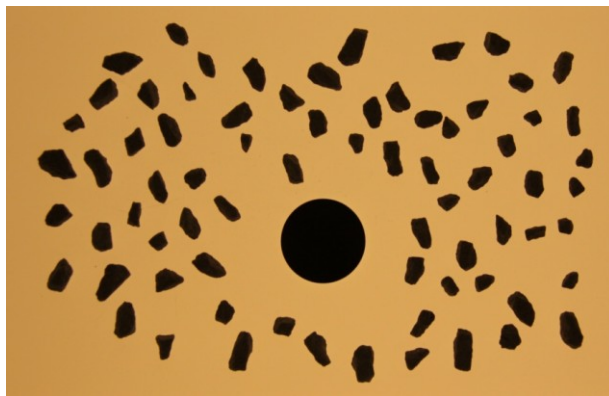
Particles of Test 11:

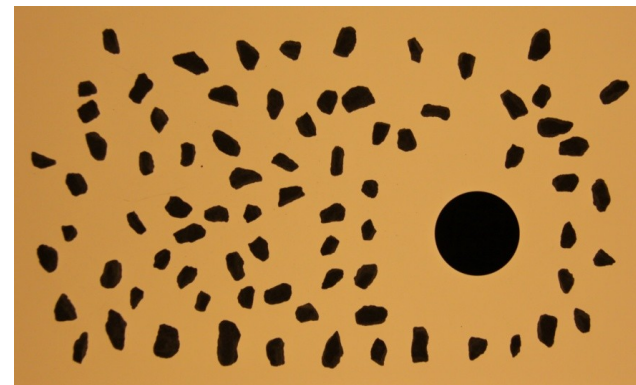
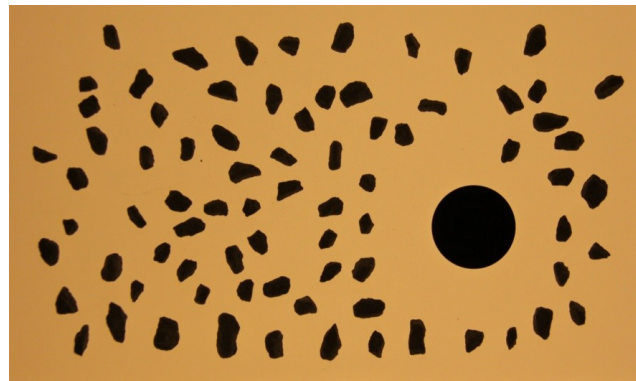
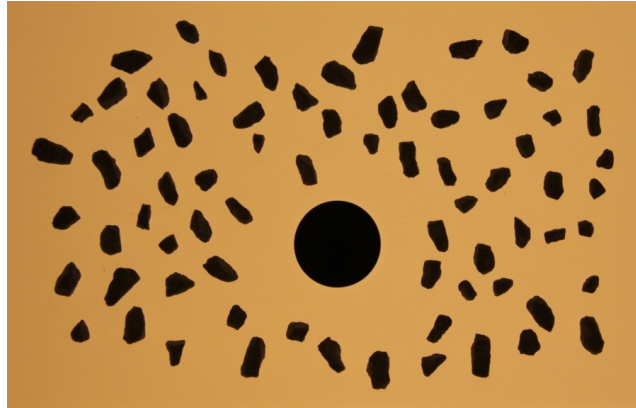


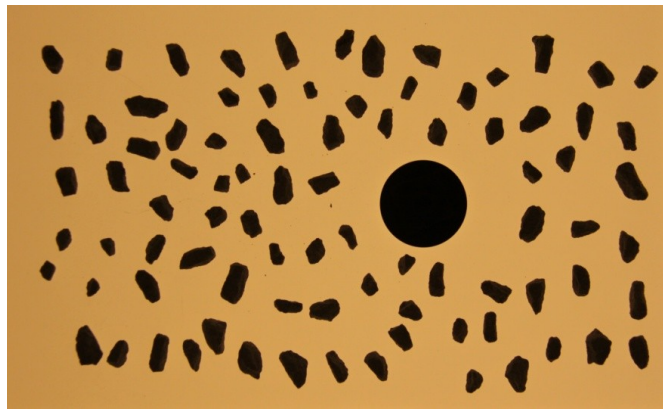
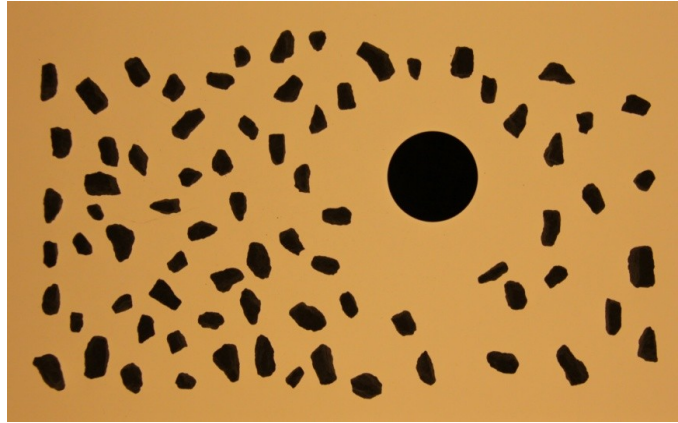




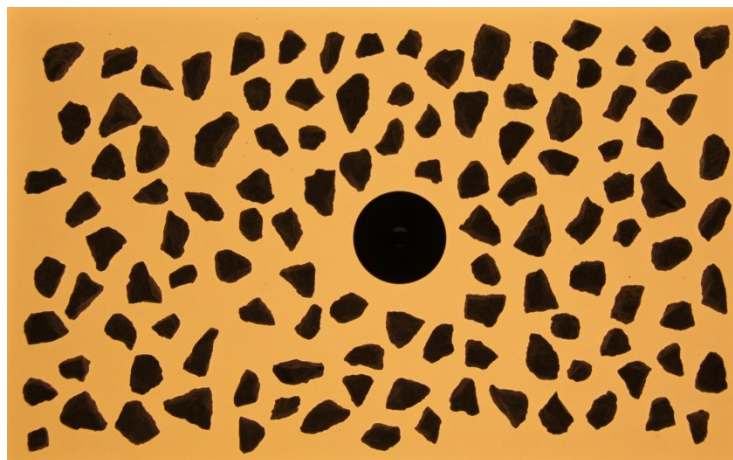
Particles of Test 12:

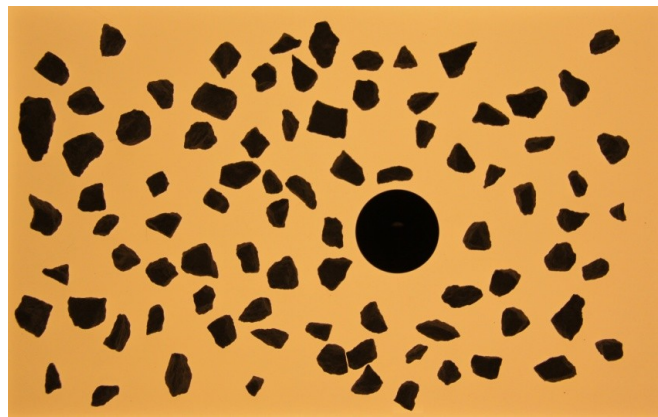
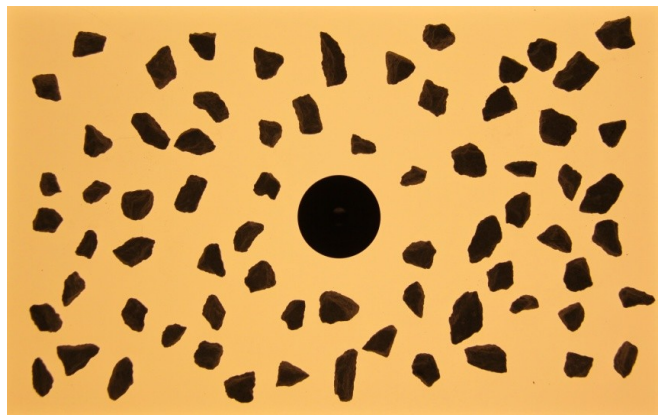
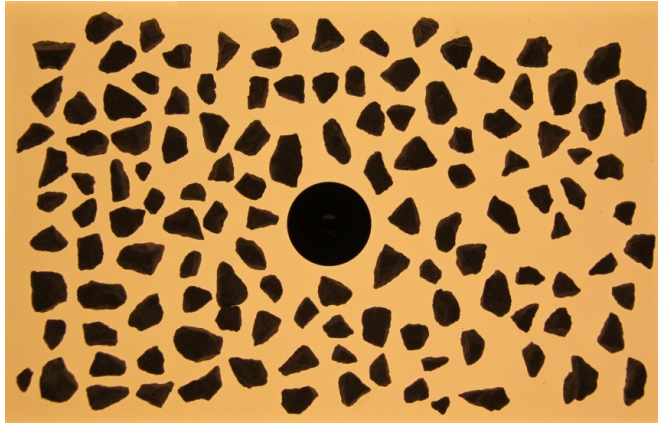


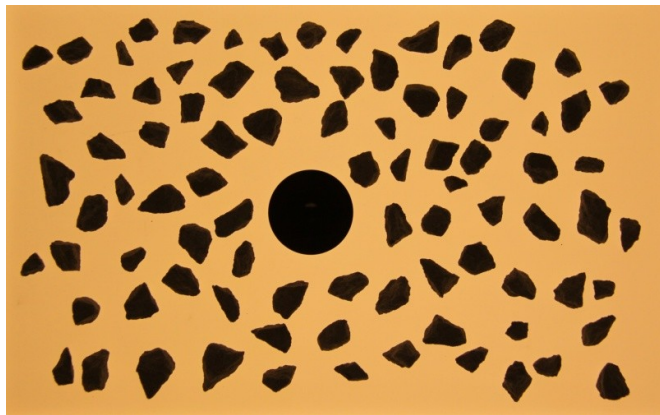
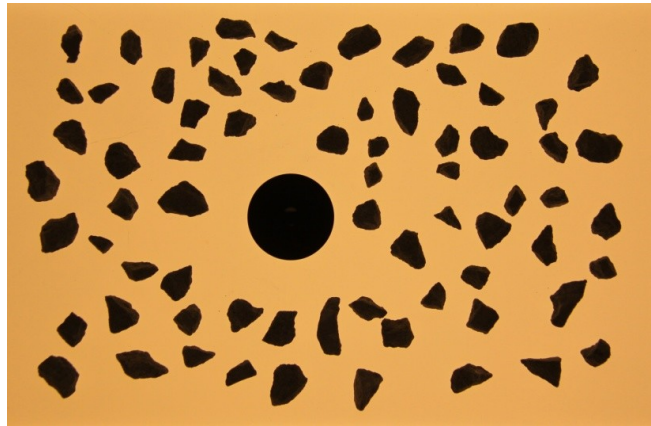
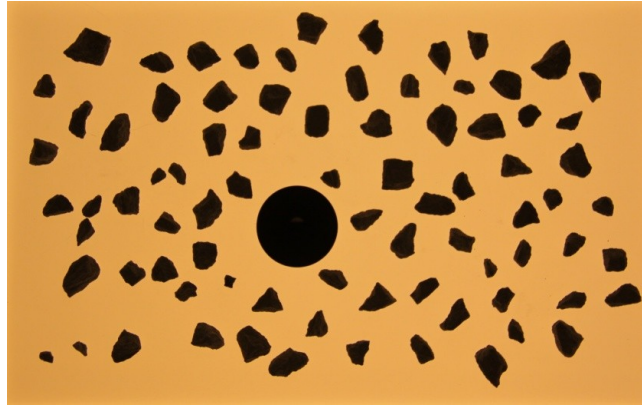


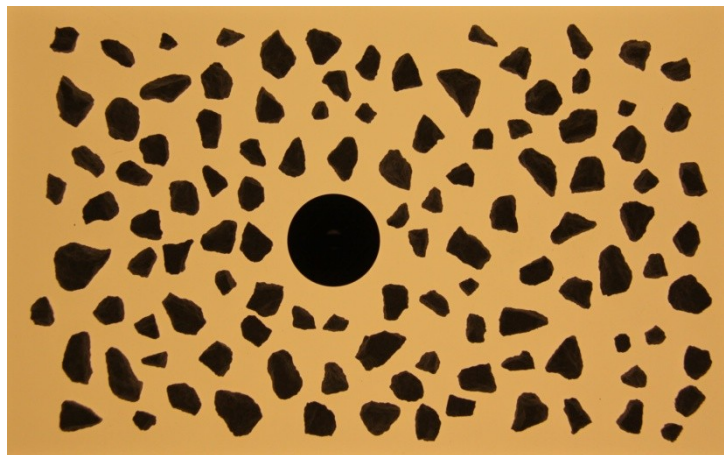
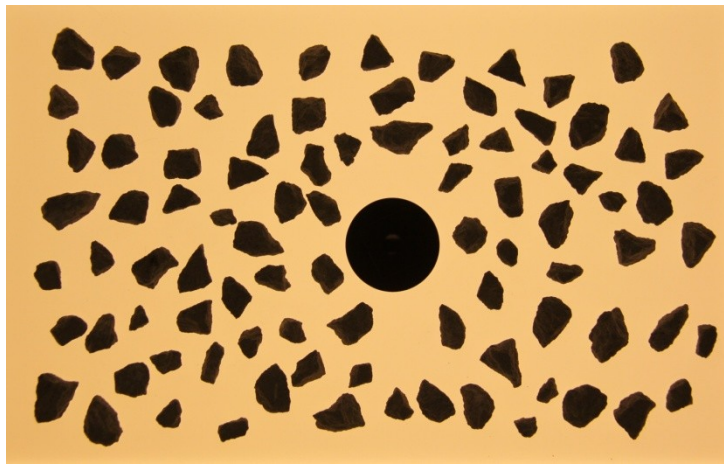
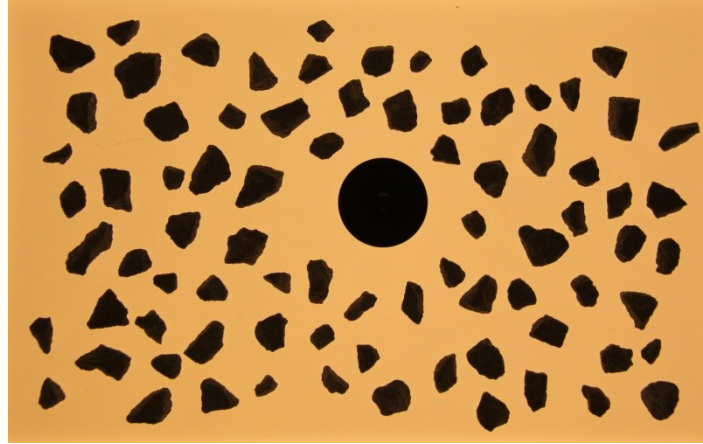


Particles of Test 13:

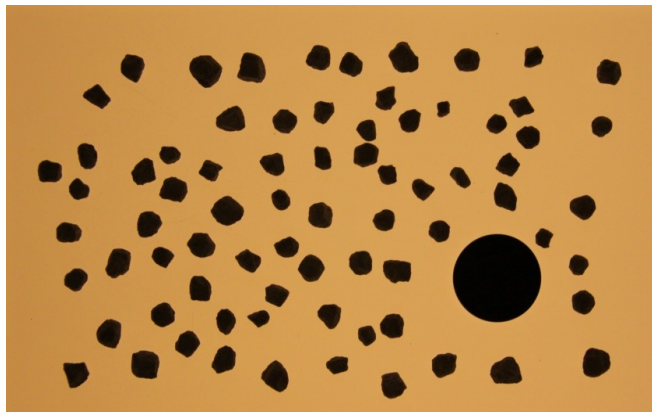
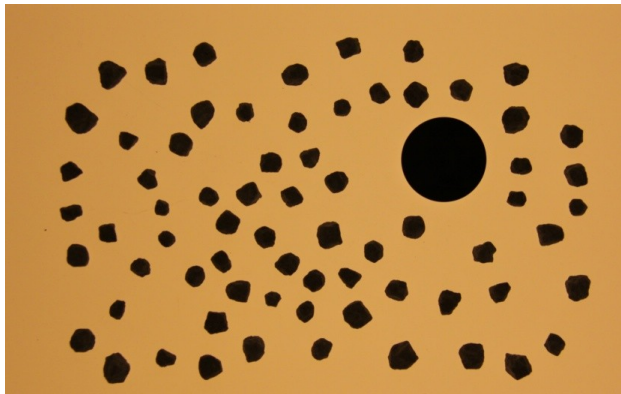
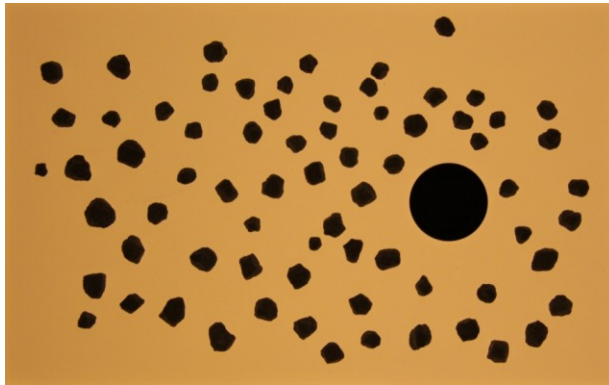


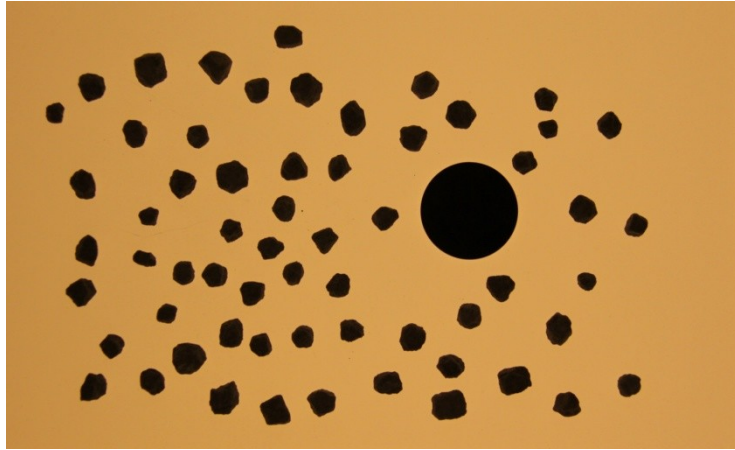




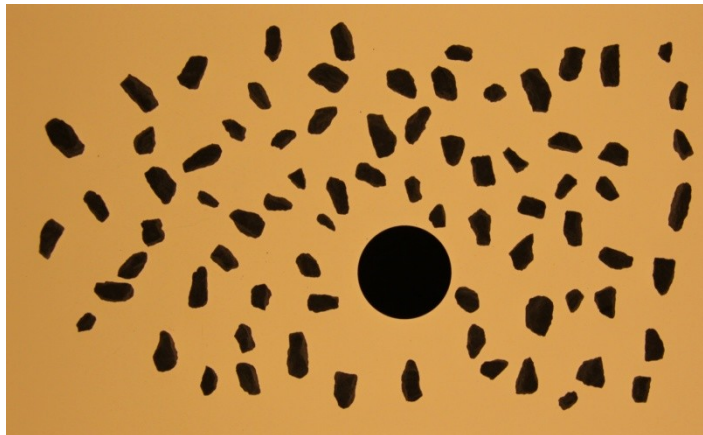
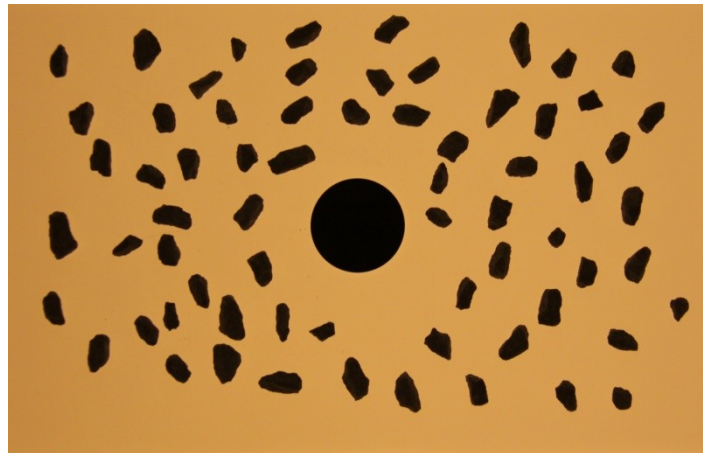


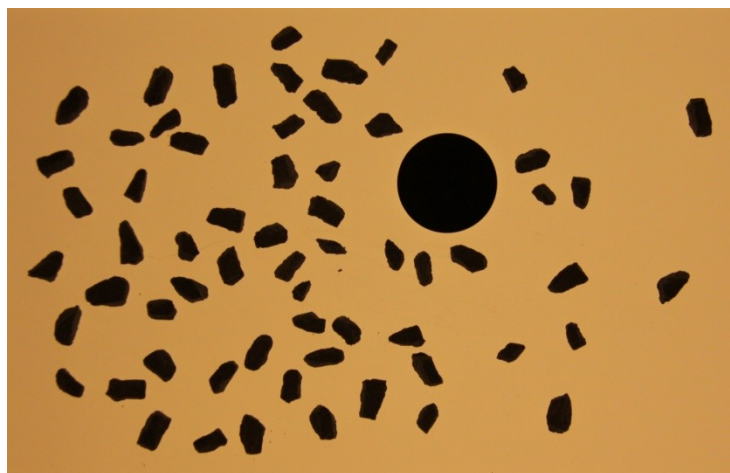
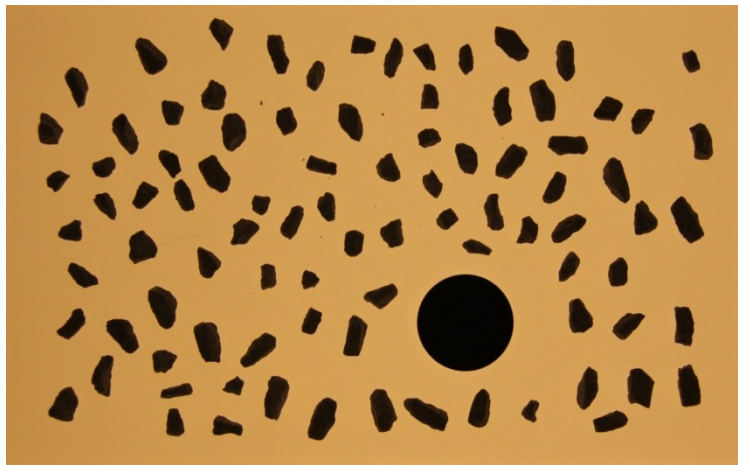
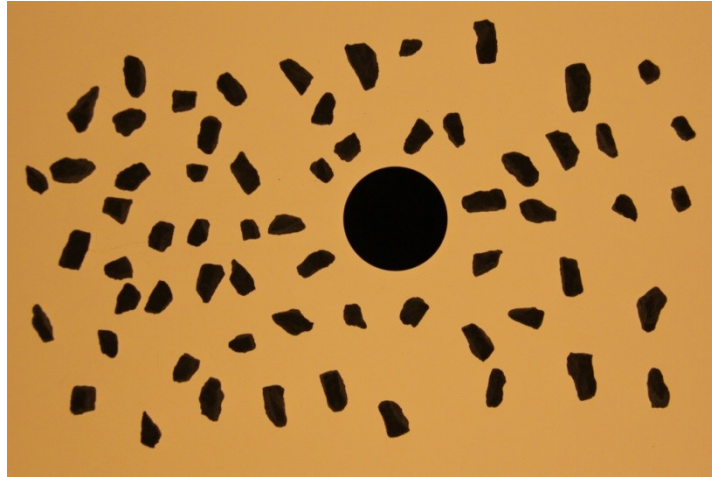
Particles of Test 14:



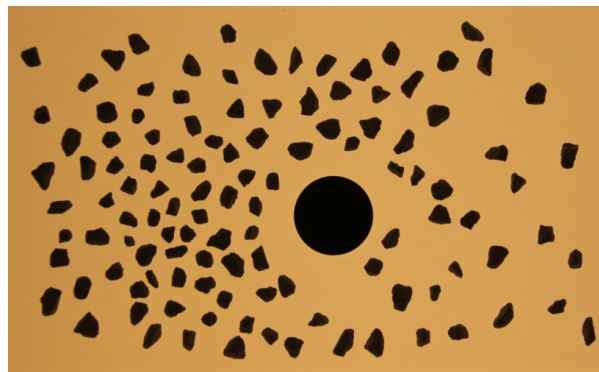
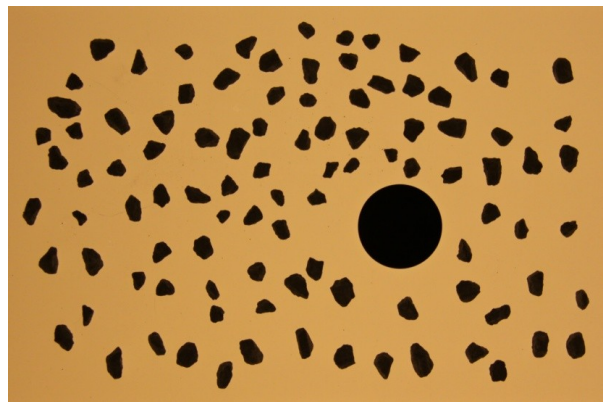
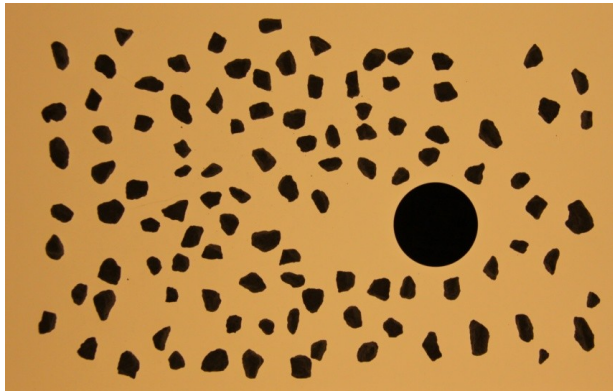


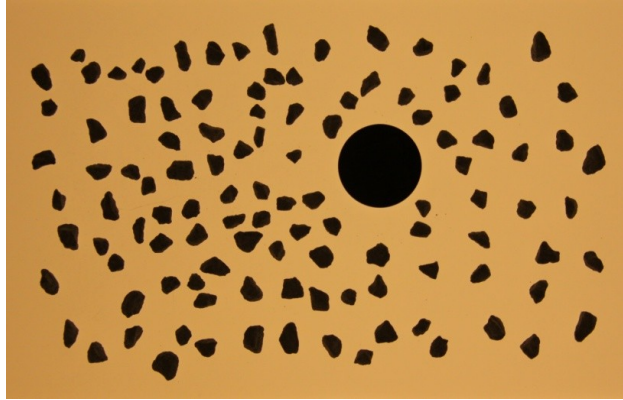
Particles of Test 15:



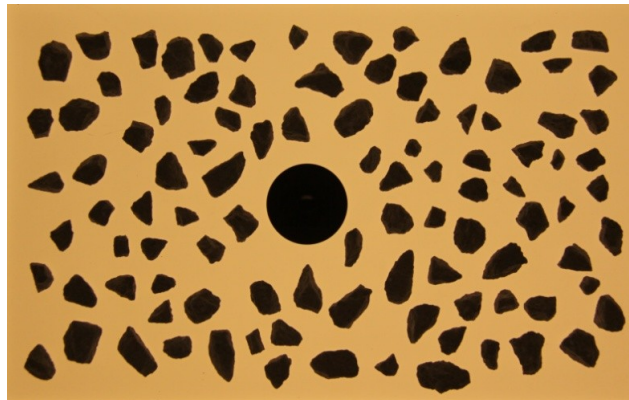
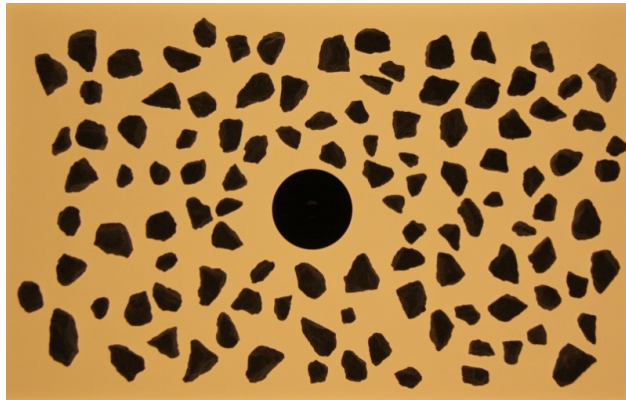


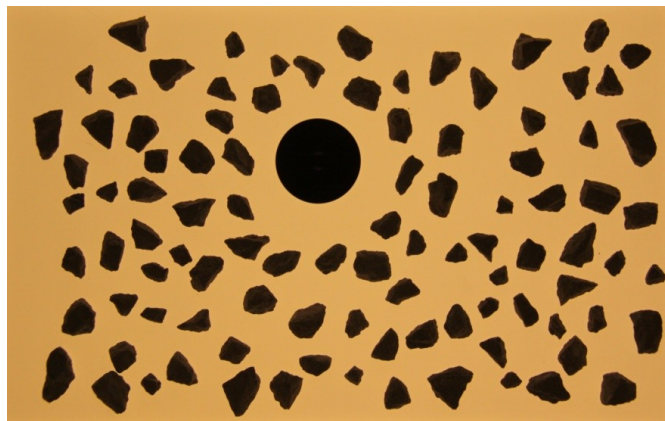
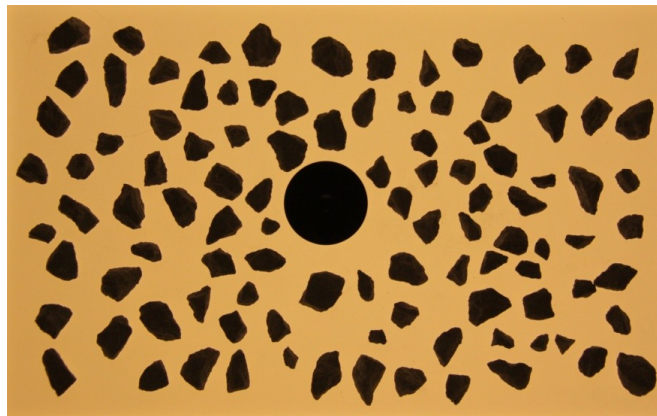
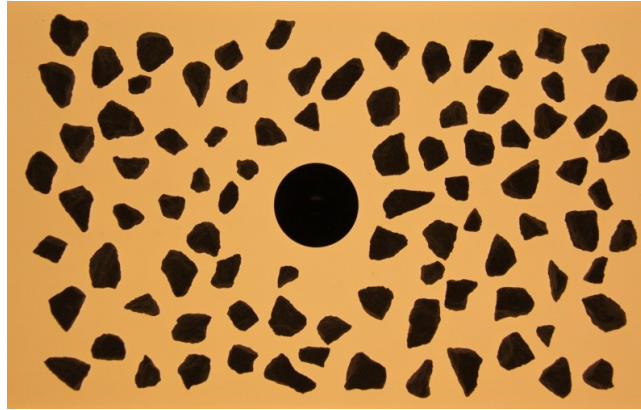
Particles of Test 16:

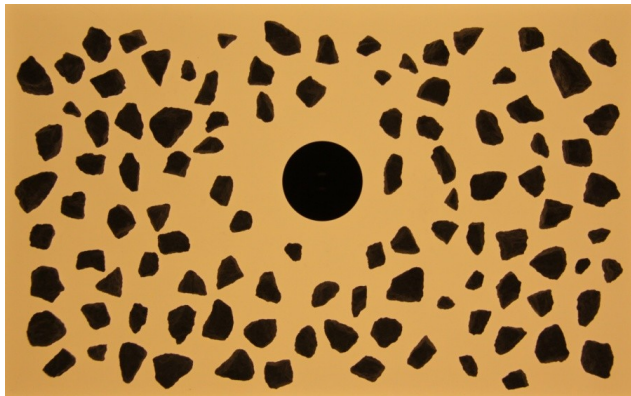
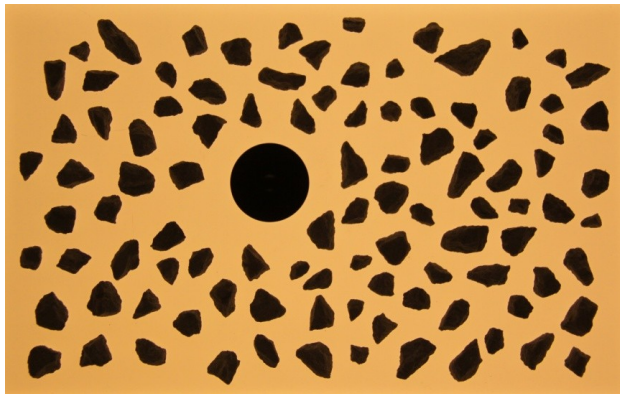
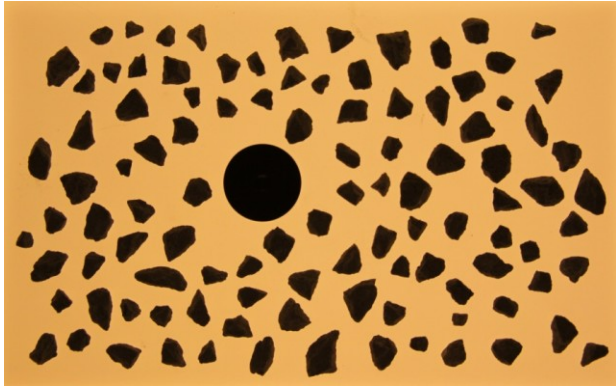




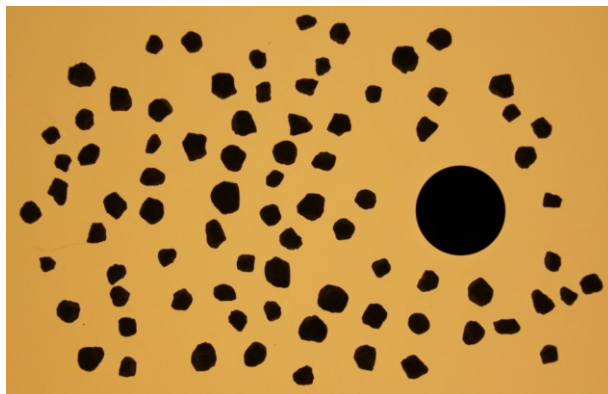
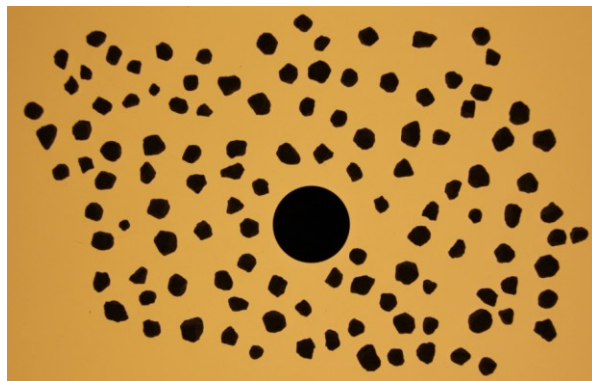
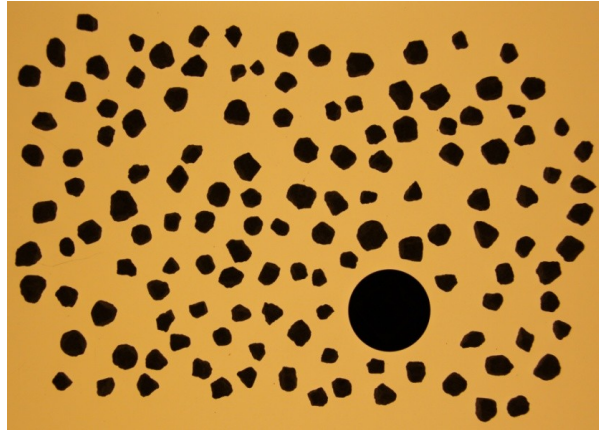
Particles of Test 17:



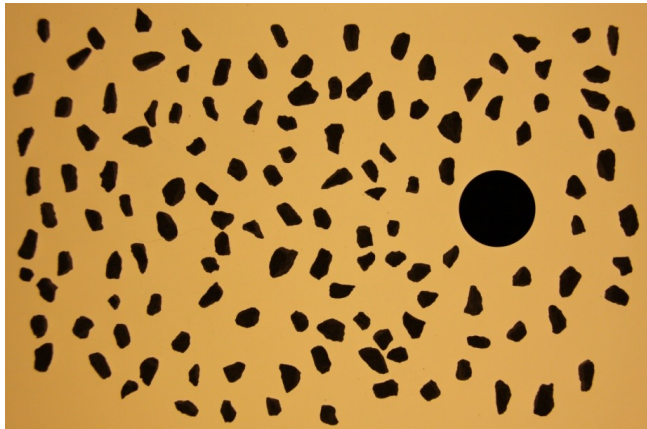
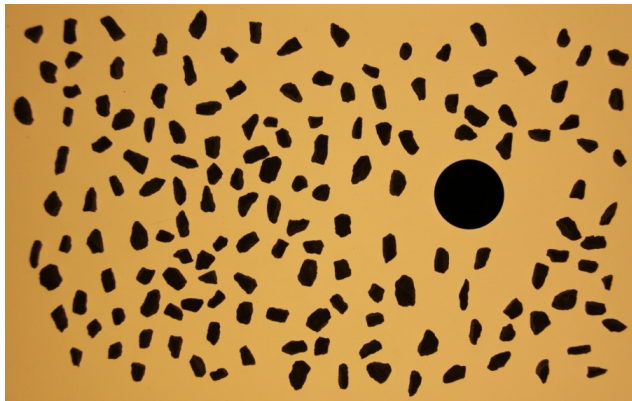
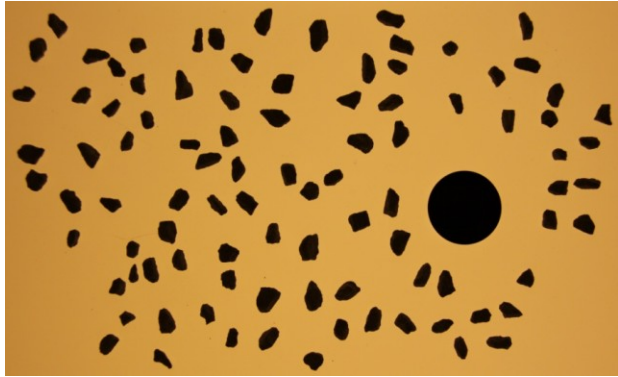


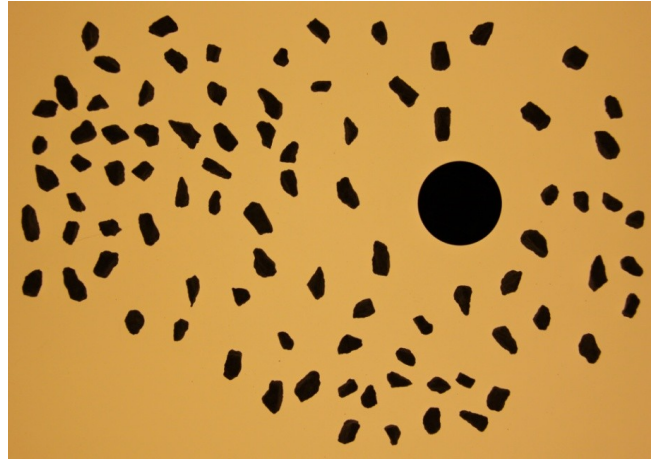


Particles of Test 18:

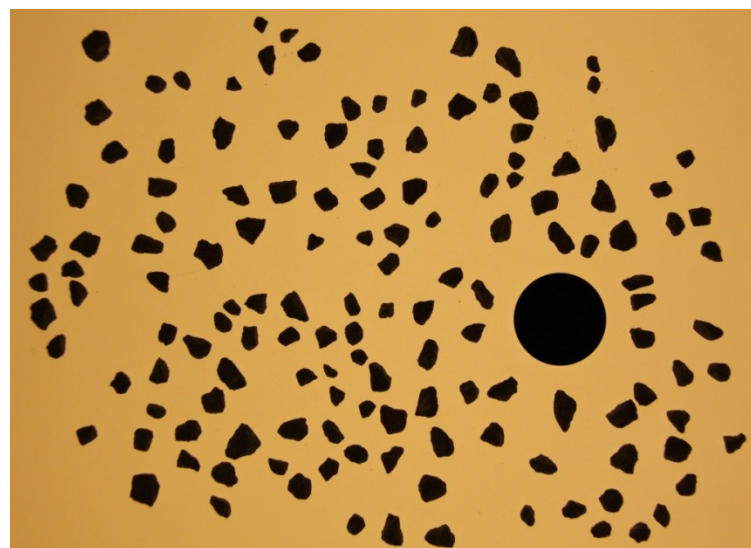
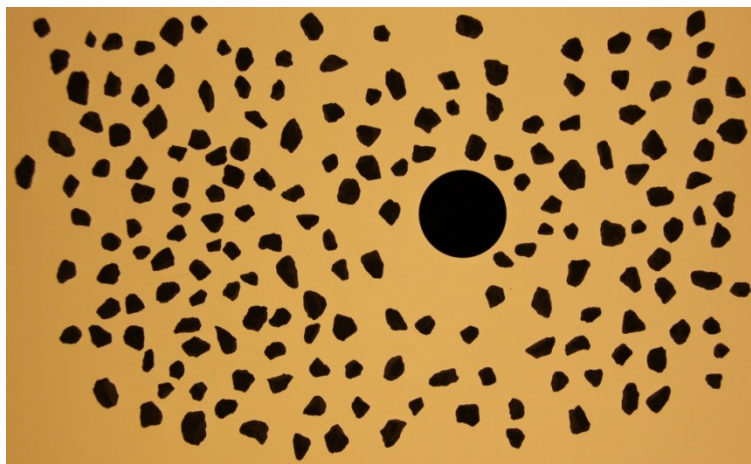


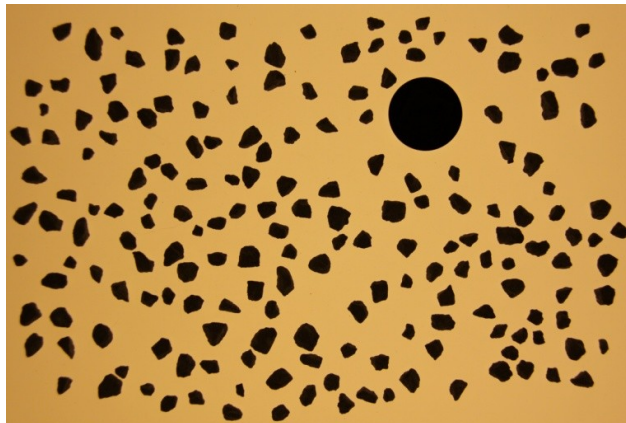
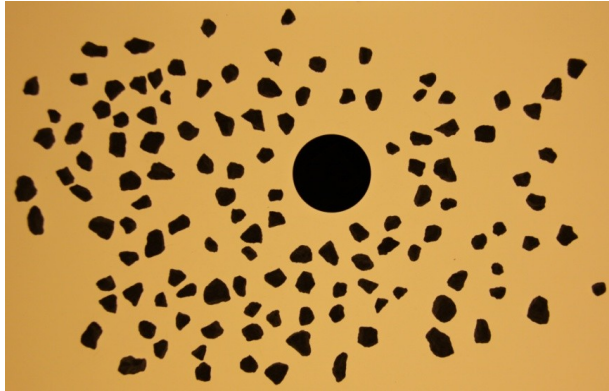
Particles of Test 19:



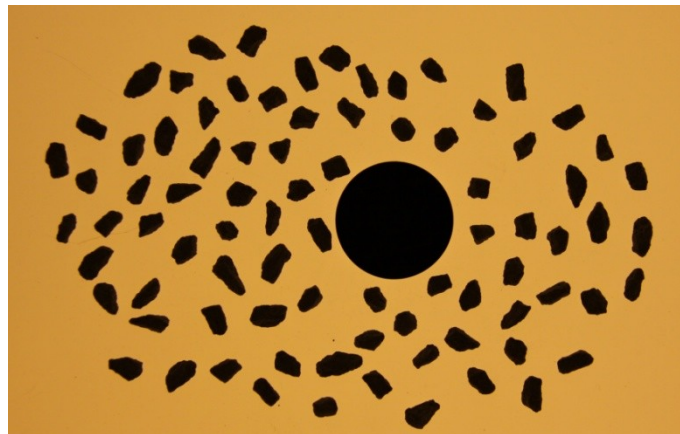


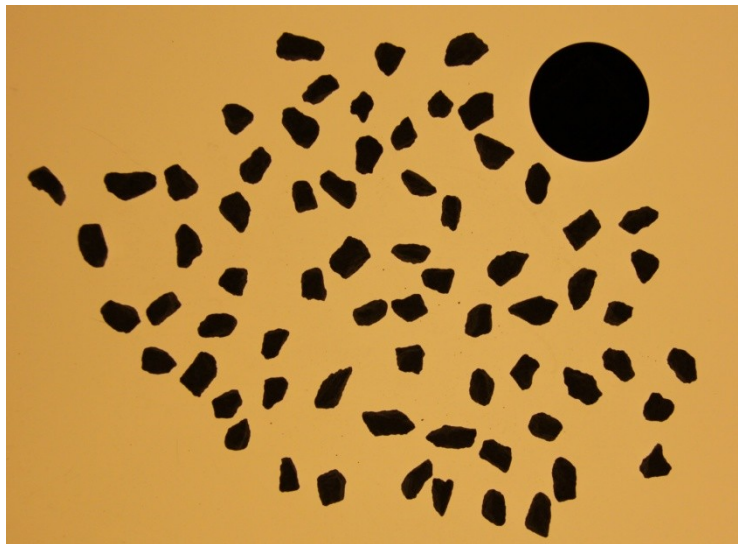
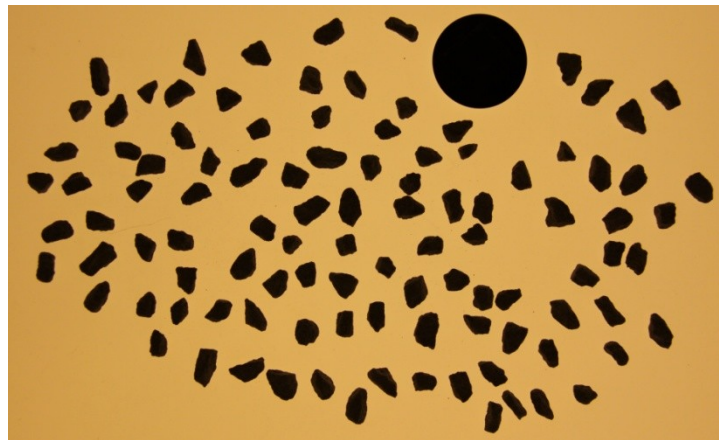
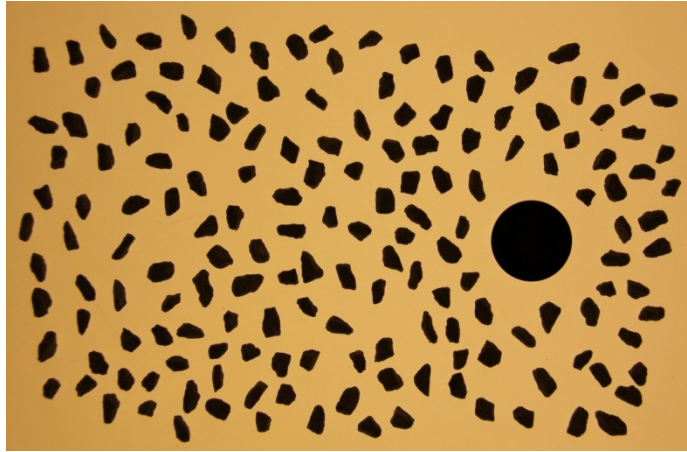
Particles of Test 20:



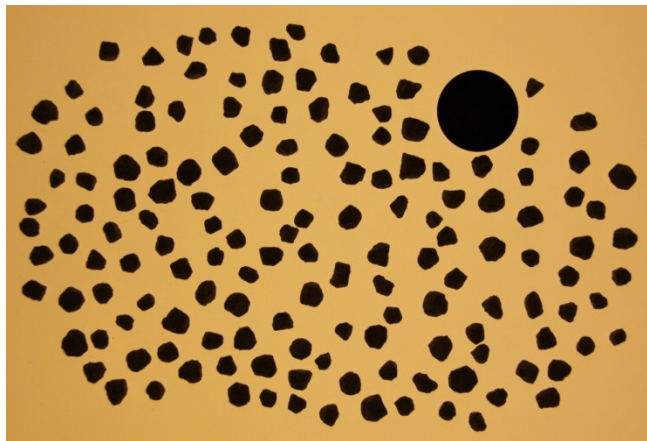
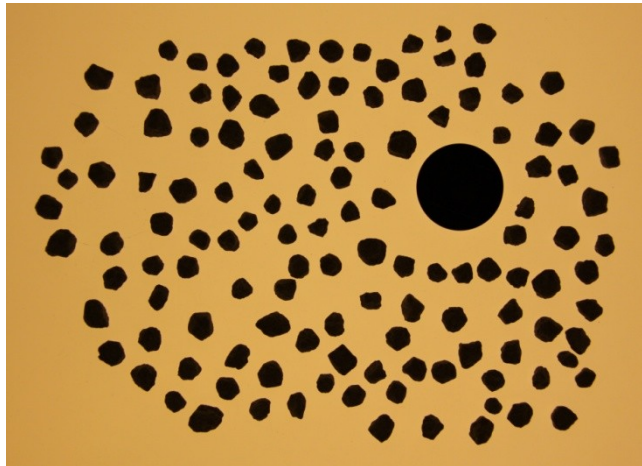
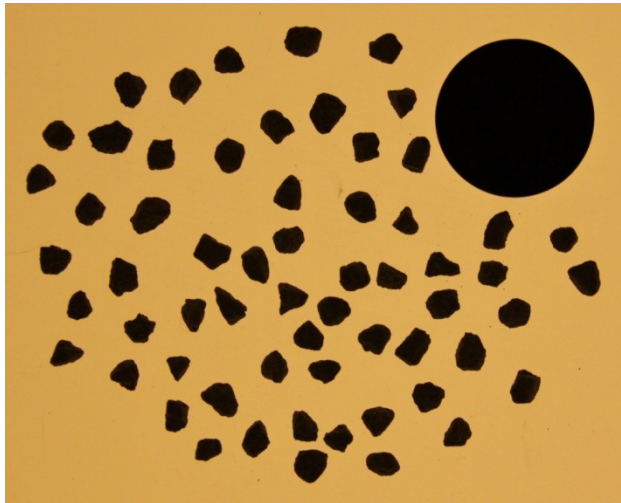


Particles of Test 21:

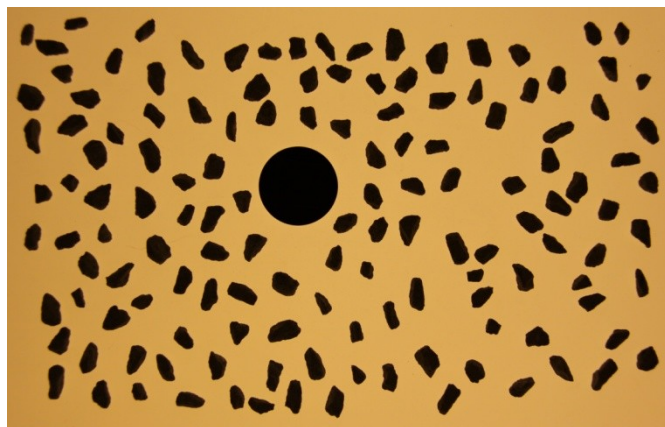
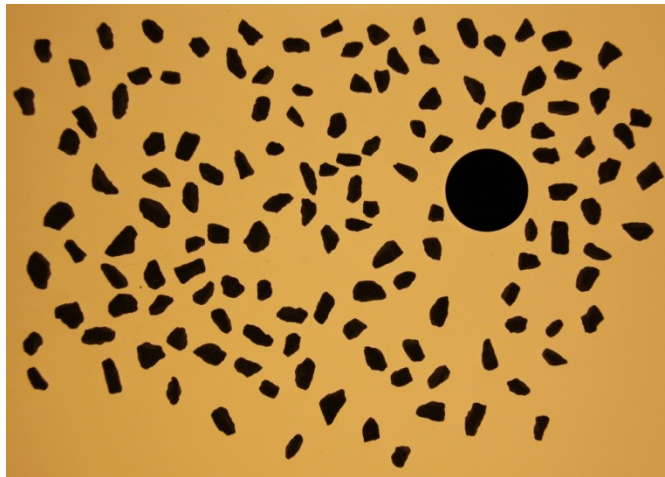
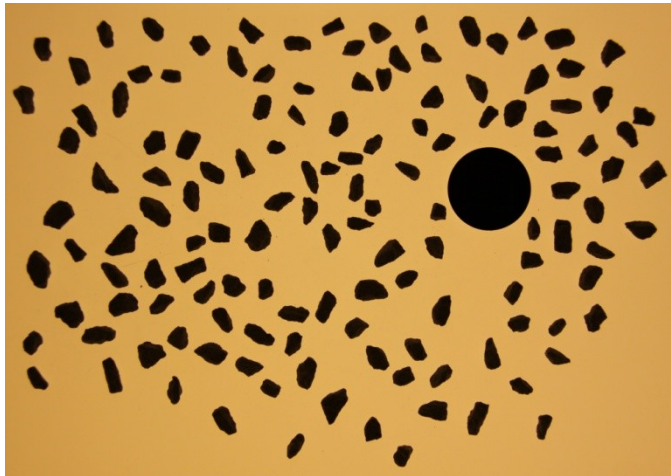


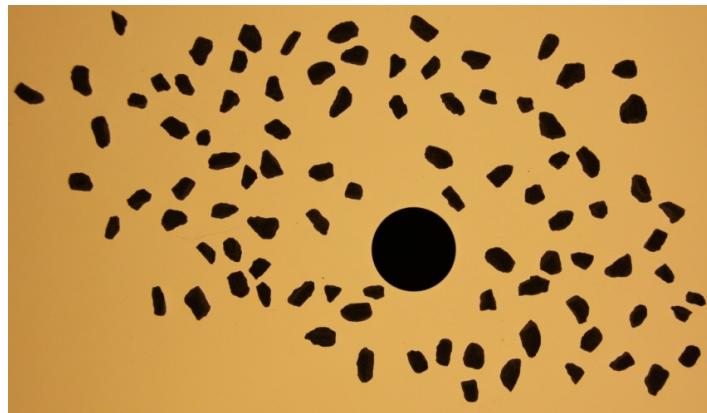
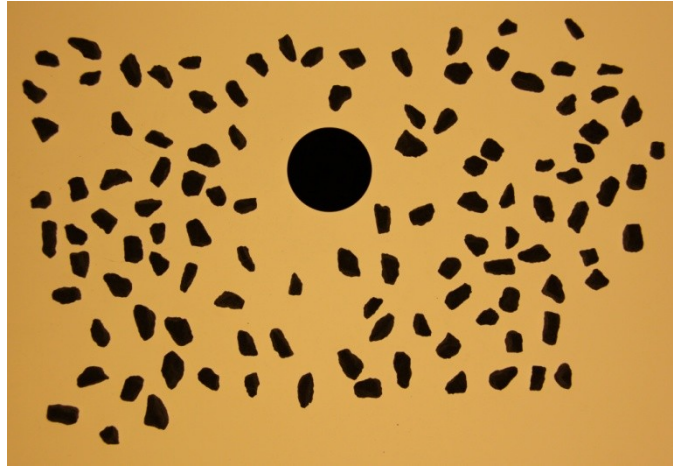


Particles of Test 22:

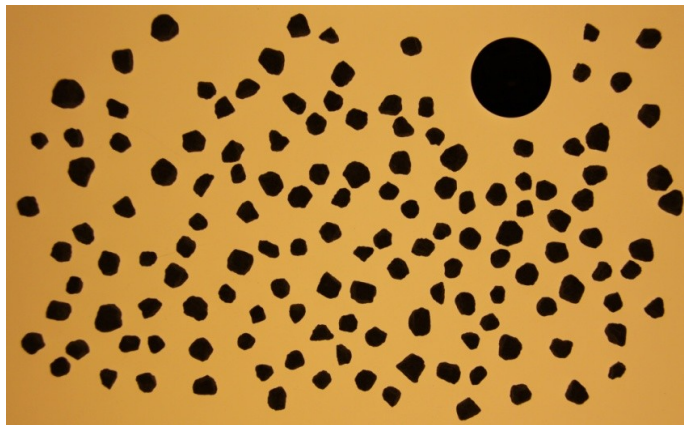


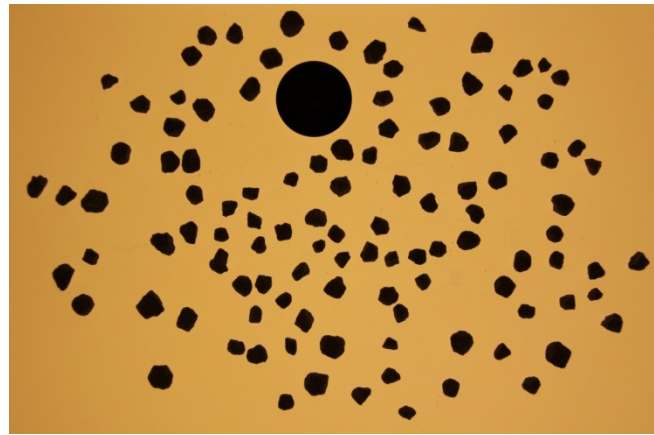
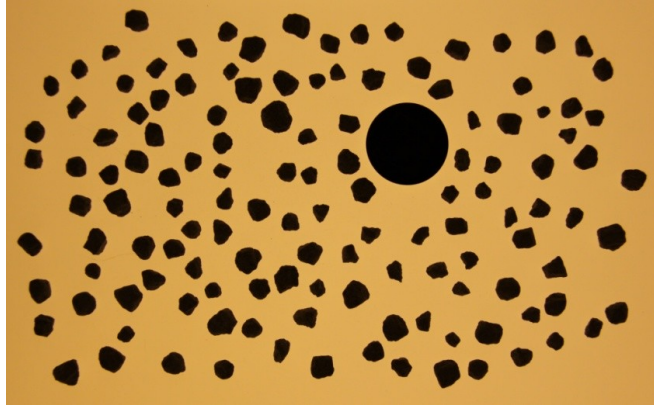
Particles of Test 23:



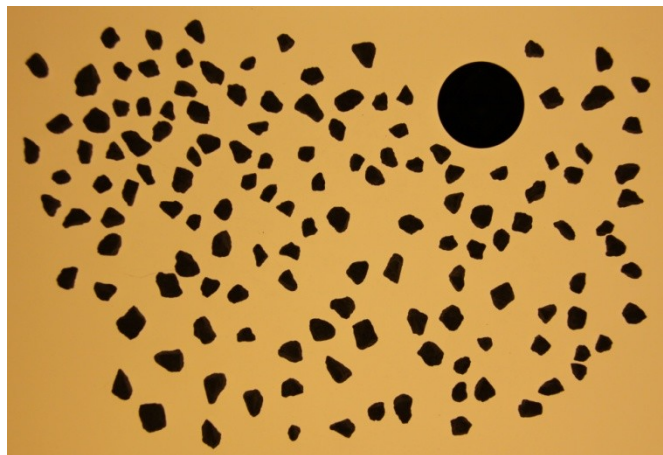


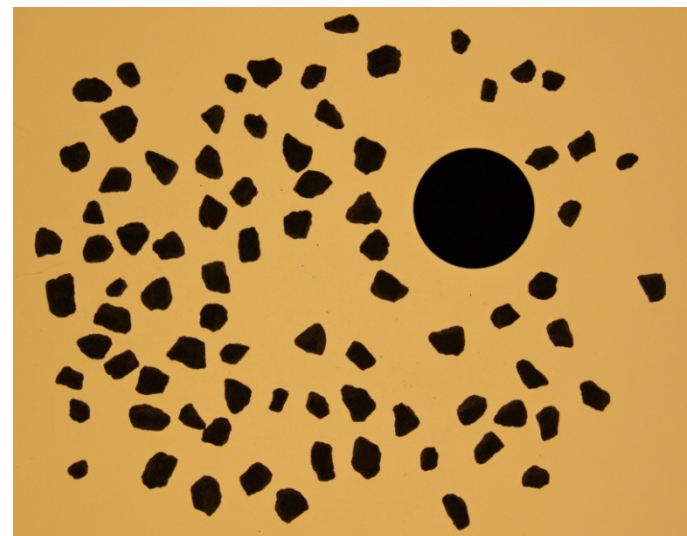
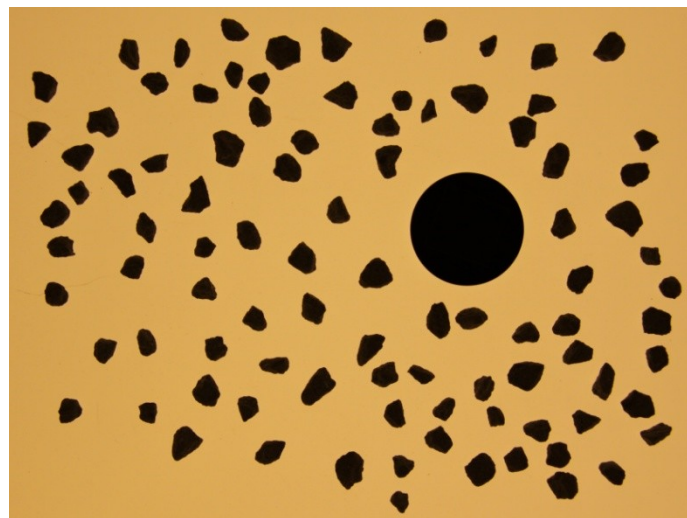
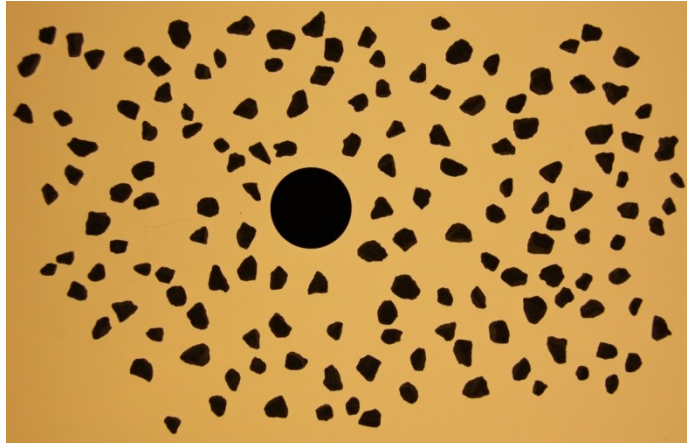
Particles of Test 24:

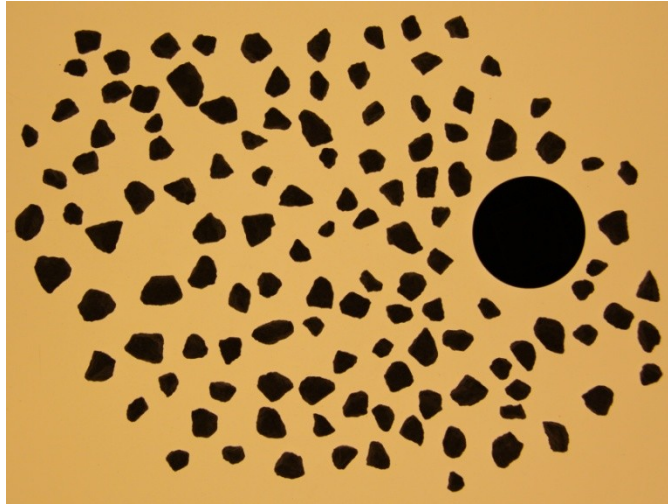




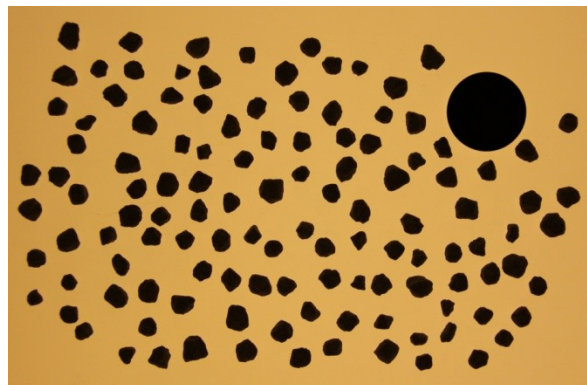
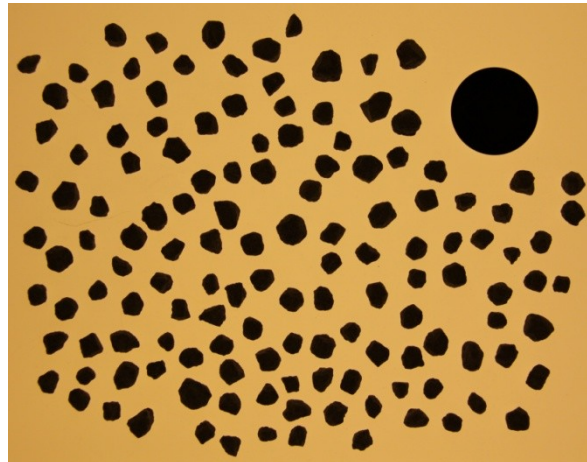
Particles of Test 25:

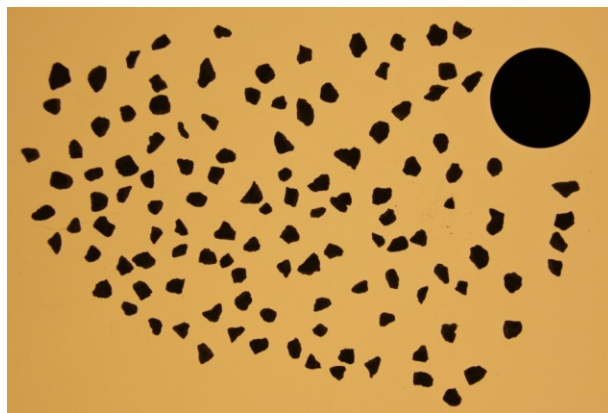
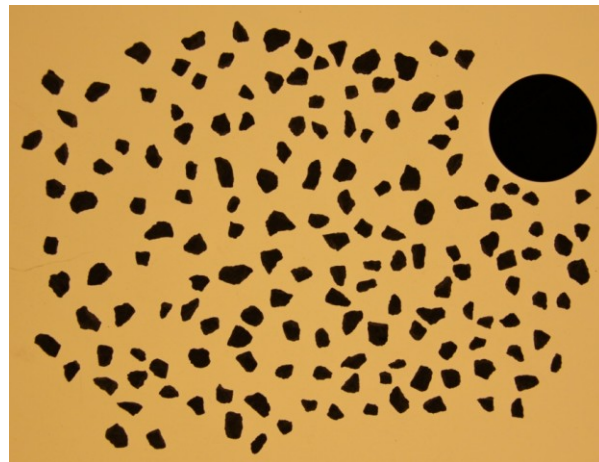
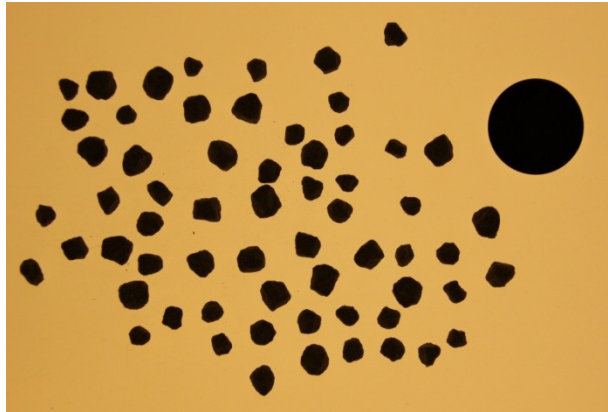




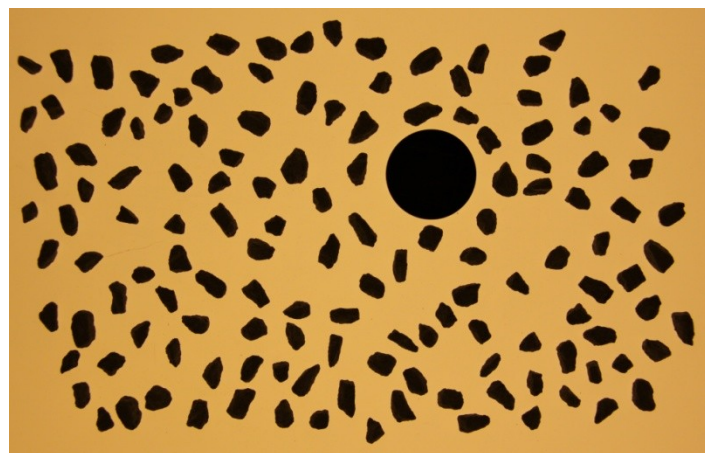
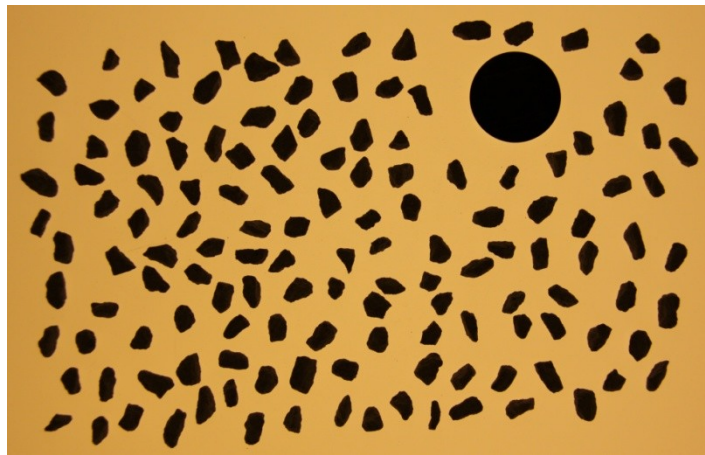
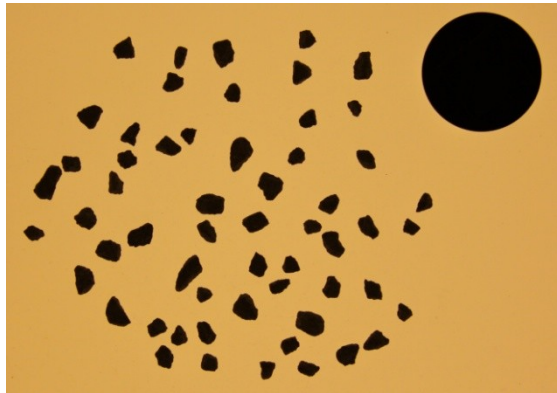


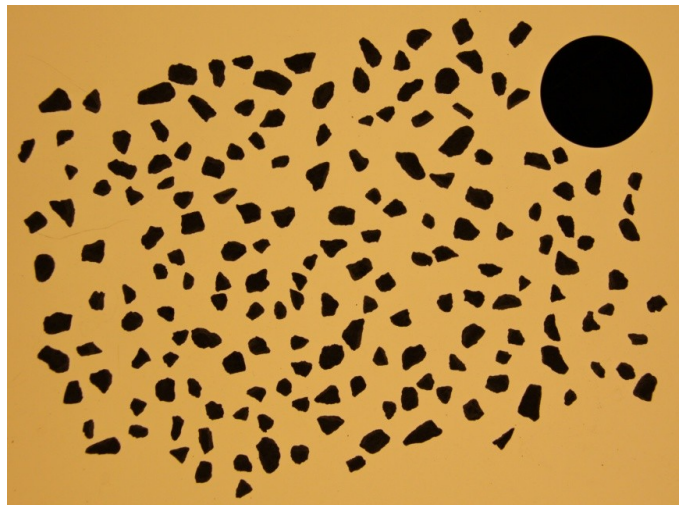
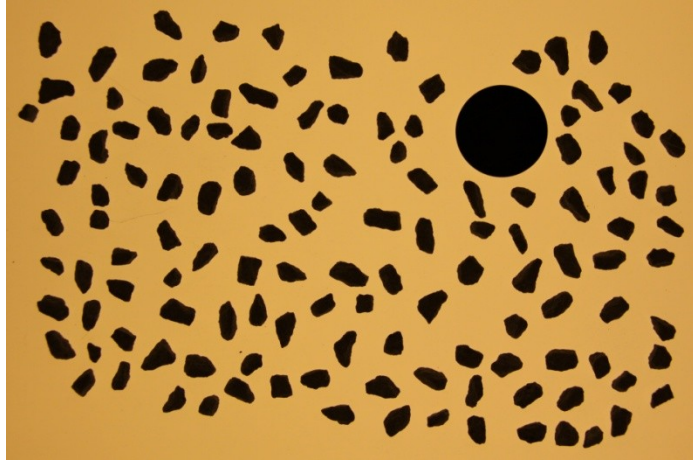
Particles of Test 26:





Particles of Test 27:





APPENDIX E

DEVELOPED CODE USING MATLAB

This appendix contains the developed code to determine the particle shape characteristics through using MATLAB.

```

function [ b ] = angularity( a )
t
%UNTITLED Summary of this function goes here
% Detailed explanation goes here
%%%%%%%%%%%%%%%%%%%%%%%%%%%%%%%%%%%%%%%%%%%%%%%%%%%%%%%%%%%%%%%%%%%%%%%%
pics = dir('*.jpg');
for k = 1:length(pics)
filename = pics(k).name;
I = imread(filename);
%I=imread('d.jpg');
imshow(I, []);

%%%%%%%%%%%%%%%%%%%%%%%%%%%%%%%%%%%%%%%%%%%%%%%%%%%%%%%%%%%%%%%%%%%%%%%%Convert to binary image
BW0=im2bw(I);
%figure; imshow(BW0, []);
%level = graythresh(I);
%BW0 = im2bw(I,level);
%figure; imshow(BW0, []);

%%%%%%%%%%%%%%%%%%%%%%%%%%%%%%%%%%%%%%%%%%%%%%%%%%%%%%%%%%%%%%%%%%%%%%%%calculate the complement of image
BW=imcomplement(BW0);
in=load('input.txt');
%figure; imshow(BW, []);

%%%%%%%%%%%%%%%%%%%%%%%%%%%%%%%%%%%%%%%%%%%%%%%%%%%%%%%%%%%%%%%%%%%%%%%%Filling holes inside the objects
BW2 = imfill(BW,in(1), 'holes');
%figure; imshow(BW2, []);

%%%%%%%%%%%%%%%%%%%%%%%%%%%%%%%%%%%%%%%%%%%%%%%%%%%%%%%%%%%%%%%%%%%%%%%%Removing the very small objects
BW3 = bwareaopen(BW2,in(2),in(1));
%figure; imshow(BW3, []);
%imwrite(BW3,'d6.jpg');

%%%%%%%%%%%%%%%%%%%%%%%%%%%%%%%%%%%%%%%%%%%%%%%%%%%%%%%%%%%%%%%%%%%%%%%%Detecting the boundary of objects
Boundary=boundaries(BW3,in(1), 'cw');

%%%%%%%%%%%%%%%%%%%%%%%%%%%%%%%%%%%%%%%%%%%%%%%%%%%%%%%%%%%%%%%%%%%%%%%%Detecting the region properties of
objects
Regin=regionprops(BW3, 'all');

%%%%%%%%%%%%%%%%%%%%%%%%%%%%%%%%%%%%%%%%%%%%%%%%%%%%%%%%%%%%%%%%%%%%%%%%
%%%%%%%%%%%%%%%%%%%%%%%%%%%%%%%%%%%%%%%%%%%%%%%%%%%%%%%%%%%%%%%%%%%%%%%%
%%%%%%%%%%%%%%%%%%%%%%%%%%%%%%%%%%%%%%%%%%%%%%%%%%%%%%%%%%%%%%%%%%%%%%%% Analysis of Shape %%%%%%%%%
%
%
%
[m1,n1]=size(Boundary);

AngularityIndex=zeros(m1,1);
Convexity=zeros(m1,1);
%%%%%%%%%%%%%%%%%%%%%%%%%%%%%%%%%%%%%%%%%%%%%%%%%%%%%%%%%%%%%%%%%%%%%%%%
AreaGrain=zeros(m1,1);

AngularityIndexEdit=zeros(m1,1);

```



```

ConvexityEdit=zeros(m1,1);

for h=1:m1
    %$$$$$$$$$$$$$$$$ Area of Grains
    AreaGrain(h,1)=Regin(h,1).Area;

    CentPoint=Regin(h,1).Centroid;

    %*****
    boun=Boundary{h,1};
    bounx=boun(:,2);
    bouny=boun(:,1);
    %****
    %figure; scatter(bounx,bouny);
    %
    %*****
    [m,n]=size(boun);
    o=zeros(m,n);
    o(:,1)=bounx-CentPoint(1,1);
    o(:,2)=bouny-CentPoint(1,2);

    b=zeros(m,n);
    b(:,1)=o(:,1);
    b(:,2)=-1*o(:,2);

    [TA0,R0] = cart2pol(b(:,1),b(:,2));
    %

    %*****
    sort0=zeros(m-1,n);
    for i=1:m-1
        if TA0(i,1)<0
            sort0(i,1)=TA0(i,1)+(2*pi);
        else sort0(i,1)=TA0(i,1);
        end
        sort0(i,2)=R0(i,1);
    end
    sorted=sortrows(sort0,1);
    [~,ix]=unique(sorted(:,1), 'first');
    finalSorted=sorted(sort(ix),:);
    TA=finalSorted(:,1);
    R=finalSorted(:,2);

    a=Regin(h,1).MajorAxisLength/2;
    b=Regin(h,1).MinorAxisLength/2;
    or=Regin(h,1).Orientation*pi/180;
    [m2,n2]=size(TA);
    rEllip=zeros(m2,1);
    for i=1:m2
        rEllip(i)=(a*b)./( (((b*cos(TA(i)-or)).^2)+((a*sin(TA(i)-or)).^2)).^0.5);
    end
    %

```

```

PerEllip=2*pi*(((a^2)+(b^2))/2)^0.5;
%*****
[m3,n3]=size(Regin(h,1).ConvexHull);

%CCCCCCCCCCCCCCCC
[m4,n4]=size(T);
AngularityIndex(h,1)=0;
for i=1:m4
    AngularityIndex(h,1)=AngularityIndex(h,1)+((abs(R(i)-
rEllip(i)))/rEllip(i));
end

%CCCCCCCCCCCCCCCC
%CCCCCCCCCCCCCCCC
Convexity(h,1)=(Regin(h,1).Solidity)^0.5;

%CCCCCCCCCCCCCCCC
%
%

end

$$$$$$$$$$$$$$$$$$$$$$$$$$$$$$$$$$$$$$$$
$$$$$$$$$$$$$$$$$$$$$$$$$$$$$$$$$$$$$$$$
[MaxRow,MaxColumn]=find(AreaGrain==max(AreaGrain));

AngularityIndexEdit=AngularityIndex;
ConvexityEdit=Convexity;

AngularityIndexEdit(MaxRow,:)=[];
ConvexityEdit(MaxRow,:)=[];

Angularity.AngularityIndex(1,k)={AngularityIndexEdit};
Angularity.Convexity(1,k)={ConvexityEdit};

Statistic.AngularityIndex.mean(1,k)=mean(AngularityIndexEdit);
Statistic.AngularityIndex.min(1,k)=min(AngularityIndexEdit);
Statistic.AngularityIndex.max(1,k)=max(AngularityIndexEdit);
Statistic.AngularityIndex.StandardDeviation(1,k)=std(AngularityInd
exEdit);

Statistic.Convexity.mean(1,k)=mean(ConvexityEdit);
Statistic.Convexity.min(1,k)=min(ConvexityEdit);
Statistic.Convexity.max(1,k)=max(ConvexityEdit);

```

Appendix E

```
Statistic.Convexity.StandardDeviation(1,k)=std(ConvexityEdit);

end

AngularityIndexOverall=[];
ConvexityOverall=[];
for s=1:k

AngularityIndexOverall=[AngularityIndexOverall;Angularity.Angulari
tyIndex{1,s}];
    ConvexityOverall=[ConvexityOverall;Angularity.Convexity{1,s}];
end

StatisticOverall.AngularityIndex.mean=mean(AngularityIndexOverall)
;
StatisticOverall.AngularityIndex.min=min(AngularityIndexOverall);
StatisticOverall.AngularityIndex.max=max(AngularityIndexOverall);
StatisticOverall.AngularityIndex.StandardDeviation=std(AngularityI
ndexOverall);

StatisticOverall.Convexity.mean=mean(ConvexityOverall);
StatisticOverall.Convexity.min=min(ConvexityOverall);
StatisticOverall.Convexity.max=max(ConvexityOverall);
StatisticOverall.Convexity.StandardDeviation=std(ConvexityOverall)
;

filename = 'angularity';

%%AngularityIndex
xlswrite(filename,AngularityIndexOverall,1,'A2')
%
xlswrite(filename,{'AngularityIndex'},1,'A1')
xlswrite(filename,{'mean'},1,'C1')
xlswrite(filename,{'mine'},1,'C2')
xlswrite(filename,{'max'},1,'C3')
xlswrite(filename,{'StandardDeviation'},1,'C4')

xlswrite(filename,StatisticOverall.AngularityIndex.mean,1,'D1')
xlswrite(filename,StatisticOverall.AngularityIndex.min,1,'D2')
xlswrite(filename,StatisticOverall.AngularityIndex.max,1,'D3')
xlswrite(filename,StatisticOverall.AngularityIndex.StandardDeviati
on,1,'D4')

%%Convexity
xlswrite(filename,ConvexityOverall,2,'A2')
%
xlswrite(filename,{'Convexity'},2,'A1')
xlswrite(filename,{'mean'},2,'C1')
xlswrite(filename,{'mine'},2,'C2')
xlswrite(filename,{'max'},2,'C3')
xlswrite(filename,{'StandardDeviation'},2,'C4')
```

```
xlswrite(filename,StatisticOverall.Convexity.mean,2,'D1')
xlswrite(filename,StatisticOverall.Convexity.min,2,'D2')
xlswrite(filename,StatisticOverall.Convexity.max,2,'D3')
xlswrite(filename,StatisticOverall.Convexity.StandardDeviation,2,'
D4')

end
function [ b ] = AngularityParameter( a )
t
%UNTITLED Summary of this function goes here
% Detailed explanation goes here
%%%%%%%%%%%%%%%%%%%%%%%%%%%%%%%%%%%%%%%%%%%%%%%%%%%%%%%%%%%%%%%%%%%%%%%%
pics = dir('*.jpg');
for k = 1:length(pics)
filename = pics(k).name;
I = imread(filename);
%I=imread('d.jpg');
imshow(I, []);

%%%%%%%%%%%%%%%%%%%%%%%%%%%%%%%%%%%%%%%%%%%%%%%%%%%%%%%%%%%%%%%%%%%%%%%%Convert to binary image
BW0=im2bw(I);
%figure; imshow(BW0, []);
%level = graythresh(I);
%BW0 = im2bw(I,level);
%figure; imshow(BW0, []);

%%%%%%%%%%%%%%%%%%%%%%%%%%%%%%%%%%%%%%%%%%%%%%%%%%%%%%%%%%%%%%%%%%%%%%%%calculate the complement of image
BW=imcomplement(BW0);
in=load('input.txt');
%figure; imshow(BW, []);

%%%%%%%%%%%%%%%%%%%%%%%%%%%%%%%%%%%%%%%%%%%%%%%%%%%%%%%%%%%%%%%%%%%%%%%%Filling holes inside the objects
BW2 = imfill(BW,in(1),'holes');
%figure; imshow(BW2, []);

%%%%%%%%%%%%%%%%%%%%%%%%%%%%%%%%%%%%%%%%%%%%%%%%%%%%%%%%%%%%%%%%%%%%%%%%Removing the very small objects
BW3 = bwareaopen(BW2,in(2),in(1));
%figure; imshow(BW3, []);
%imwrite(BW3,'d6.jpg');

%%%%%%%%%%%%%%%%%%%%%%%%%%%%%%%%%%%%%%%%%%%%%%%%%%%%%%%%%%%%%%%%%%%%%%%%Detecting the boundary of objects
Boundary=boundaries(BW3,in(1),'cw');

%%%%%%%%%%%%%%%%%%%%%%%%%%%%%%%%%%%%%%%%%%%%%%%%%%%%%%%%%%%%%%%%%%%%%%%%Convert to Gray image
GrayIm=rgb2gray(I);
%figure; imshow(GrayIm, []);

%%%%%%%%%%%%%%%%%%%%%%%%%%%%%%%%%%%%%%%%%%%%%%%%%%%%%%%%%%%%%%%%%%%%%%%%Detecting the region properties of
objects
Regin=regionprops(BW3,'all');

%%%%%%%%%%%%%%%%%%%%%%%%%%%%%%%%%%%%%%%%%%%%%%%%%%%%%%%%%%%%%%%%%%%%%%%%Detecting the region properties of
objects
%%%%%%%%%%%%%%%%%%%%%%%%%%%%%%%%%%%%%%%%%%%%%%%%%%%%%%%%%%%%%%%%%%%%%%%% In Gray Image
```

Appendix E

```
ReginGray=regionprops (BW3, GrayIm, 'all');

%
%%%%%%%%%%%%%%%%%%%%%%%%%%%%%%%%%%%%%%%%%%%%%%%%%%%%%%%%%%%%%%%%%%%%%%%% Angularity Parameter
%
%
[m1,n1]=size (Boundary);
AngularityParameter=zeros (m1,1);
AreaGrain=zeros (m1,1);

for h=1:m1
    b=Regin (h,1).ConvexHull;
    [m2,n2]=size (b);
    cp=0;

    for i=1:m2-1;
        cp=cp+(((b(i,2)-b(i+1,2))^2)+((b(i,1)-b(i+1,1))^2))^0.5;
    end

    aEllip=Regin (h,1).MajorAxisLength/2;
    bEllip=Regin (h,1).MinorAxisLength/2;
    orEllip=Regin (h,1).Orientation*pi/180;
    Ep=pi*(3*(aEllip+bEllip))-
    (((3*aEllip)+bEllip)*(aEllip+(3*bEllip)))^0.5);
    AP=(cp/Ep)^2;
    AngularityParameter (h,1)=AP;
    AreaGrain (h,1)=Regin (h,1).Area;

end

%%%%%%%%%%%%%%%%%%%%%%%%%%%%%%%%%%%%%%%%%%%%%%%%%%%%%%%%%%%%%%%%%%%%%%%%
[MaxRow,MaxColumn]=find (AreaGrain==max (AreaGrain));
AngularityParameterEdit=AngularityParameter;
AngularityParameterEdit (MaxRow,:)= [ ];

Angularity.AngularityParameter (1,k)={AngularityParameterEdit};

end

%%%%%%%%%%%%%%%%%%%%%%%%%%%%%%%%%%%%%%%%%%%%%%%%%%%%%%%%%%%%%%%%%%%%%%%%
AngularityParameterOverall=[];
for s=1:k

AngularityParameterOverall=[AngularityParameterOverall;Angularity.
AngularityParameter{1,s}];
end

filename = 'AngularityParameter';

xlswrite (filename,AngularityParameterOverall,1,'A2')
%
xlswrite (filename,{'AngularityParameter'},1,'A1')
```

```

xlswrite(filename, {'mean'}, 1, 'C1')
xlswrite(filename, {'mine'}, 1, 'C2')
xlswrite(filename, {'max'}, 1, 'C3')
xlswrite(filename, {'StandardDeviation'}, 1, 'C4')

xlswrite(filename, mean(AngularityParameterOverall), 1, 'D1')
xlswrite(filename, min(AngularityParameterOverall), 1, 'D2')
xlswrite(filename, max(AngularityParameterOverall), 1, 'D3')
xlswrite(filename, std(AngularityParameterOverall), 1, 'D4')

end

function [ b ] = form( a )
t
%UNTITLED Summary of this function goes here
% Detailed explanation goes here
%%%%%%%%%%%%%%%%%%%%%%%%%%%%%%%%%%%%%%%%%%%%%%%%%%%%%%%%%%%%%%%%%%%%%%%%
pics = dir('*.*jpg');
for k = 1:length(pics)
filename = pics(k).name;
I = imread(filename);
%I=imread('d.jpg');
%imshow(I, []);

%*****Convert to binary image
BW0=im2bw(I);
%figure; imshow(BW0, []);
%level = graythresh(I);
%BW0 = im2bw(I, level);
%figure; imshow(BW0, []);

%*****calculate the complement of image
BW=imcomplement(BW0);
in=load('input.txt');
%figure; imshow(BW, []);

%*****Filling holes inside the objects
BW2 = imfill(BW,in(1), 'holes');
%figure; imshow(BW2, []);

%*****Removing the very small objects
BW3 = bwareaopen(BW2,in(2), in(1));
%figure; imshow(BW3, []);
%imwrite(BW3, 'd6.jpg');

%*****Detecting the boundary of objects
Boundary=boundaries(BW3,in(1), 'cw');

%*****Detecting the region properties of
objects
Regin=regionprops(BW3, 'all');

%%%%%%%%%%%%%%%%%%%%%%%%%%%%%%%%%%%%%%%%%%%%%%%%%%%%%%%%%%%%%%%%%%%%%%%%
%%%%%%%%%%%%%%%%%%%%%%%%%%%%%%%%%%%%%%%%%%%%%%%%%%%%%%%%%%%%%%%%%%%%%%%%
%%%%%%%%%%%%%%%%%%%%%%%%%%%%%%%%%%%%%%%%%%%%%%%%%%%%%%%%%%%%%%%%%%%%%%%% Analysis of Shape %%%%%%%%%

```

Appendix E

```
%
%
%@@@@@@@@@@@@@@@@@@@@
%
%
[m1,n1]=size(Boundary);
FormFactor=zeros(m1,1);
Roundness=zeros(m1,1);
FormIndex=zeros(m1,1);
%$$$$$$$$$$$$$$$$
AreaGrain=zeros(m1,1);
FormFactorEdit=zeros(m1,1);
RoundnessEdit=zeros(m1,1);
FormIndexEdit=zeros(m1,1);

for h=1:m1
    %$$$$$$$$$$$$$$$$ Area of Grains
    AreaGrain(h,1)=Regin(h,1).Area;

    %@@@@@@@@@@@@@@@@@@@@

    FormFactor(h,1)=4*pi*(Regin(h,1).Area)/((Regin(h,1).Perimeter)^2);

    %@@@@@@@@@@@@@@@@@@@@
    Roundness(h,1)=1/(FormFactor(h,1));

    %@@@@@@@@@@@@@@@@@@@@
    %%%%%%%%%%
    %%%%%%%%%%
    %%%%%%%%%%
    %*****

    CentPoint=Regin(h,1).Centroid;

    %*****
    boun=Boundary{h,1};
    bounx=boun(:,2);
    bouny=boun(:,1);

    [m,n]=size(boun);
    o=zeros(m,n);
    o(:,1)=bounx-CentPoint(1,1);
    o(:,2)=bouny-CentPoint(1,2);
    %
    %*****
    b=zeros(m,n);
    b(:,1)=o(:,1);
    b(:,2)=-1*o(:,2);
    %
    [TA0,R0] = cart2pol(b(:,1),b(:,2));
    %

    sort0=zeros(m-1,n);
    for i=1:m-1
```

```

        if TA0(i,1)<0
            sort0(i,1)=TA0(i,1)+(2*pi);
        else sort0(i,1)= TA0(i,1);
        end
        sort0(i,2)=R0(i,1);
    end
    sorted=sortrows(sort0,1);
    %
    %
    [~,ix]=unique(sorted(:,1), 'first');
    finalSorted=sorted(sort(ix),:);
    TA=finalSorted(:,1);
    R=finalSorted(:,2);
    FI=zeros(in(5),1);
    for j=1:in(5)
        teta1=(j-1)*5*pi/180;
        teta2=(j)*5*pi/180;
        TA1=abs(TA-teta1);
        TA2=abs(TA-teta2);
        R1=R(find(TA1==min(TA1)),1);
        R2=R(find(TA2==min(TA2)),1);
        FI(j,1)=(abs(R1-R2))/R1;
    end
    FormIndex(h,1)=sum(FI);
end

%
[MaxRow,MaxColumn]=find(AreaGrain==max(AreaGrain));
FormFactorEdit=FormFactor;
RoundnessEdit=Roundness;
FormIndexEdit=FormIndex;
FormFactorEdit(MaxRow,:) = [ ];
RoundnessEdit(MaxRow,:) = [ ];
FormIndexEdit(MaxRow,:) = [ ];

Form.FormFactor(1,k)={FormFactorEdit};
Form.Roundness(1,k)={RoundnessEdit};
Form.FormIndex(1,k)={FormIndexEdit};

Statistic.FormFactor.mean(1,k)=mean(FormFactorEdit);
Statistic.FormFactor.min(1,k)=min(FormFactorEdit);
Statistic.FormFactor.max(1,k)=max(FormFactorEdit);
Statistic.FormFactor.StandardDeviation(1,k)=std(FormFactorEdit);

Statistic.Roundness.mean(1,k)=mean(RoundnessEdit);
Statistic.Roundness.min(1,k)=min(RoundnessEdit);
Statistic.Roundness.max(1,k)=max(RoundnessEdit);
Statistic.Roundness.StandardDeviation(1,k)=std(RoundnessEdit);

Statistic.FormIndex.mean(1,k)=mean(FormIndexEdit);
Statistic.FormIndex.min(1,k)=min(FormIndexEdit);
Statistic.FormIndex.max(1,k)=max(FormIndexEdit);
Statistic.FormIndex.StandardDeviation(1,k)=std(FormIndexEdit);

```



```

end

FormFactorOverall=[];
RoundnessOverall=[];
FormIndexOverall=[];
for s=1:k
    FormFactorOverall=[FormFactorOverall;Form.FormFactor{1,s}];
    RoundnessOverall=[RoundnessOverall;Form.Roundness{1,s}];
    FormIndexOverall=[FormIndexOverall;Form.FormIndex{1,s}];
end

StatisticOverall.FormFactor.mean=mean(FormFactorOverall);
StatisticOverall.FormFactor.min=min(FormFactorOverall);
StatisticOverall.FormFactor.max=max(FormFactorOverall);
StatisticOverall.FormFactor.StandardDeviation=std(FormFactorOverall);
StatisticOverall.Roundness.mean=mean(RoundnessOverall);
StatisticOverall.Roundness.min=min(RoundnessOverall);
StatisticOverall.Roundness.max=max(RoundnessOverall);
StatisticOverall.Roundness.StandardDeviation=std(RoundnessOverall);
;
StatisticOverall.FormIndex.mean=mean(FormIndexOverall);
StatisticOverall.FormIndex.min=min(FormIndexOverall);
StatisticOverall.FormIndex.max=max(FormIndexOverall);
StatisticOverall.FormIndex.StandardDeviation=std(FormIndexOverall);
;

filename = 'form';
%%%FormFactor
xlswrite(filename,FormFactorOverall,1,'A2')
%
xlswrite(filename,{'FormFactor'},1,'A1')
xlswrite(filename,{'mean'},1,'C1')
xlswrite(filename,{'mine'},1,'C2')
xlswrite(filename,{'max'},1,'C3')
xlswrite(filename,{'StandardDeviation'},1,'C4')

xlswrite(filename,StatisticOverall.FormFactor.mean,1,'D1')
xlswrite(filename,StatisticOverall.FormFactor.min,1,'D2')
xlswrite(filename,StatisticOverall.FormFactor.max,1,'D3')
xlswrite(filename,StatisticOverall.FormFactor.StandardDeviation,1,'D4')

%%%Roundness
xlswrite(filename,RoundnessOverall,2,'A2')
%
xlswrite(filename,{'Roundness'},2,'A1')
xlswrite(filename,{'mean'},2,'C1')
xlswrite(filename,{'mine'},2,'C2')
xlswrite(filename,{'max'},2,'C3')
xlswrite(filename,{'StandardDeviation'},2,'C4')

xlswrite(filename,StatisticOverall.Roundness.mean,2,'D1')
xlswrite(filename,StatisticOverall.Roundness.min,2,'D2')
xlswrite(filename,StatisticOverall.Roundness.max,2,'D3')

```

Appendix E

```
xlswrite(filename,StatisticOverall.Roundness.StandardDeviation,2,'
D4')

%%%FormIndex
xlswrite(filename,FormIndexOverall,3,'A2')
%
xlswrite(filename,{'FormIndex'},3,'A1')
xlswrite(filename,{'mean'},3,'C1')
xlswrite(filename,{'mine'},3,'C2')
xlswrite(filename,{'max'},3,'C3')
xlswrite(filename,{'StandardDeviation'},3,'C4')

xlswrite(filename,StatisticOverall.FormIndex.mean,3,'D1')
xlswrite(filename,StatisticOverall.FormIndex.min,3,'D2')
xlswrite(filename,StatisticOverall.FormIndex.max,3,'D3')
xlswrite(filename,StatisticOverall.FormIndex.StandardDeviation,3,'
D4')

end

function [ w ] = sieve( z )
t
%UNTITLED Summary of this function goes here
% Detailed explanation goes here
global AreaConverted
global MajorAxisLengthConverted
global MinorAxisLengthConverted
global ConvexAreaConverted
global EquivDiameterConverted
global filename

%%%%%%%%%%%%%%%%%%%%%%%%%%%%%%%%%%%%%%%%%%%%%%%%%%%%%%%%%%%%%%%%%%%%%%%%%% Reading all of the pictures
pics = dir('*.jpg');

a=cell(1,length(pics));
b=cell(1,length(pics));
c=cell(1,length(pics));
d=cell(1,length(pics));
e=cell(1,length(pics));

for k = 1:length(pics)
filename = pics(k).name;
pic = imread(filename);
%figure; imshow(pic,[]);
sieve1( pic );

%%%%%%%%%%%%%%%%%%%%%%%%%%%%%%%%%%%%%%%%%%%%%%%%%%%%%%%%%%%%%%%%%%%%%%%%%% filling the structure of the
size
%%%%%%%%%%%%%%%%%%%%%%%%%%%%%%%%%%%%%%%%%%%%%%%%%%%%%%%%%%%%%%%%%%%%%%%%%% information of the each picture
(separate
%%%%%%%%%%%%%%%%%%%%%%%%%%%%%%%%%%%%%%%%%%%%%%%%%%%%%%%%%%%%%%%%%%%%%%%%%% pictures)
a(1,k)={AreaConverted};
b(1,k)={MajorAxisLengthConverted};
```

Appendix E

```
c(1,k)={MinorAxisLengthConverted};
d(1,k)={ConvexAreaConverted};
e(1,k)={EquivDiameterConverted};

Statistic.Area.mean(1,k)=mean(AreaConverted);
Statistic.Area.min(1,k)=min(AreaConverted);
Statistic.Area.max(1,k)=max(AreaConverted);
Statistic.Area.StandardDeviation(1,k)=std(AreaConverted);

Statistic.MajorAxisLength.mean(1,k)=mean(MajorAxisLengthConverted)
;
Statistic.MajorAxisLength.min(1,k)=min(MajorAxisLengthConverted);
Statistic.MajorAxisLength.max(1,k)=max(MajorAxisLengthConverted);
Statistic.MajorAxisLength.StandardDeviation(1,k)=std(MajorAxisLengthConverted);

Statistic.MinorAxisLength.mean(1,k)=mean(MinorAxisLengthConverted)
;
Statistic.MinorAxisLength.min(1,k)=min(MinorAxisLengthConverted);
Statistic.MinorAxisLength.max(1,k)=max(MinorAxisLengthConverted);
Statistic.MinorAxisLength.StandardDeviation(1,k)=std(MinorAxisLengthConverted);

Statistic.ConvexArea.mean(1,k)=mean(ConvexAreaConverted);
Statistic.ConvexArea.min(1,k)=min(ConvexAreaConverted);
Statistic.ConvexArea.max(1,k)=max(ConvexAreaConverted);
Statistic.ConvexArea.StandardDeviation(1,k)=std(ConvexAreaConverted);

Statistic.EquivDiameter.mean(1,k)=mean(EquivDiameterConverted);
Statistic.EquivDiameter.min(1,k)=min(EquivDiameterConverted);
Statistic.EquivDiameter.max(1,k)=max(EquivDiameterConverted);
Statistic.EquivDiameter.StandardDeviation(1,k)=std(EquivDiameterConverted);

end
sieve.Area=a;
sieve.MajorAxisLength=b;
sieve.MinorAxisLength=c;
sieve.ConvexArea=d;
sieve.EquivDiameter=e;

% save sieve sieve
% save Statistic Statistic

%%%%%%%%%%%%%%%%%%%%%%%%%%%%%%%%%%%%%%%%%%%%%%%%%%%%%%%%%%%%%%%%%%%%%%%%%% Preparing The Overall Results
for each
%%%%%%%%%%%%%%%%%%%%%%%%%%%%%%%%%%%%%%%%%%%%%%%%%%%%%%%%%%%%%%%%%%%%%%%%%% Specimen, (combining all of the
pictures
%%%%%%%%%%%%%%%%%%%%%%%%%%%%%%%%%%%%%%%%%%%%%%%%%%%%%%%%%%%%%%%%%%%%%%%%%% that they have been taken for
one Specimen
```

```

AreaOverall=[];
MajorAxisLengthOverall=[];
MinorAxisLengthOverall=[];
ConvexAreaOverall=[];
EquivDiameterOverall=[];
for s=1:k
    AreaOverall=[AreaOverall;sieve.Area{1,s}];

MajorAxisLengthOverall=[MajorAxisLengthOverall;sieve.MajorAxisLength{1,s}];

MinorAxisLengthOverall=[MinorAxisLengthOverall;sieve.MinorAxisLength{1,s}];
    ConvexAreaOverall=[ConvexAreaOverall;sieve.ConvexArea{1,s}];

EquivDiameterOverall=[EquivDiameterOverall;sieve.EquivDiameter{1,s}];

end

%%%%%%%%%%%%%%%%%%%%%%%%%%%%%%%%%%%%%%%%%%%%%%%%%%%%%%%%%%%%%%%%%%%%%%%%%% filling the structure of the
overall size
%%%%%%%%%%%%%%%%%%%%%%%%%%%%%%%%%%%%%%%%%%%%%%%%%%%%%%%%%%%%%%%%%%%%%%%%%% information of the all pictures
together

StatisticOverall.Area.mean=mean (AreaOverall);
StatisticOverall.Area.min=min (AreaOverall);
StatisticOverall.Area.max=max (AreaOverall);
StatisticOverall.Area.StandardDeviation=std (AreaOverall);

StatisticOverall.MajorAxisLength.mean=mean (MajorAxisLengthOverall)
;
StatisticOverall.MajorAxisLength.min=min (MajorAxisLengthOverall);
StatisticOverall.MajorAxisLength.max=max (MajorAxisLengthOverall);
StatisticOverall.MajorAxisLength.StandardDeviation=std (MajorAxisLengthOverall);

StatisticOverall.MinorAxisLength.mean=mean (MinorAxisLengthOverall)
;
StatisticOverall.MinorAxisLength.min=min (MinorAxisLengthOverall);
StatisticOverall.MinorAxisLength.max=max (MinorAxisLengthOverall);
StatisticOverall.MinorAxisLength.StandardDeviation=std (MinorAxisLengthOverall);

StatisticOverall.ConvexArea.mean=mean (ConvexAreaOverall);
StatisticOverall.ConvexArea.min=min (ConvexAreaOverall);
StatisticOverall.ConvexArea.max=max (ConvexAreaOverall);
StatisticOverall.ConvexArea.StandardDeviation=std (ConvexAreaOverall);

StatisticOverall.EquivDiameter.mean=mean (EquivDiameterOverall);
StatisticOverall.EquivDiameter.min=min (EquivDiameterOverall);
StatisticOverall.EquivDiameter.max=max (EquivDiameterOverall);

```

Appendix E

```
StatisticOverall.EquivDiameter.StandardDeviation=std(EquivDiameter  
Overall);
```

```
filename = 'sieve';  
xlswrite(filename,AreaOverall,1,'A2')  
xlswrite(filename,MajorAxisLengthOverall,2,'A2')  
xlswrite(filename,MinorAxisLengthOverall,3,'A2')  
xlswrite(filename,ConvexAreaOverall,4,'A2')  
xlswrite(filename,EquivDiameterOverall,5,'A2')
```

```
xlswrite(filename,{'EquivDiameter'},5,'A1')  
xlswrite(filename,{'mean'},5,'C1')  
xlswrite(filename,{'mine'},5,'C2')  
xlswrite(filename,{'max'},5,'C3')  
xlswrite(filename,{'StandardDeviation'},5,'C4')
```

```
xlswrite(filename,StatisticOverall.EquivDiameter.mean,5,'D1')  
xlswrite(filename,StatisticOverall.EquivDiameter.min,5,'D2')  
xlswrite(filename,StatisticOverall.EquivDiameter.max,5,'D3')  
xlswrite(filename,StatisticOverall.EquivDiameter.StandardDeviation  
,5,'D4')
```

```
end
```

```
function [ b ] = sieve1( I )
```

```
global AreaConverted  
global MajorAxisLengthConverted  
global MinorAxisLengthConverted  
global ConvexAreaConverted  
global EquivDiameterConverted  
global filename
```

```
%*****Convert to binary image
```

```
BW0=im2bw(I);  
%figure; imshow(BW0,[]);  
%level = graythresh(I);  
%BW0 = im2bw(I,level);  
%figure; imshow(BW0,[]);
```

```
%*****calculate the complement of image
```

```
BW=imcomplement(BW0);  
in=load('input.txt');  
%figure; imshow(BW,[]);
```

```
%*****Filling holes inside the objects
```

```
BW2 = imfill(BW,in(1),'holes');  
%figure; imshow(BW2,[]);
```

```
%*****Removing the very small objects
```

Appendix E

```
BW3 = bwareaopen(BW2,in(2),in(1));
%figure; imshow(BW3,[]);
%imwrite(BW3,'d6.jpg');

%*****Detecting the boundary of objects
Boundary=boundaries(BW3,in(1),'cw');

%*****Detecting the region properties of
objects
Regin=regionprops(BW3,'all');

%
%
[m1,n1]=size(Boundary);
Area=zeros(m1,1);
MajorAxisLength=zeros(m1,1);
MinorAxisLength=zeros(m1,1);
ConvexArea=zeros(m1,1);
EquivDiameter=zeros(m1,1);

for h=1:m1
    Area(h,1)=Regin(h,1).Area;
    MajorAxisLength(h,1)=Regin(h,1).MajorAxisLength;
    MinorAxisLength(h,1)=Regin(h,1).MinorAxisLength;
    ConvexArea(h,1)=Regin(h,1).ConvexArea;
    EquivDiameter(h,1)=Regin(h,1).EquivDiameter;
end

%%%%%%%%%%%%%%%%%%%%%%%%%%%%%%%%%%%%%%%%%%%%%%%%%%%%%%%%%%%%%%%%%%%%%%%%
%%%%%%%%%%%%%%%%%%%%%%%%%%%%%%%%%%%%%%%%%%%%%%%%%%%%%%%%%%%%%%%%%%%%%%%%d is diameter of scale

AreaReal=d*d*pi/4;
MajorAxisLengthReal=d;
MinorAxisLengthReal=d;
ConvexAreaReal=d*d*pi/4;
EquivDiameterReal=d;

[MaxRow,MaxColumn]=find(Area==max(Area));

AreaConverted=Area(:,1)*AreaReal/Area(MaxRow,MaxColumn);
AreaConverted(MaxRow,:)=[];

MajorAxisLengthConverted=MajorAxisLength(:,1)*MajorAxisLengthReal/
MajorAxisLength(MaxRow,MaxColumn);
MajorAxisLengthConverted(MaxRow,:)=[];

MinorAxisLengthConverted=MinorAxisLength(:,1)*MinorAxisLengthReal/
MinorAxisLength(MaxRow,MaxColumn);
MinorAxisLengthConverted(MaxRow,:)=[];
```

Appendix E

```
ConvexAreaConverted=ConvexArea(:,1)*ConvexAreaReal/ConvexArea(MaxRow,MaxColumn);
ConvexAreaConverted(MaxRow,:) = [ ];

EquivDiameterConverted=EquivDiameter(:,1)*EquivDiameterReal/EquivDiameter(MaxRow,MaxColumn);
EquivDiameterConverted(MaxRow,:) = [ ];

end
function [ b ] = texture( a )
t
%UNTITLED Summary of this function goes here
% Detailed explanation goes here
%%%%%%%%%%%%%%%%%%%%%%%%%%%%%%%%%%%%%%%%%%%%%%%%%%%%%%%%%%%%%%%%%%%%%%%%
pics = dir('*.jpg');
for k = 1:length(pics)
filename = pics(k).name;
I = imread(filename);
%I=imread('d.jpg');
%imshow(I, []);

%%%%%%%%%%%%%%%%%%%%%%%%%%%%%%%%%%%%%%%%%%%%%%%%%%%%%%%%%%%%%%%%%%%%%%%%Convert to binary image
BW0=im2bw(I);
%figure; imshow(BW0, []);
%level = graythresh(I);
%BW0 = im2bw(I,level);
%figure; imshow(BW0, []);

%%%%%%%%%%%%%%%%%%%%%%%%%%%%%%%%%%%%%%%%%%%%%%%%%%%%%%%%%%%%%%%%%%%%%%%%calculate the complement of image
BW=imcomplement(BW0);
in=load('input.txt');
%figure; imshow(BW, []);

%%%%%%%%%%%%%%%%%%%%%%%%%%%%%%%%%%%%%%%%%%%%%%%%%%%%%%%%%%%%%%%%%%%%%%%%Filling holes inside the objects
BW2 = imfill(BW,in(1), 'holes');
%figure; imshow(BW2, []);

%%%%%%%%%%%%%%%%%%%%%%%%%%%%%%%%%%%%%%%%%%%%%%%%%%%%%%%%%%%%%%%%%%%%%%%%Removing the very small objects
BW3 = bwareaopen(BW2,in(2),in(1));
%figure; imshow(BW3, []);
%imwrite(BW3,'d6.jpg');

%%%%%%%%%%%%%%%%%%%%%%%%%%%%%%%%%%%%%%%%%%%%%%%%%%%%%%%%%%%%%%%%%%%%%%%%Detecting the boundary of objects
Boundary=boundaries(BW3,in(1), 'cw');

%%%%%%%%%%%%%%%%%%%%%%%%%%%%%%%%%%%%%%%%%%%%%%%%%%%%%%%%%%%%%%%%%%%%%%%%Convert to Gray image
GrayIm=rgb2gray(I);
%figure; imshow(GrayIm, []);

%%%%%%%%%%%%%%%%%%%%%%%%%%%%%%%%%%%%%%%%%%%%%%%%%%%%%%%%%%%%%%%%%%%%%%%%Detecting the region properties of
objects
Regin=regionprops(BW3, 'all');

%%%%%%%%%%%%%%%%%%%%%%%%%%%%%%%%%%%%%%%%%%%%%%%%%%%%%%%%%%%%%%%%%%%%%%%%Detecting the region properties of
objects
```

```

%***** In Gray Image
ReginGray=regionprops (BW3,GrayIm,'all');

%%%%%%%%%%%%%%%%%%%%%%%%%%%%%%%%%%%%%%%%%%%%%%%%%%%%%%%%%%%%%%%%%%%%%%%%
%%%%%%%%%%%%%%%%%%%%%%%%%%%%%%%%%%%%%%%%%%%%%%%%%%%%%%%%%%%%%%%%%%%%%%%%
%%%%%%%%%%%%%%%%%%%%%%%%%%%%%%%%%%%%%%%%%%%%%%%%%%%%%%%%%%%%%%%%%%%%%%%% Analysis of Shape %%%%%%%%%
%
%
%CCCCCCCCCCCCCCCC
%
%
[m1,n1]=size (Boundary);
StandardDeviationIntensity=zeros (m1,1);
MeanIntensity=zeros (m1,1);
%MinIntensity=zeros (m1,1);
%MaxIntensity=zeros (m1,1);
%$$$$$$$$$$$$$$$$
AreaGrain=zeros (m1,1);
StandardDeviationIntensityEdit=zeros (m1,1);
MeanIntensityEdit=zeros (m1,1);

for h=1:m1
    %$$$$$$$$$$$$$$$$ Area of Grains
    AreaGrain (h,1)=Regin (h,1) .Area;

    %*****
    %
    CentPoint=Regin (h,1) .Centroid;

    %*****
    boun=Boundary {h,1};
    bounx=boun (:,2);
    bouny=boun (:,1);
    %
    [m,n]=size (boun);
    o=zeros (m,n);
    o (:,1)=bounx-CentPoint (1,1);
    o (:,2)=bouny-CentPoint (1,2);
    %figure;
    %*****
    b=zeros (m,n);
    b (:,1)=o (:,1);
    b (:,2)=-1*o (:,2);
    %
    [TA0,R0] = cart2pol (b (:,1),b (:,2));
    %
    sort0=zeros (m-1,n);
    for i=1:m-1
        if TA0 (i,1)<0
            sort0 (i,1)=TA0 (i,1)+(2*pi);
        else sort0 (i,1)= TA0 (i,1);
        end
        sort0 (i,2)=R0 (i,1);
    end
    sorted=sortrows (sort0,1);

```



```

%

%**
[~,ix]=unique(sorted(:,1), 'first');
finalSorted=sorted(sort(ix),:);
TA=finalSorted(:,1);
R=finalSorted(:,2);
%

%%%%%%%%%%%%%%%%%%%%%%%%%%%%%%%%%%%%%%%%%%%%%%%%%%%%%%%%%%%%%%%%%%%%%%%%

StandardDeviationIntensity(h,1)=
std(double(ReginGray(h,1).PixelValues));
MeanIntensity(h,1)= RegInGray(h,1).MeanIntensity;

%%%%%%%%%%%%%%%%%%%%%%%%%%%%%%%%%%%%%%%%%%%%%%%%%%%%%%%%%%%%%%%%%%%%%%%%
[m3,n3]=size(Regin(h,1).ConvexHull);
Perconvex=0;

end

%%%%%%%%%%%%%%%%%%%%%%%%%%%%%%%%%%%%%%%%%%%%%%%%%%%%%%%%%%%%%%%%%%%%%%%%
%%%%%%%%%%%%%%%%%%%%%%%%%%%%%%%%%%%%%%%%%%%%%%%%%%%%%%%%%%%%%%%%%%%%%%%%
[MaxRow,MaxColumn]=find(AreaGrain==max(AreaGrain));
StandardDeviationIntensityEdit=StandardDeviationIntensity;
MeanIntensityEdit=MeanIntensity;

StandardDeviationIntensityEdit(MaxRow,:) = [ ];
MeanIntensityEdit(MaxRow,:) = [ ];

Texture.StandardDeviationIntensity(1,k)={StandardDeviationIntensityEdit};
Texture.MeanIntensity(1,k)={MeanIntensityEdit};

Statistic.StandardDeviationIntensity.mean(1,k)=mean(StandardDeviationIntensityEdit);
Statistic.StandardDeviationIntensity.min(1,k)=min(StandardDeviationIntensityEdit);
Statistic.StandardDeviationIntensity.max(1,k)=max(StandardDeviationIntensityEdit);
Statistic.StandardDeviationIntensity.StandardDeviation(1,k)=std(StandardDeviationIntensityEdit);

Statistic.MeanIntensity.mean(1,k)=mean(MeanIntensityEdit);
Statistic.MeanIntensity.min(1,k)=min(MeanIntensityEdit);
Statistic.MeanIntensity.max(1,k)=max(MeanIntensityEdit);
Statistic.MeanIntensity.StandardDeviation(1,k)=std(MeanIntensityEdit);

```

```

end

%%%%%%%%%%%%%%%%%%%%%%%%%%%%%%%%%%%%%%%%%%%%%%%%%%%%%%%%%%%%%%%%%%%%%%%%%% Preparing The Overall Results for each
test
StandardDeviationIntensityOverall=[];
MeanIntensityOverall=[];

for s=1:k

StandardDeviationIntensityOverall=[StandardDeviationIntensityOvera
ll;Texture.StandardDeviationIntensity{1,s}];

MeanIntensityOverall=[MeanIntensityOverall;Texture.MeanIntensity{1
,s}];

end

StatisticOverall.StandardDeviationIntensity.mean=mean(StandardDevi
ationIntensityOverall);
StatisticOverall.StandardDeviationIntensity.min=min(StandardDeviat
ionIntensityOverall);
StatisticOverall.StandardDeviationIntensity.max=max(StandardDeviat
ionIntensityOverall);
StatisticOverall.StandardDeviationIntensity.StandardDeviation=std(
StandardDeviationIntensityOverall);

StatisticOverall.MeanIntensity.mean=mean(MeanIntensityOverall);
StatisticOverall.MeanIntensity.min=min(MeanIntensityOverall);
StatisticOverall.MeanIntensity.max=max(MeanIntensityOverall);
StatisticOverall.MeanIntensity.StandardDeviation=std(MeanIntensity
Overall);

filename = 'texture';
%%%StandardDeviationIntensity
xlswrite(filename,StandardDeviationIntensityOverall,1,'A2')
%
xlswrite(filename,{'StandardDeviationIntensity'},1,'A1')
xlswrite(filename,{'mean'},1,'C1')
xlswrite(filename,{'mine'},1,'C2')
xlswrite(filename,{'max'},1,'C3')
xlswrite(filename,{'StandardDeviation'},1,'C4')

xlswrite(filename,StatisticOverall.StandardDeviationIntensity.mean
,1,'D1')
xlswrite(filename,StatisticOverall.StandardDeviationIntensity.min,
1,'D2')
xlswrite(filename,StatisticOverall.StandardDeviationIntensity.max,
1,'D3')
xlswrite(filename,StatisticOverall.StandardDeviationIntensity.Stan
dardDeviation,1,'D4')

%%%MeanIntensity
xlswrite(filename,MeanIntensityOverall,2,'A2')
%

```

```
xlswrite(filename, {'MeanIntensity'}, 2, 'A1')
xlswrite(filename, {'mean'}, 2, 'C1')
xlswrite(filename, {'mine'}, 2, 'C2')
xlswrite(filename, {'max'}, 2, 'C3')
xlswrite(filename, {'StandardDeviation'}, 2, 'C4')
xlswrite(filename, StatisticOverall.MeanIntensity.mean, 2, 'D1')
xlswrite(filename, StatisticOverall.MeanIntensity.min, 2, 'D2')
xlswrite(filename, StatisticOverall.MeanIntensity.max, 2, 'D3')
xlswrite(filename, StatisticOverall.MeanIntensity.StandardDeviation
, 2, 'D4')

end
function [ b ] = TextureParameter( a )
t
%UNTITLED Summary of this function goes here
% Detailed explanation goes here
%%%%%%%%%%%%%%%%%%%%%%%%%%%%%%%%%%%%%%%%%%%%%%%%%%%%%%%%%%%%%%%%%%%%%%%%
pics = dir('*.jpg');
for k = 1:length(pics)
filename = pics(k).name;
I = imread(filename);
%I=imread('d.jpg');
imshow(I, []);
%%%%%%%%%%%%%%%%%%%%%%%%%%%%%%%%%%%%%%%%%%%%%%%%%%%%%%%%%%%%%%%%%%%%%%%%Convert to binary image
BW0=im2bw(I);
%figure; imshow(BW0, []);
%level = graythresh(I);
%BW0 = im2bw(I,level);
%figure; imshow(BW0, []);

%%%%%%%%%%%%%%%%%%%%%%%%%%%%%%%%%%%%%%%%%%%%%%%%%%%%%%%%%%%%%%%%%%%%%%%%calculate the complement of image
BW=imcomplement(BW0);
in=load('input.txt');
%figure; imshow(BW, []);

%%%%%%%%%%%%%%%%%%%%%%%%%%%%%%%%%%%%%%%%%%%%%%%%%%%%%%%%%%%%%%%%%%%%%%%%Filling holes inside the objects
BW2 = imfill(BW,in(1), 'holes');
%figure; imshow(BW2, []);

%%%%%%%%%%%%%%%%%%%%%%%%%%%%%%%%%%%%%%%%%%%%%%%%%%%%%%%%%%%%%%%%%%%%%%%%Removing the very small objects
BW3 = bwareaopen(BW2,in(2),in(1));
%figure; imshow(BW3, []);
%imwrite(BW3, 'd6.jpg');

%%%%%%%%%%%%%%%%%%%%%%%%%%%%%%%%%%%%%%%%%%%%%%%%%%%%%%%%%%%%%%%%%%%%%%%%Detecting the boundary of objects
Boundary=boundaries(BW3,in(1), 'cw');

%%%%%%%%%%%%%%%%%%%%%%%%%%%%%%%%%%%%%%%%%%%%%%%%%%%%%%%%%%%%%%%%%%%%%%%%Convert to Gray image
GrayIm=rgb2gray(I);
%figure; imshow(GrayIm, []);

%%%%%%%%%%%%%%%%%%%%%%%%%%%%%%%%%%%%%%%%%%%%%%%%%%%%%%%%%%%%%%%%%%%%%%%%Detecting the region properties of
objects
Regin=regionprops(BW3, 'all');
```

```

%*****Detecting the region properties of
objects
%***** In Gray Image
ReginGray=regionprops (BW3,GrayIm, 'all');
%%%%%%%%%%%%%%%%%%%%%%%%%%%%%%%%%%%%%%%%%%%%%%%%%%%%%%%%%%%%%%%%%%%%%%%% TextureParameter
%%
[m1,n1]=size (Boundary);
TextureParameter=zeros (m1,1);
AreaGrain=zeros (m1,1);

for h=1:m1
    b=Regin (h,1) .ConvexHull;
    [m2,n2]=size (b);
    cp=0;

    for i=1:m2-1;
        cp=cp+((b(i,2)-b(i+1,2))^2)+((b(i,1)-b(i+1,1))^2)^0.5;
    end
    TP=(Regin (h,1) .Perimeter/cp)^2;
    TextureParameter (h,1)=TP;
    AreaGrain (h,1)=Regin (h,1) .Area;

end

%%%%%%%%
[MaxRow,MaxColumn]=find (AreaGrain==max (AreaGrain));
TextureParameterEdit=TextureParameter;
TextureParameterEdit (MaxRow,:) = [ ];

Texture.TextureParameter (1,k)={TextureParameterEdit};
end

%%%%%%%%
TextureParameterOverall=[];
for s=1:k

TextureParameterOverall=[TextureParameterOverall;Texture.TexturePa
rameter{1,s}];
end
filename = 'TextureParameter';

xlswrite (filename,TextureParameterOverall,1, 'A2')
%
xlswrite (filename, {'TextureParameter'},1, 'A1')
xlswrite (filename, {'mean'},1, 'C1')
xlswrite (filename, {'mine'},1, 'C2')
xlswrite (filename, {'max'},1, 'C3')
xlswrite (filename, {'StandardDeviation'},1, 'C4')

xlswrite (filename,mean (TextureParameterOverall),1, 'D1')
xlswrite (filename,min (TextureParameterOverall),1, 'D2')
xlswrite (filename,max (TextureParameterOverall),1, 'D3')
xlswrite (filename,std (TextureParameterOverall),1, 'D4')

end

```

APPENDIX F

PARTICLE SIZE DISTRIBUTION OF

SPECIMENS

This appendix contains the particle size distribution of the specimens.

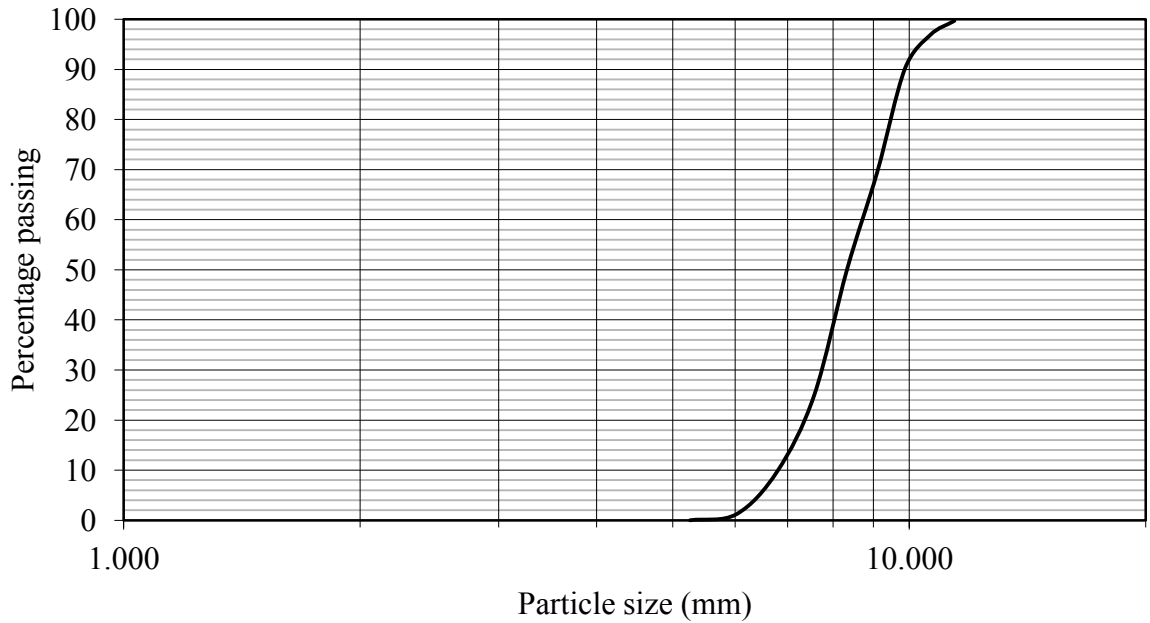


Figure F-1- Size distribution of specimen (Test 1), $D_{60}=8.6$ mm, $D_{50}=8.4$ mm, $D_{10}=6.8$ mm and $F_{\text{corr}}=1$

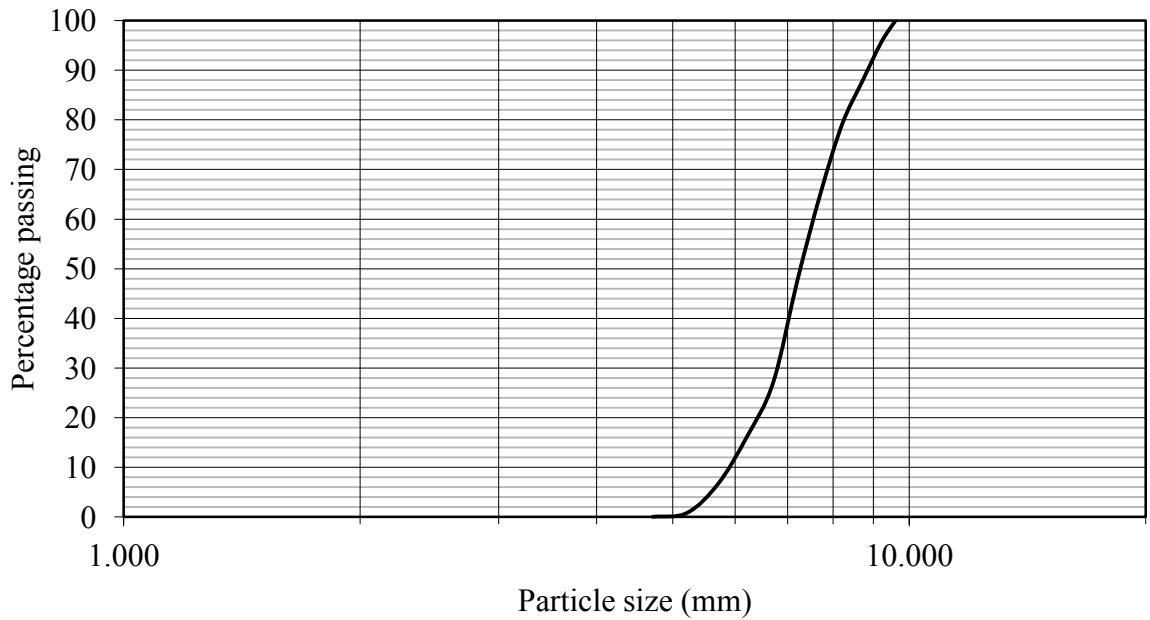


Figure F-2- Size distribution of specimen (Test 2), $D_{60}=7.5$ mm, $D_{50}=7.3$ mm, $D_{10}=5.9$ mm and $F_{\text{corr}}=0.8$

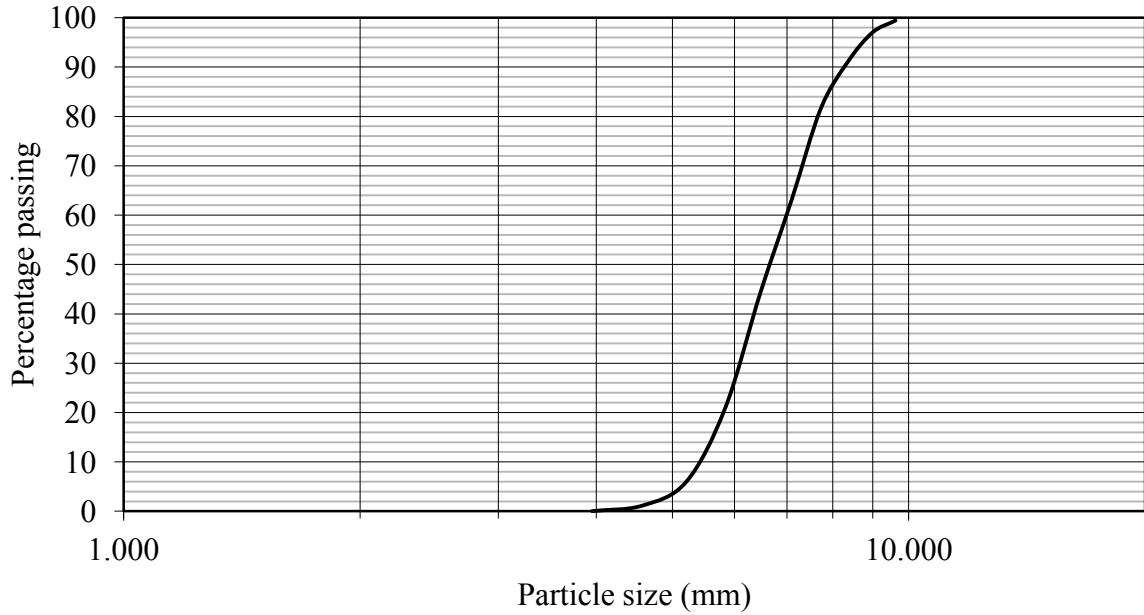


Figure F-3- Size distribution of specimen (Test 3), $D_{60}=7.0$ mm, $D_{50}=6.8$ mm, $D_{10}=5.4$ mm and $F_{corr}=0.88$

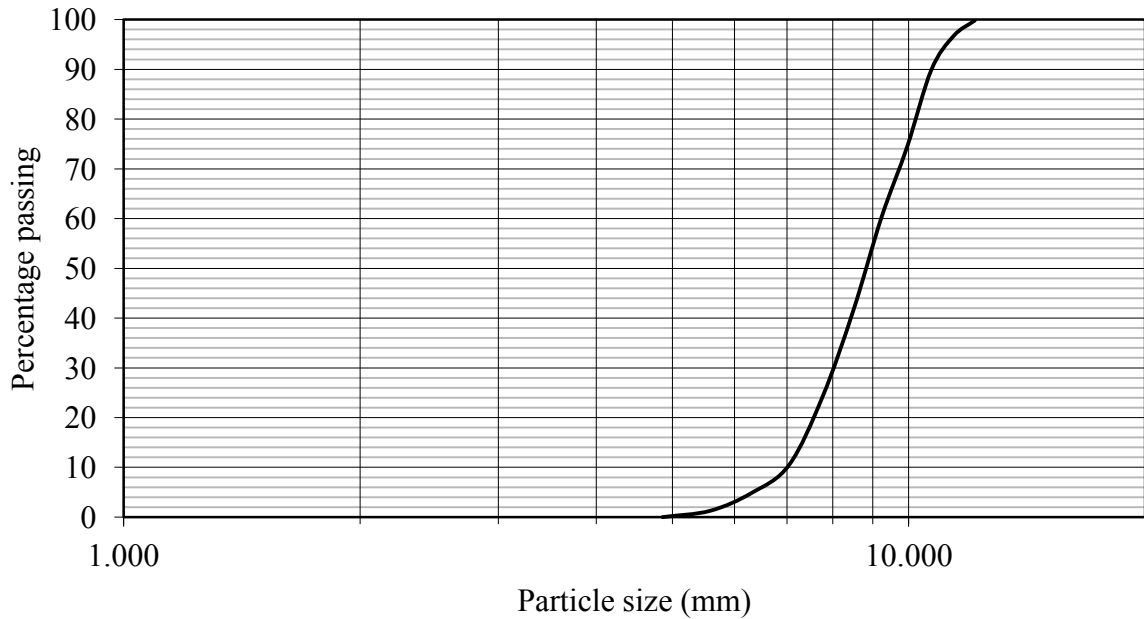


Figure F-4- Size distribution of specimen (Test 4), $D_{60}=9.2$ mm, $D_{50}=8.8$ mm and $D_{10}=7.0$ mm, $F_{corr}=0.8$

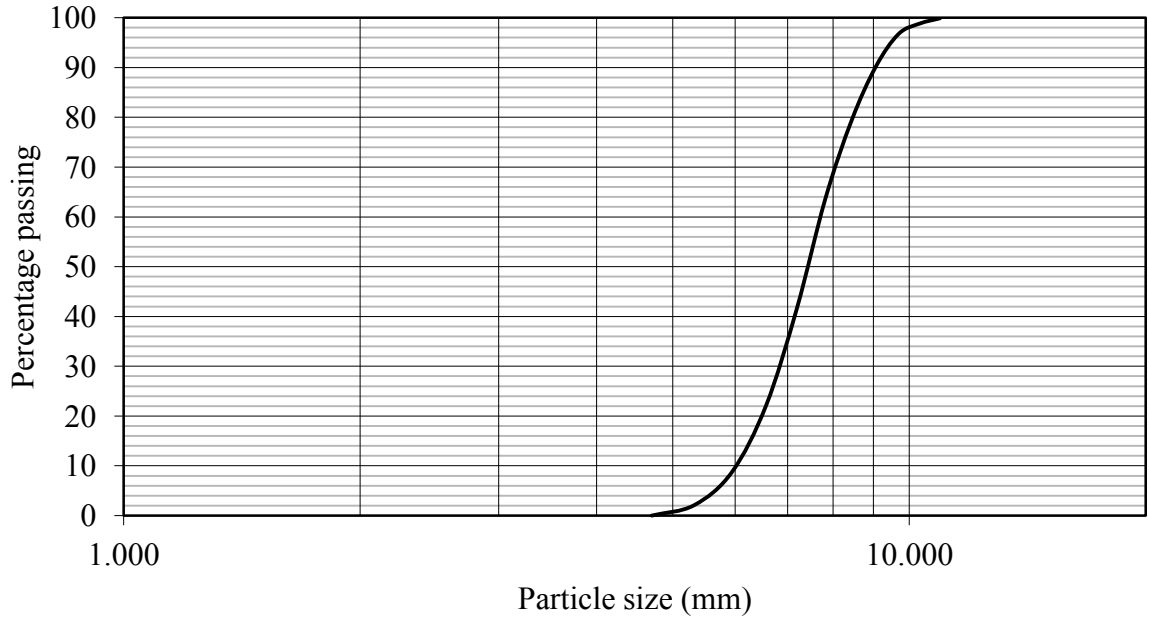


Figure F-5- Size distribution of specimen (Test 5), $D_{60}=7.6$ mm, $D_{50}=7.5$ mm,
 $D_{10}=6.0$ mm and $F_{corr}=0.8$

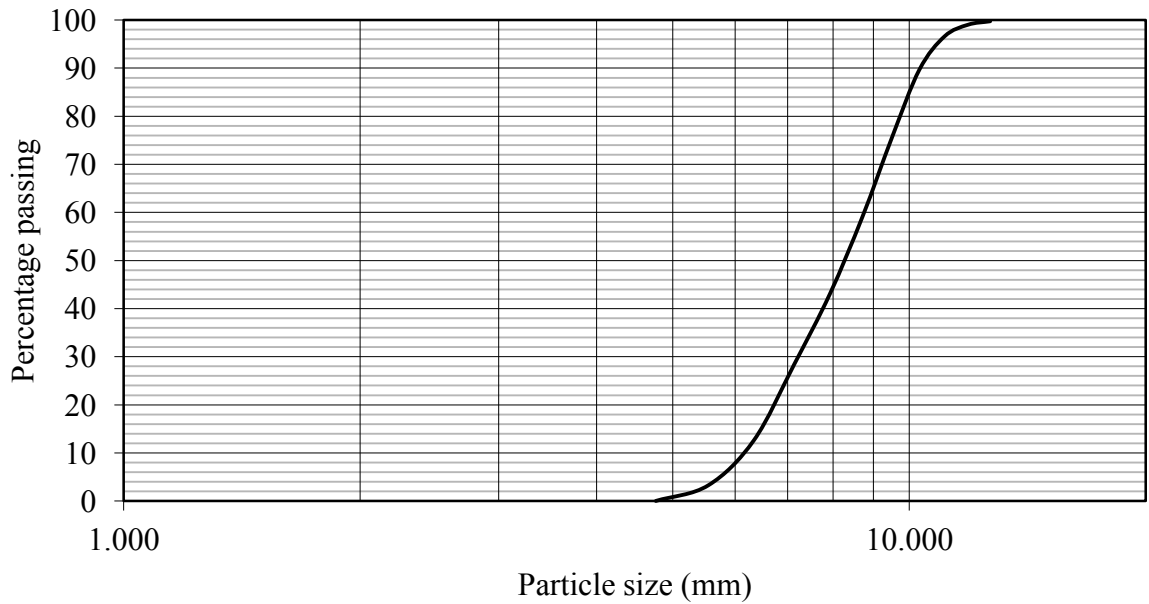


Figure F-6- Size distribution of specimen (Test 6), $D_{60}=8.7$ mm, $D_{50}=8.3$ mm,
 $D_{10}=6.1$ mm and $F_{corr}=0.87$

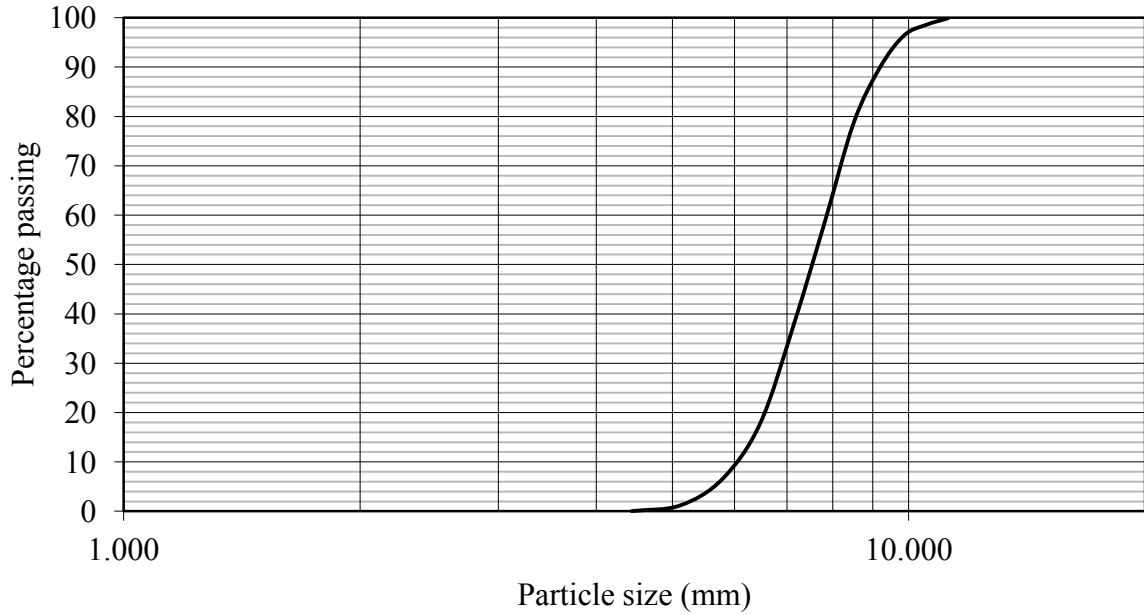


Figure F-7- Size distribution of specimen (Test 7), $D_{60}=7.9$ mm, $D_{50}=7.6$ mm, $D_{10}=6.0$ mm and $F_{corr}=0.8$

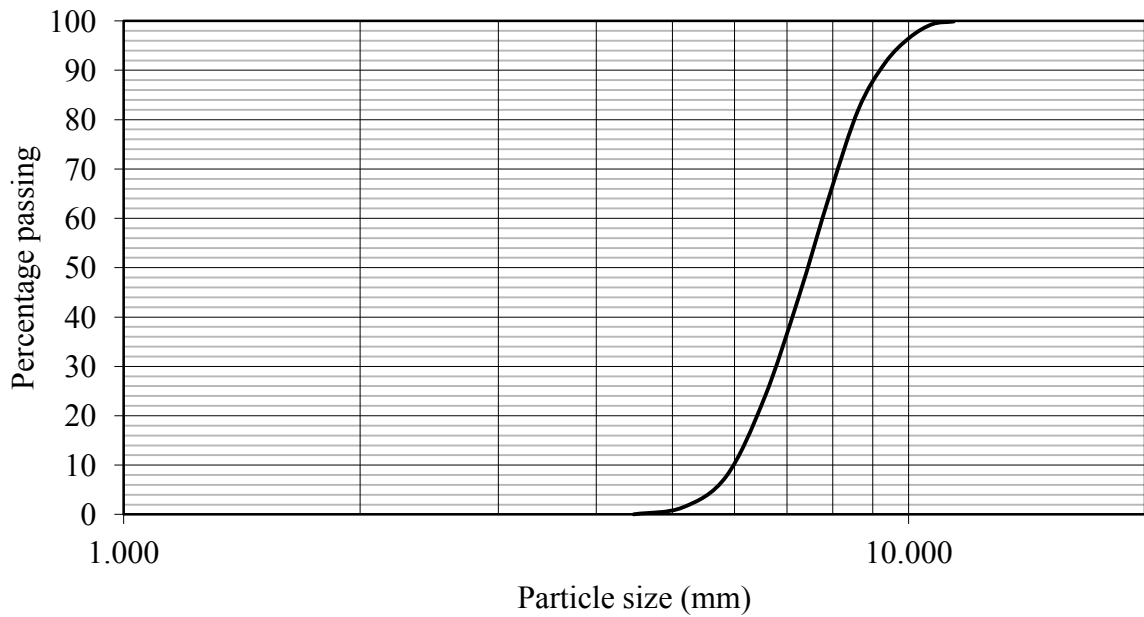


Figure F-8- Size distribution of specimen (Test 8), $D_{60}=7.8$ mm, $D_{50}=7.5$ mm, $D_{10}=5.9$ mm and $F_{corr}=0.8$

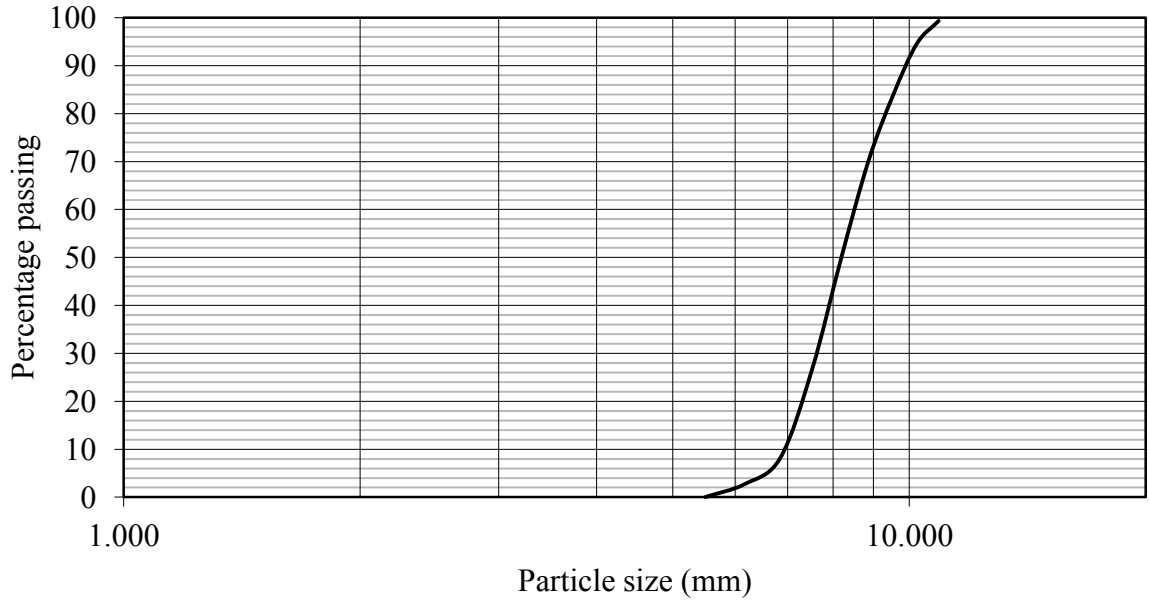


Figure F-9- Size distribution of specimen (Test 9), $D_{60}=8.5$ mm, $D_{50}=8.3$ mm, $D_{10}=7.0$ mm and $F_{corr}=1$

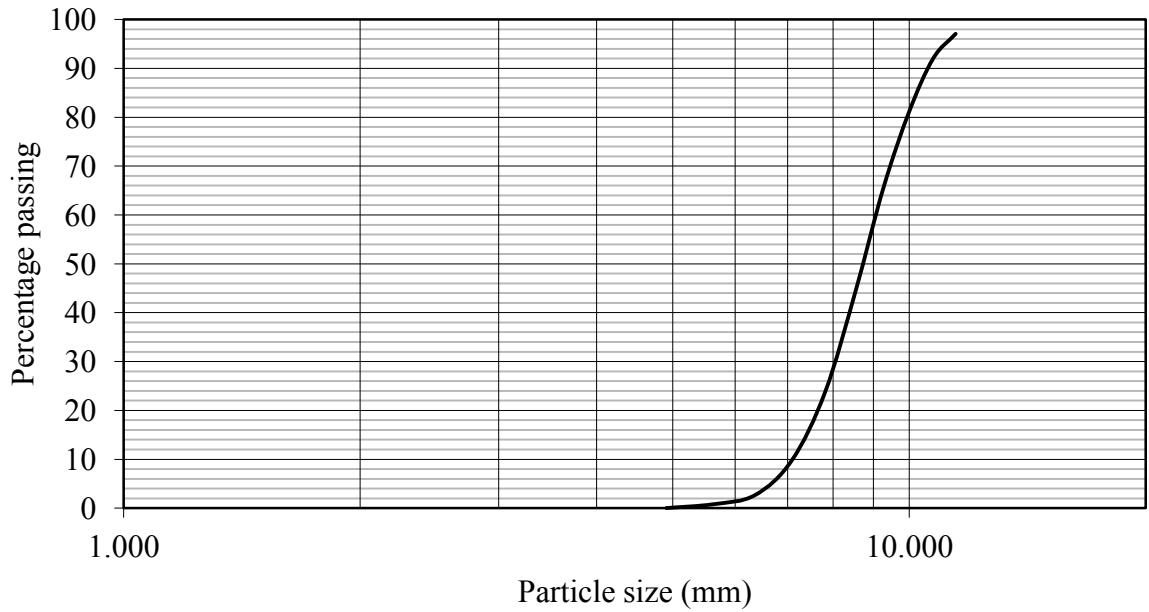


Figure F-10- Size distribution of specimen (Test 10), $D_{60}=9.1$ mm, $D_{50}=8.8$ mm, $D_{10}=7.1$ mm and $F_{corr}=0.8$

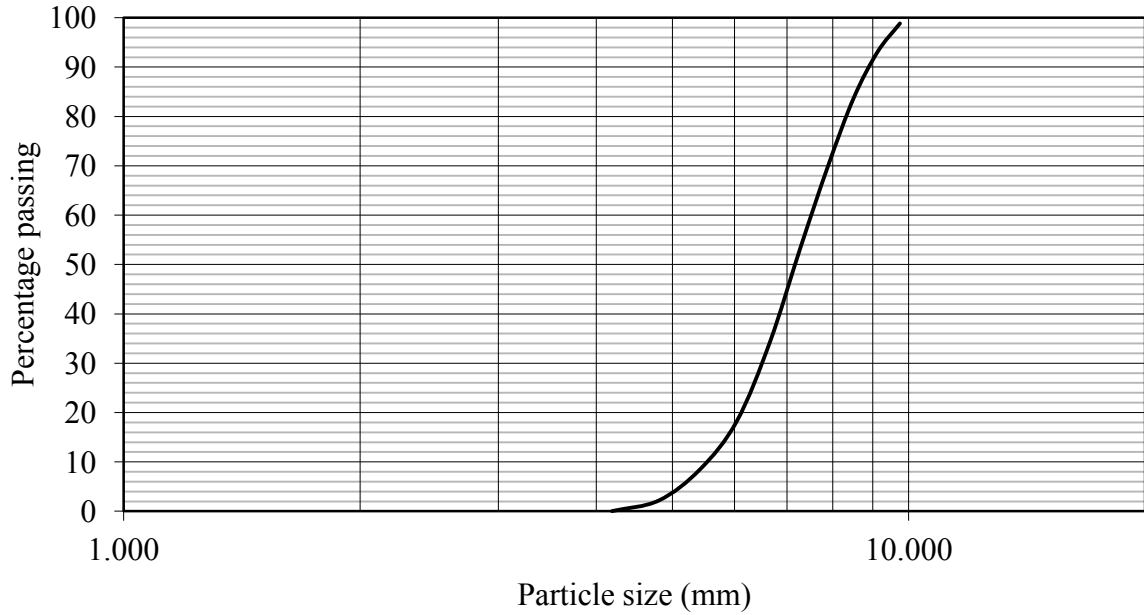


Figure F-11- Size distribution of specimen (Test 11), $D_{60}=7.6$ mm, $D_{50}=7.1$ mm, $D_{10}=5.7$ mm and $F_{corr}=0.87$

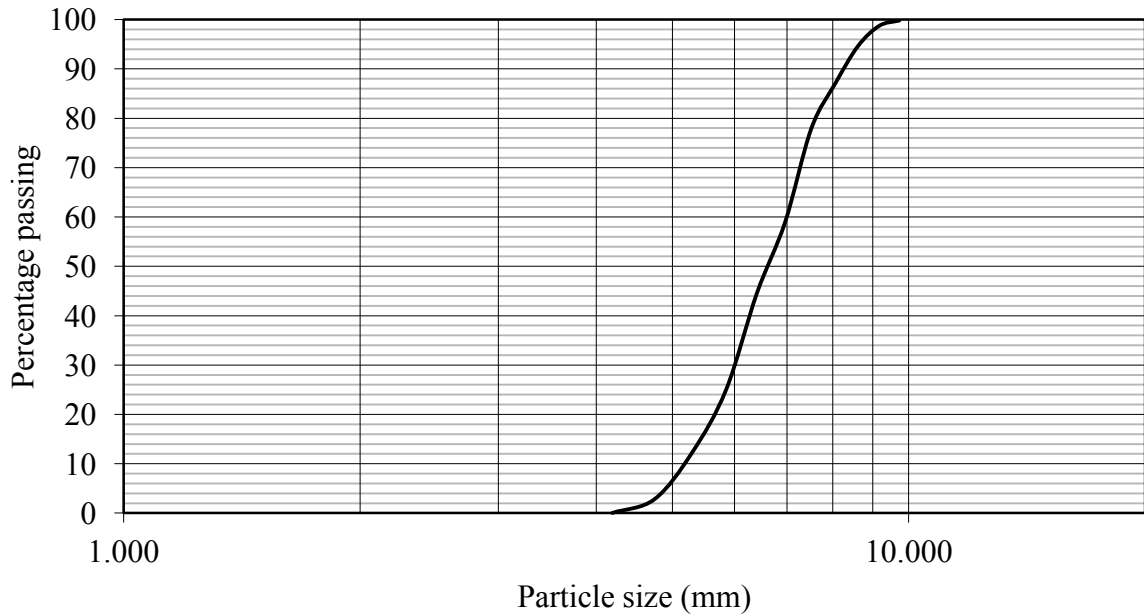


Figure F-12- Size distribution of specimen (Test 12), $D_{60}=7.0$ mm, $D_{50}=6.6$ mm, $D_{10}=5.2$ mm and $F_{corr}=0.8$

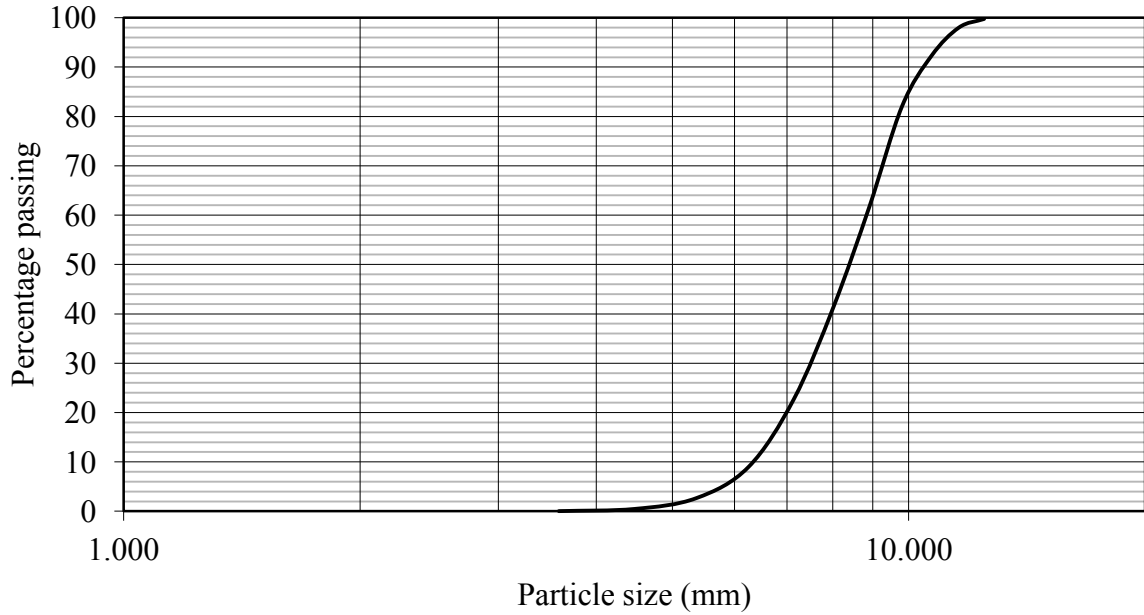


Figure F-13- Size distribution of specimen (Test 13), $D_{60}=8.8$ mm, $D_{50}=8.4$ mm,
 $D_{10}=6.4$ mm and $F_{corr}=0.8$

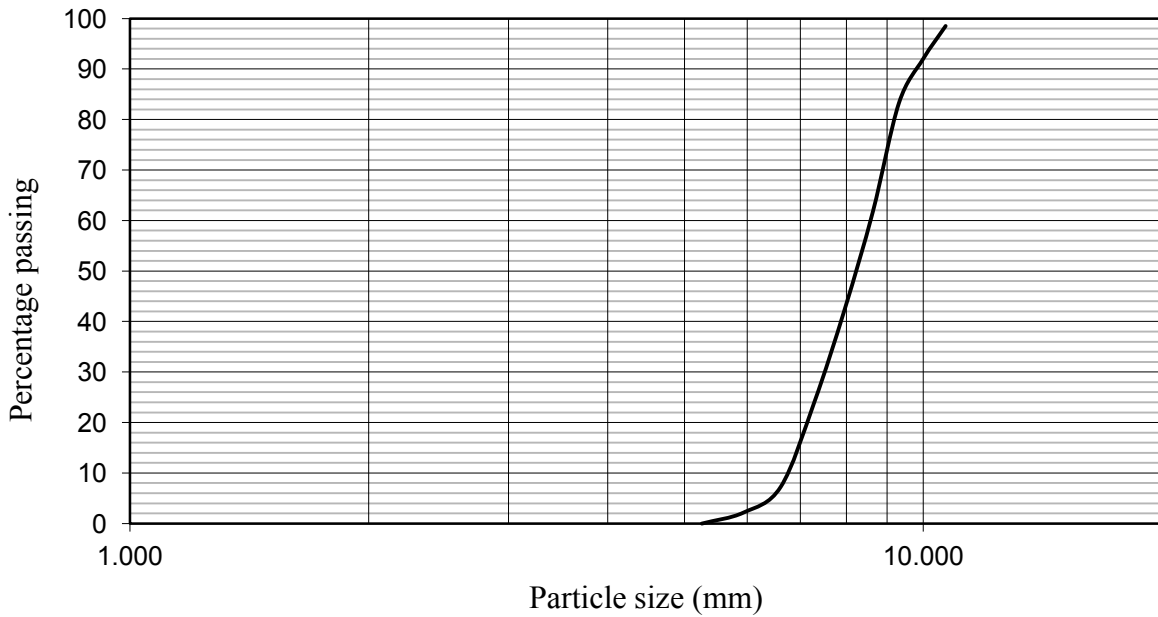


Figure F-14- Size distribution of specimen (Test 14), $D_{60}=8.5$ mm, $D_{50}=8.2$ mm,
 $D_{10}=6.7$ mm and $F_{corr}=1$

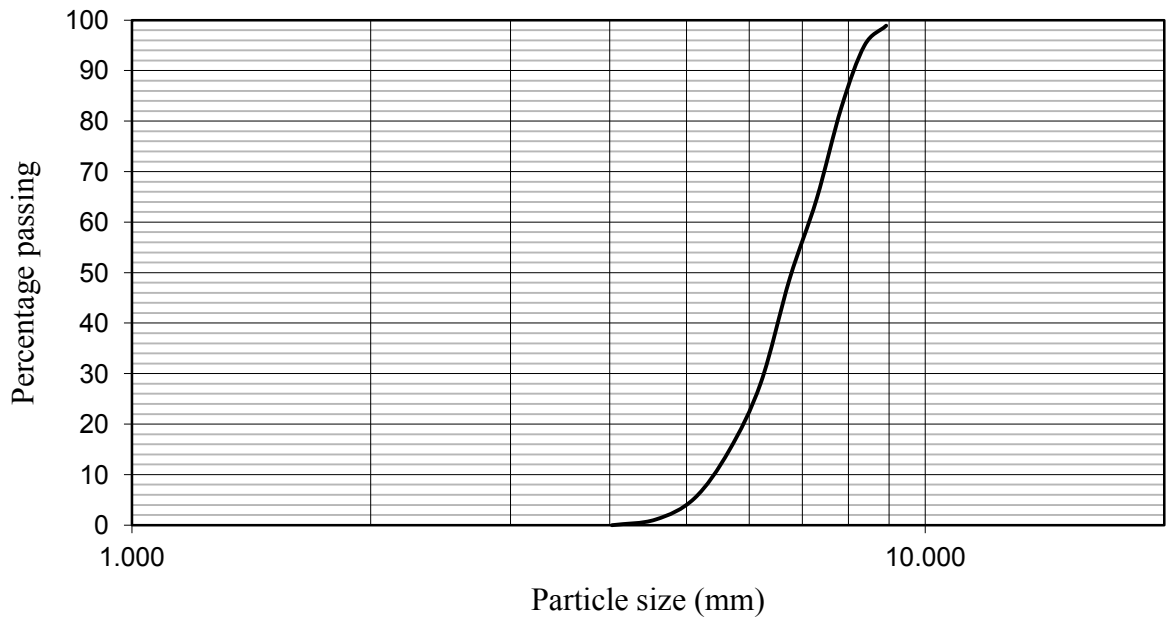


Figure F-15- Size distribution of specimen (Test 15), $D_{60}=7.2$ mm, $D_{50}=6.8$ mm,
 $D_{10}=5.4$ mm and $F_{corr}=0.8$

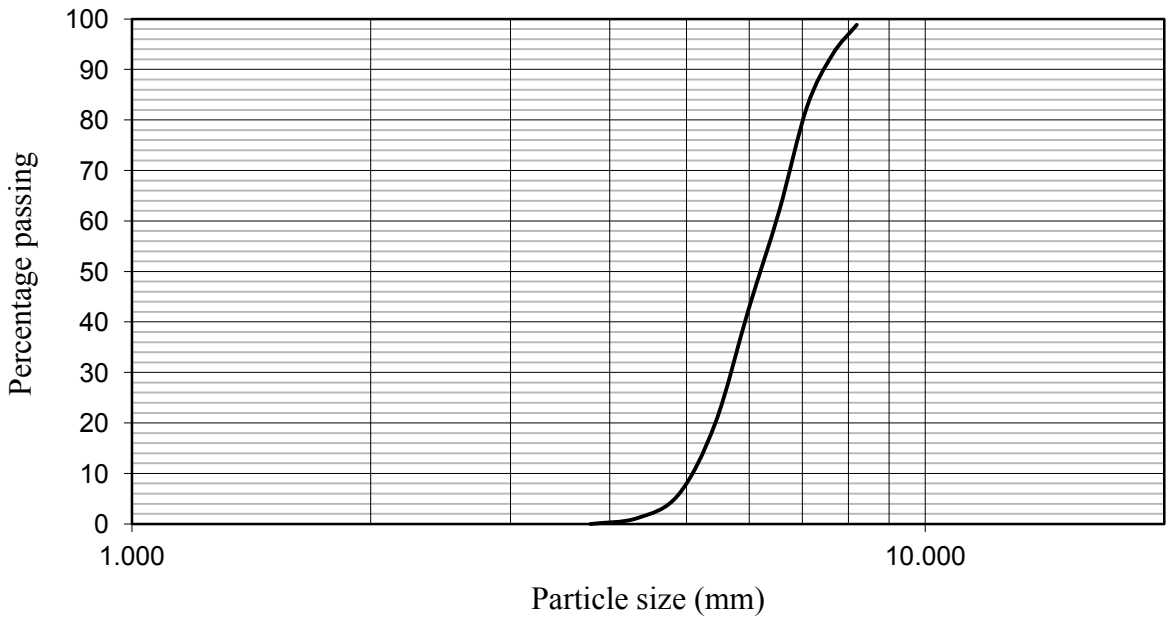


Figure F-16- Size distribution of specimen (Test 16), $D_{60}=6.5$ mm, $D_{50}=6.2$ mm,
 $D_{10}=5.1$ mm and $F_{corr}=0.86$

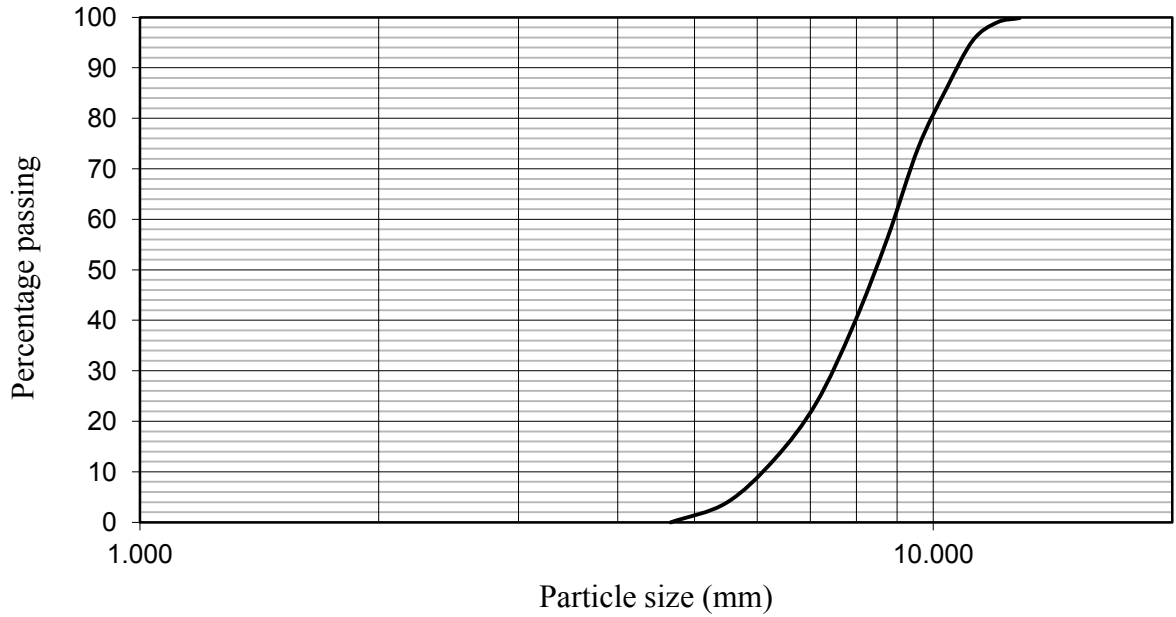


Figure F-17- Size distribution of specimen (Test 17), $D_{60}=9.0$ mm, $D_{50}=8.4$ mm, $D_{10}=6.0$ mm and $F_{corr}=0.8$

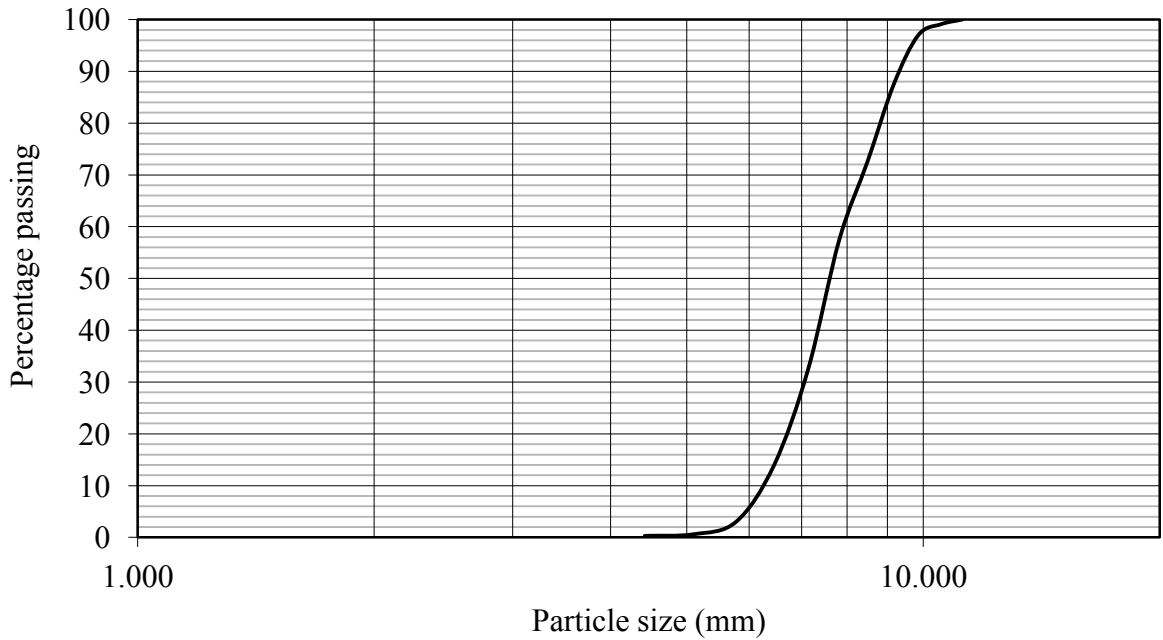


Figure F-18- Size distribution of specimen (Test 18), $D_{60}=7.9$ mm, $D_{50}=7.7$ mm, $D_{10}=6.2$ mm and $F_{corr}=1$

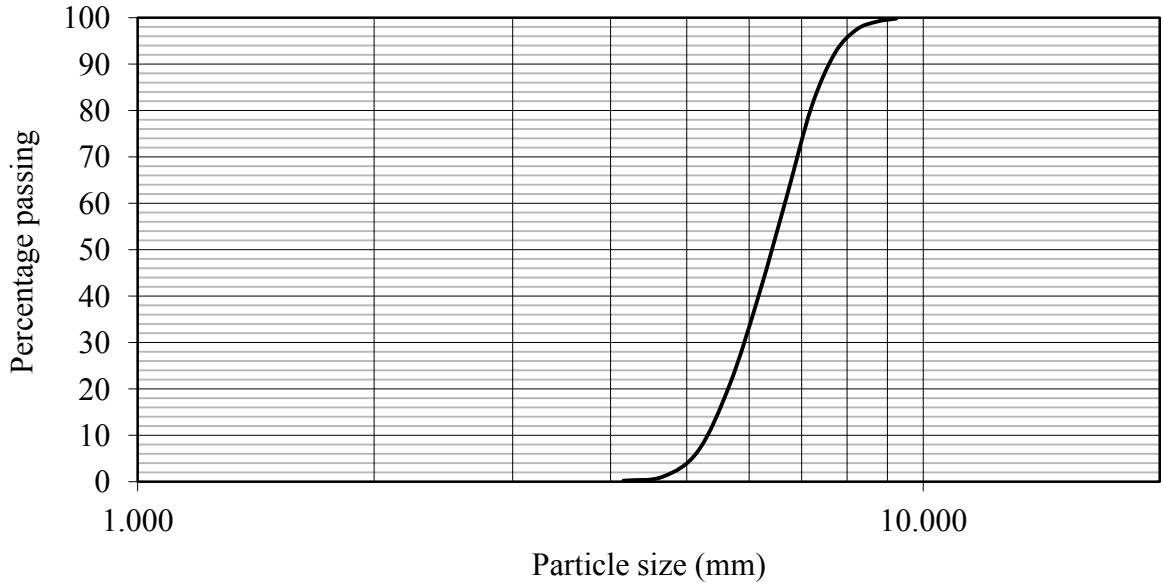


Figure F-19- Size distribution of specimen (Test 19), $D_{60}=6.7$ mm, $D_{50}=6.4$ mm, $D_{10}=5.4$ mm and $F_{corr}=0.8$

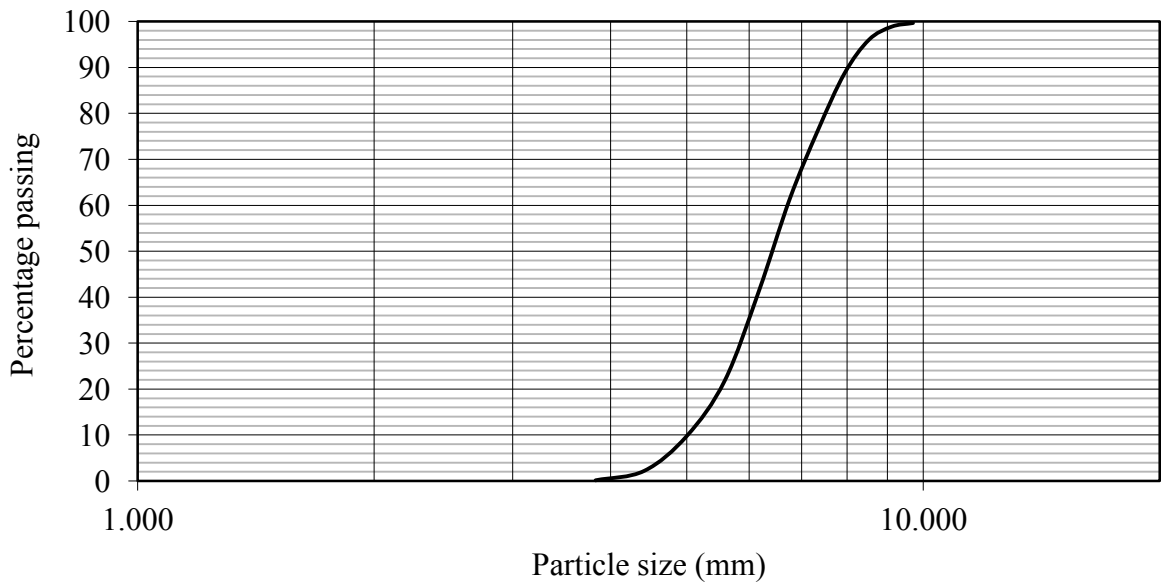


Figure F-20- Size distribution of specimen (Test 20), $D_{60}=6.7$ mm, $D_{50}=6.4$ mm, $D_{10}=5.0$ mm and $F_{corr}=0.89$

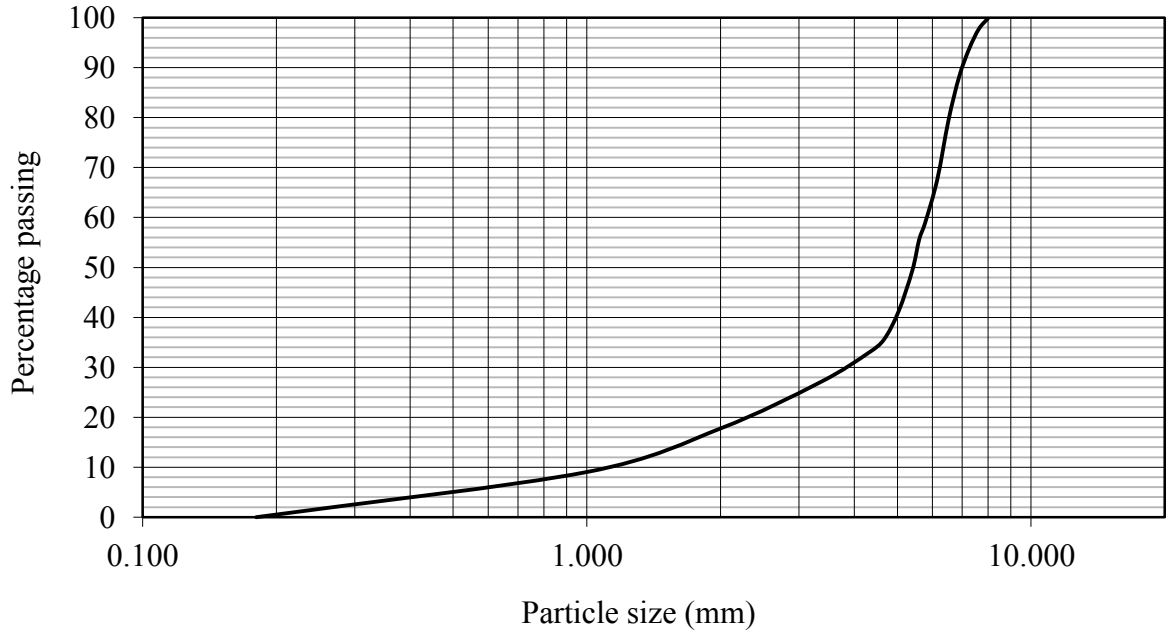


Figure F-21- Size distribution of specimen (Test 21), $D_{60}=5.9$ mm, $D_{50}=5.4$ mm,
 $D_{10}=1.1$ mm and $F_{corr}=0.8$

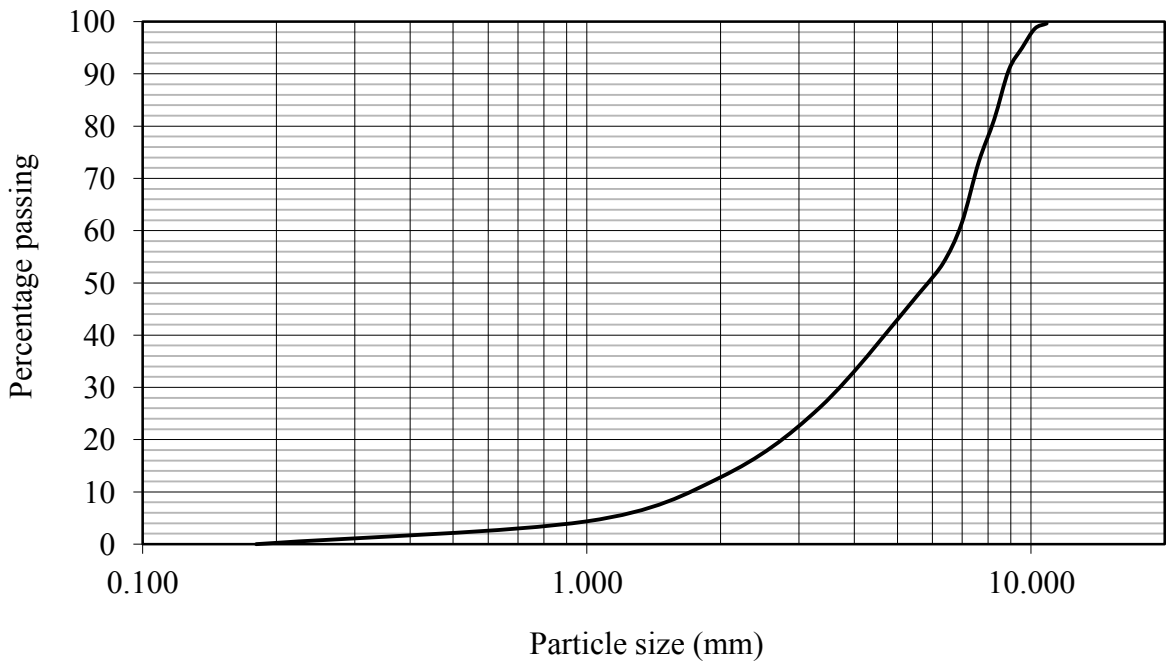


Figure F-22- Size distribution of specimen (Test 22), $D_{60}=6.9$ mm, $D_{50}=6.0$ mm,
 $D_{10}=1.8$ mm and $F_{corr}=1$

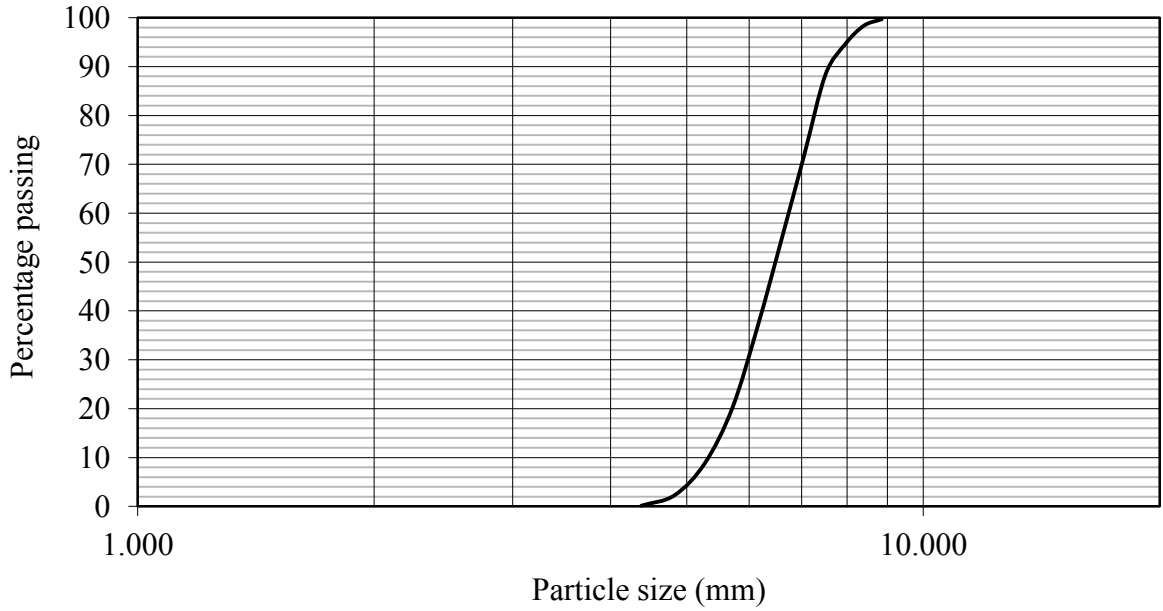


Figure F-23- Size distribution of specimen (Test 23), $D_{60}=6.7$ mm, $D_{50}=6.5$ mm, $D_{10}=5.3$ mm and $F_{corr}=0.8$

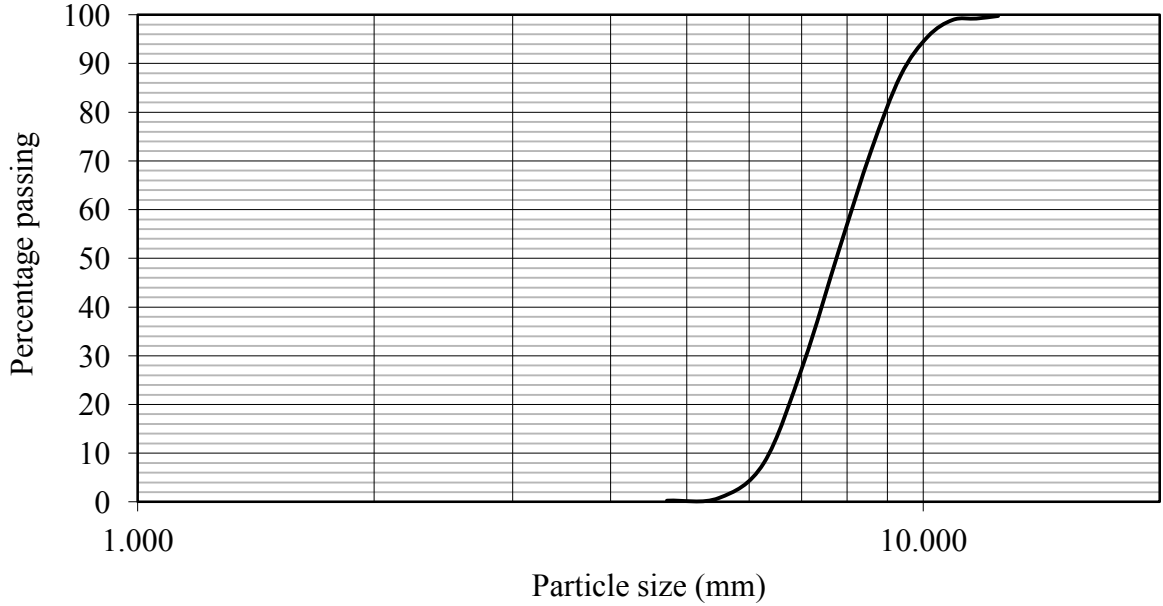


Figure F-24- Size distribution of specimen (Test 24), $D_{60}=8.1$ mm, $D_{50}=7.8$ mm, $D_{10}=6.3$ mm and $F_{corr}=1$

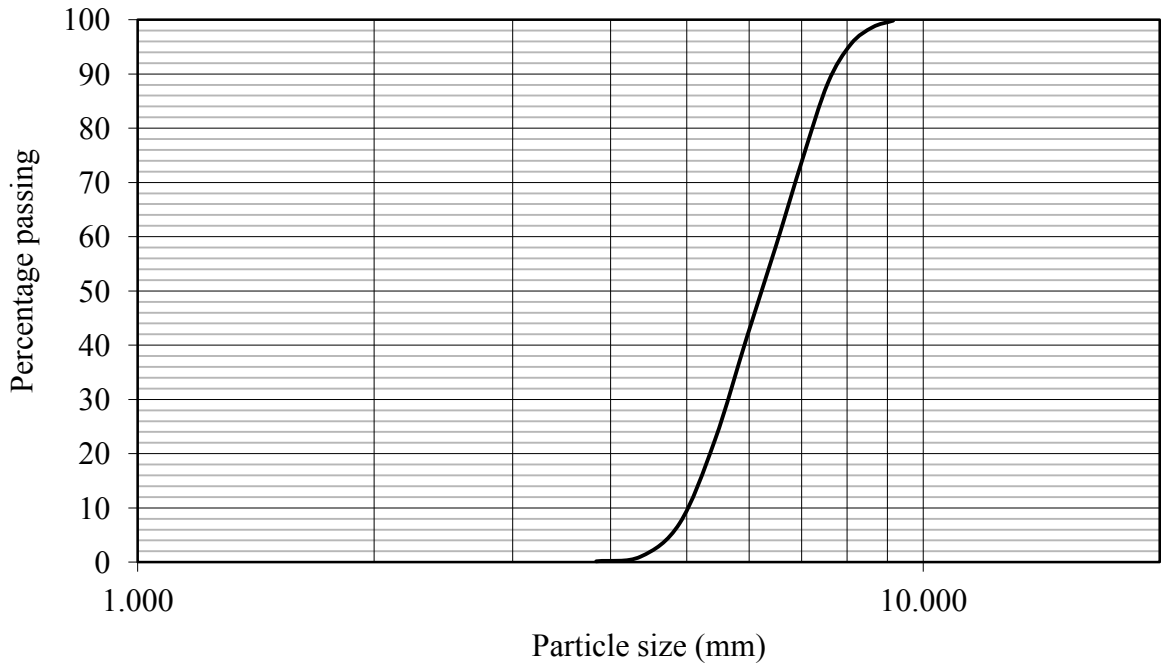


Figure F-25- Size distribution of specimen (Test 25), $D_{60}=6.6$ mm, $D_{50}=6.3$ mm,
 $D_{10}=5.1$ mm and $F_{corr}=0.88$

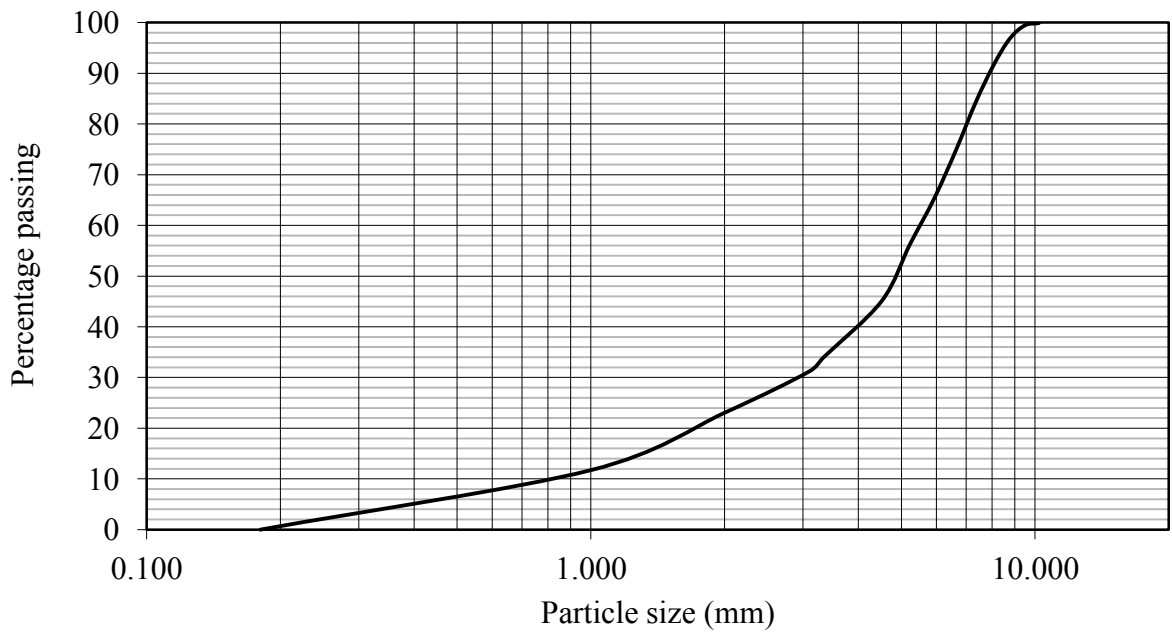


Figure F-26- Size distribution of specimen (Test 26), $D_{60}=5.6$ mm, $D_{50}=4.9$ mm,
 $D_{10}=0.9$ mm and $F_{corr}=0.92$

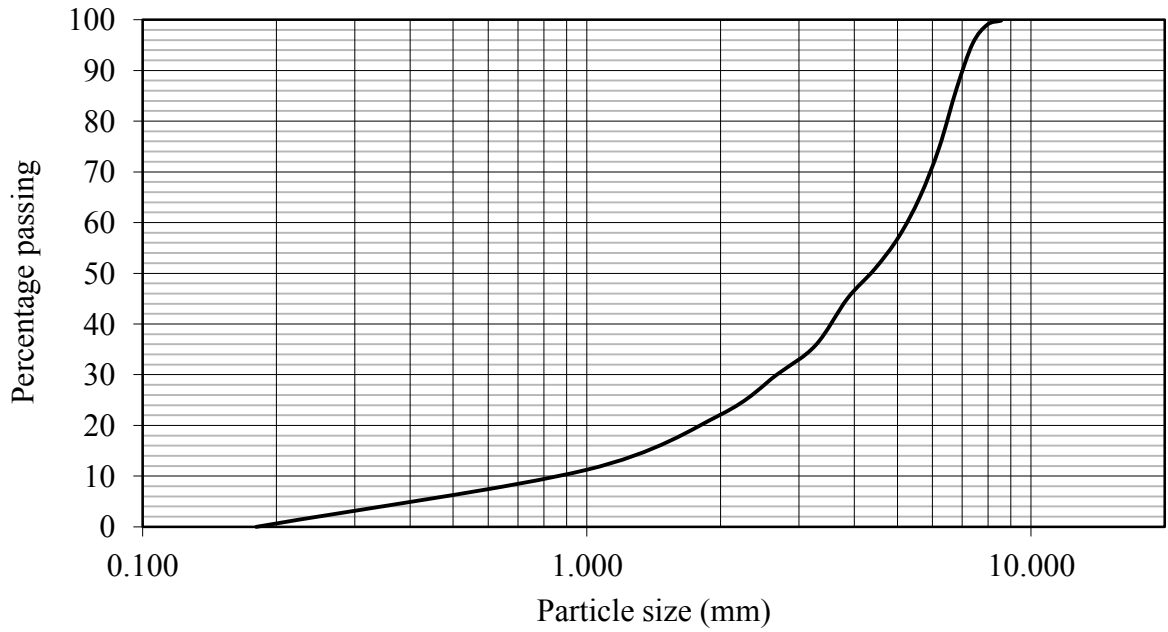


Figure F-27- Size distribution of specimen (Test 27), $D_{60}=5.2$ mm, $D_{50}=4.4$ mm,
 $D_{10}=0.9$ mm and $F_{corr}=0.8$